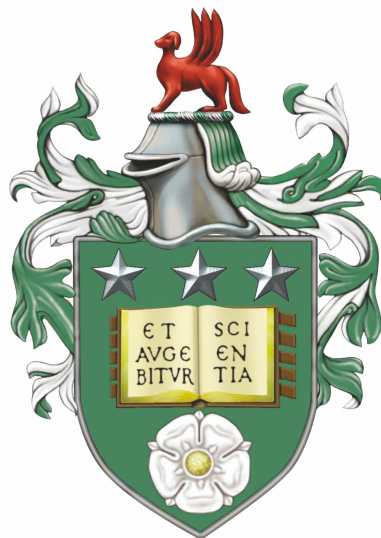


Navigating Networks:
The Translation of Single Molecule Properties to
Multi-Molecular Hierarchical Protein Networks



Matthew David George Hughes

School of Physics and Astronomy
The University of Leeds

Submitted in accordance with the requirements for the degree of Doctor of Philosophy

February 2021

Declaration

The candidate confirms that the work submitted is their own, except where work which has formed part of jointly authored publications has been included. The contribution of the candidate and the other authors to this work has been explicitly indicated below. The candidate confirms that appropriate credit has been given within the thesis where reference has been made to the work of others. This copy has been supplied on the understanding that it is copyright material and that no quotation from the thesis may be published without proper acknowledgement.

©2021 The University of Leeds and Matthew David George Hughes.

The right of Matthew David George Hughes to be identified as Author of this work has been asserted by him in accordance with the Copyright, Designs and Patents Act 1988.

Inclusion of published material:

Figures and text were reproduced from the publication entitled “Single molecule protein stabilisation translates to macro-molecular mechanics of a protein network” (*Soft matter*, 2020, Issue: 27) in chapter 3 with permission from the Royal Society of Chemistry. The experimental work, analysis and writing of the publication was performed by Matthew David George Hughes (author of this thesis). Protein production required for the publication was performed by research technician Sophie Cussons. Beamtime assistance was provided by research technician Sophie Cussons and Dr Najet Mahmoudi. Edits and feedback were provided by Dr Najet Mahmoudi, Prof David J. Brockwell, and Prof Lorna Dougan.

Work presented in chapter 4 is currently under review at the American Chemical Society: *ACS Nano*, entitled “Control of intra-protein nano-staples defines network architecture and mechanics of protein hydrogels due to *in situ* protein unfolding.”. The experimental work, analysis and writing of the publication was performed by Matthew David George Hughes (author of this thesis). Computational work and analysis was performed by Dr Benjamin S. Hanson, and is clearly marked and credited in the text, where appropriate. Protein production for the publication were performed by research technician Sophie Cussons. Beamtime assistance was provided by research technician Sophie Cussons and Dr Najet Mahmoudi. Edits and feedback were provided by Dr Benjamin S. Hanson, Dr Najet Mahmoudi, Prof David J. Brockwell, and Prof Lorna Dougan.

For everyone who always believed in me.

“Something that you receive because you are lucky and something you are given because you are recognized are different in essence”

– Toshinori ‘All Might’ Yagi to Izuku ‘Deku’ Midoriya

Acknowledgements

First and foremost my largest thanks goes to my supervisors Prof. Lorna Dougan and Prof. David Brockwell, who were mad enough to take me on as a Ph.D student even after meeting me in person. When I think about how far I have come, I honestly struggle to believe its true and I never would have got this far if it wasn't for the help, guidance and support of Lorna and David. They have both taught me so much and I will always be grateful for everything I have learnt. Thank you to Lorna for: guiding me through this project; helping me to believe in myself and building my confidence in my ability to do science; and tempering my desire to constantly do experiments and getting me to write them down. Discussions with Lorna about new projects, experiments, and new results have been some of the best conversations of my Ph.D, always putting a smile on my face. I really admire her unending enthusiasm for science, her imagination and her ability to express and convey complex scientific ideas. Thank you to David who was a font of knowledge and always knew what to suggest when something wasn't working. Discussions with David and his insightful questioning have helped me build the confidence to defend my science and learn new ways to improve it. His unique insight into problems and seemingly endless supply of knowledge and solutions make me really admire him (even though he is from Enfield, which everyone knows isn't as good as Potters Bar). I would also like to thank the White Rose Consortium for making this research possible.

Thank you to my collaborator Dr Najet Mahmoudi, for her help on beam time experiments which was irreplaceable and for letting me return to ISIS even after things went ... less than smoothly on some beam times. Also I would like to thank Najet for supervising me during my PIPS at ISIS, which was a fantastic opportunity in-which I learnt so much about scattering, giving me a lasting love for this awesome technique.

A big shout out needs to go to Sophie, who deserves a massive thank you for growing the large quantities of protein needed for this project and for not murdering me where I stood as I made more outrageous demands for grams of protein.

The rest of the Dougan group have also been fantastic for all the help and support they have given me: from sharing an office with Ben and Kalila; to bouncing less than sober ideas off an even less than sober Harry; to the compliments and helpful criticisms when presenting work at group meetings. Thank you to Sophie, Kalila and Harry for their help on beam times at ISIS, providing both fantastic experimental support and making sure I didn't have a complete breakdown as everything went wrong (especially on **that** beam time). And thank you to everyone who read chapters of my thesis, especially Ben who read my first chapter which was so poorly written LaTeX barely recognised it was in English.

So many thanks go to my partner Alicia who has been an unbelievable source of support during my Ph.D: making sure that I looked after myself when experiments required long days; making dinners for me when I'd been working late, celebrating all my small achievements along the way. But the thing I'd most like to thank her for is for always telling me I could do it and believing in me, especially when I didn't believe

in myself.

I also need to thank my friends who have been brilliant in helping me maintain some semblance of sanity throughout my Ph.D and in particular while writing my thesis. Also thank you to all my friends who were unwillingly ‘rubber ducked’ and had to listen to me explain my science so I could work out what to write.

Thank you to my family for their support, continued interest and tolerance to endless hear me talk about science, especially my little brother Alex, who told me that what I do is very impressive (I think he also said cool but he’ll deny that). In particular, I’d like to thank two very important people in my life, who I have only ever wanted to make proud. Firstly, I want to give a huge thanks to my Mum who is probably the most headstrong person I have ever met, a quality that she has passed on to me (to the continued frustration of my friends), a quality without which I would not have been able to and complete this Ph.D. And secondly, I want to thank my Nan who has always help drive me and always been excited to hear about my studies, from being offered a Ph.D studentship, to the publication of my first paper, to hopefully the submission of this thesis. My Mum and Nan are two of the most amazing people, who’s love and support has helped me achieve more than I ever thought I could.

Finally, I’d like to give a special mention to both my father and grandfather, who were the best Dad and Grandad I could ever have asked for and who are always with me. I hope this thesis makes them both proud.

Abstract

Hierarchical networks of semi-flexible biopolymers are ubiquitous in nature and are fascinating for their paradoxical combination of extraordinary mechanical strength and ability to grow, reshape and adapt to their environment. These biological hierarchical networks serve as inspiration for novel bio-mimic/bio-inspired materials. However, despite the ubiquity of these systems in nature it remains a fundamental challenge in soft matter physics and network theory to relate the properties of an individual building block to the collective response of a network of building blocks. Here, we utilise folded globular protein-based hydrogels constructed from maltose binding protein (MBP) and bovine serum albumin (BSA) to investigate the translation of single molecule stability and force lability, respectively, to the architectural and mechanical properties of a protein network. To achieve this, we employ a multi-modal cross length-scale characterisation approach, combining circular dichroism (CD), small-angle scattering (SAS), and rheology. Using this combined approach, we show that the single molecule stability of the building block translates to the mechanical strength of the network and that *in situ* force-induced unfolding is crucial in defining the architecture of folded protein networks. Furthermore, we have deconvoluted the contributions of building block thermodynamic and mechanical stabilities, illustrating that different types of stability have distinct roles in defining network properties.

This thesis has demonstrated the importance of the building block stability on network structural and mechanical properties and the necessity of a multi-modal cross-length scale approach. Furthermore, our work has shown that consideration of only the cross-linking network is not sufficient to produce a complete theory connecting the behaviour of a single building block to the collective behaviour of a network of building blocks. This is an important step in understanding, providing insight into fundamental hierarchical mechanics and a novel route to develop and tune new biomaterials for future applications.

Contents

Abstract	vi
Contents	vii
Publications	xi
List of Abbreviations	xiv
List of Tables	xviii
List of Figures	xviii
1 Introduction	1
1.1 Hierarchical networks in living systems	2
1.1.1 Collagen fibrils	3
1.1.2 Fibrin blood clots	4
1.1.3 Relating the behaviour of an individual to the properties of a network of individuals	6
1.2 Hierarchical systems in biology at the nano-scale	7
1.2.1 Proteins: from amino acids to folded structure	7
1.2.2 Protein stability	10
1.3 Hydrogels: synthetic hierachical networks	20
1.3.1 Tailoring the properties of hydrogel networks	21
1.4 Folded protein-based hydrogels	25
1.4.1 Folded proteins as hydrogel building block	25
1.4.2 Determining design rules for protein based hydrogels	27
1.5 Aims and objectives	30

2	Materials and methods	32
2.1	Materials, buffers and stocks	32
2.1.1	Materials	32
2.1.2	Growth Media	33
2.1.3	Buffers	33
2.1.4	Reagent Stocks	34
2.2	Protein expression, purification, storage and resuspension	35
2.2.1	Transformation of cells	36
2.2.2	Full-scale Expression	37
2.2.3	Cell Lysis	37
2.2.4	Purification	38
2.2.5	Storage of Protein	39
2.3	Hydrogel sample preparation and photochemical gelation	40
2.3.1	Resuspension of high concentration protein stock	40
2.3.2	Preparation of pre-gelation hydrogel solution	41
2.3.3	Photo-chemical cross-linking reaction	41
2.4	Characterisation of the protein building block	45
2.4.1	Circular Dichroism Spectroscopy	45
2.4.2	Differential Scanning Calorimetry	49
2.5	Characterisation of the network architecture	53
2.5.1	Theory of scattering	53
2.5.2	Analysis of scattering data - the form and structure factor	60
2.5.3	Small-angle scattering experiments	62
2.6	Bulk mechanical characterisation via rheology	63
2.6.1	Shear Rheology and the shear modulus	64
2.6.2	Anton Paar pseudo-strain controlled rheometer	67
3	Single Molecule Protein Stabilisation Translates to Macromolecular Mechanics of a Protein Network	74
3.1	Selection of hydrogel building block and model system	75
3.1.1	Desired properties of a model protein hydrogel building block	75

3.1.2	Maltose binding protein	75
3.1.3	Model system to investigate the effects of building block stability on bulk mechanics of protein networks	80
3.2	Modulation of Hydrogel Mechanics	80
3.2.1	Characterisation of the Linear Mechanics of MBP Hydrogels . . .	80
3.2.2	Characterisation of the Load-Unload Behaviour of MBP Hydrogels	82
3.2.3	Determination of MBP thermal stability and MBP:maltose disso- ciation constant	86
3.2.4	Occupation model of Hydrogel mechanical modulation	87
3.3	Modulation of Hydrogel Structure	90
3.4	Modulation of Hydrogel Dynamics	94
3.5	Discussion	97
4	Unravelling Nature’s Networks: <i>In situ</i> protein unfolding defines network architecture and mechanics of protein hydrogels	100
4.1	Selection of model protein and design of model system to investigate the role of <i>in situ</i> protein unfolding in network architecture and mechanics . .	102
4.1.1	Selection of BSA as a model protein	102
4.2	Modulation of structure on the molecular scale	105
4.3	Modulation of structure on the network scale	108
4.3.1	Characterisation of BSA hydrogel network architecture via small- angle scattering	108
4.3.2	Computational modelling of BSA hydrogel network formation . . .	116
4.4	Modulation of Mechanics on the Bulk Scale	119
4.4.1	Effects of <i>in situ</i> unfolding on the linear mechanical response of BSA hydrogels	119
4.4.2	Effects of <i>in situ</i> unfolding on the behaviour of BSA hydrogels under load	123
4.4.3	Effects of <i>in situ</i> unfolding on the non-linear behaviour of BSA hydrogels	125
4.5	Discussion	126

5	A Tale of Two Stabilities: Deconvoluting the Roles of Protein Thermodynamic and Mechanical Stability in Hierarchical Networks	128
5.1	Introduction	128
5.2	Selection of model protein building block and design of model system . . .	130
5.2.1	Effects of urea on folded proteins	130
5.3	Characterisation of building block stability	132
5.4	Effect of thermodynamic and mechanical stability on hydrogel network architecture	134
5.5	Differential effects of building block thermodynamic and mechanical stability on network bulk mechanics	144
5.5.1	Effects on linear mechanical behaviour	144
5.5.2	Effects on non-linear mechanical behaviour	156
5.6	Conclusion	160
6	Discussion and Future Work	166
6.1	The translation of intrinsic stability of the network building block to the structural and mechanical properties of the network	167
6.1.1	Deconvolution of the distinct roles of building block thermodynamic and mechanical stability in hierarchical protein networks . .	171
6.2	The defining role of <i>in situ</i> unfolding on hierarchical network architecture and subsequent mechanics	175
6.3	Future Work	178
6.3.1	Determination of the formation process of photo-chemically cross-linked protein networks	179
6.3.2	Crossover from globular to fibrous protein networks	179
A	List of chemicals and experimental apparatus	181
A.1	List of Chemicals	182
B	Additional Formulae and Derivations	184
B.1	Derivation of the proportion of bound-MBP	184
B.2	Langmuir-type equation	185

B.3	Derivation of fractal structure factor	185
B.4	Derivation of the number of monomers in a finite-sized fractal	187
C	Supplementary info for chapter 3	189
C.1	Additional rheological measurements of MBP hydrogels	189
C.2	SAS form factor measurements of MBP and exemplar SAS fitting	197
D	Supplementary info for chapter 4	199
D.1	Additional structural information for the modulation of architecture due to <i>in situ</i> protein unfolding	200
D.2	Additional information regarding the mechanical characterisation of BSA hydrogels	203
E	Supplementary info for chapter 5	204

Publications

Refereed Journals

Marcelo A. da Silva, Samuel Lenton, **Matt D.G. Hughes**, David J. Brockwell and Lorna Dougan. Assessing the Potential of Folded Globular Polyproteins As Hydrogel Building Blocks. *Biomacromolecules*, 18(2):636–636, 2017.

Matt D.G. Hughes, Sophie Cussons, Najet Mahmoudi, David J. Brockwell and Lorna Dougan. Single molecule protein stabilisation translates to macromolecular mechanics of a protein network. *Soft Matter*, 16:6389–6399, 2020.

Anders Aufderhorst-Roberts, **Matt D.G. Hughes**, Andrew Hare, David A. Head, Nikil Kapur, David J. Brockwell and Lorna Dougan. Reaction Rate Governs the Viscoelasticity and Nanostructure of Folded Protein Hydrogels. *Biomacromolecules*, 21(10):4253–4260, 2020.

Under review

Matt D.G. Hughes, Benjamin S. Hanson, Sophie Cussons, Najet Mahmoudi, David J. Brockwell and Lorna Dougan. Control of intra-protein nano-staples defines network architecture and mechanics of protein hydrogels due to *in situ* protein unfolding. *ACS Nano*, (under review).

Delanyo Kpeglo, **Matt D.G. Hughes**, Lorna Dougan, Malcolm Haddrick, Margaret A. Knowles, Stephen D. Evans, and Sally A. Peyman. Modelling the *In Vivo* Mechanical Stiffness of Pancreatic Ductal Adenocarcinoma. *Advanced Biology*, (under review).

List of abbreviations

Experimental Technique

AFM	Atomic force microscopy
CD	Circular dichroism
DSC	Differential scanning calorimetry
SAS	Small-angle scattering
SAXS	Small-angle X-ray scattering
SANS	Small-angle neutron scattering
SMFS	Single molecule force spectroscopy

Model/Properties

ΔG	Change in Gibbs free energy
ΔH	Change in enthalpy
S	Entropy
ΔS	Change in entropy
P	Pressure
V	Volume
T	Temperature
T_m	Thermal melting temperature
Ω	Number of accessible states
ΔV	Change in volume
ΔE	Change in internal energy

ΔU	Change in Helmholtz free energy
ΔG_{un}	Difference in Gibbs free energy between the folded and unfolded state of a protein
ΔG_{TS}	Difference in Gibbs free energy between the folded and transition state of a protein
k_u	Rate of unfolding
k_f	Rate of folding
F_u	Unfolding force
F_b	Rupture force of cross-linker
Δx_u	Distance between the folded and transition state of a protein
ΔG_{un}^{urea}	Difference in Gibbs free energy between the folded and unfolded state of a protein in the presence of the denaturant urea
ΔG_{TS}^{urea}	Difference in Gibbs free energy between the folded and transition state of a protein in the presence of the denaturant urea
ΔG_{TS}^{apo}	Difference in Gibbs free energy between the folded and transition state of a protein in its apo state i.e. no ligand bound
$\Delta G_{TS}^{malt-urea}$	Difference in Gibbs free energy between the folded and transition state of a protein with the ligand maltose bound and in the presence of urea
λ	wavelength of radiation
Q	The momentum transfer between scattering particle and the scattering object
$p(q)$	Form factor
$S(q)$	Structure factor
D_f	Fractal dimension
ξ	Correlation length

σ	Shear stress
γ	Shear strain
ω	Angular frequency of applied strain
G	Shear modulus
G^*	Complex shear modulus
G'	Storage modulus
G''	Loss modulus
τ_1	Post-cross-linking relaxation timescale due to network rearrangement
τ_2	Post-cross-linking relaxation timescale due to protein unfolding or entanglement
B_1	Coefficient of τ_1 relaxation
B_2	Coefficient of τ_2 relaxation
μ	Cross-link density

Quantities

μg	microgram
mg	milligram
g	gram
kg	kilogram
ml	millilitre
μl	microlitre
l	litre
M	Molar
M_r	Molecular Weight
kPa	kilopascal
Pa	pascal
pN	piconewton

nN	nanonewton
Å	Ångstroms
nm	nanometre
μm	micrometre
mm	millimetre
cm	centimetre
m	metre
s	seconds
min	minutes

Databases

PDB	Protein data bank
-----	-------------------

Biological molecules

BSA	Bovine serum albumin
MBP	Maltose binding protein
DNA	Deoxyribonucleic acid

Important Chemicals

PB	Sodium phosphate buffer
Ru(II)bpy_3^{2+}	Tris-bipyridylruthenium(II)
NaPS	Sodium persulfate
DTT	Dithiothreitol

Constants

k_b	Boltzmann's constant
h	Plank's constant

List of Tables

1.4.2.2	Molecular level mechanical hierarchy and expected hydrogel properties	28
2.1.2.2	Growth media and its components	33
2.1.3.2	Sodium phosphate buffer and its components	34
2.1.3.4	Purification buffers and their components	34
2.1.4.2	Cross-linking reagent stocks and their components	35
2.5.1.2	Properties of X-rays and neutrons	59
3.3.0.2	Structural parameters extracted from SAS curves of MBP hydrogels in presence and absence of maltose.	92

List of Figures

1.0.0.1	Structure hierarchy in the Eiffel tower	1
1.1.1.1	Structure hierarchy of collagen fibrils	3
1.1.2.1	Structure hierarchy of fibrin clots	5
1.2.1.1	An amino acid	7
1.2.1.2	The 20 naturally occurring amino acids	8
1.2.1.3	The hierarchy of folded protein structure	9
1.2.2.1	A 1-D energy landscape of a protein	13
1.2.2.2	The 3D energy landscape of a protein	14

1.2.2.3	Different pulling geometries in force induced unfolding	17
1.2.2.4	The different mechanical clamps in proteins	18
1.3.0.1	2D example of hydrogel structure	20
1.3.1.1	A composite hydrogel network	21
1.3.1.2	An example of a double network hydrogel	23
1.3.1.3	An example of a β -peptide hydrogel network	24
1.4.1.1	An example of a folded protein hydrogel network	26
1.4.2.1	Folded protein hydrogel network to explore the interplay between cross-linker and load bearing molecule stability	28
2.3.3.1	Proposed mechanism of ruthenium/persulfate-mediated photo- chemical cross-linking	42
2.3.3.2	<i>In situ</i> rheometer lighting rig	44
2.4.1.1	Schematic of linearly and circularly polarised light	46
2.4.1.2	Exemplar circular dichroism spectra for different types of protein sec- ondary structure	47
2.4.2.1	Expected profile of a melting obtainable from a DSC experiments . . .	50
2.4.2.2	DSC scan temperature profile	52
2.5.1.1	Visualisation of the Principle of Superposition	54
2.5.1.2	Visualisation of Bragg diffraction	55
2.5.1.3	A schematic representation of a particle being scattered by a sample .	57
2.5.1.4	Vector diagram for elastic scattering, through an angle of 2θ	58
2.6.1.1	Visualisation of shear deformation	64
2.6.1.2	Applied oscillatory strain and the subsequent stress response	66
2.6.2.1	Parallel plate sample schematic	68
2.6.2.2	Exemplar protein hydrogel gelation curve	70
2.6.2.3	Exemplar Frequency sweep data for protein-based hydrogels	71
2.6.2.4	Exemplar stress-strain curve for protein-based hydrogels	72
2.6.2.5	Exemplar strain amplitude sweep data for protein-based hydrogels . .	73

3.1.2.1	Crystal structure of MBP in the absence and presence of maltose . . .	76
3.1.2.2	Modulation of mechanical stability of MBP in the presence of Maltose	77
3.1.2.3	Equilibrium reaction between apo- and bound-MBP	79
3.1.3.1	Schematic of MBP:maltose model hydrogel system	80
3.2.1.1	Frequency sweeps of MBP Hydrogels in varying concentrations of mal- tose	81
3.2.2.1	Stress-strain curves and energy dissipation of MBP hydrogels in vary- ing concentrations of maltose.	83
3.2.2.2	Efficiency of MBP hydrogels as a function of maltose concentration . .	84
3.2.2.3	Circular dichroism spectra of MBP <i>in situ</i> in hydrogels and the ex- tracted proportion of folded MBP	85
3.2.3.1	MBP:maltose affinity curve of MBP T_m as a function of maltose con- centration	86
3.2.4.1	Hydrogel mechanical strength as a function of proportion of 'occupied' MBP	88
3.3.0.1	SAS curves of MBP hydrogels in the absence and presence of maltose	90
3.3.0.2	Schematic representation of the network structure of MBP hydrogels .	93
3.4.0.1	Gelation curves of MBP hydrogels in varying concentrations of maltose	94
3.4.0.2	Unfolding time constants and internal forces present in MBP hydrogels during post-gelation relaxation	96
4.1.1.1	Crystal structure and topograph of BSA	103
4.1.1.2	Schematic of the model BSA, BSA:DTT hydrogel system	104
4.2.0.1	Normalised circular dichroism spectra of BSA <i>in situ</i> in hydrogels . .	105
4.2.0.2	Post-gelation protein unfolding in BSA hydrogels	106
4.3.1.1	SAS curves of BSA hydrogels illuminated by either neutrons or x-ray sources	108
4.3.1.2	Extracted fractal dimension and correlation length for BSA hydrogels in the absence and presence of DTT	109

4.3.1.3	Fractal-like cluster morphology of BSA hydrogels in the absence and presence of DTT	111
4.3.1.4	Volume fractions of the fractal-like clusters and the inter-cluster region of BSA hydrogels in the absence and presence of DTT	113
4.3.1.5	Schematic representation of the predicted structures of BSA hydrogels in the absence and presence of DTT	115
4.3.2.1	Computationally predicted structures of BSA hydrogels compared to experimentally observed structural results	117
4.4.1.1	Frequency sweeps of BSA hydrogels in the absence and presence of DTT	119
4.4.1.2	Shear moduli of BSA Hydrogels soaked post-gelation in DTT	121
4.4.1.3	Gelation curves of BSA hydrogels and extracted time constants of relaxation	122
4.4.2.1	Stress-stress strain curves of BSA hydrogels in the absence and presence of DTT and the extracted energy dissipated and efficiency	124
4.4.3.1	Strain amplitude ramps of BSA hydrogels in the absence and presence of DTT	125
5.2.1.1	Effect of urea on protein folding energy landscape	131
5.3.0.1	Effect of urea on MBP free energy of unfolding	133
5.4.0.1	SAXS curves of apo- and bound-MBP hydrogels in varying concentrations of urea	135
5.4.0.2	Extracted structural parameters of apo- and bound-MBP hydrogels in varying concentrations of urea	136
5.4.0.3	Fractal-like cluster morphology of apo- and bound-MBP hydrogels in varying concentrations of urea	138
5.4.0.4	Volume fractions of the fractal-like clusters and the inter-cluster region of apo- and bound-MBP hydrogels as a function of MBP thermodynamic stability	140

5.4.0.5	Schematic representation of the predicted structures of apo- and bound-MBP hydrogels in the presence and absence of urea	143
5.5.1.1	Frequency sweeps of apo- and bound-MBP hydrogels in varying concentrations of urea	145
5.5.1.2	Shear moduli of apo- and bound-MBP hydrogels as function of MBP thermodynamic stability	146
5.5.1.3	Gelation curves of apo- and bound-MBP hydrogels in varying concentrations of urea	148
5.5.1.4	Extracted relaxation time constants of apo- and bound-MBP hydrogels as a function of MBP thermodynamic stability	149
5.5.1.5	Extracted coefficient of relaxation of apo- and bound-MBP hydrogels as a function of MBP thermodynamic stability	151
5.5.1.6	Stress-strain curves of apo- and bound-MBP hydrogels in varying concentrations of urea	152
5.5.1.7	Energy dissipation and efficiency of apo- and bound-MBP hydrogels as a function of MBP thermodynamic stability	153
5.5.2.1	Non-linear behaviour of apo- and bound-MBP hydrogels in varying concentrations of urea	157
5.6.0.1	Suggested energy landscape model for the distinct roles of building block thermodynamic and mechanical stabilities	163
6.1.0.1	Chapter 3 key results summary figure	168
6.1.1.1	Chapter 5 key results summary figure	172
6.2.0.1	Chapter 4 key results summary figure	175
C.1.0.1	Extracted power law exponent of the frequency dependence of MBP hydrogel's G' and G'' as a function of maltose concentration	189
C.1.0.2	Strain amplitude ramps of MBP hydrogels in varying concentrations of maltose	190

C.1.0.3	Additional stress-strain curves of MBP hydrogels in varying maltose concentrations	191
C.1.0.4	Exemplar linear fit to hydrogel stress-strain curves	191
C.1.0.5	Residual strain at 0Pa upon unloading of MBP hydrogels as a function of maltose concentration	192
C.1.0.6	Exemplar stress-strain load curves of MBP hydrogels as a function of maximum strain	193
C.1.0.7	Additional energy dissipation values of MBP hydrogels as a function of maximum applied strain	194
C.1.0.8	Gelation time of MBP hydrogel in the presence of varying concentrations of maltose	194
C.1.0.9	Normal force of MBP hydrogel during gelation	195
C.1.0.10	Exemplar fit to MBP hydrogel gelation curves	196
C.2.0.1	SAS form factor measurements of MBP monomers	197
C.2.0.2	Exemplar fitting of SAS curves and kiessig analysis	198
D.0.0.1	Exemplar High Tension of CD spectrometer measuring high concentration BSA samples	199
D.1.0.1	Molecular level structural comparison of BSA in the absence and presence of DTT	200
D.1.0.2	Comparison of SAS curves from BSA and MBP hydrogels	200
D.1.0.3	Exemplar fit for the extraction of cluster size and number of protein monomers in fractal-like cross-linked clusters	201
D.1.0.4	Box-counting results for the determination of the fractal dimension of computationally predicted structures	202
D.2.0.1	Extracted rheological relaxation timescales of BSA hydrogels, pre-and post-DTT soak	203
D.2.0.2	Exemplar fits of BSA hydrogel gelation curves	203
E.0.0.1	SAXS curves of high concentration (100mg/ml) MBP solutions	204

Chapter 1

Introduction

This thesis presents structural and mechanical evaluations of novel folded protein based-hydrogel networks to investigate their design rules and possible translation of single molecule properties to the bulk properties of a hierarchical network. Hierarchical networks are composed of structural elements that themselves have structure, resulting in structure at multiple length-scales [1]. A fantastic example is the Eiffel tower.

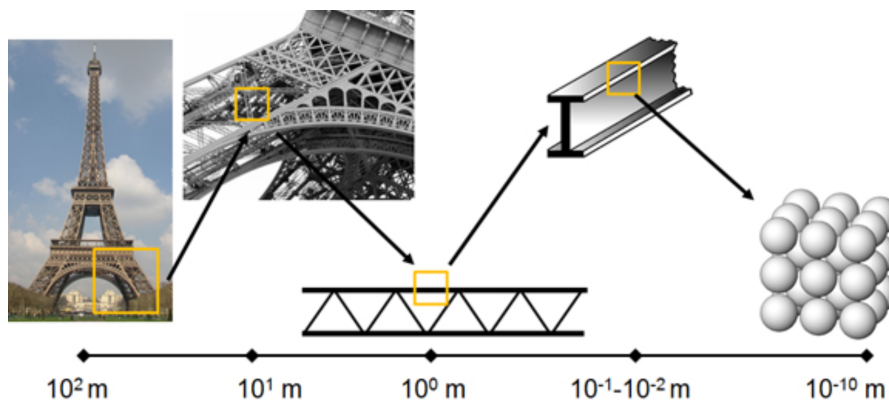


Figure 1.0.0.1: Schematic depicting the levels of structural hierarchy present in the Eiffel tower. Reproduced with permission from the Bone Biology and Mechanics Lab at IUPUI [2].

Figure 1.0.0.1 shows the different structures present in the Eiffel tower; from the lattice of iron and carbon atoms at the Ångström scale in the wrought iron girders, to the shape of the girders on the centimetre scale, to the welded scaffold of girders on the

metre scale, which then combine to construct the whole tower. The multi length-scale structure of the tower allows it to remain structurally sound even though less than 1% of the volume is made of wrought iron, which is weaker than structural steel used to construct most skyscrapers of similar height [1]. Furthermore the hierarchical structure allows small subunits of girders to be used for ease of construction. This is a macro-scale example of a hierarchically structured network, such hierarchy of structure on the multiple length scales is prevalent in soft materials and in biological systems.

This chapter will discuss the prevalence of hierarchical networks in living systems as well as several well-studied examples, before covering the background on hierarchical bio-systems on the nano-scale in particular focusing on protein structure and stability. Section 1.3 introduces the hierarchically structured soft material - hydrogels, and discusses methods that have been used to tune the properties of such materials. This is followed by the introduction of a relatively new novel bio-material: folded protein based hydrogels and the studies that have been conducted to try and determine their design parameters. Finally the chapter will end by outlining the aims and objectives of this project as well as the methods taken to achieve these.

1.1 Hierarchical networks in living systems

Hierarchical assemblies of semi-flexible bio-polymers are crucial to all living systems [3–5], and are fascinating because they paradoxically demonstrate extraordinary mechanical strength and resilience, while also being able to grow, change and adapt to environment changes as the organism requires [6]. These hierarchical assemblies are ubiquitous in living systems. The reasons for this ubiquity are two-fold; i) they allow smaller molecules (e.g. proteins [7] and polysaccharides [8]) to be used in the construction of large scale biological structures that are on the order of cells or larger (e.g. cell cytoskeletons and bones), and ii) they are crucial for the translation of properties across length-scales and time-scales, leading to a diverse range of behaviour including, but not limited to, reversible softening under compression [9], as well as both stiffening [10] and negative normal stress under shear [11].

Numerous examples of such hierarchical biopolymer assemblies are found in all domains of life, from the staggered architecture of collagen in the tendons of animals [12], to the regular structure of peptidoglycan in the cell walls of bacteria [13, 14], to the dendritic branching network of fibrin blood clots [15]. Two of these examples are explained in more detail below.

1.1.1 Collagen fibrils

Collagen is a fibrous structural protein that is found in tissue that is exposed to high tensile or compressive loads including tendons, bone, cartilage and teeth [16–19]. Collagen’s prevalence in such load bearing tissues is the result of the superior mechanical properties of collagen, with collagen molecules observed to withstand up to 50% tensile strain and stresses of several gigapascals [20]. Molecular collagen consists of 3 helical tropocollagen (TC) molecules that are twisted together to form ‘nano-ropes’ with lengths on the order of 300 nm [21, 22].

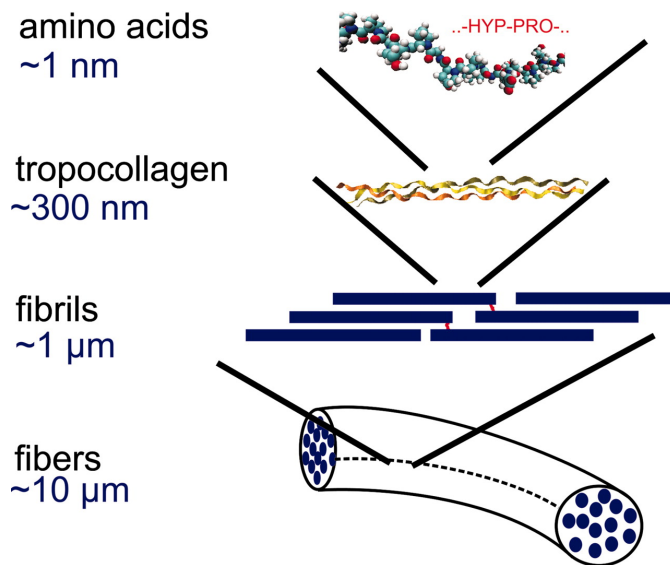


Figure 1.1.1.1: Schematic depicting the cross length-scale structural hierarchy in collagen fibrils. Reproduce from ref [23] with permission from National Academy of Sciences, ©(2006).

Figure 1.1.1.1 shows the staggered hierarchical architecture of these ‘nano-ropes’

of collagen fibrils on the order of micrometres. In 2006, Buehler [23] investigated the mechanical strength and energy dissipation behaviour of a single assembly of two staggered TC molecules. Buehler found that the length of the TC molecules and strength of inter-molecule interactions governed the regime of mechanical behaviour, i.e. short TC molecules correspond to a molecular shear-dominated regime, while long TC with weak intermolecular interactions correspond to an intermolecular slippage-dominated regime (however if the intermolecular interactions are strong then the assembly undergoes brittle-like rupture). Demonstrating that the staggered architecture of collagen is crucial in increasing the toughness and energy dissipation behaviour of load-bearing tissues, as it allows the force to be dissipated by molecular slipping within the structure rather than by the rupture of bonds between the TC ‘nano-ropes’ [23, 24]. This study and others [17, 25] have shown that due to this staggered architecture the properties of collagen are scale dependent. Single TC molecules exhibit a Young’s modulus and fracture strength of ~ 7 GPa and 11.2 GPa, respectively, whereas the Young’s modulus and fracture strength of a collagen fibril are ~ 5 GPa and 0.5 GPa respectively [17, 23]. It has been suggested, specifically for bones, that the observed length scales at each hierarchical level (Fig. 1.1.1.1) are the result of structural evolutionary adaptations towards maximising the particular tissues properties (such as strength or energy dissipation) through geometric size effects [26]. The specific hierarchical architecture of collagen demonstrates the importance of the overall hierarchical arrangements formed at different characteristic length-scales as it allows the translation of mechanical properties across length scales.

1.1.2 Fibrin blood clots

Blood clots consist of a dendritic gel-like mesh of branching fibers composed of the protein fibrinogen, which can form spontaneously at the site of trauma in order to stem the flow of blood from a wound [27]. This is a stark contrast to collagen rich tissues (e.g. tendons) in which contain collagen fibrils in parallel with one another and are purposefully constructed by organisms to build up tissues. In order for fibrin networks to perform their biological function effectively they must have suitable levels of stiffness and plasticity to block the flow of blood through the network, while also being permeable

enough to allow enzymes into the network to lyse it once the wound is repaired [28]. Blood clots have been observed to exhibit a wide range of elastic moduli from 0.1 Pa to up to 1500 Pa, dependant upon the branching structure of the clot and the physiological environment [29].

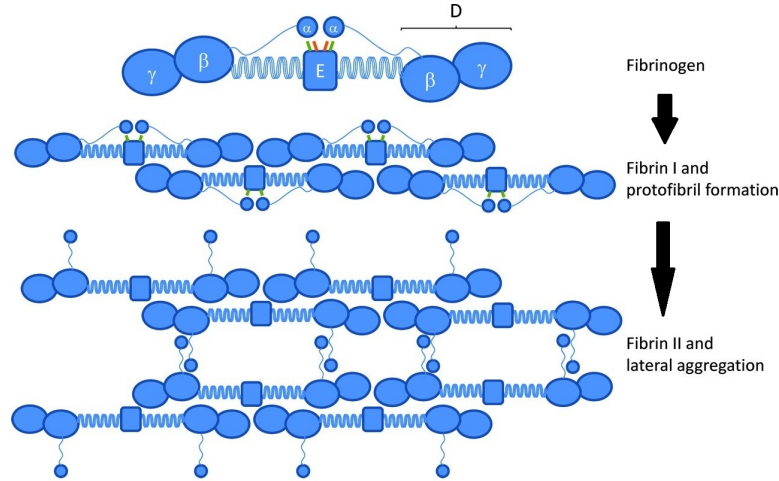


Figure 1.1.2.1: Schematic depicting the structural hierarchy in fibrin fibers. At the lowest level of hierarchy is the fibrinogen molecule consisting of a central globular, E, (with two associated α domains) connected by α -helical coiled-coil connector to globular end nodes, D, (which each consist of an β and γ domain). At the next level of hierarchy are the protofibrils which are formed from a staggered architecture of fibrinogen due to associated of the D end nodes and the E central domain. Formation of the protofibrils releases the α domains, which facilitate the lateral aggregation of protofibrils to form fibrin fibers.¹ Reproduced from ref [15] with permission from American Heart Association, Inc. ©2011

The hierarchical structure of fibrin fibers, that branch and connect to form the clot network, is shown in figure 1.1.2.1. The fibrinogen molecule has a rod-like shape approximately 45 nm in length and 2-5 nm in width, consisting of a central globular node (labelled E in Fig. 1.1.2.1) connected to two globular end nodes (labelled D in Fig. 1.1.2.1) by 17 nm long triple α -helical coiled-coil connectors [30, 31]. The globular nodes in the protein structure are crucial for the formation of fibrin protofibrils¹. Similar to collagen fibrils a staggered architecture is observed in the structure of the protofibrils that are formed from approximately 2 dozen fibrinogen monomers with lengths between 0.5-0.6 μm [32, 33]. These protofibrils then aggregate laterally to form thick fibers. As these

¹A detailed description of this formation process can be found in references [15, 27]

fibers thicken and increase in length, via lateral aggregation, they also branch and continue to laterally aggregate from the branch points, eventually yielding a self-supporting space-filling 3D network [34]. It is the difference in this branching 3D structure that leads to the wide range of elastic moduli exhibited by fibrin networks. It has been suggested that the stiffness of fibrin networks originates from the bending of fibers as opposed to the stretch of fibers seen in collagen networks [35]. Part of the basis for this hypothesis is that the fibers are likely to be stiffer when stretched along their axis rather than bent. Recent work [28, 36, 37] on the interesting non-linear properties of fibrin networks, has shown that upon compression the fibrin network exhibits strain softening, which is attributed to the buckling and bending of fibers in the network, before being followed by dramatic strain stiffening as a result of densification of the network [37]. This suggests that the mechanical behaviour of blood clots are controlled more by the bending of fibrin fibers than by their extension.

1.1.3 Relating the behaviour of an individual to the properties of a network of individuals

The examples above show that despite both networks having similar fibrous building blocks and staggered architecture at one level of hierarchy, the mechanical properties of the overall networks differ. This demonstrates that small changes in the structure at one characteristic length scale (in the cases above the inter-fiber length scale) can lead to remarkably different properties of the network. Predicting the outcome of changes to the building block or the structure of the network on the properties of the overall network is extremely non-trivial (i.e. not a simplistic scaling from single building block properties to network properties). In fact despite the prevalence of these hierarchical systems in nature and the growing literature in this area [38–43], it remains a fundamental challenge in soft matter physics to relate the properties of an individual polymer building block to the collective response of a network of such building blocks [44]. New insight into this fundamental problem would both further our understanding of biopolymer assemblies ubiquitous in living systems and allow for the development of novel bio-mimetic and bio-inspired materials [45–48].

1.2 Hierarchical systems in biology at the nano-scale

In the previous section the prevalence and importance of hierarchical assemblies was discussed, including macro-scale examples of such network. However structural hierarchy also exists in living systems on the nano-scale. A powerful example of this nano-scale hierarchy in living systems is proteins. This section will cover the levels of structure within proteins and discuss both the thermodynamic and mechanical stability of these folded 3D structures.

1.2.1 Proteins: from amino acids to folded structure

Proteins are fundamental to all life on Earth and are observed in all living systems currently known [49]. This is due to their involvement in a plethora of biological functions from enzymatic activity to force mediation to catalysis, or put more colloquially if a process occurs in a living system it almost certainly involves a protein. These crucial bio-polymers are long poly-peptide chains and have a hierarchy of structure starting on the Ångstrom level with single amino acids building up to complex 3-dimensional structures that are crucial to their *in vivo* functional ranging from several to hundreds of nanometres in size.

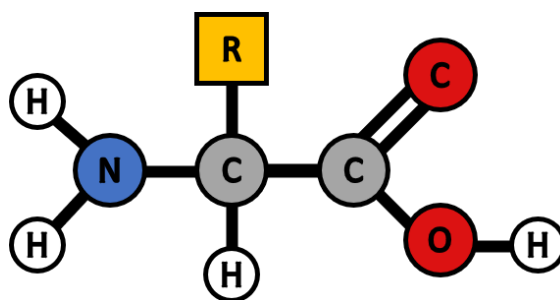


Figure 1.2.1.1: The structure of an amino acid, consisting of a common backbone structure and a side chain or R-group (R) that is unique to a given amino acid.

The small sub-unit monomers that construct proteins are called amino acids, and are connected together covalently via peptide bonds [50]. Amino acids are organic molecules consisting of a central carbon atom that is covalently bonded to a carboxylic acid group

(-COOH), an amino group (-NH₂), a hydrogen atom and a side chain group that is unique to any given amino acid. Figure 1.2.1.1 shows the generic structure of an amino acid, where the R-group is the side chain group.

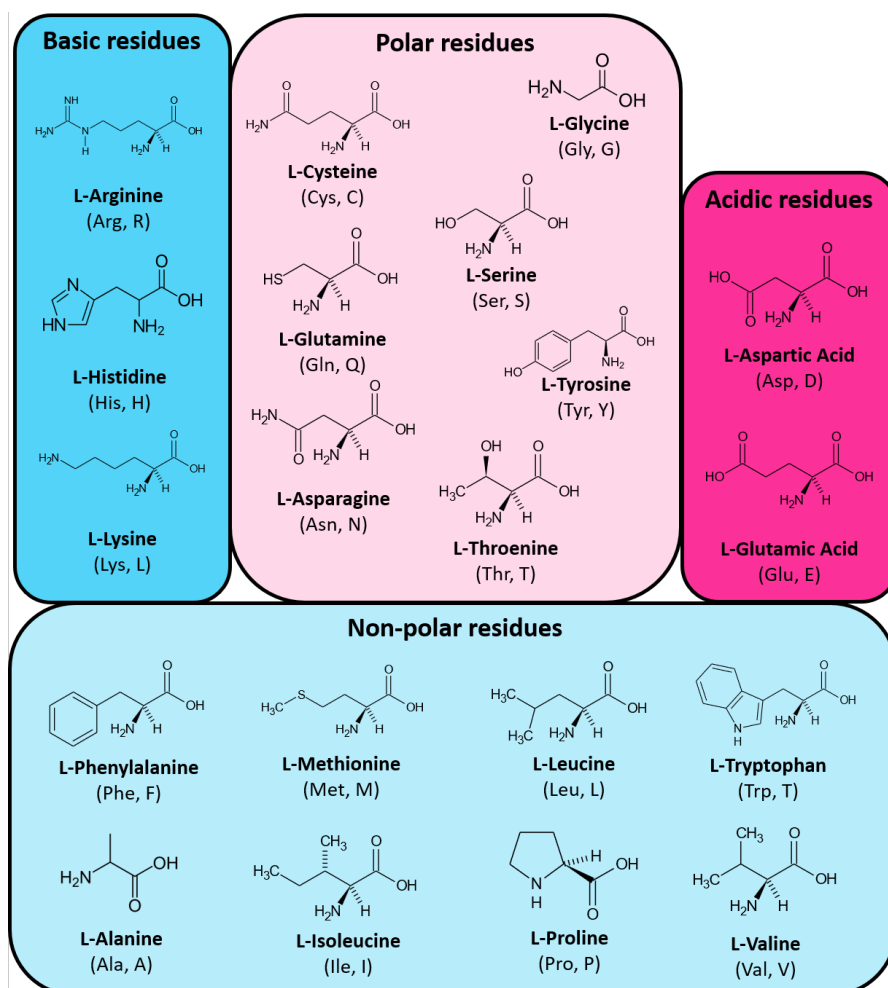


Figure 1.2.1.2: The 20 naturally occurring amino acids that are encoded by DNA. Each amino acid structure is shown with its three-letter and one-letter in addition to the full name.

There are 20 naturally occurring amino acids that are encoded for by DNA² each with a unique side chain conferring different physical and chemical properties. These amino acids are shown in figure 1.2.1.2 grouped according to similar chemical properties of their side chain R-group [53]. Their functional groups vary in terms of polarity, hydrophilicity

²The encoding and transcription processes of DNA to amino acids are not described in this thesis, however many references are available dedicated to describing this, including [51, 52].

(positive interaction with water), and charge. The order of these amino acids in the polypeptide chain is referred to as the protein sequence and forms the primary structure of a protein. This is the first level of hierarchy within the protein structure and the particular sequence of the amino acids at this level determines the higher order folded structure of the protein by defining the intra-chain interactions.

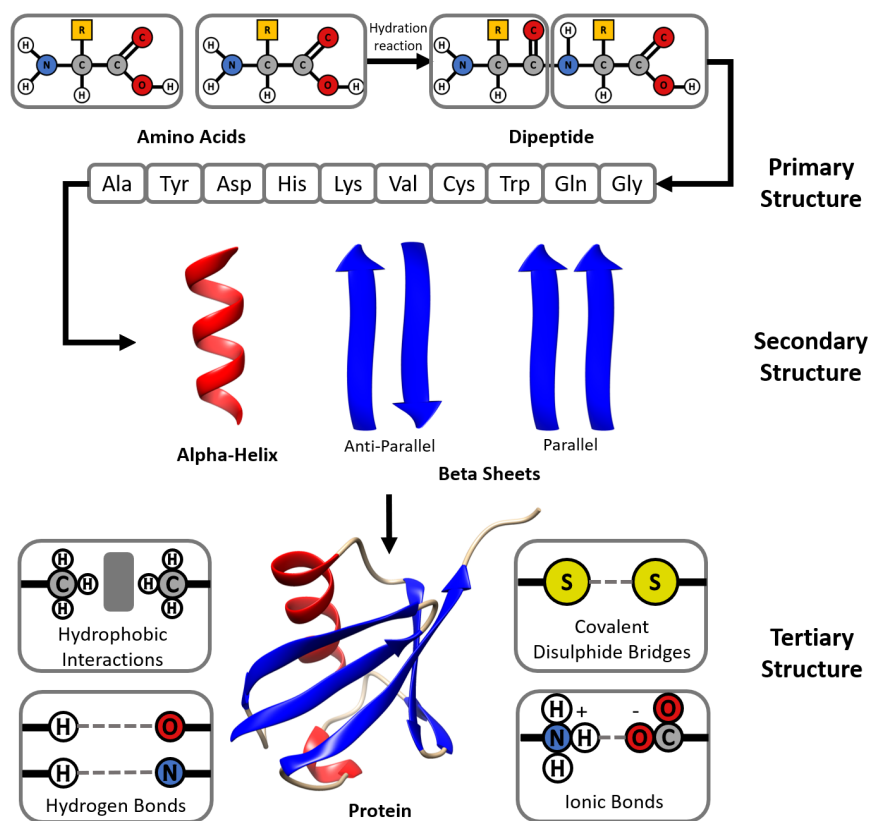


Figure 1.2.1.3: The hierarchy of protein folded structure. **Primary Structure** is the particular sequence of amino acids (residues) that are joined by peptide bonds. **Secondary Structure** consists of α -helices and β -sheets (both parallel and anti-parallel), which are formed by hydrogen bonding interactions between the residues in the primary structure. **Tertiary Structure** is the 3D folded structure of polypeptide chain and secondary structure elements and is formed via multiple intra-chain interactions including hydrophobic interactions, ionic bonds and disulphide bridges. The example protein shown here is ubiquitin (PDB code: 1UBQ [54])

Figure 1.2.1.3 shows the hierarchy of protein structure from a single amino acid through to folded structure. The functional groups, i.e. the amide group, and side chains of the residues in the primary structure are able to interact with one another non-covalently to form the higher order secondary and tertiary structures. The amide

groups in the backbone of the polypeptide chain can participate in intra-chain hydrogen bonding, which can result in the formation of secondary structure elements. These structures are α -helices and β -sheets, the latter of which is formed from multiple β -strands. This is the secondary level of hierarchy beyond the simple chain of amino acids. Non-covalent interactions between the residues of the primary structure and the secondary structure elements allow the protein to take a unique 3-D structure. The 3D configuration of the polypeptide chain and secondary structure elements is called the tertiary structure and is often referred to as the protein fold and is intimately linked to the biological function of the protein. Another level of hierarchy exist above the protein fold, known as the quaternary structure, which refers to complexes formed by multiple folded protein domains (e.g. hemoglobin [55]), for simplicity we shall focus on the single protein tertiary structure. The interactions that hold the 3D tertiary folded structure together include; i) hydrophobic interactions, where residues with ‘water-hating’ hydrophobic side chains are packed into the core of the protein fold and ‘water-loving’ hydrophilic residues are decorated on the surface (assuming the protein’s native environment is aqueous), ii) hydrogen bonds, where partially charged polar side chains interact weakly with partially charged hydrogen atoms in other side chains and in the hydrating water (the interaction is weak compared to ionic bonding due to small partial charges involved), iii) ionic bonds, where protonated basic and deprotonated acidic residues interact strongly (more strongly than hydrogen bonds due to the larger charges involved) via electrostatic Coulomb attraction, and iv) covalent disulphide bonds, where the thiol (-SH) side chains of two cysteine residues are oxidised forming a covalent bond between the two sulfur atoms [56–58]. All of these interaction work in conjunction to produce the unique and specific folded structure of a functional protein.

1.2.2 Protein stability

These interactions make folded proteins robust nano-building blocks with intrinsic properties, such as thermodynamic and mechanical stability as well as chemical functionality such as catalysis or enzymatic activity. The specific folded structure of proteins is crucial for proteins to be able to perform their biological functions, as such it is typically

important for the protein to maintain its folded state [59]. As stated in the last section a combination of non-covalent (and one covalent) interactions are involved in forming the folded structures of functional proteins, however these interactions are extremely sensitive to small changes in the environment. Understanding how a protein maintains its folded state in a range of physiological conditions is important to understanding their roles *in vivo*.

1.2.2.1 Thermodynamic stability and the Gibbs free energy

One method to quantify the stability of a protein fold is as a thermodynamic process from a folded state to an unfolded state and consider the free energy change associated with this kinetic change. The absolute free energy of a system is a measure of how favourable a state is, where states with the lowest free energy are the most favourable [59]. For a thermodynamic process, if the change in free energy from the initial state to the final state is negative the process will occur spontaneously, conversely if the free energy change is positive then the process will require energy to occur. The free energy change is a measure of the work done on a system to transfer it from one state to another, while the system exchanges heat with its environment [50]. Considering an isobaric (constant pressure) and isothermal (constant temperature) process, the change in the Gibbs free energy can be defined as [50]:

$$\Delta G = \Delta H - T\Delta S \quad (1.2.2.1)$$

Where ΔH and ΔS are the change in enthalpy and entropy, respectively. The change in enthalpy is defined as [50]:

$$\Delta H = \Delta E + P\Delta V \quad (1.2.2.2)$$

Where ΔE is the change in internal energy of the system and $P\Delta V$ is the work done on the system at constant pressure. The change in entropy of a system is a measure of

the change in the number of available conformational states between the initial and final systems. The entropy of a system is defined as [50]:

$$S = k_b \sum_i P_i \ln P_i \quad (1.2.2.3)$$

Where P_i is the probability of a single particle occupying the i th state. If it is assumed that probability of a single particle occupying all states is equal (i.e. $P_i = \frac{1}{\Omega}$) then equation 1.2.2.3 reduces to:

$$S = k_b \ln \Omega \quad (1.2.2.4)$$

Where Ω is the number of accessible states of a single particle. Each accessible state has an associated energy, so the greater the number of states, the higher the entropy because the energy dispersion is greater.

If we instead consider an isochoric (constant volume) and isothermal process a similar free energy expression exists:

$$\Delta U = \Delta E - T\Delta S \quad (1.2.2.5)$$

This expression is known as the Helmholtz free energy, and only differs from the Gibbs free energy by PV . For liquids PV is negligible as both the volume and pressure are small, meaning the value is less than the thermal energy, $k_b T$, of the system. Therefore in the case of liquids there is a negligible difference between the Helmholtz and Gibbs free energy [50]. In this thesis the change in free energy refers to the change in the Gibbs free energy of the system. The parity of the Gibbs free energy (Eqn. 1.2.2.1) gives information on whether a process is energetically favourable or unfavourable (i.e. if ΔG is negative (positive) the process is energetically favourable (unfavourable)). Keeping the importance of the parity in mind equation 1.2.2.1 demonstrates 2 key points;

- A large decrease in entropy (i.e. a large reduction in the number of accessible states available in a system) is unfavourable,
- A large increase in enthalpy (i.e. a large amount of energy is required for the process to take place) is unfavourable.

In the context of protein fold stability the free energy change discussed above is the difference between the free energies of folded state and the unfolded state, as depicted by ΔG_{un} in figure 1.2.2.1. ΔG_{un} is commonly referred to as the thermodynamic stability of the protein folded structure.

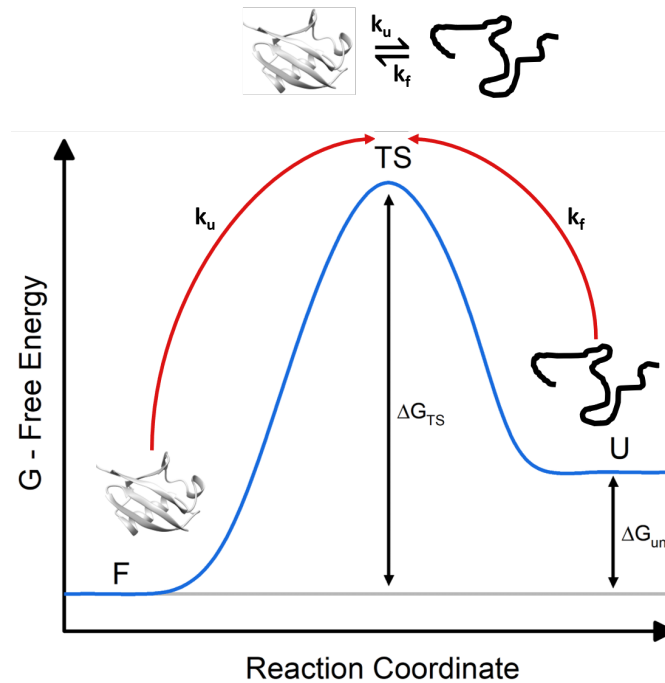


Figure 1.2.2.1: Top: The equilibrium reaction between the folded state (F) and the unfolded state (U), where k_u and k_f are the rate of unfolding and folding, respectively. Bottom: Schematic of a two-state energy landscape of protein, where the free energy of the system is plotted against the reaction coordinate being followed. The reaction is the parameter being probed when the protein system is being perturbed, for example in a chemical denaturation experiment the solvent accessible surface area is the reaction coordinate. Where ΔG_{un} is the free energy change between the folded state and the unfolded state, and ΔG_{TS} is the free energy change from the folded state to the transition state (TS).

Figure 1.2.2.1 shows an example of a two state energy landscape, where the thermodynamically stable folded state is separated, by a transition state energy barrier, from

the less thermodynamically stable unfolded state. If a single barrier to unfolding exists then the folding/unfolding of the protein is known as a two-state process. In general proteins have more complex landscapes with multiple stable intermediate between the folded and the unfolded state, due to multiple energy barriers along the reaction coordinate [60]. In fact it has been hypothesised that the energy landscapes of proteins is funnel shaped (Fig. 1.2.2.2) [60, 61].

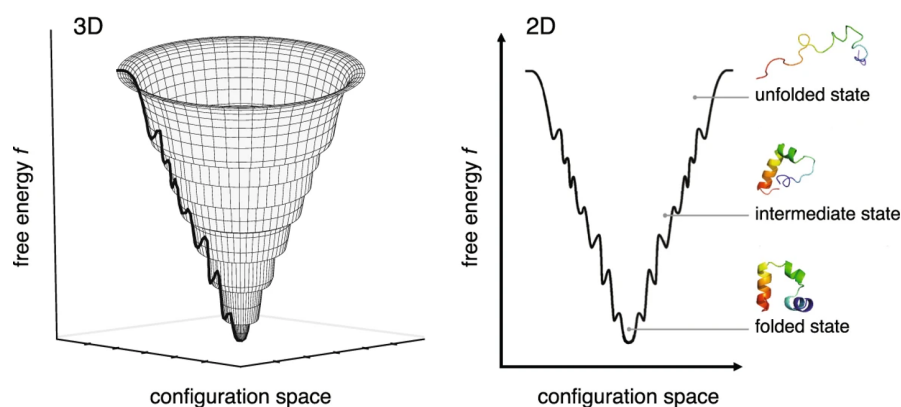


Figure 1.2.2.2: Schematic of the 3-D (right) and 2-D (left) energy landscape profile, where the z-axis (y-axis in 2-D) is the free energy of the particular configuration and the y and x axes (only x-axis in 2D) map the configuration space. Reproduced from ref [62] Nature Springer Ltd: Scientific Reports, ©2009.

At the top of the folding funnel the protein is in the unfolded state and has a large amount of conformational freedom. As the protein begins to fold and moves down through the funnel the number of conformational states available to the poly-peptide chain are restricted. The protein can explore many conformations between the unfolded and folded states, resulting a rough surface with multiple local minima corresponding to intermediate states [63]. The folded state has the lowest level of conformational freedom but is the global free energy minima of the system.

For a protein fold to be stable the Gibbs free energy of unfolding must be positive to make spontaneous unfolding unfavourable. As shown in figure 1.2.2.2 the unfolded state has the largest conformational freedom (high entropy), while the folded state has the smallest conformational space (low entropy) [59, 63]. This means that there is a large increase in the entropy of the system going from the folded to the unfolded state. In

accordance with equation 1.2.2.1, for the folded state to be stable (i.e. the Gibbs free energy of unfolding needs to be positive) the change in enthalpy from the folded to the unfolded state must be positive and larger than the $T\Delta S$ term. In order for a protein to unfold the non-covalent interactions, predominately hydrogen bonds, that hold the protein fold together need to be broken. This breakage of bonds requires energy to be input into the system resulting in an increase in the enthalpy of the system upon unfolding [50, 59, 64]. Interestingly, the hydrophobic interactions do not contribute to the enthalpy of the system but instead increase the entropy of the system in the folded state, reducing the absolute magnitude of $-T\Delta S$ term [63, 64]. This is due to the fact that in folded proteins the hydrophobic side chains are packed into the core of the protein, allowing the water molecules hydrating the protein surface to occupy more conformational states. In contrast in the unfolded state the hydrophobic residues of the protein are exposed to the solvent and the water molecules form a specific ‘cage’ structure around them. This cage structure of water restricts the number of conformational states the water molecules in the cage can take, hence lowering the entropy of the unfolded system [63, 64]. Hence, the hydrophobic interactions lower the magnitude of the $T\Delta S$ term. If these interactions within the protein molecule are sufficiently strong, such that $\Delta H > T\Delta S$, then the Gibbs free energy of unfolding will be positive and the protein fold will be stable. So, these interaction are crucial to the stability of the protein’s structure and by extension crucial to their biological function [65, 66].

By considering the interactions within the protein poly-peptide chain and the difference in entropy between the folded and unfolded states, the Gibbs free energy of unfolding, ΔG_{un} , gives a measure of the thermodynamic stability of the protein’s folded structure. It is worth noting that this is a global measurement of stability over the entire folded structure, rather than a measure of the local stability in specific regions of the protein fold.

1.2.2.2 Mechanical stability of protein fold domains

Another method to characterise the stability of proteins, that probes the specific local interactions within the folded structure is through force-induced mechanical denaturation. Single molecule force spectroscopy (SMFS) techniques, including atomic force microscopy (AFM), and magnetic/laser tweezers, allow for the probing of the mechanical stability of the proteins folded structure, and are in principle no different than classical stretching experiments performed in high school (though the equipment is much more sophisticated due to the low forces (order of 1-100 pN) and small length scales (order of nanometres) involved). Over the last few decades a diverse range of proteins have been mechanically unfolded; some proteins have been found to be completely mechanically labile presenting no resistance to the applied force, while others have been found to be mechanically robust withstanding forces ranging from tens to hundreds of piconewtons [67, 68]. The reason for this range of mechanical stabilities, as determined by higher unfolding force, lies in the bonding network that forms as a result of the structural hierarchy of proteins. The most mechanically stable proteins have been those that have an all β secondary structure, followed by proteins with α/β structures and the most mechanically liable proteins being those with all α structures [69, 70] This unfolding force corresponds to breaking of bonds, predominately hydrogen bonds, in the backbone of the protein [71]. All α -helical proteins (those that lack intra-strand covalent bonds e.g. disulphide bonds), in which the helices are predominately held together by hydrophobic interactions with few intra-strand hydrogen bonds, readily unfold to force. This suggests that the hydrogen bonds between β -strands in a β -sheet conformation provide more mechanical stability than the hydrophobic interactions holding α -helices together in all- α proteins.

While the general trend suggesting the secondary structure of a protein is the key determinant of its mechanical stability, it does not explain the range of unfolding forces observed for proteins with similar secondary and tertiary structures. For example the protein TmCSP unfolds at a force of 60 pN (at a pulling speed of 600 nm/s) [72], while a similarly structured protein, I27 unfolds at a force of 204 pN (at a pulling speed of 600

nm/s) [73]. It was suggested that this difference arose as a result of different hydrogen bond geometries [71, 74, 75] in proteins, though this was challenging to directly measure due to difference in the protein sequence and stabilities. In 2003 a study by Brockwell et al. [76] on the protein E2lip3 addressed this challenge. In this study the protein could be immobilised on a surface in two different positions, which enabled the bonds in the protein to be either ‘peeled’ or ‘sheared’ (depicted in Fig. 1.2.2.3).

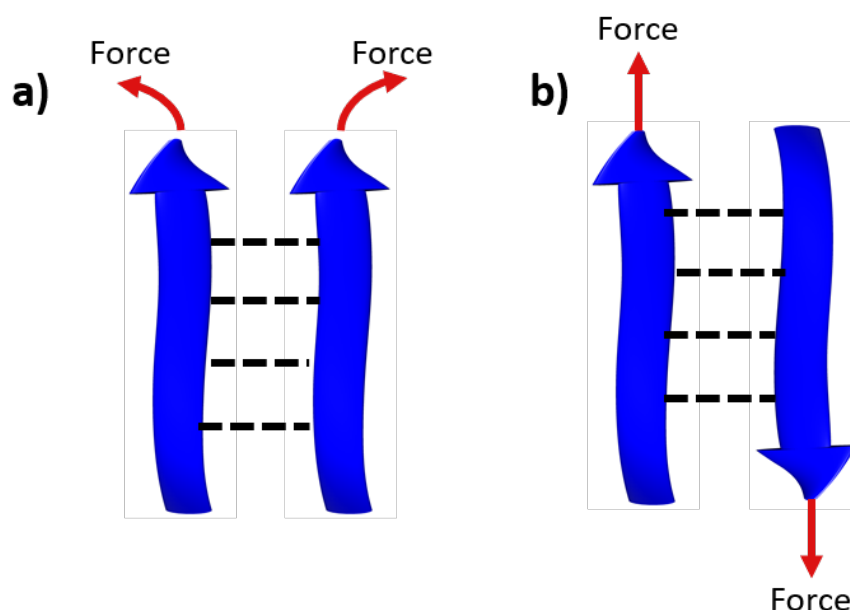


Figure 1.2.2.3: Illustration of the a) peeling and b) shear geometries of hydrogen bonded β -strands upon the application of applied force.

In the shear geometry E2lip3 was observed to unfold at a force of 177 pN (at a pulling speed of 700 nm/s), conversely in peeling geometry no measurable force was observed. This striking difference in unfolding forces is explained by considering the pulling geometries. In the shear geometry the hydrogen bonds are perpendicular to the applied force, while in the peeling geometry they are parallel. This means that in the shear geometry all the hydrogen bonds must be broken simultaneously to allow separation of the β -strands, while in the peeling geometry they can be broken sequentially allowing for easier separation of the strands. Since this study, many experimental [77–84] and theoretical [85–88] investigations have been conducted to determine the importance

structure elements within a protein can result in significant changes in the mechanical behaviour.

This section has discussed the mechanical characterisation of proteins as a method to investigate their stability. SMFS techniques have shown that proteins possess a wide range of mechanical stabilities; from proteins that are completely labile to force to proteins that extremely robust resisting unfolding until high forces are applied. Furthermore mechanical characterisation of proteins is far more effectively able to probe the local stability of a protein more effectively than thermodynamic techniques, with large variations in mechanical stability observed due to changes in the axis of applied force and subtle changes in the tertiary structure of proteins. Similar to what is observed in hierarchical networks of proteins, subtle changes in structure lead to large changes in the mechanical behaviour however, while on the single molecular level the motifs that govern the mechanics of the whole protein are understood, this same understanding is not present for hierarchical assemblies of proteins.

1.3 Hydrogels: synthetic hierachical networks

Hydrogels are three-dimensional hygroscopic networks formed from cross-linked (either chemically or physically) hydrophilic building blocks, such as synthetic polymers and short peptide chains, and are swollen by relatively large volumes of water (Fig. 1.3.0.1). By definition, for a material to be classed as a hydrogel it must be a gel in which the swelling agent is water [93]. Due to the significant water content hydrogels often possess a degree of flexibility and elasticity similar to that of natural tissue.

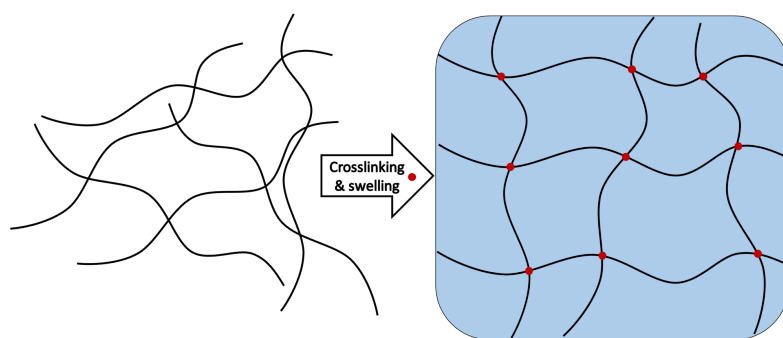


Figure 1.3.0.1: Schematic of a simple cross-linked polymer hydrogel network both (left) pre- and (right) post-gelation. Where the black lines and red dots represent the polymer building blocks and cross-linking points, respectively.

Hydrogels were first proposed for biological use by Wichterle et al. in 1960, with a gel constructed from co-polymers of glycolmonomethacrylate [94]. They found that glycolmonomethacrylate gels formed a porous network, with adjustable mechanical properties, and that these gels could be embedded in living organisms with no irritation reactions observed. Since this initial report in the later half of the 20th century hydrogels have become an extremely popular engineered material, due in large part to their high biocompatibility which makes them ideal for biomedical applications such as stitches and wound dressings [95, 96]. Compared to the simple structures of crystalline materials such as metals and some plastics, hydrogels have more complex porous structures, sometimes containing multiple levels of structural hierarchy [97–99]. This complex hierarchy of structure that is possible in hydrogels makes them ideal model systems to investigate and understand the collective response of a network of polymers, allowing for the design of novel hydrogels with tailored properties.

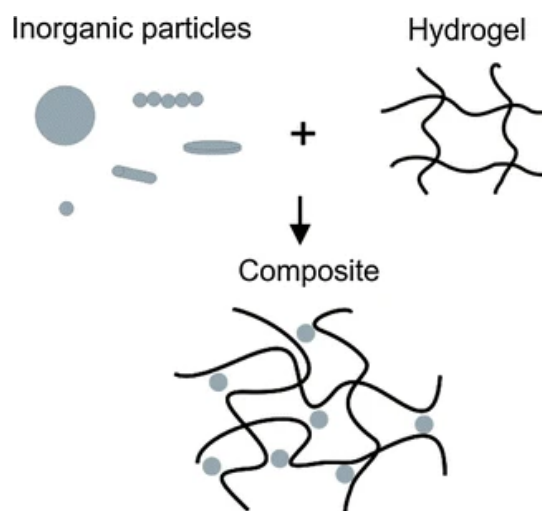


Figure 1.3.1.1: Schematic of a composite hydrogel system. Reproduced from ref [103] with permission from Springer Nature Ltd: Journal of Materials Science. ©2016.

1.3.1 Tailoring the properties of hydrogel networks

In order to design hydrogels for a specific purpose it is necessary to understand how to tune and tailor the mechanical properties of the hydrogel to its application. The mechanical properties of hydrogel network structures have previously been modulated using various different methods, some key examples are outlined below.

1.3.1.1 Filling voids in the hydrogel network

One approach employs so-called “fillers” to occupy the void space between the connected building blocks in the hydrogel network, and in doing so restrict the movement of the overall network [100, 101]. These systems are known as composite gel systems, where rigid or viscoelastic particles (the filler) are embedded in a continuous viscoelastic matrix [102].

It has been demonstrated that the mechanical properties of composite gels depend on the rigidity of the gel matrix, the rigidity and volume fraction of the filler particle, and the interaction or affinity between the filler and the gel matrix [104]. In 1988, using a composite system of polyvinyl alcohol (PVA) - Congo red (CR) gels, van Vliet showed

that if a non-interacting filler particle (in this case natural milk fat globules) was added to the hydrogel matrix then there was a decrease in the shear modulus of the composite gel as the volume fraction of the filler is increased (where a volume fraction of milk fat globules of 0.5 results in a 50% decrease in the shear modulus of the gel) [101]. It was also demonstrated that if the filler particle interacts with the gel matrix (in this case PVA stabilised paraffin droplets) then there is an increase in the storage modulus of the system as a function of filler volume fraction (where a volume fraction of milk fat globules of 0.5 results in a 3-fold increase in the shear modulus of the gel) [101]. Furthermore it should be noted that the trend with interacting particles is inverted if the filler particle is softer than the gel matrix [100]. Recently, cellulose has been used as a filler [105, 106] to reinforce synthetic hydrogel networks such as poly(N,N-dimethylacrylamide) gels, some yielding an order of magnitude increase in storage modulus with the addition of 0.8wt% cellulose nanocrystals [105]. These systems also exhibit enhanced shear-stiffening behaviour, up to 2-fold increase in the degree of shear stiffening in the presence of 0.8 wt% cellulose nanocrystal [105] and up to 6-fold increase in the presence of 8wt% cellulose [106].

1.3.1.2 Inclusion of an interwoven secondary network

An alternative method of altering hydrogel mechanical behaviour involves the inclusion of a secondary network in the hydrogel (either permanent [107] or stimuli-responsive [108]) to act as a scaffold for the original network. These “double-network” hydrogels [109–111] can be carefully selected to create networks which are ‘inter-woven’, resulting in gels with unique mechanical properties [112, 113]. Double network hydrogels typically include a rigid network within a softer, more flexible network. The resulting hydrogel can be imbued with the desirable properties of both networks, including the high mechanical stability of the rigid network and the repetitive elasticity (i.e. the ability of the system to be deformed multiple without change in it’s mechanical characteristics, such as weaken) of the flexible network.

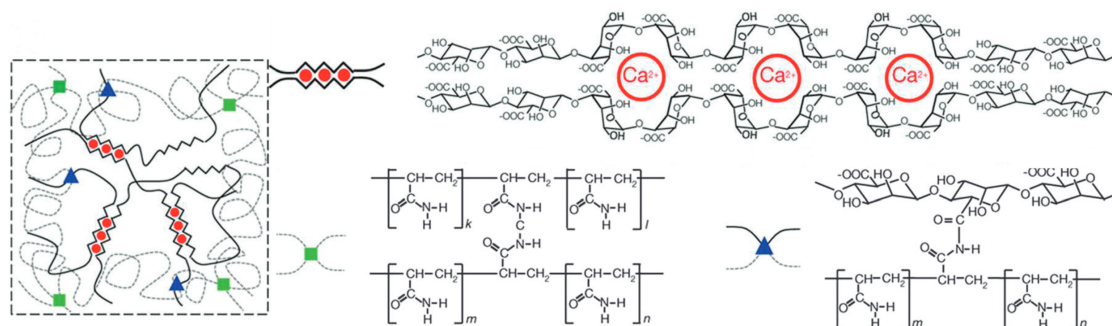


Figure 1.3.1.2: A schematic of a double network hydrogel constructed from an Ca^{2+} ionically cross-linked alginate networks (top right) and a chemically cross-linked polyacrylamide network (bottom right). Reproduced from ref [110] with permission from Springer Nature Ltd: Nature ©2018.

This was demonstrated in a pioneering study [111] with two intertwined networks; an Ca^{2+} ionically cross-linked alginate network and a covalently cross-linked polyacrylamide (PAAm) network. Both of these networks individually form gels, where the alginate gel exhibits high energy dissipation and a low fracture energy of 10 Jm^{-2} due to the transient ionic cross-linking scheme, and the polyacrylamide gel exhibits low energy dissipation and a higher fracture energy of 250 Jm^{-2} due to the chemically permanent cross-links. When these networks were combined into a Ca^{2+} -alginate-PAAm hybrid gel, the resulting daughter gel had a level of energy dissipation between the two parent systems and a fracture energy of $\sim 8700 \text{ Jm}^{-2}$, far larger than either of the parent gel systems. These hybrid gels also exhibited extremely high stretch-ability (over 2-fold larger) and toughness with a rupture stress far in excess (a factor of ten) of either of the individual networks. These enhanced behaviours resulted from the synergy of the two networks cross-linking mechanisms, such that the ionic bonds break first under load, dissipating energy, while the covalent bonded network retains memory of the initial state allowing for healing upon unloading. The two networks are therefore suitably coupled to compensate for each of the individual network weaknesses, resulting in a gel that is more than the sum of its parts. This study demonstrated that in principle interweaving of networks is an effective way to tailor and tune the properties of hydrogels.

1.3.1.3 Altering the strength of the inter-building block self-assembly interactions

In contrast, unstructured short chain peptides, alpha helices and beta strands have been utilised to investigate how the inter-peptide interactions of the network at the molecular level affects the self-assembly of the fibrous microstructure and subsequent mechanics of the hydrogel. Multiple investigations have focused on tuning the structure and mechanics of the hydrogels through precise control of the amino acid composition of these structurally simple, short peptide chain building blocks [114–117].

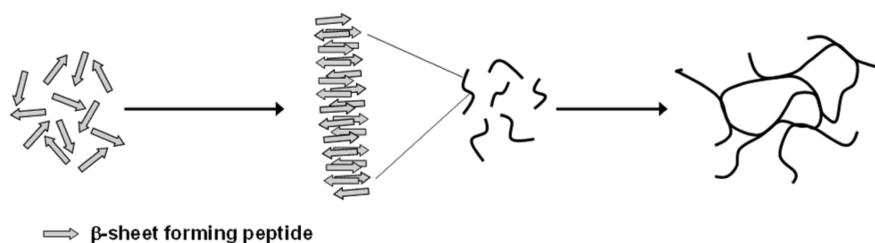


Figure 1.3.1.3: A schematic showing the formation of filaments from beta-sheet forming peptides and the subsequent network formed. Reprinted (adapted) with permission from [115]. Copyright (2017) American Chemical Society.

An example of such a study, by Gao et al., investigated the importance of altering the hydrophobic interaction between the self assembling peptide, on the structure and mechanical properties of the self assembled hydrogel. To do this the authors utilised two short beta-strand forming octa-peptides, each with an alternating series of 8 hydrophobic and hydrophilic residues, the key difference between these peptides is the replacement of a lysine residue with a highly interacting hydrophilic residue arginine. These peptides form gels by lateral self-assembly into fibers which then associate/bundle to form a self supporting 3D network. The gels formed by the arginine containing peptide exhibit a shear modulus that is on the order of 100-fold stronger than gels formed from the other peptide. This dramatic change in the strength of the network was attributed to an alteration of the network topology, with the gel moving from a branched to associated structure which was due to an increase in the fiber-fiber interaction. This study and others have demonstrated that control of the hydrophobic interactions of the peptide building block, and the resulting fibers they form, yields significant shifts in the network

morphology, increases in the shear moduli ranging from to 10-fold [116] to 100-fold [115], and fibrous hydrogels with novel thermo-mechanical properties [117].

1.4 Folded protein-based hydrogels

The previous section discussed multiple methods to alter the mechanical behaviour of hydrogel networks. Both the filler method and the double network method involve the alteration of the hydrogel at the network level, whereas studies on peptide hydrogels have demonstrated that the mechanical and structural properties of a hydrogel can be tuned by altering the interactions between the monomeric building blocks. The recent studies on peptide-based hydrogels highlight the critical role of molecular level interactions on the structure and mechanics of the hydrogel. However these hydrogel systems use either unstructured synthetic polymers or simplistically structured peptide chains as hydrogel building blocks, with changes in the mechanical behaviour occurring as a result of changes to cross-linking in the network. This limited or lack of inherent thermodynamic stability and chemical or mechanical functionality in the hydrogel building block severely limits the range of functionality and tunability of hydrogels. In the last decade, folded globular proteins have been utilised as hydrogel building blocks due to their evolutionarily optimised and highly specialised molecular functions, well defined structures and thermodynamic/mechanical stability [92, 118, 119] (section 1.2.1). The mechanically robust folded structures of globular proteins provide the unique opportunity to investigate the translation of mechanical stability of individual building blocks to assemblies of building blocks, all while retaining the inherent biological functionality of the protein.

1.4.1 Folded proteins as hydrogel building block

An initial study by Li et al. [120] involved an engineered protein construct containing the mechanically robust GB1 domain and the flexible resilin domain (Fig. 1.4.1.1a), in order to replicate the hierarchical mechanical properties of the giant muscle protein titin.

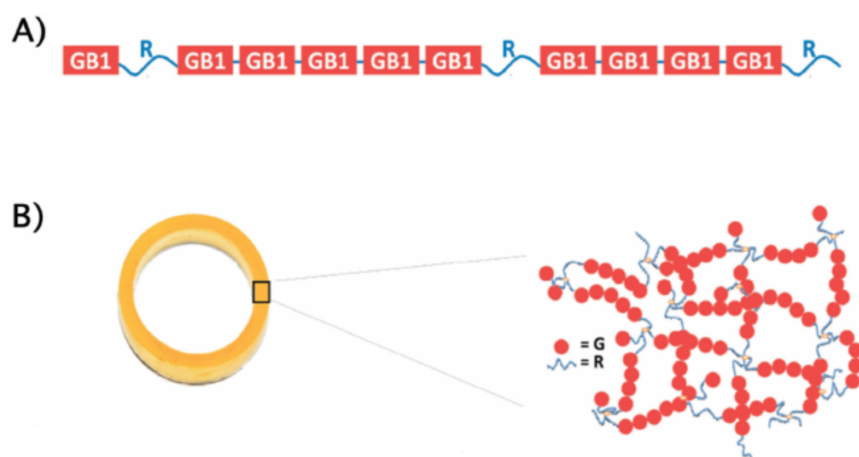


Figure 1.4.1.1: Schematic depicting A) GB1 (red boxes) - resilin (blue lines, R) polyprotein construct and B) a cast GB1-resilin hydrogel ring with a magnification of the imagined internal network structure. Reproduced (adapted) from ref [121] with permission from Wiley-VCH Verlag GmbH & Co. ©(2016).

In this case, the mechanical properties of the component proteins were determined by single molecule unfolding experiments in which GB1 was found to unfold at forces >100 pN, while resilin displayed no measurable unfolding force but led to an increase in extensibility before unfolding occurred [120]. By chemically cross-linking GB1 to form a hydrogel (Fig. 1.4.1.1b), the authors produced a material with properties similar to that of muscle tissue. This pioneering study demonstrated that, in principle, by understanding and mimicking the molecular mechanical properties of modular protein building blocks of a complex material such as tissue, it is possible to replicate the mechanical properties of the bulk material artificially. Importantly, since functionality is encoded in the folded protein building block, the subsequent gels are imbued with functionality. Since this initial study, protein-based hydrogels have emerged as a new class of biomaterial, exhibiting rich properties such as mimicking the mechanical properties of tissues [120, 122], forming highly elastic and stimuli-responsive materials [123–125], and dynamically regulating their properties and shape [126–128]. Such gels include those that have been constructed from an engineered pair of mutually exclusive folded proteins (containing two proteins of which only one can be folded at any one time). Here the folded:unfolded ratio of each protein was controlled by the presence of Ni^{2+} ions

[123]. By controlling the folded:unfolded ratio of each protein domain the stiffness of the network as well as the level of energy dissipation can be tuned. Another example of such a gel, is BSA-polyelectrolyte gels, which exhibit shape memory. These gels lose their casting shape when soaked in guanidinium hydrochloride (a powerful protein denature) due partial unfolding of the BSA domains, however upon soaking in buffer (to remove the guanidinium hydrochloride) the casting shape of the gel returns. This shape memory is as result of the polyelectrolyte providing a scaffold for the refolding BSA, allowing the system to return to its pre-unfolded configuration and hence retain its casting shape [129]. These studies demonstrated that chemical stimuli and changes on the molecular scale can be used to modulate the mechanical properties of the hydrogel, however a complete understanding of the translation of molecular properties to multi-molecular networks, which will allow for the rational design of hydrogels with predictable and tuneable properties, remains a fundamental challenge.

1.4.2 Determining design rules for protein based hydrogels

Several recent studies have sought to address this challenge. For example Wu et al. [130] examined the interplay between the mechanical stability of the folded protein building block and the mechanical strength of the cross-linker. To do this they utilised a hydrogel network constructed from four-armed polyethylene glycol (PEG) linker molecules where the ends were functionalised with a C-terminal tail peptide (denoted as Kir) and an ABA protein block consisting of the load bearing molecule and Tax-interacting protein 1 (TIP-1), which binds to the Kir peptide, on both ends (Fig. 1.4.2.1).

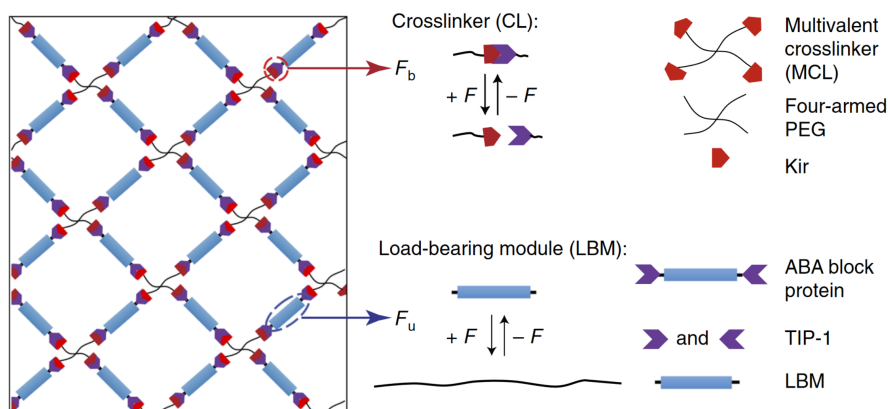


Figure 1.4.2.1: A schematic of a folded protein hydrogel network to explore the interplay between cross-linker and load bearing molecule stability. Reproduced from ref [130] with permission from Springer Nature Ltd: Nature Communications ©2018.

Hydrogel	Load-bearing molecule	Designed Mechanical hierarchies	Expected hydrogel properties
Gel 1	GB1 ($F_{un} = 25$ pN)	$F_b < F_{un}$	Rigid and brittle
Gel 2	SH3 ($F_b = 25$ pN)	$F_{un} < F_b$	Rigid, extensible and tough

Table 1.4.2.2: Molecular level mechanical hierarchy and the expected mechanical behaviour of the resultant hydrogels. Where F_b and F_{un} are the rupture force of the cross-link and the unfolding force of the load bearing molecule. Note: all unfolding forces were quoted for a pulling speed of 400nm/s the rupture force of the cross-link is ≈ 50 pN. Reproduced from ref[130] with permission from Springer Nature Ltd: Nature Communications ©2018.

By selecting the load bearing protein (termed in ref[130] the load bearing molecule), such that the unfolding force of the protein is greater or less than the rupture force of the TIP-1:Kir cross-link complex, the authors were able to investigate the interplay between the mechanical stability of the building block bearing the load or the system and the cross-links holding the network together. Doing this they demonstrated that there were two different regimes of hydrogel mechanical behaviour based on the interplay

between the mechanical strength of the load-bearing molecule and the cross-linker (Tab. 1.4.2.2). The first regime, where the cross-linker is less mechanically stable than the fold of the load bearing protein, produces gels that are rigid but brittle, exhibiting limited extensibility. This is as a result of the rupture of the cross-links holding the network together before the unfolding of the protein. Conversely the second regime, where cross-linker is more mechanically stable than the fold of the load bearing protein, produces gels that are rigid and extensible, due to the protein unfolds before the cross-links break. This unfolding leads to an increase in contour length of the load bearing molecule and hence more extensibility in the gel. So, the authors demonstrated that the building block and cross-linker selection and specifically the mechanical hierarchy between them are crucial in defining the mechanical regime of the hydrogel.

Another study which attempts to address the challenge of rational design of hydrogels, by Kim et al. [131], investigated the role of rigidity and flexibility in hydrogels by exploiting protein engineering to make constructs contain both folded proteins and unstructured peptide chains, as approximations of rigid rods and flexible chains respectively. They found that hydrogels with the rigid poly-protein linkers were approximately twice as mechanically strong as those with flexible unstructured peptide linkers of the same length, with distinct relaxation mechanics. This result demonstrated the importance of the rigidity and flexibility of the building block on the mechanical strength of the network.

These studies have given an insight into the underlying design rules of hierarchical networks and have shown the importance of considering the building block properties as an important parameter to control the mechanical properties of a network. However, these studies do not investigate the direct translation of the intrinsic single molecule properties of the building block, such as the thermodynamic stability or force lability, to the structural and mechanical properties of the network.

1.5 Aims and objectives

In this chapter the properties of folded proteins were introduced, in particular their thermodynamically stable and mechanical robust folded structure. Their exploitation as novel hydrogel building blocks was discussed as well as recent studies seeking to understand the underlying design principles of protein hydrogels and by extension hierarchical protein networks. It was also noted that while these studies showed the importance of building block properties on the mechanical behaviour, they did not investigate the translation of the inherent single molecule properties of the building block to the bulk properties of the network.

It is the aim of this thesis to investigate the direct translation of single molecule properties to the architectural and mechanical properties of multi-molecular hierarchical networks. Folded protein based hydrogels offer the unique opportunity to explore this direct cross-length scale translation of single molecule properties, furthermore folded protein based hydrogels provide good analogues for hierarchical networks observed in living systems. To achieve our aim we utilise a combined structural and mechanical experimental approach that allows for the characterisation of folded protein hydrogel systems across multiple length scales, from the single protein level to the bulk mechanical level. This approach of in-depth analyses of hydrogels, constructed from synthetic polymers and peptides, using combined experiment modalities is common in the literature, in particular through the use of structural techniques in conjunction with bulk mechanical characterisation [115, 116, 132]. This same style of analysis has not yet been applied to folded globular protein hydrogels, in particular the structural characterisation of folded globular protein hydrogels is lacking, with many works presenting structural schematics with no supporting structural data.

Utilising the combined structural and mechanical approach described above, this thesis seeks to answer three main questions:

- i) How, if at all, does the stability of the protein building block translate across length-scales to the bulk properties of the hierarchical protein network?

- ii) What are the effects of the differing thermodynamic and mechanical stabilities of the protein building block on the structural and mechanical properties of the hierarchical protein network?
- iii) What role does *in situ* protein unfolding play in defining the architecture and subsequent mechanics of protein hierarchical networks?

The first two questions are addressed in chapters 3 and 5, with data presented on a novel hydrogel system constructed from the globular maltose binding protein (MBP) which exploits the well-documented [81, 82, 133] increase in protein stability upon the binding of maltose. The final question is answered in chapter 4 by toggling the force lability of the bovine serum albumin (BSA) building block *in situ* in the well characterised BSA based hydrogel system [128, 129, 134].

Chapter 2

Materials and methods

In the hydrogel field, it is common to utilise a multi-technique approach to gain insight and understanding of the underlying science techniques such as rheology, small angle scattering, microscopy and computational modelling. A multi-modality approach is crucial for characterising systems over a wide range of length-scales, and while such approaches have been applied to peptide hydrogels [115, 116], they have only recently been applied to hydrogels constructed from folded proteins [135, 136]. This chapter outlines the methods and techniques of our combined experimental approach to characterise folded protein hydrogels over a wide range of length-scales; from the single molecule properties to network architecture to bulk mechanics.

2.1 Materials, buffers and stocks

2.1.1 Materials

A detailed list of apparatus, chemicals and manufacturers is given in the appendix (Chapter A). All buffers and media were made with Purite 18.2 M Ω distilled (Milli-Q) water unless otherwise stated.

2.1.2 Growth Media

This section describes the growth media used for the production of maltose binding protein (MBP) used in this work (full procedure of the expression and purification is described in section 2.2). All components of growth media were dissolved before autoclave sterilisation.

Growth Media	Components
Lysogeny Broth (LB)	25g of premix dissolved in 1l of Milli-Q. Premix: 40% bacto-tryptone, 20% yeast extract, 40% NaCl.
Auto-induction media (500ml)	5g Yeast Extract, 10g Bacto-tryptone, 25ml 20x NPSC, 10ml 50x LAC, 1ml 1M MgSO ₄
20x NPSC (1L)	53.52g NH ₄ Cl, 32.2g Na ₂ SO ₄ , 68g KH ₂ PO ₄ , 70g Na ₂ HPO ₄
50x LAC (500ml)	125g Glycerol, 12.5g Glucose, 50g Lactose
Agar Plates	15g/l agar suspended in LB media, with 100 μ g/ml carbenicillin added

Table 2.1.2.2: Table listing the components and proportions of auto-induction media growth media used in this project.

2.1.3 Buffers

This section describes the buffer used for all measurements, protein resuspensions and reagent stocks, and outlines the buffers used during the purification of MBP. The powder components of the sodium phosphate buffer (PB) are dissolved in distilled water and the pH of the resulting solution adjusted using high concentration HCl or NaOH.

Buffer	Components
25 mM Sodium Phosphate Buffer pH 7.4	5.65mM sodium monobasic phosphate and 19.35mM sodium dibasic phosphate

Table 2.1.3.2: Table listing the components of the sodium phosphate buffer used in this project.

Additional buffers were needed in the purification of MBP these are outlined in table 2.1.3.4 with their corresponding components. All purification buffers were vacuum filtered through a 0.22 μ m filter to ensure sterility and to de-gas the buffers.

Purification buffers	Components
x100 Protease inhibitor cocktail	100mM PMSF, 200mM benzamide dissolved in ethanol
Lysis buffer	300mM NaCl, 20mM Tris.HCl, 10mM Imidazole. 0.5ml (per 1l of lysis buffer) 100% Triton-X-100, 1mM PMSF, 2mM Benzamide, pH 8.0
Wash buffer	300mM NaCl, 20mM Tris.HCl, 10 mM Imidazole, pH 8.0
Elution buffer	300mM NaCl, 20mM Tris.HCl, 500mM Imidazole, pH 8.0

Table 2.1.3.4: Table listing the components of the buffers used for the extraction and purification of MBP used in this project.

2.1.4 Reagent Stocks

The reagents needed for the photo-chemical crosslinking reaction (section 2.3.3), namely sodium persulfate (NaPS) and tris-bipyridylruthenium(II) (Ru(II)bpy_3^{2+}), are sus-

pended in PB, mixed together and diluted to the desired concentration to form stocks before being frozen and stored at -80°C . Additional chemicals including D-maltose, Urea and dithiothreitol (DTT), are also mixed into the reagent stocks before freezing and storage.

Reagent stock	Components
MBP HG crosslinking x2 reagent stock with maltose	60mM NaPS, 200 μM Ru(II)bpy ₃ ²⁺ and varying concentration of D-maltose between 0mM and 20 mM
MBP HG crosslinking x2 reagent stock with urea	60mM NaPS, 200 μM Ru(II)bpy ₃ ²⁺ , either 0mM or 20mM D-maltose and varying concentration of urea between 0M and 2M
BSA HG crosslinking x2 reagent stock with DTT	100mM NaPS, 200 μM Ru(II)bpy ₃ ²⁺ and either 0mM or 3mM DTT

Table 2.1.4.2: Table listing the components of the cross-linking reagent stocks used in this project.

2.2 Protein expression, purification, storage and resuspension

The expression and purification of MBP was predominately conducted by research technician Sophie Cussons. For completeness this section outlines the method of protein production that was employed.

2.2.1 Transformation of cells

To begin expression of MBP, a pMal-c5x¹ expression vector plasmid [137, 138], with a stop codon inserted at position 378 by Q5 mutagenesis [139], was transformed into the expression host *Escherichia coli* (*E.coli*). This process involves heat shocking competent cells² to induce uptake of the DNA plasmid.

Initially, competent *E.coli* BL21 (DE3) pLysS cells were defrosted on ice. 50 μ l of the defrosted cells were transferred to a sterile 0.5ml centrifuge tube whereupon 2-4 μ l of the pMal-c5x plasmid (stock concentration of 100 μ g/ μ l) was added, before being left on ice. Once the bacteria and DNA had incubated for 20 minutes on ice, the cells were heat shocked at 42°C in a water bath for 45s before immediately being returned to the ice. This step is crucial as the heat shock treatment increases the permeability of the cell membrane allowing for the diffusion of the DNA plasmid into the cell. 400 μ l of sterile LB was added to the 0.5ml centrifuge tube, after 10 minutes of incubation on ice, and the bacteria was grown 1 hour at 37°C, 200rpm. This growth step allows the bacteria to express the antibiotic resistant protein (found in the expression vector plasmid) to make the *E.coli* resistant to carbenicillin.

Once the bacteria has grown for 1 hour it is plated on to an agar plate containing 100 μ g/ml carbenicillin (Tab 2.1.2.2). Plating the bacteria involves pipetting 100 μ l of the bacteria onto one side of the agar plate and then spread across the plate using a sterile glass rod. The agar plates were then incubated overnight at 37°C. Two controls plates were run in parallel to determine the success of the transformation, the first involved repeating the above procedure but with the addition of water instead of DNA. The second control was the untransformed cells. If both control plates were clear then the transformation was deemed to have been successful.

Once the transformation was shown to be successful, colonies were selected and grown overnight in 10ml of LB (Tab 2.1.2.2) at 37°C, 200rpm to form starter cultures. 0.5ml of

¹The pMal-c5x expression vector contain all correct inserts was generously donated to the POI in this project by Dr David Brockwell

²Cell competence refers to a cell's ability to uptake extracellular DNA from its environment

these starter cultures were mixed with 0.5ml of sterile glycerol, before being snap frozen in liquid nitrogen and stored at -80°C , to form glycerol stocks. These glycerol stocks are used to form future starter cultures for full-scale protein expression without the need to perform another transformation of the same expression vector.

2.2.2 Full-scale Expression

To begin full-scale expression of MBP $\sim 50\mu\text{l}$ of glycerol stock (see section 2.2.1) was added to 20ml of sterile LB (see table 2.1.2.2) containing $50\mu\text{g/ml}$ carbenicillin and incubated at 37°C , 200rpm the night preceding the full-scale growth, in order to from starter cultures. 2ml of these starter cultures was used to inoculate 0.5l of auto-induction media (Tab 2.1.2.2) in 2.5l baffled conical flasks, these cultures were incubated for 48 hours at 37°C , 200rpm. Auto-induction media contains both glucose and an inducing sugar (in this case lactose) as the cells have exhausted the supply of glucose (this is *E.coli*'s preferred food source), they start to uptake the inducing sugar [140]. This uptake causes induction of certain genes, in particular the gene in the expression vector corresponding to the protein of interest, in this case MBP. The advantage of using auto-induction media is that cell cultures do not need to be monitored for manual gene induction and higher cell densities can be achieved potentially leading to higher yields of expressed protein. After the expression cultures were incubated for 48 hours, the cells were harvested by centrifugation (Avanti J-E centrifuge, JLA-8.1 rotor, Beckman Coulter, UK) at 5000rpm for 20 minutes at 4°C . After centrifugation, the supernatant was removed and the cell pellet recovered and stored at -20°C overnight before the protein is extracted and purified.

2.2.3 Cell Lysis

In order to extract the MBP from the *E.coli* expression host, the cells were first lysed. To achieve lysis, protease inhibitor cocktail (Tab 2.1.3.4) was added to lysis buffer (Tab 2.1.3.4) to give a final concentration of 1mM PMSF and 2mM benzamidine³. The har-

³PMSF and benzamide both inhibit proteases, which are responsible for breaking down proteins

vested cell pellets (section 2.2.2) were each defrosted and resuspended in ~ 200 ml of this lysis buffer, after which small amounts of DNAase⁴ was added. To encourage complete lysis of the *E.coli*, cell solutions were homogenised using an electronic disperser before being passed through a cell disruptor (30Kpsi, 25°C). The solution was then centrifuged at 25,000rpm for 25 minutes to separate and pellet the cell debris from the MBP-containing supernatant (lysate).

2.2.4 Purification

To purify the MBP from the lysate, Nickel-nitrilotriacetic acid (Ni^{2+} -NTA) protein purification was employed. Ni^{2+} -NTA purification is a type of immobilised metal-affinity chromatography [141, 142], in which Ni^{2+} (other transition metals can be used) is immobilised in a resin matrix but is importantly still able to bind chemical groups such as imidazole. The MBP used in this study had previously been engineered to include a hexa-histidine tag⁵ at the N-terminus of the protein. Histidine has a high affinity of binding to Ni^{2+} ions due to the electron donor of the imidazole side chain, this affinity is boosted by the inclusion of six histidine, allowing for strong binding to the column matrix. Introduction of large quantities of imidazole or changing the pH can disrupt this interaction and unbind the protein, allowing for controlled elution of the bound protein from the column.

The Ni^{2+} -NTA column was attached to an ÄKTA prime⁶ in order to allow monitoring of the absorption at 280nm (A_{280})⁷. This monitoring allows accurate determination of the concentration of proteins with known extinction coefficients and enables protein peaks to be distinguished during the elution stage of purification.

The purification column was primed by washing with ~ 10 x column volume of filtered de-gassed milli-Q, after which they were equilibrated into lysis buffer, until the A_{280} remained constant (this was recorded as the baseline absorption). The purification process

⁴Breaks down DNA molecules

⁵A chain of six histidines, an amino acid with an imidazole side chain

⁶An automated pump system for buffers and sample

⁷Proteins absorb light with a wavelength of 280nm when they contain tryptophan, tyrosine or cysteine disulphide bonds

was performed in three stages: loading, washing and elution, each of which is outlined below.

Loading: The MBP containing lysate was cyclically loaded onto the equilibrated column at a flow rate of 2ml/min overnight to ensure maximum binding of the hexahistidine-tagged MBP.

Washing: Once the lysate had been loaded onto the Ni²⁺-NTA column, the column was flushed with wash buffer (Tab 2.1.3.4), until the A₂₈₀ returned to approximately the baseline value.

Elution: In order to elute and collect the MBP from the Ni²⁺ column, elution buffer (Tab 2.1.3.4) was run through the column in a ratio of 1:3 to the wash buffer. The mixing was automated using the ÄKTA prime. During this step, the solution exiting the column is collected in 5ml fractions. A peak in the A₂₈₀ is presumed to correspond to the elution of MBP. Fractions corresponding to the elution peak were pooled together, and the A₂₈₀ measured to estimate the yields of MBP after growth and purification. Average yields of MBP were ~250 mg per litre of growth culture. The collected eluted solutions were then dialysed and freeze-dried for long term storage (see section 2.2.5).

2.2.5 Storage of Protein

After the purification process the extracted MBP solution was dialysed out of elution buffer and into Milli-Q before being rapidly frozen using liquid nitrogen. Dialysis is a necessary step in order to remove the salts from the elution buffer, this was achieved by placing ~ 100ml of the protein/elution buffer solution into Snakeskin dialysis tubing (3kDa MWCO) and submerging the tubing in 5l of Milli-Q. The semi-permeable tubing allows small molecules to pass through by osmosis whilst keeping large molecules inside. The dialysis Milli-Q in which the tubing is submerged was repeatedly changed, removing essentially all of the salt from the protein solution, at which point it was recovered and rapidly frozen. The frozen samples were then lyophilised on a vacuum freeze drier. It is important to note that protein should be freeze-dried in large bulb flasks to optimise

the resuspension of the protein to high concentrations. The freeze dried protein powder was stored at -20°C .

2.3 Hydrogel sample preparation and photochemical gelation

This section will cover the preparation of folded protein hydrogels used in this project, from the resuspension of the lyophilised protein building block, to the mix of protein and reagent stock, to the details of the photo-chemical cross-linking reaction.

2.3.1 Resuspension of high concentration protein stock

To resuspend protein to the high concentrations used in this project ($\sim 100\text{-}200\text{mg/ml}$) an iterative method was used, where lyophilised protein powder was ‘gently’ packed into multiple centrifuge tubes and 25mM PB (pH 7.4) was added and transferred from tube to tube until all the lyophilised powder was resuspended. To resuspend the powder in each tube, they are rotated until all the powder is dissolved. Once all the powder in one tube is dissolved the protein-containing PB is transferred to the next tube and is repeated until the powder in all the centrifuge tubes is resuspended. Once the lyophilised protein is resuspended, the high concentrated protein solution is centrifuged at $5000g$ for 1 minute in order to pellet out any denatured and aggregated protein. The supernatant is transferred to a fresh centrifuge tube and the concentration of the resulting protein solution is determined using UV absorbance at 280nm and the Beer-Lambert Law [143].

$$A_{280} = c\epsilon\Delta L \tag{2.3.1.1}$$

Where A_{280} is the absorption of the sample (minus the absorption of 25 mM PB pH 7.4), c is the concentration of the protein, ϵ is the extinction coefficient of the protein at

280nm^8 , and ΔL is the path length of the sample. In order to accurately experimentally measure the concentration of the protein stock, the stock must be diluted (200-300x) to ensure the level of absorbance does not saturate the UV absorbance spectrometer detector. Once the concentration of the supernatant is determined, it is diluted to the desired concentration, and in this project the concentration of all protein stock solutions was 200 mg/ml. It is important to note that the volume of the centrifuge tubes used should be comparably sized when compared to the final volume of protein stock desired, in order to limit the size of the air/water interface during resuspension which could lead to unfolding and aggregation of the protein being resuspended.

2.3.2 Preparation of pre-gelation hydrogel solution

Hydrogel samples are prepared by mixing in a 1:1 ratio a 200 mg/ml stock of the relevant building block protein (in this work either MBP or BSA) and defrosted 2x concentrated cross-link reagent stock (Tab 2.1.4.2) for a final protein concentration of 100 mg/ml. As described in section 2.1.4, additional chemicals, such as D-maltose or DTT, were added to the reagent stocks in order to investigate the effects on the hydrogel properties.

2.3.3 Photo-chemical cross-linking reaction

The hydrogels used in this project were formed using a tyrosine-targeted, ruthenium-catalysed photo-activated chemical reaction (mechanism shown in Fig. 2.3.3.1).

⁸Extinction coefficients of MBP and bovine serum albumin (BSA) are $66350\text{ M}^{-1}\text{cm}^{-1}$ and $42925\text{M}^{-1}\text{cm}^{-1}$ respectively

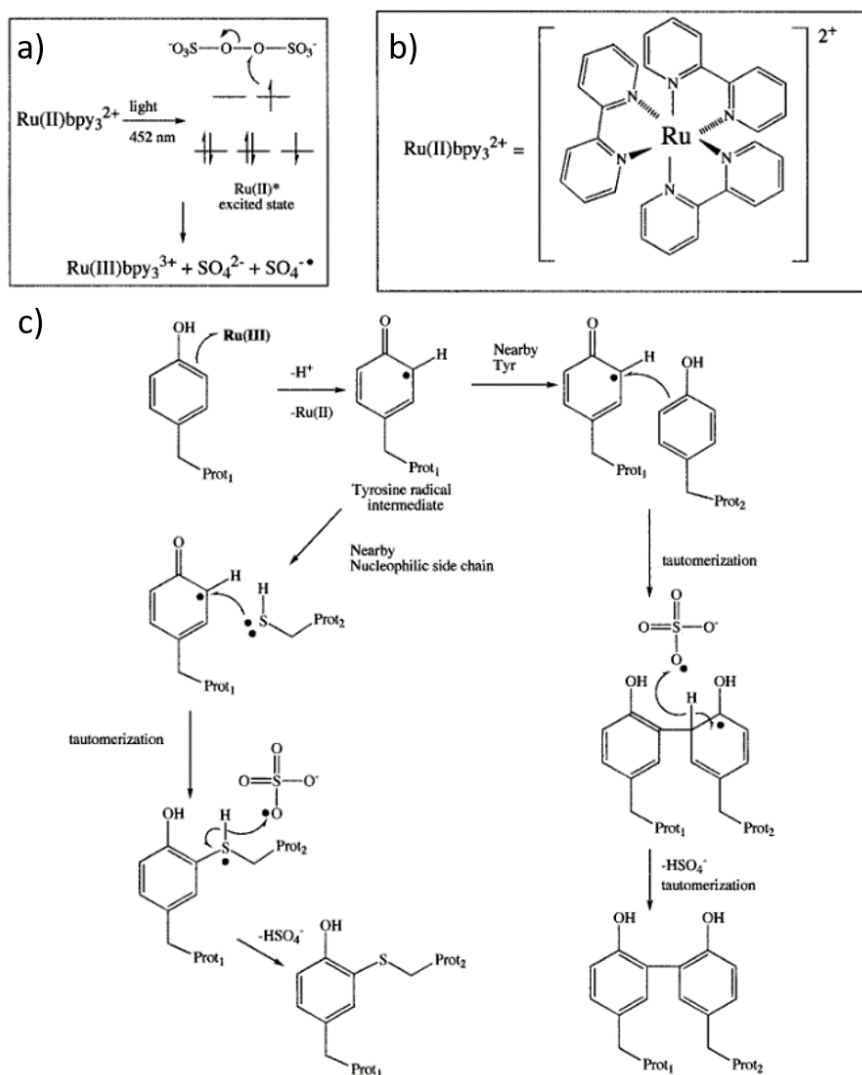


Figure 2.3.3.1: Reaction mechanism of a photo-initiated protein cross-linking reaction. a) Schematic showing the electron flow when Ru(II)bpy_3^{2+} (structure shown in b) is photolyzed in the presence of a persulfate, generating Ru(III) and sulfate radical. Ru(III) would be expected to oxidise residues such as tyrosine due to being a potent one-electron oxidant. c) Two possible reaction mechanisms of cross-linking two associated proteins via radicalised tyrosine (oxidised by Ru(III)). (Right) If another tyrosine residue is nearby, then arene coupling would be expected. (Left) alternatively a nearby cysteine group could attack the tyrosine radical to produce a heteroatom-arene linkage. In both these cases, a hydrogen atom must be lost in order to form stable products and it is likely the sulfate radical produced during Ru(III) formation plays a key role in this step. This figure represents only the mechanistic hypothesis on which the authors designed the reaction, though the true mechanism of Ru(II)bpy_3^{2+} /persulfate-mediated cross-linking remains to be experimentally determined. Adapted from ref [144] with permission from PNAS ©1999.

The suggested mechanism of photo-chemical tyrosine-tyrosine cross-linking is shown in Fig. 2.3.3.1. The proposed mechanism, as suggested by Fancy et al. [144], involves the photo-oxidation of Ru(II) to Ru(III) in the presence of persulfate ions (see Fig. 2.3.3.1a). The resulting Ru(III) is a potent one-electron acceptor and is expected to oxidise aromatic residues, in particular tyrosine. In the presence of Ru(III) and H^+ ions, tyrosine is oxidised to form highly reactive tyrosine free radicals, with a free electron on the carbon atoms adjacent to the hydroxyl carbon in the benzene ring (see Fig. 2.3.3.1). This free radical tyrosine attacks the aromatic ring of other non-radicalised tyrosine residues to form a covalent carbon-carbon bond between the carbon atoms that are adjacent to the hydroxyl group.

An additional route considers cysteine side chains interacting and cross-linking with the tyrosine free radical. Previous work [145] has shown that free cysteine quenches the reaction by a similar amount as free tyrosine, demonstrating that both tyrosine and cysteine are equally likely to react with the initial free radical. It is for this reason that the protein selected in this project either contain no cysteine residues (MBP) or cysteine residues that are already bonded in disulphide bridges (BSA).

In order to perform the reaction and gelate the samples *in situ* on the rheometer, a custom lighting rig was designed and constructed in collaboration with the School of Physics and Astronomy's electronic and mechanical workshops. Figure 2.3.3.2 shows an image of the lighting rig used in this project.

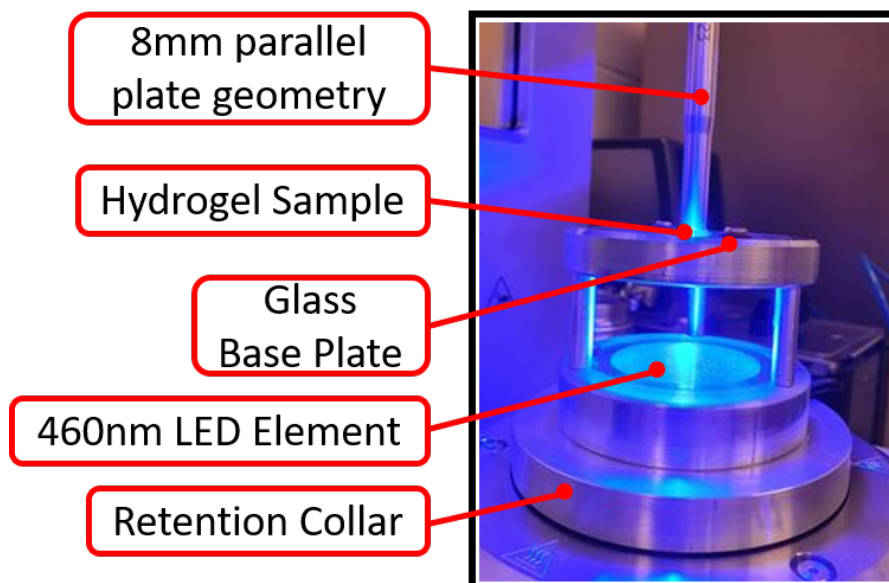


Figure 2.3.3.2: Image of the *in situ* rheometer lighting rig used to initiate the photo-chemical cross-linking reaction and gelate the sample.

The lighting apparatus consists of 3 main parts: the retention collar, the LED element and enclosure, and raised glass base plate.

Retention collar: The retention collar was designed to fit over the existing base plate of an Anton Paar MCR502 rheometer, and tightened down using Teflon screws to ensure the lighting rig does not move during measurements. The retention collar was designed this way to allow easy attachment and removal from the rheometer without causing damage to the equipment.

LED element and enclosure: An LED element with a emission spectrum centred around a wavelength of 460nm was chosen as this wavelength closely matches the excitation wavelength of Ru(II)bpy_3^{2+} (452nm, see Fig. 2.3.3.1a). The blue LED was encased in an aluminium frame with a glass top. The frame was made from aluminium due to its high thermal conductance allowing it to act as a heat-sink and avoid overheating of the LED. The LED was connected in parallel with a 30Ω resistor to a variable DC current power supply supplying a current of 0.48Amps.

Raised glass base plate: A transparent glass base plate (on which the sample is

placed) was set into an aluminium frame and raised on aluminium struts 5cm above the LED element where the sample was placed for measurement and *in situ* gelation on the rheometer. Initially the design did not include a raised base plate and the sample was placed directly on the glass encasing the LED element. However, this initial design resulted in significant heating of the sample during gelation, hence a separate base plate was included and raised on struts to distance the sample from the heat source and allow passive cooling to keep the sample at room temperature.

2.4 Characterisation of the protein building block

For the work presented in this thesis, it is crucial to be able to characterise the molecular-level structure and stability. This was done using 2 techniques: i) circular dichroism (CD) and ii) differential scanning calorimetry (DSC).

2.4.1 Circular Dichroism Spectroscopy

CD spectroscopy was developed in the later half of the 20th century [146] as a method to investigate the structure of chiral molecules. Chirality is prevalent in nature, as evidenced by the fact that all amino acids (with the exception of glycine) are chiral. A molecule is said to be chiral if it cannot be superimposed upon its own mirror image by any Euclidean transformation. The most common cause of chirality in a molecule is an asymmetric carbon atom that is bonded to 4 different groups in the chemical structure. Examples of these systems include amino acids (excluding glycine), sugars and other small biological molecules. Importantly for the study of proteins and other biomacromolecules chirality can also be the consequence of a 3-D structure adopted by the molecule, in the case of proteins this could be α -helices and β -sheets. CD spectroscopy utilises the differential absorption of left- (anti-clockwise) and right-handed (clockwise) circularly polarised light by different isomers, when it is passed through a sample, to investigate the structure of chiral molecules. Circularly polarised light is produced when a monochromatic light source is linearly polarised and then passed through a quarter-wave plate (QWP).

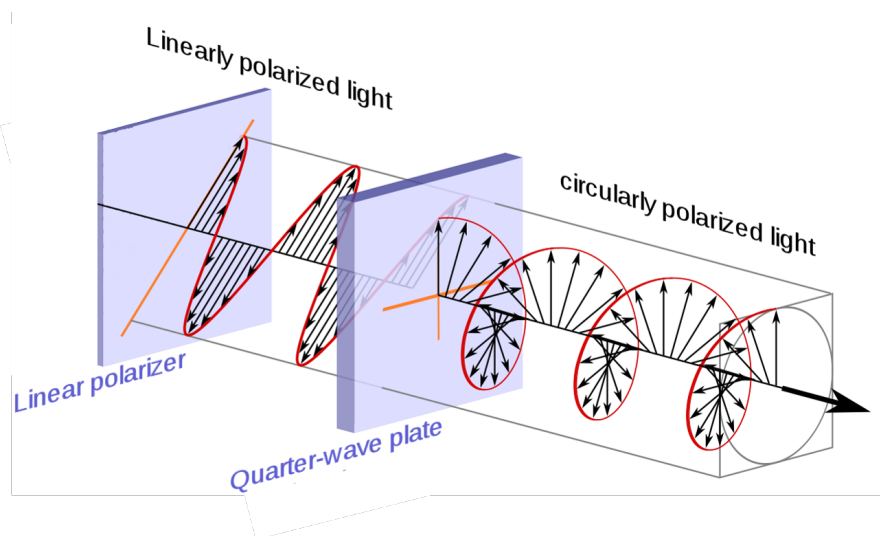


Figure 2.4.1.1: Schematic illustrating the production of circularly polarised light. In linearly or plane polarised light the resultant vectors of the light wave oscillate in a single plane, however upon passing through a QWP the light is circularly polarised with the vector continuously rotating transverse to the direction of travel. Adapted from ref [147].

Linearly polarised light is light where the oscillations in the electric field are in a single plane (this electric field will be comprised of two orthogonal vector components with equal phase and amplitude). As linearly polarised light passes through the birefringent QWP, the two vector component of the electric field are de-phased to be 45° out of phase with one another. This phase difference between the electric field components results in a constantly changing electric field giving rise to circularly polarised light. If the left- and right-handed circularly polarised light incident on the sample are not absorbed or are absorbed in equal proportions, then the same circularly polarised light that was incident on the sample will be emitted (though the amplitude maybe be decreased depending on absorption). However, chiral molecules will absorb the left- and right-handed circularly polarised light in different amounts, and therefore will emit light that has a different polarisation than was incident. This change is typically reported by CD instruments as ellipticity, θ , of a sample where $\theta = \arctan(a/b)$, where a and b are the minor and major axis of the elliptical light, respectively. The ellipticity can be calculated using $\theta = 32.98\Delta A$, where $\Delta A = A_L - A_R$ [146]. CD spectra are obtained, by measuring the ellipticity of the sample as a function of incident wavelength.

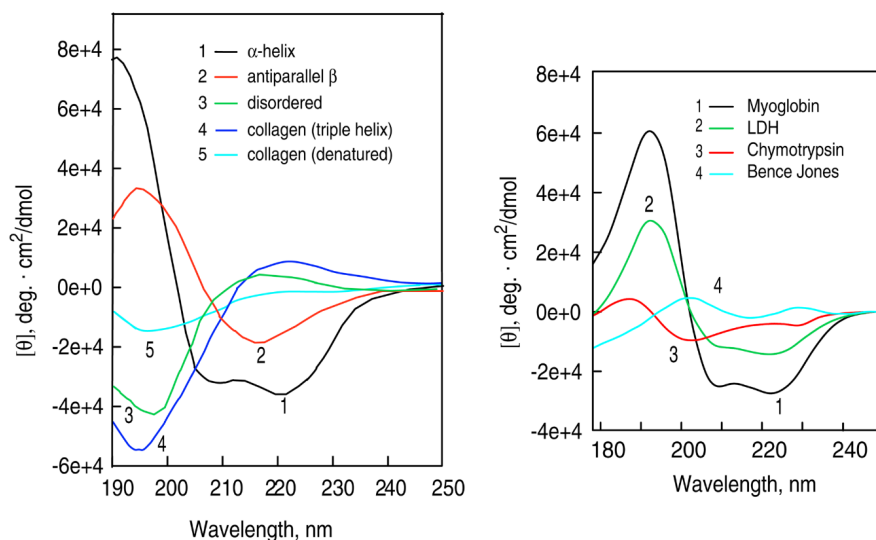


Figure 2.4.1.2: Examples of CD spectra for different secondary structure elements and model proteins. (left) CD spectra of poly-L-lysine in the α -helical (1, black), antiparallel β -sheet (2, red) and extended disordered conformations (3, green) as controlled by pH [148], and collagen in both its native triple-helical (5, cyan) and denatured (5, cyan) forms. (right) CD spectra of exemplar model proteins with varying secondary structure elements, demonstrating the sensitivity of the technique to different molecular level structures. Reprinted by permission from Macmillan Publishers Ltd: Nature Protocols ([149]), copyright (2006).

Peptide bonds and aromatic amino acids absorb electromagnetic radiation in the wavelength range 260-329 nm, while disulphide bonds absorb below 240 nm [150]. The absorption characteristic of peptide bonds and the chirality of secondary structure elements formed by protein peptide backbones make ultraviolet (UV) CD spectroscopy an ideal technique to study the structure of proteins in solution. Figure 2.4.1.2 shows the exemplar CD spectra of different protein secondary structural features and model proteins including myoglobin (globular α -helical protein), collagen(triple twisted α -helical protein), and chymotrypsin (α,β -protein). The characteristic spectra of three distinct structure elements namely α -helices (characterised by two negative peaks at ~ 209 nm and ~ 222 nm and a positive peak at ~ 190 nm), β -sheets (characterised by less intense negative and positive peaks at ~ 215 nm and ~ 195 nm, respectively) and disordered coil-coil (characterised by a strong negative peak at ~ 195 nm) are shown in figure 2.4.1.2. By considering these characteristic spectra and their relative intensities the proportions of each secondary structure element in a protein can be determined from its CD spectra.

2.4.1.1 Determination of *in situ* folded protein proportion using circular dichroism spectroscopy

CD spectroscopy was used in this project to investigate the proportion of protein that remains folded *in situ* in photo-chemically cross-linked hydrogels. CD experiments were performed on MBP and BSA hydrogels, using a Chirascan plus circular dichroism spectrometer (Applied PhotoPhysics). Gels were loaded into a 10 μ m path length cuvette. The path length is reduced in order to account for the larger level of UV absorption due to the high concentration of protein (100 mg/ml). Additionally while the CD spectra were recorded over the same wavelength range (178-260 nm) and 1 nm interval, the bandwidth was increased to 2 nm to increase the flux of incident light and improve the signal to noise ratio of the recorded signal. In order to determine the proportion of protein that unfolded due to gelation, the spectra of protein samples in pre-gelation solution was recorded before the sample was photo-chemically cross-linked (see section 2.3.3). Once the sample had been photo-chemically cross-linked, the CD spectra was repeatedly recorded over the course of 10 hours. To give a measure of the proportion of unfolded protein over time, the ellipticity value at 222nm of each spectra was normalised by the value at 222 nm of the pre-gelation spectra. Since it is the same protein (either BSA or MBP) under consideration the ‘intensity’ of the spectra can be assumed to be dependent on only the folded protein concentration and the path length⁹, the latter of which does not change over the course of the measurement, this results in a record of proportion of folded protein over time. Important to note that over the course measure (approx. 10 hours) dehydration is significant factor, this was corrected for by fitting the natural log of the data at large t (>6 hours to ensure that protein unfolding due to gelation has reached a steady state) to determine the rate of dehydration. Using this rate the whole data set was fit with a double exponential decay function (with the rate of one exponential fixed as the measured dehydration rate). The exponential corresponding to the dehydration was then removed from the data set.

⁹It is assumed that the secondary structure of the protein of interest (either BSA or MBP) which remains folded is not altered, i.e. Folded BSA will remain all α -helical and folded MBP will remain the same proportion of α -helices and β -sheets

2.4.2 Differential Scanning Calorimetry

DSC is a technique which involves measurement of the differential heat flow between a sample and an appropriate reference as a function of temperature, and has been used since the mid-1960s as a method to study the stability, unfolding and refolding of proteins [150]. In a simple DSC experiment a sample (e.g. protein suspended in buffer) and a reference (e.g. suspension buffer) are heated (or cooled) at a constant rate and the difference in heat flow between the sample and the reference is recorded. When selecting a reference it is important that it is comparable to the sample that is measured, for example if a protein in buffer is measured, then the reference should be the same weight of buffer within the sample not the same volume as the sample. Studying the heat flow into a material as function of temperature allows for the investigation of first order thermodynamic transitions within the material including melting and crystallisation, as well as second order transitions, such as glass transitions [151]. The rest of this section will discuss DSC data analysis in terms of the ‘melting’ of protein domains, which is the focus of the DSC experimental work presented in this thesis, before outlining the experimental parameters used in each study. Melting is an endothermic process which involves the breaking of bonds at a critical temperature i.e. the melting temperature. In the case of proteins this refers to the breaking of the intra-molecular bonds (predominately hydrogen bonds, but can also consist of salt bridges, disulphide bonds, etc) holding the protein domain fold together and allowing the melting of the domain from the folded state to the unfolded state [150].

Figure 2.4.2.1a shows the expected profile heat flow¹⁰ of a protein unfolding melt peak. The two key features of this curve are: i) a linear decrease in the heat flow, as a result of more energy being needed to heat the sample to temperature compared to the reference, and ii) a negative peak corresponding to a large amount of energy needed to break bonds and melt¹¹ the sample (a similar trend is noted for any first order phase transition that involves breaking bonds). Fitting the peak of the melting curve allows

¹⁰Heat flow is commonly defined as exothermic in the positive direction and endothermic in the negative direction

¹¹Note: this trend is reversed for the formation of bonds and the solidifying of samples, i.e. a positive peak is observed as energy is given out to form bonds.

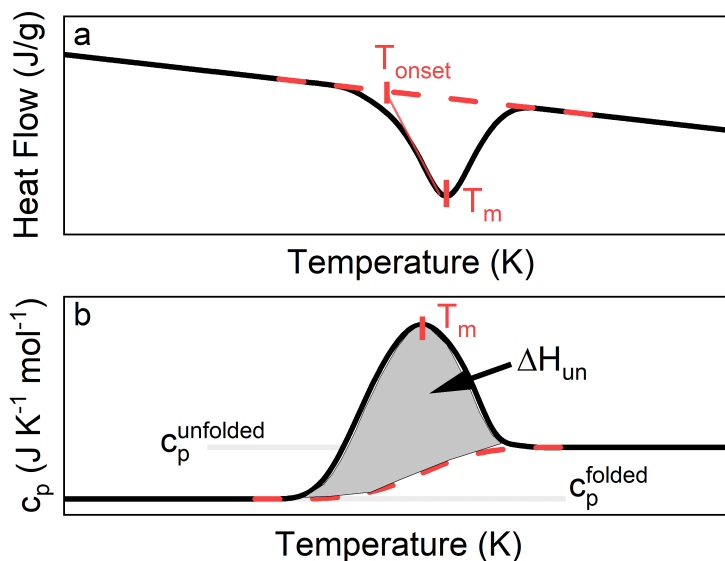


Figure 2.4.2.1: Expected a) heat flow and b) specific heat capacity profiles of melting obtainable from a DSC experiment. Where T_{onset} and T_m are the onset temperature of melting and the midpoint temperature of melting referred to as the melting temperature, respectively. c_p^{folded} and $c_p^{unfolded}$ are the specific heat capacity of the folded and unfolded state respectively, and ΔH_{un} is the enthalpy change due to unfolding.

for the extraction of the melting temperature of the sample, T_m . In addition fitting the linear decrease and the highest rate of increase in the melting peak (Fig. 2.4.2.1a) and determining the intercept, the temperature of onset of melting, T_{onset} , can be found.

To gain more information on the free energy change associated with the melting/unfolding of protein, the specific molar heat capacity, c_p , can be determined as a ratio of the heat flow per mole of sample, $\frac{dQ}{dt}$, and the heating rate, $\frac{dT}{dt}$.

$$c_p = \frac{dQ}{dt} \bigg/ \frac{dT}{dt} \quad (2.4.2.1)$$

Figure 2.4.2.1b shows the expected profile of the change in c_p as a function of temperature during the melting of a sample. There is a peak in c_p centred at T_m which is due to the ‘melting’ transition of the protein sample from its ‘solid’ folded state to its ‘liquid’ unfolded state. Additionally, there is an increase in the c_p of the protein between the folded to the unfolded state, this is due to an increase in the degree of freedom of

the more flexible unfolded protein chain compared to the specific structure of the folded protein. By fitting a sigmoid (where the midpoint of the sigmoid is T_m) the change from the c_p of the folded state to the c_p of the unfolded state can be modelled. The area bounded by the fitted sigmoid and the c_p profile is equal to the enthalpy change, ΔH of the thermodynamic process; in the case of protein melting this is the enthalpy change associated with unfolding [152]. By considering the definition of the Gibbs free energy, ΔG ,

$$\Delta G = \Delta H - T\Delta S, \quad (2.4.2.2)$$

and that at the melting temperature $\Delta G=0$, the change in entropy of the protein upon melting/unfolding, ΔS , can be calculated as,

$$\Delta S = \frac{\Delta H}{T_m} \quad (2.4.2.3)$$

Once the values for the change in both enthalpy and entropy as a result of melting/unfolding are known they can be used to calculate the Gibbs free energy of unfolding at any experimentally relevant temperatures.

2.4.2.1 Determination of protein molecular-level properties using DSC

DSC was utilised in this thesis exclusively to characterise MBP. Melting experiments were performed on MBP pre-gel solutions and chemically cross-linked to determine two key properties of MBP: i) the ligand binding affinity of the ligand maltose in highly concentrated solutions of MBP and ii) the Gibbs free energy of unfolding in varying chemical conditions (i.e. urea and maltose). Experiments were completed between $30^\circ C$ to $90^\circ C$ according to the temperature profile shown in figure 2.4.2.2.

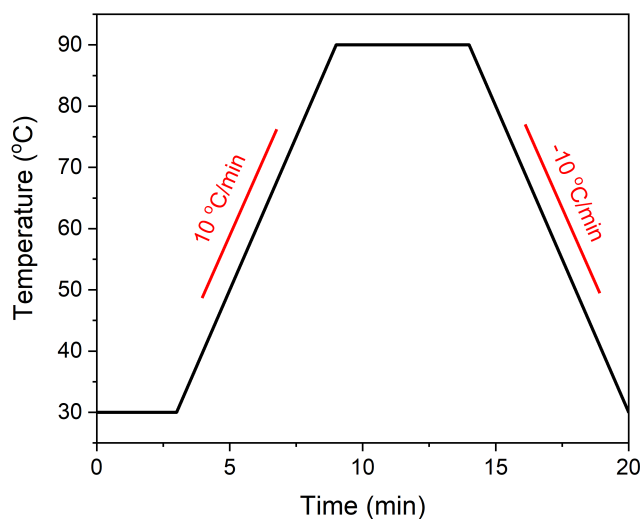


Figure 2.4.2.2: The temperature profile of the DSC melt experiments conducted in this thesis, where the system is held isothermally at 30°C for 3min before increasing in temperature at a rate of 10°C/min up to 90°C. The system is held at 90°C for 5min before cooling back down to 30°C at a rate of 10°C/min.

The sections below outline the details of the ligand binding affinity measurements and the Gibbs free energy determination measurements were conducted.

2.4.2.1.1 Ligand binding affinity measurements 10 μ l of both MBP pre-gelation solution and cross-linked hydrogel samples, which contained varying concentrations of maltose were loaded into Tzero hermetically sealed pans. 9.26 μ l of PB buffer was used as a reference for each sample. The melting experiments were performed on a TA Instruments Q20 DSC with an autosampler. Melting temperatures were extracted using the method shown in figure 2.4.2.1a.

2.4.2.1.2 MBP Urea stability measurements Similarly 10ul of MBP pre-gelation solution and hydrogel samples were loaded into Tzero hermetically sealed pans and 9.26 μ l of PB buffer was used as a reference. In these measurements the samples contained varying concentration of urea and either 0 or 10 mM maltose. The measurements were performed on a TA Instruments Q2000 DSC, which was calibrated with a sapphire

standard of known heat capacity to ensure accurate determination of the protein heat capacity. Values of the melting temperature and the enthalpy change were extracted as shown in figure 2.4.2.1b and values for the entropy change calculated using equation 2.4.2.3.

2.5 Characterisation of the network architecture

The network structures of protein based hydrogels in this thesis were probed and analysed in this thesis using small-angle scattering (SAS) techniques, including small-angle x-ray scattering (SAXS) and small-angle neutron scattering (SANS). These techniques provide structural information over the length-scales of tens to hundreds of Ångstroms and rely on the diffraction of elastically scattered coherent radiation. It is not possible to cover all of the aspects of diffraction and scattering in detail¹², however this section will cover the basic theory behind elastic scattering and using diffraction to probe distances. The section will also outline the analysis of scattering patterns by breaking down the measured profile into the form and structure factors before finally describing the details of the scattering experiments performed in this thesis.

2.5.1 Theory of scattering

2.5.1.1 Diffraction as a method to probe structure

Diffraction is a physical phenomenon where a wave apparently bends around or spreads out when encountering an obstacle or aperture respectively e.g. ripples on the sea entering through the narrow inlet of a bay. A key principle in diffraction and diffraction patterns is the Principle of Superposition (Fig. 2.5.1.1), which defines the interference between waves. When waves interfere, the resultant wave has an amplitude that is some proportion of the sum of the amplitudes of the constituent waves that were superimposed.

¹²Many references are available that are dedicated to explaining these phenomena in further detail, including references (153–155)

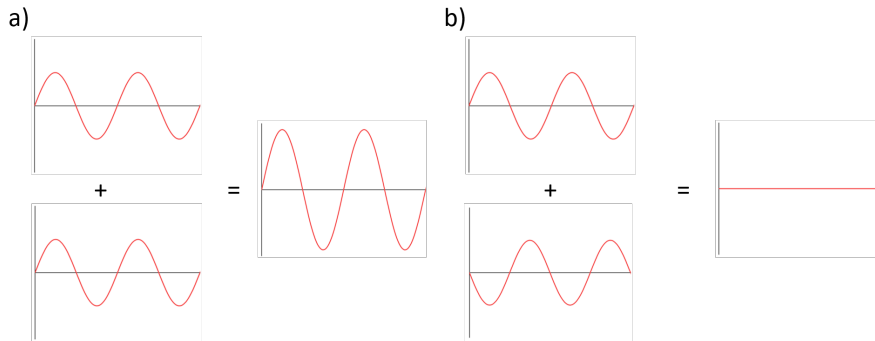


Figure 2.5.1.1: The two key cases of the principle of superposition: a) Constructive interference, where the two coherent waves are in phase and superimpose such that the resultant wave has an amplitude that is the sum of the amplitudes of the two constituent waves. b) Destructive interference, where the two coherent waves are out of phase and superimpose such that the the amplitudes of the two constituent waves cancel out.

Figure 2.5.1.1 shows the two key cases of interference between two waves. The amplitude in each case is dependant on the phase difference between the two superimposed coherent waves. The first case (Fig. 2.5.1.1a), where the constituent waves are in-phase, the resultant superimposed wave has an amplitude that is equal to the sum of the amplitudes, known as constructive interference. In contrast, if the constituent waves are completely out of phase with one another, then the amplitudes of the constituent waves cancel each other, termed destructive interference. Both of the scenarios can be more formally described as;

$$\text{Constructive Interference } n\lambda = X, \quad (2.5.1.1)$$

$$\text{Destructive Interference } n\lambda = X + \frac{\lambda}{2}, \quad (2.5.1.2)$$

where λ is the wavelength, n is an integer, and X is a derivable quantity e.g. the path length difference. A particular combination of constructive and destructive interference leads to particular interference pattern depending upon the structure that the waves were diffracted on. A prime example of this is Young's double slit experiment, where the interference of the diffracted waves from both each slit interfere to produce a pattern of

light and dark fringes, where the distance between the fringes, Δy ,

$$\Delta Y = \frac{L\lambda}{a} \quad (2.5.1.3)$$

is inversely proportional to the separation of the slits, a (where L is the distance from the slits to the detector). This example demonstrates that there is a dependency of the diffraction pattern on the object the incident waves are scattered from and in principle demonstrates the power of diffraction and scattering as a structural technique. However, in the example of Young's double slits, the distance between the slits is more easily determined through direct measurement i.e. with a ruler. In order to be able to use scattering as an effective probe of the internal meso-scale structure of materials, the slits we considered in Young's experiment are replaced with planes of atoms in a lattice separated by a distance, d .

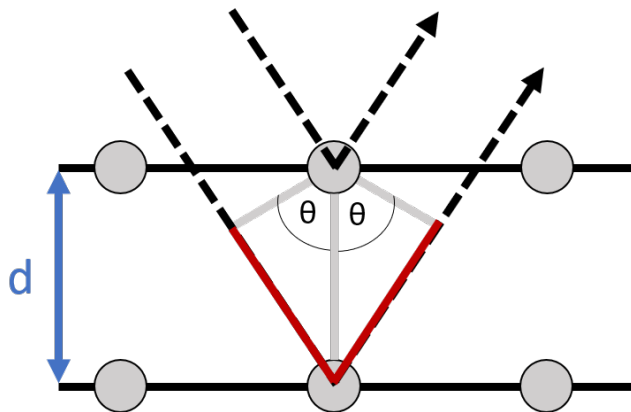


Figure 2.5.1.2: Visualisation of Bragg diffraction from planes of atoms in a crystal lattice. Where θ is the angle of incidence and the red line depicts the path difference between the two waves.

Figure 2.5.1.2 shows the diffraction of two waves incident on planes of atoms. The path difference between the two waves can be found via trigonometry (i.e. half the path length is equal to $d \cdot \sin\theta$). By considering X in equation 2.5.1.1, as the path difference between the two waves, we arrive at the following equation:

$$n\lambda = 2d\sin\theta \quad (2.5.1.4)$$

where θ is the scattering angle. This equation is known as Bragg's Law and is arguably one of the most important laws determined in history, and highlights that diffraction can be used to find distances within a system [156]. In a diffraction experiment the angle subtended between the incident and scattered wave is measured, which is termed 2θ . Diffractometers are classified by the angular range they are able to probe, i.e. small-angle or wide-angle. Bragg's Law (Eqn. 2.5.1.4) shows that there is an inverse relationship between the distance of interest, d , and the scattering angle, θ meaning that in order to study large structures, scattering events with a small scattering angle should be investigated, while the converse is true for small length scales (i.e. larger angles should be studied to probe the short length scales).

It is important to note that in order to perform a diffraction experiment and extract meaningful information about the length-scales in the system, the wavelength incident upon the sample must be known. Furthermore the wavelength must be tailored to be comparable to the sizes within the sample in order for diffraction to occur.

2.5.1.2 An idealised scattering experiment and elastic scattering

The previous section discussed the use of diffraction and scattering as a tool to probe distances in a system. In this section some of the key concepts involved in a scattering experiment will be covered. Consider an ideal scattering experiment (Fig. 2.5.1.3), where a particle¹³ or wave of wavevector \vec{k}_i is incident upon a sample and is scattered emerging with some final wavevector \vec{k}_f .

¹³The wave-particle duality of matter, in which it is possible for particles to behave as waves and vice versa

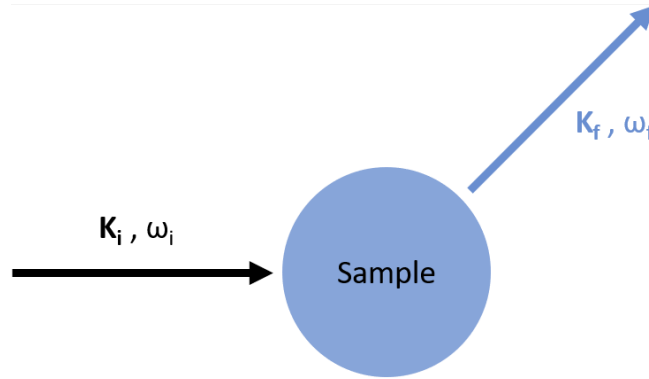


Figure 2.5.1.3: A schematic representation of a particle being scattered by a sample

The conservation of momentum enables the momentum to be expressed as:

$$\bar{P} = \hbar\bar{k}_i - \hbar\bar{k}_f = \hbar\bar{q} \quad (2.5.1.5)$$

where \hbar is Planck's constant divided by 2π and \bar{q} is

$$\bar{q} = \bar{k}_i - \bar{k}_f \quad (2.5.1.6)$$

For simplicity and relevance¹⁴ we shall only discuss the special case when the system scatters elastically (i.e. the energy of the scattered wave particle/wave is equivalent to the energy of the incident particle/wave) which can be expressed as:

$$|\bar{k}_i| = |\bar{k}_f| = \frac{2\pi}{\lambda} \quad (2.5.1.7)$$

From equation 2.5.1.6 it can be seen that \bar{q} is the difference between the wavevectors. q is a quantity used regularly in scattering experiments and can be further defined by considering the geometry of the scattering.

¹⁴All scattering data presented in this work is based on elastic scattering

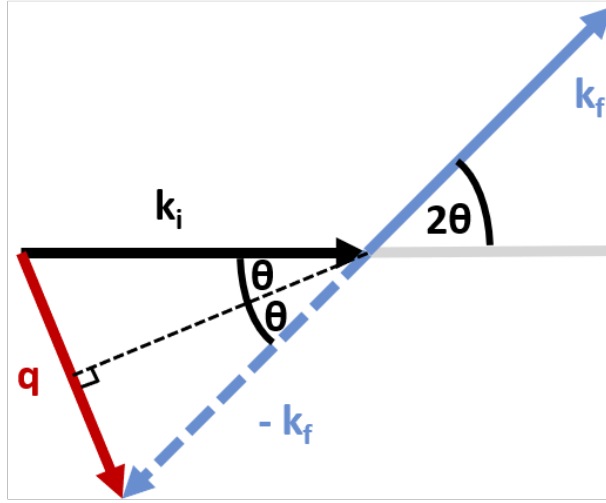


Figure 2.5.1.4: Vector diagram for elastic scattering, through an angle of 2θ

Figure 2.5.1.4 shows the vector diagram for an elastic scattering, where an incident particle is scattered through an angle 2θ , such that $|\bar{k}_i| = |\bar{k}_f|$. Given the identity in equation 2.5.1.7 and that the angle between \bar{k}_i and \bar{k}_f is 2θ , q can be expressed as:

$$q = 2 \left(\frac{2\pi \sin\theta}{\lambda} \right) = \frac{4\pi \sin\theta}{\lambda} \quad (2.5.1.8)$$

Equation 2.5.1.8 shows that q links the magnitude of the momentum transfer to the wavelength and the scattering angle, furthermore by incorporating Bragg's law (Eqn. 2.5.1.4) in to 2.5.1.8,

$$q = \frac{2\pi}{d}, \quad (2.5.1.9)$$

it can be shown that q is inversely related to d . This inverse relation means that q gives a measure of the real-space distances in reciprocal space. Obtaining results in reciprocal space is a more convenient way to extract structural information, as the real-space distances probed in experiments are on the order of 10^{-8} to 10^{-10} m, making them extremely difficult to access in real-space. It is important to note at this point, that it

can be shown [155] that the length-scales that characterise a function and the Fourier transform of a function are inversely related, i.e. reciprocal space (q-space) is related to the Fourier transform of real-space. This relation between reciprocal space and the Fourier transform of real-space means that extracting information from the reciprocal space (i.e. scattering data) is the same as extracting information from the Fourier domain (i.e. transformations of real-space functions).

2.5.1.3 X-rays and neutrons as diffraction probes

In the previous section an ideal scattering experiment considering an arbitrary scattering particle was discussed. In this section the properties of two well-used scattering probes will be discussed, namely X-rays and neutrons.

Property	X-rays	Neutrons
Charge	0	0
Mass	0	1.675×10^{-27} kg
Spin	1	$\frac{1}{2}$
Magnetic Moment	0	$1.913 \mu_N$
Energy	$\hbar\omega = \frac{hc}{\lambda}$	$\frac{1}{2}m\nu^2 = \frac{\hbar^2 k^2}{2m}$

Table 2.5.1.2: Properties of x-rays and neutrons

Table 2.5.1.2 compares some of the key properties of X-rays and neutrons. While both probes are uncharged it can be seen that the main differences are that the neutron has a mass, a half integer spin and a magnetic moment compared to the massless, non-magnetic x-ray photon with integer spin. The origin of this difference is that the photon is an elementary particle belonging to the boson family¹⁵, in contrast the neutron is an atomic composite particle made up of 3 subatomic quarks which belong to the fermion family¹⁶. These differences make X-rays and neutrons fantastic complimentary scattering

¹⁵In the standard model of the universe bosons are the force carrying particles that obey Bose-Einstein statistics i.e. particles are able to occupy the same quantum state.

¹⁶In the standard model, fermions are the 'mass' particles that obey Fermi-Dirac statistics i.e. two fermions are forbidden from occupying the same quantum state as each other.

probes, as the X-ray photons interact strongly with, and are scattered by, the negatively charged electron cloud surrounding atoms and molecules (due to the fact that photons are the mediating particle for the electromagnetic force), while neutrons do not interact with the electron cloud due to their lack of charge. Neutrons instead interact weakly with matter, only scattering off the nuclei of atoms (due to strong force interactions with the protons and neutrons in the nucleus). This means that X-rays are able to capture the shape of the electron cloud of a scattering object, while neutrons are sensitive to the arrangement of the atomic nuclei. Using both these particles to probe structure allows for the detection of subtle structure motifs by comparing the different patterns derived from scattering off the electron clouds or atomic nuclei with X-rays or neutrons.

2.5.2 Analysis of scattering data - the form and structure factor

This section has so far discussed the basic theory of scattering and the different structural probes, now the section will move on to discuss how useful information can be extracted from scattering curves. If we consider a collection of scattering objects of some arbitrary shape and distribution then the overall structure of the the system in real space can be formulated as;

$$\mathcal{S}(r) \propto P(r) * g(r), \quad (2.5.2.1)$$

where $P(r)$ is the pair-pair distribution function (i.e. a function that describes the distances between pairs of particles in a given volume) of the shape and $g(r)$ is the radial distribution function (i.e. a function that describes the variation in density of objects in a system as a function of distance from some reference point). The expression (the proportionality stems from the fact that the right hand side has not been normalised, by number, mass or volume as the choice of normalisation varies across discipline) for the structure of the system in real space (2.5.2.1) shows that $P(r)$ (which describes the shape of a single scattering object) and $g(r)$ (which describes the distributions of a collection of scattering objects) are convoluted together. Convolution is a mathematical operation

acted on 2 functions (f and g) in order to produce a third function ($f * g$) that expressed, how the profile of one function is altered by the other [157]. This definition explains why it makes sense that $P(r)$ and $g(r)$ are convoluted together as one would expect the structural profile of an arbitrary shape to be altered as the distribution of objects was changed, and altered shape would describe the structure of the system. When investigating structure of a system, one is usually interested in extracting information about both the shape of the individual scattering object and the distribution of these scattering objects. However, convolution is quite an intimate process making the separation of the shape information, $P(r)$, and the organisational information, $g(r)$, extremely difficult. Fortunately the convolution theorem

$$\mathcal{F}\{f(x) * g(x)\} = \mathcal{F}\{f(x)\} \cdot \mathcal{F}\{g(x)\} = \hat{f}(t) \cdot \hat{g}(t) \quad (2.5.2.2)$$

states that the Fourier transform of the convolution of two functions is equivalent to the product of the individual Fourier transform of each function (Eqn. 2.5.2.2). Applying this theorem to equation 2.5.2.1 yields

$$\hat{S}(q) = I(q) \propto P(q) \cdot S(q), \quad (2.5.2.3)$$

Recall that in section 2.5.1.2 it was stated that the Fourier transform of real-space distances were equal to the ‘distances’ in reciprocal space or q -space. By taking the Fourier transform of the real-space structure, $S(r)$, and applying the convolution theorem, the structure of the system in q -space is found and is proportional to the product of two factors, $P(q)$ and $S(q)$, termed the form and structure factor, respectively. The form factor, $P(q)$, is a function that describes the shape or form of the scattering object in reciprocal space, while the structure factor, $S(q)$, is a function in reciprocal space that describes the organisation of the scattering objects and is ultimately controlled by the interaction between scattering objects. Equation 2.5.2.3 shows that these two functions are multiplied together in reciprocal space (as opposed to the convolution seen in real-space) which makes them significantly easier to separate them and gain information

about the shape and organisation of the scattering objects in the system. Furthermore since both of these factors are described in reciprocal space (q-space) it is easy to probe them directly via diffraction and scattering. While this description lacks the in-depth mathematical rigour of a full derivation, it still demonstrates the important point that by analysing scattering data in reciprocal space it is possible to separate and extract information about the shape of the scattering object and how these objects are arranged in real space. In chapters 3 and 4 the selection of the form and structure factor to fit the scattering curves and extract real space information about the structure of folded protein hydrogel is discussed.

2.5.3 Small-angle scattering experiments

This section outlines the details of the SAXS and SANS experiments performed in this thesis. All SAS curves obtained, via either technique, were fitted with SasView¹⁷.

2.5.3.1 SAXS

SAXS measurements were conducted in the Materials Characterisation Laboratory of the ISIS Neutron and Muon Source, on the Nano-inXider instrument using a micro-focus sealed-tube Cu 30 W/30 μ m X-ray source (Cu K α , $\lambda=1.54$ Å). Samples were loaded and gelled in 1 mm path length glass capillary tubes. The q-range investigated was 0.0045 - 0.37Å⁻¹, and measurements were made at room temperature. Frame acquisitions of samples were taken with an acquisition time of 30 mins. A number of frames were taken depending on the samples protein concentration. High concentration samples (>100mg/ml) were measured for 4 frames (total measure time of 2 hours), while low concentration samples (<10mg/ml) were measured for 20 frames (total measure time of 10 hours). Multiple frames were taken and averaged to ensure good statistics the difference in measurement time is as a result of the reduction in the scattering power of lower concentration solutions.

¹⁷<http://www.sasview.org>

2.5.3.2 SANS

SANS measurements were conducted at the ISIS Neutron and Muon Spallation Source (STFC Rutherford Appleton Laboratory, Didcot, UK). All samples were loaded and gelled in 1 mm path length quartz cuvettes and measured at room temperature. Consistent temperatures were ensured by an external circulating thermal bath. All raw SANS data was processed using the Mantid framework following the standard procedures for the instrument (detector efficiencies, measured sample transmissions, absolute scale using the scattering from a standard polymer, etc) [158].

Samples of MBP in solution and MBP hydrogels discussed in chapter 3, were measured on the time-of-flight diffractometer instruments LOQ and ZOOM, respectively. The Q ranges explored on the LOQ and ZOOM instruments¹⁸ are 0.006–0.24 Å⁻¹ and 0.0025–0.43 Å⁻¹ respectively.

SANS measurements on samples of BSA hydrogel discussed in chapter 4 were conducted on the time-of-flight instrument Sans2d¹⁹. Sans2d front and rear detectors were set up at 5 and 12m, respectively, from the sample, defining the accessible q-range as 0.002 - 0.5Å⁻¹.

2.6 Bulk mechanical characterisation via rheology

Rheology is the study of the flow of matter, primarily on visco-elastic fluids and solids. Varying rheological properties of matter are apparent in nature: from water, which flows freely exhibiting only viscous behaviour, to iron, which deforms upon the constant application of force, behaving only elastically. Purely elastic materials store the energy input, in contrast viscous materials dissipate the energy input. These examples are the extreme cases of rheological behaviour, visco-elastic materials are materials that are somewhere between these two extremes, i.e. these are materials that exhibit both elastic and viscous properties [159]. The properties of visco-elastic materials arise directly as

¹⁸experiment number RB1820509

¹⁹experiment number RB1920289

a result of interactions between the atoms or molecules within the material, hence rheological characterisation of materials can give information on the microscopic structure and dynamics of materials.

In this section, the basic principles of shear rheology will be outlined as well as how the storage and loss moduli of a material are determined. Along with this, the rheological equipment and testing methods will be discussed.

2.6.1 Shear Rheology and the shear modulus

A shear deformation is a deformation in which parallel internal surfaces slide past one another as depicted in figure 2.6.1.1.

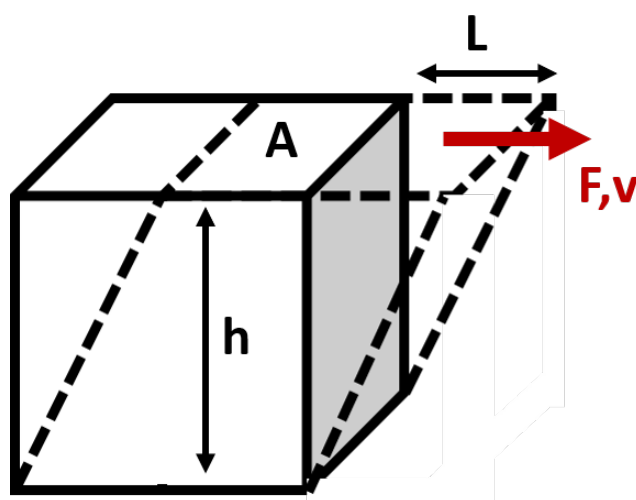


Figure 2.6.1.1: Visualisation of a shear deformation as the result of an applied shear force, F .

From figure 2.6.1.1 key quantities can be defined, namely:

- Shear stress, σ , which is the ratio of the shear force, F to the perpendicular cross-sectional area, A , i.e. $\sigma = \frac{F}{A}$.
- Shear strain, γ , is the normalised deformation of the material, defined as $\gamma = \frac{L}{h}$.
- Shear rate, $\dot{\gamma}$, is the rate of change of shear strain, defined as $\dot{\gamma} = \frac{d\gamma}{dt}$.

The modulus of this deformation is the shear modulus, G , and is a measure of the material's resistance to shear, while the viscosity, η , of the deformation is a measure of the materials resistance to flow. Both are defined in equation 2.6.1.1 and 2.6.1.2.

$$\sigma = G\gamma \quad (2.6.1.1)$$

$$\sigma = \eta\dot{\gamma} \quad (2.6.1.2)$$

These equations represent the basic definitions of a Hookean solid (Eqn. 2.6.1.1) and a Newtonian fluid (Eqn. 2.6.1.2), and describe the behaviour of an ideally elastic and ideally viscous sample, respectively. These equations hold for a linearly applied shear strain field, so would require linear shear experiments to be able extract useful information about the mechanics of the system such as traditional stress-strain curves. What if instead of a linear strain an oscillatory strain ($\gamma(t) = \gamma_0 \sin(\omega t)$, where γ_0 is the amplitude of the oscillatory strain) is applied to the system? If this is the case then equations 2.6.1.1 and 2.6.1.2 can be rewritten as

$$\sigma = G\gamma(t) = G\gamma_0 \sin(\omega t) \quad (2.6.1.3)$$

$$\sigma = \eta\dot{\gamma}(t) = \eta\gamma_0\omega \cos(\omega t) = \eta\gamma_0\omega \sin\left(\omega t + \frac{\pi}{2}\right) \quad (2.6.1.4)$$

The choice of applying an oscillatory strain can be understood by comparing equations 2.6.1.3 and 2.6.1.4 to the oscillatory strain ($\gamma(t) = \gamma_0 \sin(\omega t)$). It can be seen that Hookean solids (Eqn. 2.6.1.3) respond instantaneous or in-phase to the applied strain i.e. the stress-strain phase difference, $\delta=0$. In contrast ideally viscous materials exhibit a stress response (Eqn. 2.6.1.4) that is out of phase with the applied strain by $\delta=\pi/2$. Viscoelastic materials exhibit both elastic and viscous behaviour and as such have a phase difference in their stress response between 0 and $\pi/2$.

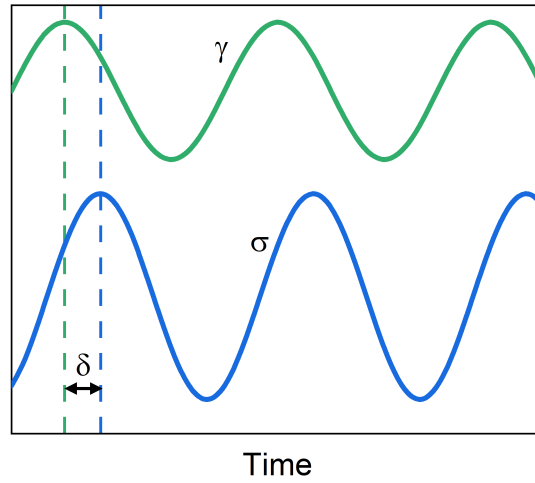


Figure 2.6.1.2: An applied oscillatory strain, γ , resulting in a stress response, σ , which is δ degrees out of phase.

Figure 2.6.1.2 show an example of the stress-strain behaviour of a viscoelastic material, where upon the application of an oscillatory strain there is a lag in the stress response of the material by some phase angle, δ . From this behaviour we can define the complex shear modulus of the material as

$$G^* = \frac{|\sigma_0|}{|\gamma_0|} e^{i\delta} = G' + iG'' \quad (2.6.1.5)$$

Where σ_0 and γ_0 are the amplitudes of the oscillatory stress and strain respectively. Using Euler's relation ($e^{i\delta} = \cos(\delta) + i\sin(\delta)$), the storage modulus, G' , (the real component of G^* and gives a measure of the energy stored during deformation which returns the material to its original shape once unloaded) and loss modulus, G'' , (the imaginary component of G^* , and gives a measure of the energy lost during deformation)[159] can be expressed as,

$$G' = \frac{|\sigma_0|}{|\gamma_0|} \cos(\delta) \quad (2.6.1.6)$$

$$G'' = \frac{|\sigma_0|}{|\gamma_0|} \sin(\delta) \quad (2.6.1.7)$$

These quantities help characterise the elastic and viscous behaviours of the materials. Additionally it can be helpful to calculate the loss ratio

$$\tan\delta = \frac{G''}{G'}, \quad (2.6.1.8)$$

which describes whether a material is elastically dominated ($\tan\delta < 1$) or viscously dominated ($\tan\delta > 1$).

2.6.2 Anton Paar pseudo-strain controlled rheometer

In order to measure the storage and loss moduli of the protein hydrogels investigated in this thesis, an Anton Paar MCR 302 stress-controlled rheometer in pseudo-strain controlled mode was used. This rheometer was used in conjunction with the lighting apparatus shown in figure 2.3.3.2, to allow for the measurement of protein hydrogel from pre-gel solution to fully cross-linked gel. The schematic in figure 2.6.1.1 shows a simple rectangular deformation, however the MCR 502 rheometer deforms the sample rotationally (Fig. 2.6.2.1), using a rotary actuator with a torque and an angular frequency range of $0.5 \times 10^{-7} < M < 0.2 \text{ Nm}$ and $10^{-9} < \omega < 3.14 \times 10^2 \text{ rad/s}$, respectively. Different geometries, including cone-plate and concentric cylinder, allow for the probing of a wide range of viscosities and shear moduli. In this project, a parallel plate geometry consisting of a circular top plate of radius, r , and a glass base plate separate by a gap height, h , was used. A basic schematic of the sample between these two plates is shown in figure 2.6.2.1.

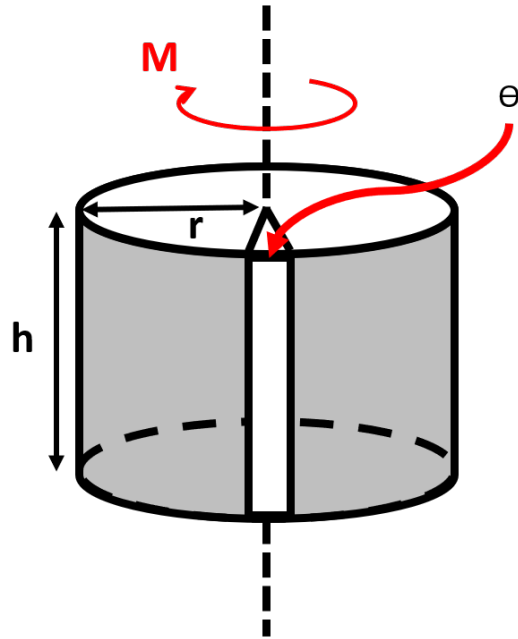


Figure 2.6.2.1: Parallel plate sample of height, h , and radius, r . A torque, M , is applied which shears the sample, resulting in an angular deformation, θ .

A parallel plate geometry was selected over a cone-plate geometry, to ensure a uniform light field across the cross-section of the sample. For a parallel plate geometry the applied shear stress and strain can be calculated using equations 2.6.2.1 and 2.6.2.2.

$$\sigma = \frac{2M}{\pi r^3} \quad (2.6.2.1)$$

$$\gamma = \frac{r\theta}{h} \quad (2.6.2.2)$$

Where, r , h , θ and M are the radius of sample, gap height of the sample, angular deformation of the rotary actuator and the necessary transducer torque to achieve the deformation, respectively. As equation 2.6.2.2 shows the strain field in the sample is inhomogeneous i.e. the strain is zero at the centre of the plate and maximum as the plate perimeter. However this is not an issue due to the fact that the majority of the measurements and analysis performed within this work are in the linear viscoelastic

region, in which the stress-strain response is approximately constant as a function of applied strain. By combining equations 2.6.2.1 and 2.6.2.2 the complex shear modulus can be defined as

$$G^* = \frac{\sigma^*}{\gamma^*} = \frac{2M^*h}{\pi\theta^*r^4} \quad (2.6.2.3)$$

Where M^* and θ^* are the complex torque and angular deformation respectively. The r^4 dependency makes it clear that a small error in the radius of the samples leads to a large error in the measured values of G' and G'' , highlighting the importance of maintaining a consistent sample shape throughout experiments and between samples.

The procedures below outline the specific parameters used in each test and shows exemplar data set for folded protein-based hydrogels obtained from each procedure. In all tests a 8mm diameter plate was used with a constant gap height between 0.65 to 0.75 mm, and to avoid dehydration of the sample low-viscosity silicone oil (≈ 5 ct) was placed around the geometry.

2.6.2.1 Time-dependant gelation curves of protein hydrogels

To probe the gelation kinetics of the folded protein hydrogels pre-gel solutions of samples were loaded on to the rheometer. Experiments were conducted over a period of 1 hour and 6 minutes at a frequency and shear strain of 1Hz and 0.5%, respectively. At time $t=60$ s the samples were illuminated with blue light for 5 mins to ensure complete cross-linking.

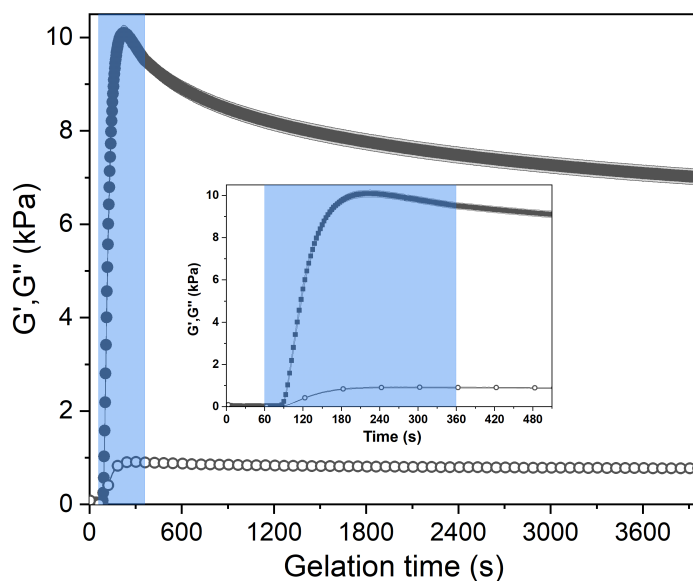


Figure 2.6.2.2: Exemplar gelation curve of folded protein hydrogels, showing the evolution of storage (closed), G' , and loss (open), G'' , moduli with time. The blue transparency signifies when the sample is illuminated with blue light (from $t= 60$ s to $t= 360$ s) and the photo-activated cross-linking reaction is taking place. The key features to note from the exemplar gelation curve are the rapid increase in G' and G'' during the photo-chemical cross-linking as a result of cross-link and network formation, and the long relaxation post-photo-chemical cross-linking, the origins of which are explored later in this thesis. (inset) A magnification of the gelation curve to highlight the early stages of gelation.

2.6.2.2 Frequency-dependant mechanical spectra of protein hydrogels

Once the gelation measurements were completed, the frequency dependant mechanical spectra of the samples were measured at a shear strain of 0.5% and a frequency range of 0.01 to 10Hz.

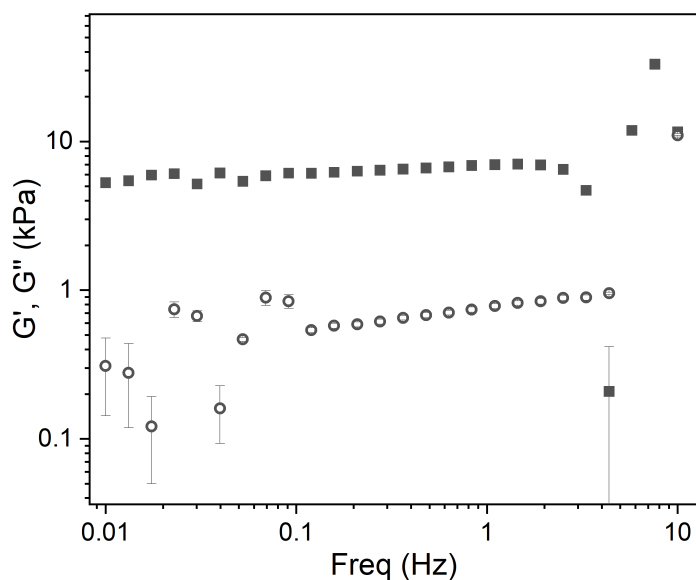


Figure 2.6.2.3: Exemplar frequency dependency of the storage (closed), G' , and loss (open), G'' , moduli of a folded protein-based hydrogel. Where above a fundamental frequency of 2Hz there is a large increase in the G' and G'' this is due to a common artefact with rheometers where the torque contribution needed to move the the geometry at high frequencies is not removed from the signal accurately. Note the diverging relationship between the linear sections of the frequency dependencies as the frequency approaches zero of G' and G'' implying that the system behaves as a solid even over long time scales.

2.6.2.3 Stress-strain curves of protein hydrogels

The load and unload characteristics of protein hydrogels were investigated by repeatedly loading the samples to a max strain and then unloading back to zero strain. Initially samples were loaded up to a strain of 10% at a rate of 1%/s before being unloaded at the same rate. After the samples were un-strained for 5 mins (to ensure relaxation of the system), the gels were loaded up to 30% at a rate of 1%/s before being unloaded at the same rate. This process was repeated for samples loaded up to 50% and in some cases 75%.

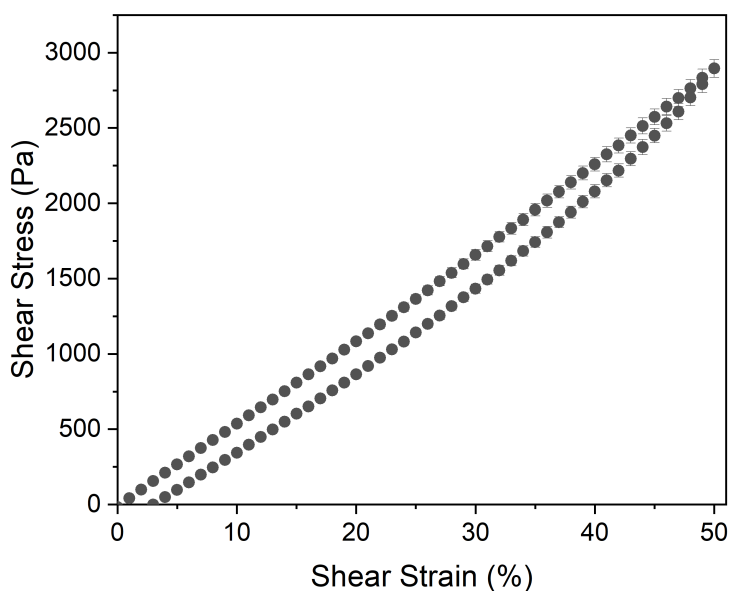


Figure 2.6.2.4: Exemplar load-unload stress strain curve of a folded protein-based hydrogel, loaded up to a strain of 50% at a rate of 1%/s, before being unloaded to a strain of 0% at the same rate. The linear section can be fitted to give the storage modulus of the system, while the hysteresis area is a measure of the level of energy dissipated per unit volume of the system upon loading and unloading.

2.6.2.4 Non-linear behaviour of protein hydrogels

Despite the inhomogeneous strain fields present due to the parallel plate geometry, preliminary measurements to investigate the non-linear behaviour of folded protein based hydrogels were conducted by oscillator rheological measurements at a frequency of 1Hz and an increasing shear strain from 1% to 1000%.

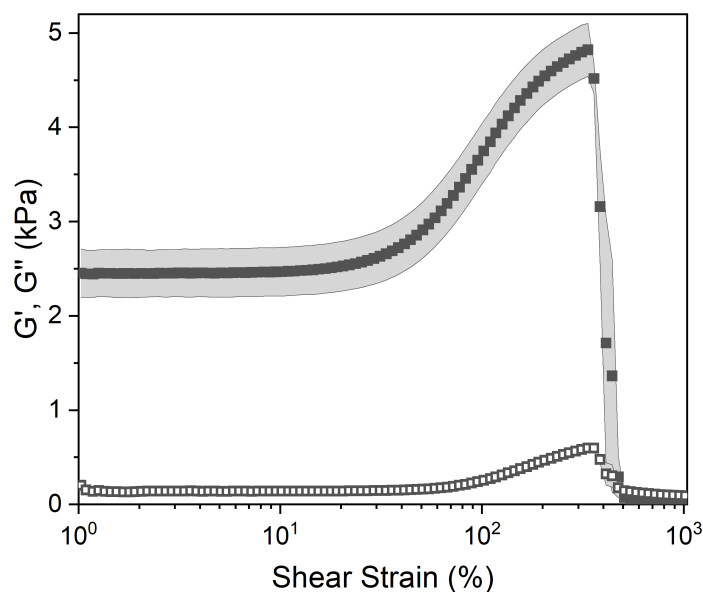


Figure 2.6.2.5: Exemplar strain dependency of the storage (closed), G' , and loss (open), G'' , moduli of a folded protein-based hydrogel. Three key features from this curve are; i) The reasonable invariance of G' and G'' at low strain values which corresponds to the linear mechanical response of the hydrogel; ii) the stiffening of the sample with increasing strain at high strain values corresponding to the non-linear mechanical response of the hydrogel; and iii) the sharp decrease in both G' and G'' at very high strain values which corresponds to fracture of the sample.

Chapter 3

Single Molecule Protein Stabilisation Translates to Macromolecular Mechanics of a Protein Network

To begin to address the challenge of relating the properties of an individual building block to the collective properties of a network of individuals, the first experimental study of this work will investigate the cross length-scale translation of single molecule stability. The goal of this study was to determine if the molecular-level properties scale up to the network level or scale out (i.e. the bulk properties of the network are invariant of the building block properties). To achieve this goal a novel folded protein hydrogel constructed from maltose binding protein (MBP) is mechanically and structurally characterised in the absence and presence of the ligand maltose. This chapter will begin by outlining the selection of MBP as a model protein and the novel hydrogel system. The effects of protein building block stability on hydrogel bulk mechanics and relaxation behaviour will be then explored and discussed. This chapter will also introduce a structural model of folded MBP protein hydrogels through a combination of structural techniques.

3.1 Selection of hydrogel building block and model system

To perform this study a model protein building block was needed, this section will outline the desired properties of such a model protein hydrogel building block. Furthermore the section will discuss why MBP was selected as the model protein of choice and the design of the hydrogel model system constructed via photo-chemical cross-linking.

3.1.1 Desired properties of a model protein hydrogel building block

Three key properties were identified as essential in a protein hydrogel building block for this study. These properties are:

- i) Contain at least 4 solvent-accessible, cross-linking, tyrosine residues (this is a geometric requirement [160] for the formation of a network via residue specific photo-chemical cross-linking (section 2.3.3)).
- ii) The protein must be obtainable in high quantities, either high expression yields or easily purifiable, in order to obtain the large quantities necessary for full structural and mechanical characterisation of the protein hydrogels.
- iii) Finally and most importantly the protein must have a simple and controllable mechanism in which to tune/alter the stability of the protein's folded structure.

3.1.2 Maltose binding protein

MBP was selected as a model system to investigate the relationship between building block stability and the macroscopic properties of a cross-linked MBP protein network. MBP is a 370 residue globular protein that is part the maltose/maltodextrin system of *E.coli*, and is responsible for the uptake and catabolism of maltodextrins [161].

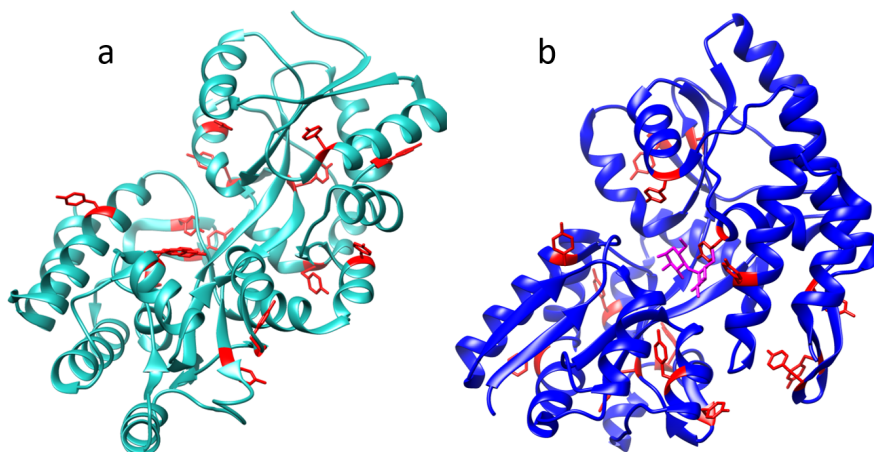


Figure 3.1.2.1: Crystal structures of MBP in the a) absence (light blue, PDB code: 1JW5) and b) presence (dark blue, PDB code: 1Y4C) of maltose. The cross-linking tyrosine residues are coloured red and the bound maltose is coloured magenta, for clarity.

Figure 3.1.2.1 shows the structure of MBP in both its apo state and with maltose bound as determined by x-ray crystallography [162, 163]. The structures show that MBP is an α - β protein with an approximately 'Pac-Man'-like shape [164], furthermore the crystal structures show no significant change in the size or shape upon the binding of maltose (root mean square difference (RMSD) = 4 Å). This is also confirmed by SAXS measurements of MBP in solution in the absence and presence of maltose (Fig. C.2.0.1). The primary structure of MBP contains 15 tyrosine residues and analysis of the solvent accessible surface area (using the calculate solvent accessible area function in USCF Chimera 1.14) shows that 14 out of the 15 tyrosines are solvent accessible (i.e. $>1\text{\AA}^2$ solvent accessible surface area of the residue side chain). This fulfils the first condition in section 3.1.1. MBP is both a highly soluble and a highly expressing protein (in the host system *E.coli*), this makes MBP a valuable protein in molecular biology as an solubility/expression tag for insoluble/difficult to express proteins [165]. This high expression level of MBP ($\sim 250\text{mg}$ per litre of growth culture, see section 2.2.2) fulfils the second condition required for a model protein outlined in section 3.1.1. The final criterion for a model protein is the ability to change the inherent stability of the folded structure of the protein. This is possible for MBP upon the binding of maltose.

3.1.2.1 Effect of Maltose Binding on MBP stability

The ligand maltose is a disaccharide formed from two units of glucose, that binds in the ‘mouth’ (as depicted in Fig. 3.1.2.2a and b) of the ‘Pac-Man’-like MBP, between the hydrophobic cores of the protein. Upon the binding of the ligand maltose an increase in the thermal stability of MBP is observed, as measured by an enhancement in the melting temperature of MBP by 8–14°C, depending on pH [133]. This increase in thermal stability is attributed to additional hydrogen bonds introduced by the maltose leading to an increase in the enthalpy of unfolding. In addition to the increase in thermal stability the bind of maltose also modulates the mechanical stability of MBP. A number of SMFS studies have successfully demonstrated that the mechanical stability of single proteins can be modulated upon ligand binding.[166–171]

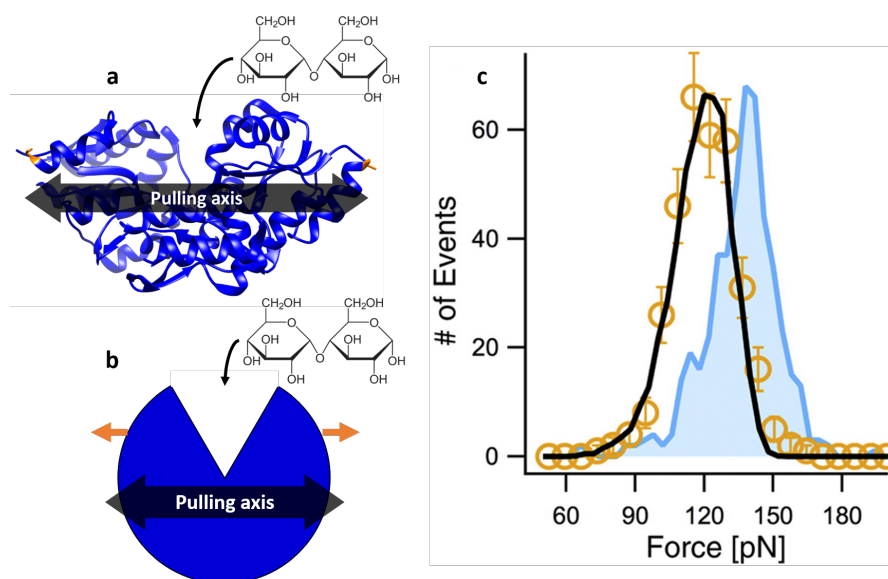


Figure 3.1.2.2: (a) Crystal structure (b) simplified schematic representation of MBP (PDB code: 1Y4C) with residue 53 and 141 highlighted orange to denote the pulling axis across the lobes of MBP. The binding site of maltose is denoted by the black arrow. (c) The number of MBP unfolding events recorded as a function of the measured peak force applied to MBP in the 53-141 pulling direction depicted in (a) and (b), in the absence (orange point with black line) and presence (blue curve) of the ligand maltose. Taken from [82]

In the case of MBP binding maltose, the ‘mouth’ motif, consisting of two structural lobes connected by a hinge region, changes from an open to closed confirmation (Fig.

3.1.2.2). Bertz and Rief demonstrated that when stretched from its N–C termini, the binding of maltose did not change the mechanical stability of MBP [81]. However, utilising protein engineering to control the pulling direction, such that the two lobes of MBP are forced to move apart along the hinge axis (specifically extended via residues 53 and 141, Fig. 3.1.2.2a and b), the binding of maltose enhanced the mechanical stability of MBP by 12% (from ≈ 120 pN to ≈ 135 pN, Fig. 3.1.2.2c)[82]. The measured increase in mechanical stability was attributed to 11 additional hydrogen bonds in the maltose binding site upon ligand binding [172]. This study demonstrates the importance of hydrogen bonding for the mechanical stability of proteins [82, 167, 173, 174]. The opposing results between the two pulling directions tested on MBP highlight the importance of considering pulling direction when predicting if an enhancement in the mechanical stability will be measured. For MBP the majority of cross-linking tyrosine residues (9 out of 14) are located either side of the hinge region (Fig. 3.1.2.1), consistent with the hinge axis reported by Rief et al. (these tyrosine are all within 26\AA of the maltose binding site in agreement with residues 53 (25\AA from binding site) and 141 (35\AA from binding site)). Given the prior work of Rief et al., we would expect cross-linking of tyrosines across the hinge region and the presence of maltose to result in an increase in the mechanical stability of chemically cross-linked MBP. These properties make MBP an suitable candidate protein to investigate the effects of molecular level stability on the mechanical properties of a hierarchically structured macroscopic system. However, an important caveat of the third criterion (section 3.1.1) to consider is that the change in stability of the building block must be controllable.

Ligand binding is an equilibrium between the apo and bound state of a protein [175]. The binding of a ligand is governed by the association constant, k_a , while the unbinding is governed by the dissociation constant, k_d , shown for MBP in figure 3.1.2.3.

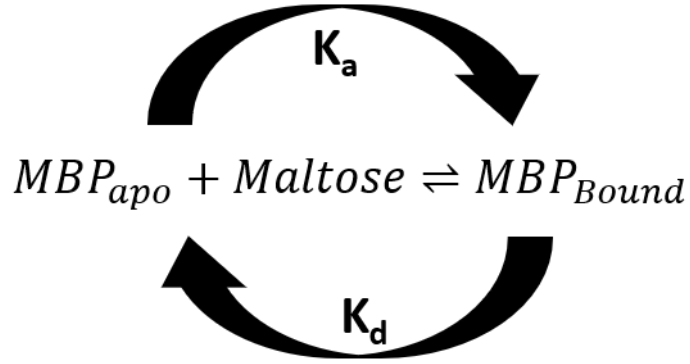


Figure 3.1.2.3: Equilibrium reaction of apo-MBP with maltose to form bound MBP:maltose, where k_a and k_d are the association constant and dissociation constant respectively.

By varying the concentration of the ligand, in this case maltose, the equilibrium can be shifted between the apo- and bound-state according to the binding affinity of the ligand which is governed by k_d . For MBP binding maltose the k_d value is $(1.20 \pm 0.05)\mu\text{M}$ [176, 177]. By considering the definition of k_d and making the relevant substitutions (see full derivation in section B.1) the proportion of MBP occupied by maltose, P_{occ} , can be expressed in terms of terms of known quantities, namely the total concentration of MBP, $[MBP]$, the total concentration of maltose, $[maltose]$, and k_d .

$$P_{occ} = \frac{([MBP] + [maltose] + k_d) - \sqrt{([MBP] + [maltose] + k_d)^2 - 4[MBP][maltose]}}{2[MBP]} \quad (3.1.2.1)$$

Equation 3.1.2.1 shows that the proportion of 'occupied' MBP can be controlled by varying the maltose concentration. By controlling the proportion of more stable and robust ligand bound MBP, the ensemble molecular stability can be tuned. This control combined with the other properties discussed above makes MBP an ideal model protein to construct a novel protein hydrogel to investigate the effects of single molecule thermal and mechanical stabilisation on the mechanical properties of a hierarchically structured macroscopic system.

3.1.3 Model system to investigate the effects of building block stability on bulk mechanics of protein networks

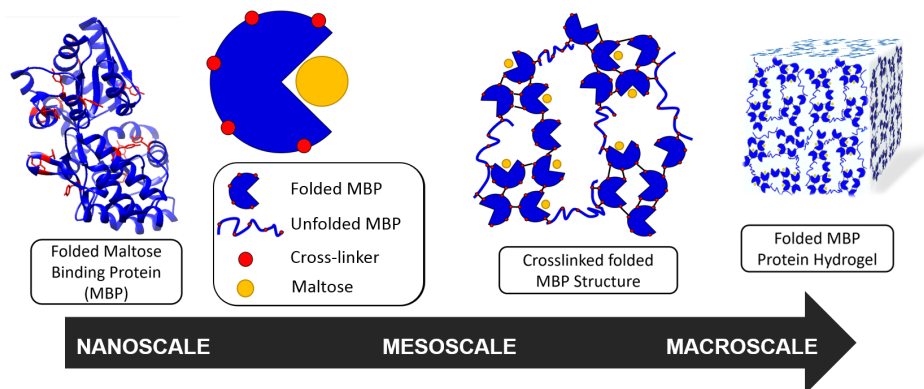


Figure 3.1.3.1: Schematic representation of the MBP hydrogel model system with a proportion of maltose 'occupied' MBP, P_{occ} , demonstrating the translation from the nanoscale to the macroscale.

The model hydrogel system used in this chapter, consists of folded MBP monomers cross-linked together via photo-chemical cross-linking (section 2.3.3), in the presence of varying concentrations of maltose (Fig. 3.1.3.1). As discussed in the previous section by varying the concentration of maltose present in the solution pre-gelation the ensemble building block stability can be tuned. So, in principle the molecular-level stability can be controlled and the translation to a bulk network investigated using rheology.

3.2 Modulation of Hydrogel Mechanics

3.2.1 Characterisation of the Linear Mechanics of MBP Hydrogels

To investigate whether an increase in the stability of MBP changes the macroscopic properties of a cross-linked MBP hydrogel, concentrated solutions of MBP (100mg/ml, 7.4% vol fraction) were photo-chemically cross-linked (see section 2.3.3) in the presence of 0mM to 10mM maltose (Fig. 3.2.1.1a). The frequency sweep curves (Fig. 3.2.1.1a) of MBP hydrogels, as determined by applied shear rheology, show how the storage, G' ,

and loss, G'' , moduli (which are the real and imaginary component of the complex shear modulus and are a measure of hydrogel elasticity and in-elasticity, respectively) vary as a function of both applied frequency and maltose concentration.

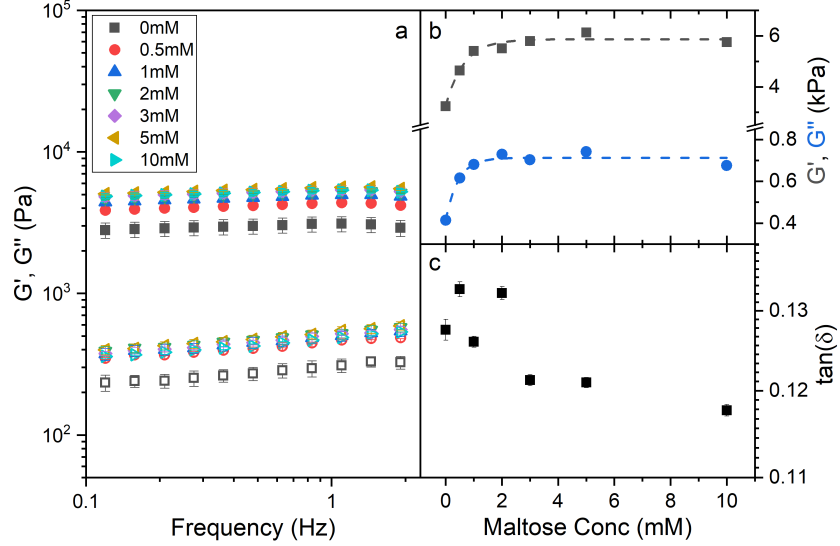


Figure 3.2.1.1: (a) Frequency sweeps showing the (filled) storage, G' , and (open) loss moduli, G'' , of chemically cross-linked MBP hydrogels (final concentrations: 100 mg/ml MBP, 30mM NaPS, $100\mu\text{M}$ Ru(II)bpy₃²⁺) as a function of maltose concentration. An oscillatory strain of 0.5% was applied to each sample. (b) G' , G'' at an oscillator frequency of 1 Hz as a function of maltose concentration. Dashed lines added as a guide for the eye. (c) Ratio of G'' to G' ($\tan(\delta)$) at 1 Hz as a function of maltose concentration.

Both moduli decrease as the frequency decreases and decrease linearly below 2Hz, the slopes of this region differ between the storage and loss moduli and appear to diverge implying that the elastic behaviour is dominant even over long timescales. Fitting the linear region between 0.1 and 2Hz allows for the determination of the storage and loss modulus at 1Hz (Fig. 3.2.1.1b) and by extension $\tan(\delta)$ (defined as G''/G') shown in figure 3.2.1.1c as a function of maltose concentration. In addition, the exponent of the power law dependence of the storage and loss moduli can be extracted as a function of maltose concentration (Fig. C.1.0.1), and shows little variation between maltose concentrations. The storage and loss moduli appear to increase sharply as a function of maltose concentration, with the former reaching an upper plateau at just over 2mM maltose, and the latter at approximately 1mM. It is interesting to consider what sets the

critical concentration of 2mM maltose for the storage modulus beyond which mechanical properties are insensitive to maltose content. One possibility is that the saturation point of the system is reached, and all the MBP building blocks have maltose bound. This seems intuitive given the MBP protein concentration is approximately 2mM, and we revisit this explanation later in the paper. While the addition of maltose increases the storage and loss moduli of the hydrogels, the ratio of loss to storage modulus remains relatively unchanged (approximately 0.125) suggesting that the degree of elasticity is the same in the presence and absence of maltose.

3.2.2 Characterisation of the Load-Unload Behaviour of MBP Hydrogels

The initial results show that the addition of maltose increases mechanical stability of the MBP hydrogels without changing the relative elasticity, to further investigate the effects of maltose on the hydrogels mechanical properties the hydrogels were investigated under load.

Figure 3.2.2.1a shows shear stress-strain loading curves up to 50% strain of MBP hydrogels from applied rotational rheology. A maximum strain of 50% was chosen as this corresponds to the beginning of the strain stiffening region as determined by strain amplitude ramp experiments (Fig. C.1.0.2). Additional stress-strain curves for maximum load strains of 10% and 30% were also performed (Fig. C.1.0.3). For all measured maltose concentrations, the stress-strain curves in figure 3.2.2.1a show clear linear elasticity up to shear strains of at least 15% (Fig. C.1.0.4). In this work the behaviour of hydrogels in the linear regime is focused on, but it is important to note that biopolymer gels exhibit rich non-linear [178–180] and delayed yielding behaviour [181–183], which would warrant subsequent studies and future work. Fitting the linear region of the stress-strain curves (Fig. C.1.0.4) and extracting the gradient yields a measurement of the storage modulus, G' . The storage modulus appears to increase sharply as a function of maltose concentration, reaching an upper plateau at just over 2mM maltose, in good agreement with the values extracted from the frequency sweep data (Fig. 3.2.1.1). The stress-strain

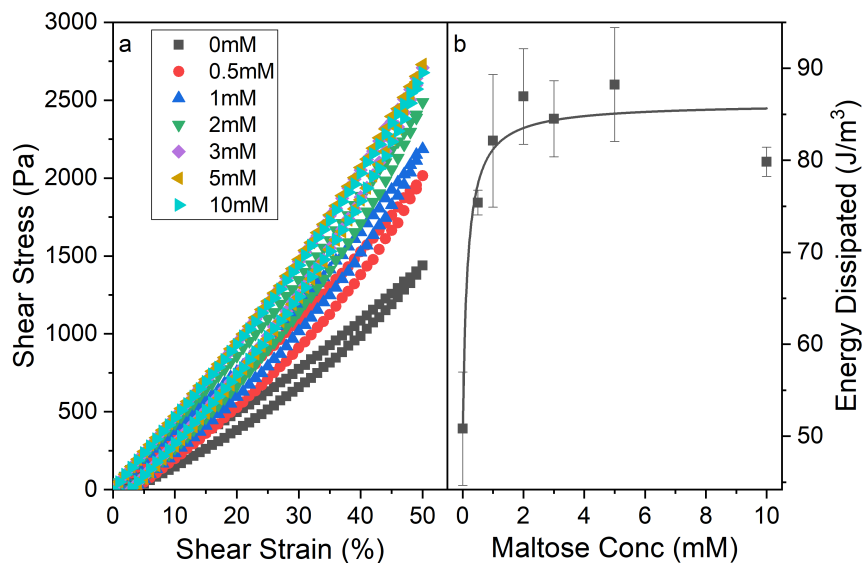


Figure 3.2.2.1: (a) Stress–strain curves of chemically crosslinked MBP hydrogels (final concentrations: 100 mg/ml MBP, 30 mM NaPS, $100\mu\text{MRu(II)bpy}_3^{2+}$) as a function of maltose concentration. Samples were strained to 50% at a rate of 1%/s and then unloaded down to 0% at the same rate. (b) Energy dissipation during load–unload cycle of MBP hydrogels as a function of maltose concentration. Solid line shows fit to Langmuir type model (Eqn. B.2.0.1)

curves all show some level of residual strain at 0Pa suggesting the gels have not yet fully recovered from the applied force, this residual strain appears to show no trend with maltose concentration (Fig. C.1.0.5). To determine that this residual strain was not indicative of permanent damage to the gels progressive strain loads were performed on the same sample (with appropriate time between to wait for relaxation of the sample). This showed that the sample followed the same load path each time demonstrating, that no permanent damage was caused (Fig. C.1.0.6).

In addition, the stress-strain curves (Fig. 3.2.2.1a) display more prominent hysteresis behaviour in the presence of increasing maltose concentrations. This hysteresis is indicative of the energy dissipated during loading and unloading and suggests that MBP hydrogels formed in the presence of higher concentrations of maltose dissipate more energy upon straining and relaxing. The area enclosed by the stress-strain provides a quantitative measure of the energy dissipated to the internal energy of the material. Calculating the energy dissipated from the curves in figure 3.2.2.1a as a function of maltose

concentration, generates the graph in figure 3.2.2.1b. The energy dissipation, like the storage modulus, increases and plateaus with maltose concentration. In folded protein hydrogels, the main source of energy dissipation is believed to be force-induced unfolding [120, 129], where more energy is required to unfold the more robust ligand bound MBP. Thus, increasing the maltose concentration results in stiffer gels with increased energy dissipation. Interestingly, using equation 3.2.2.1,

$$Efficiency = 1 - \frac{EnergyDissipated}{Strain_{Max} \cdot Stress_{Max}}, \quad (3.2.2.1)$$

the efficiency can be calculated from the curves in figure 3.2.2.1a and is shown in figure 3.2.2.2.

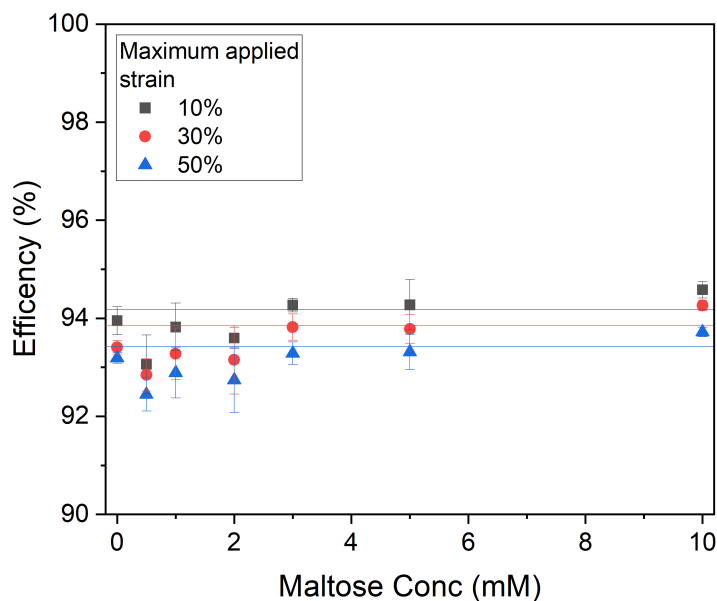


Figure 3.2.2.2: The efficiency of MBP based hydrogels extracted from stress-strain curves in figure 3.2.2.1 as a function of both maltose concentration and max strain.

The efficiency gives a measure of the proportion of the energy stored in the system that is returned upon unloading of the system. The invariance of the hydrogel efficiency with maltose concentration suggests that the same number of protein domains are unfolded irrespective of maltose concentration in order to accommodate the 50% strain

on the system. The invariance of the hydrogel efficiency with maltose is consistent between other measured load strains, even with lower energy dissipation measured at lower strains (Fig. C.1.0.7) suggesting that the number of protein domains being unfolded is invariant of maltose concentration but is dependent on the maximum applied strain.

3.2.2.1 Quantification of the Proportion of Folded MBP

To quantify the proportion of folded MBP in our cross-linked hydrogels we performed CD experiments of MBP in solution and in the cross-linked hydrogel, both in the presence and absence of maltose.

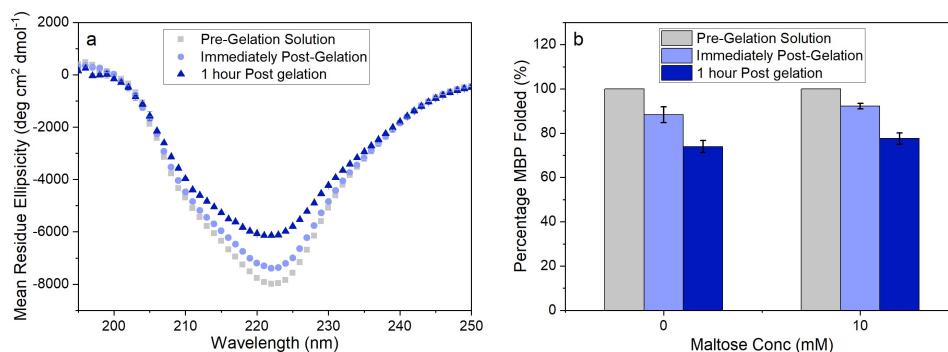


Figure 3.2.2.3: (a) Circular dichroism spectra of MBP hydrogels samples pre-, immediately post- and 1 hour post-gelation. (b) Comparison of the percentage of folded protein estimated using circular dichroism spectroscopy in the presence and absence of maltose, and as a function of time after gelation.

CD allows for measurement of the secondary structure of MBP and figure 3.2.2.3 shows the mean residue ellipticity spectra of MBP pre- and post-gelation, in the absence of maltose. In both the MBP solution and the hydrogel, the spectra exhibit the expected secondary structure profile for the α - β protein MBP, with negative peaks at 222nm and 209nm signalling α -helices and a positive peak at 195nm signalling the presence of β -sheets. The small shift in magnitude of the peaks in the mean residue ellipticity signal post gelation shows that there is a reduction in the amount of folded protein present, both immediately following gelation and 1-hour post-gelation. The spectra can be used to extract the relative folded fraction of MBP protein post-gelation in the absence and presence of maltose (Fig. 3.2.2.3b), at times that are comparable to the

rheology experiments. In both samples the relative folded fraction shows an initial reduction of approximately 10%, and a further reduction of 15% after 1 hour. These experiments show that while gelation results in unfolding of a proportion of the MBP protein, the folded population dominates and is relatively unchanged with increasing maltose concentration ((74±3)% folded MBP in the absence, and (77±3)% in presence, of maltose). This insignificant difference is unlikely to account for the over (1.7±0.2)-fold increase in storage modulus (Fig. 3.2.2.3b), as if we consider the proteins as springs in parallel we would expect the sample with 10mM maltose to have 1.7x as much folded protein *in situ*, compared to the sample with 0mM maltose.

3.2.3 Determination of MBP thermal stability and MBP:maltose dissociation constant

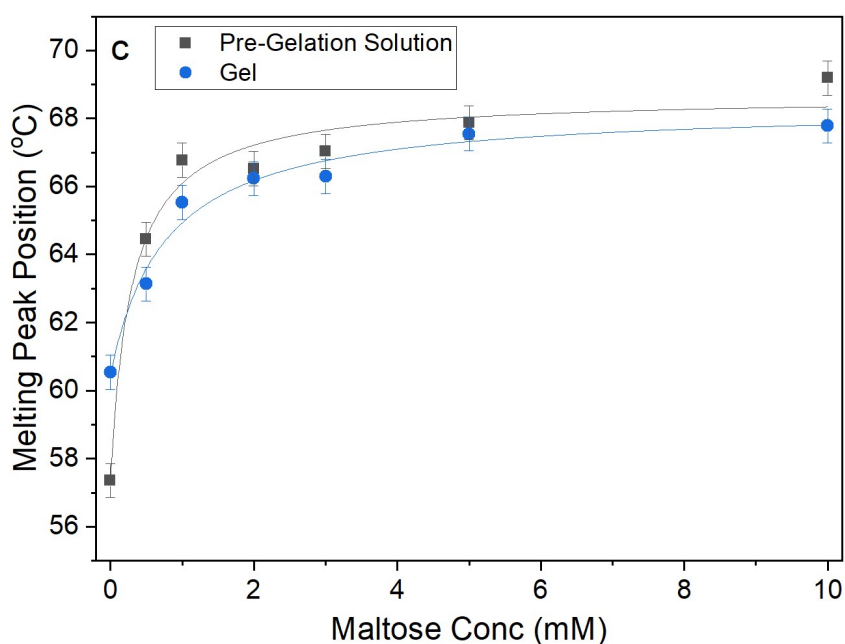


Figure 3.2.3.1: Melting temperature of MBP at 100mg/ml both in pre-gelation solution, and *in situ* in a hydrogel, as a function of maltose concentration. Error bars are the standard deviation determined from asymmetric Gaussian fitting.

Previous studies have demonstrated that maltose bound MBP is more thermodynamically stable[133]. To determine if enhanced thermal stabilisation is still present in a

cross-linked hydrogel, differential scanning calorimetry was used, a technique which measures the heat flow in and out of a material upon heating and cooling. We first measured the melting temperature, T_m , of MBP in solution in the absence of maltose, obtaining a value of 58°C in good agreement with published literature.[133] We then measured T_m as a function of maltose concentration and observed an increasing T_m with increasing maltose concentration (Fig. 3.2.3.1). The same DSC experiments were also completed for the MBP hydrogels, showing similar results. The increase in T_m in the hydrogels shows a slower rate of increase to the max T_m , compared to the solution data (Fig. 3.2.3.1), suggesting a lower apparent K_d value.

$$T_m^{[maltose]} = \frac{\Delta T \cdot [maltose]}{K_d + [maltose]} + T_m^0 \quad (3.2.3.1)$$

Using the DSC data and applying the Langmuir thermal shift equation[184] (Eqn. 3.2.3.1), we extracted the apparent K_d values of maltose to MBP both in pre-gelation solution (290 ± 90) μ M and *in situ* in the gel (800 ± 200) μ M. The values obtained are larger than previously determined in literature (1.20 ± 0.05) μ M [176, 177] likely due to comparable protein (2.4mM) and ligand (0-10mM) concentrations in the present study causing high depletion of ligands, which is not consistent with the assumptions in binding assays that the change in ligand concentration due to binding is negligible. The apparent binding affinity allows us to calculate the number of maltose bound MBP, or ‘occupied protein’ as a function of concentration (Fig. 3.2.4.1, insert).

3.2.4 Occupation model of Hydrogel mechanical modulation

By combining the rheology (Fig. 3.2.1.1), CD (Fig. 3.2.2.3a, b) and DSC (Fig. 3.2.3.1) results we propose an ‘occupation model’ to describe the observed modulation of the mechanical properties of MBP hydrogels. With increased maltose concentration the probability of MBP binding to maltose increases. We expect that this would result in a greater number of mechanically more robust maltose bound MBP, or ‘occupied’ MBP. This enhancement of the mechanical stability of the folded protein building block trans-

lates to the cross-linked folded protein hydrogel, which exhibits increased mechanical strength (Fig. 3.2.4.1).

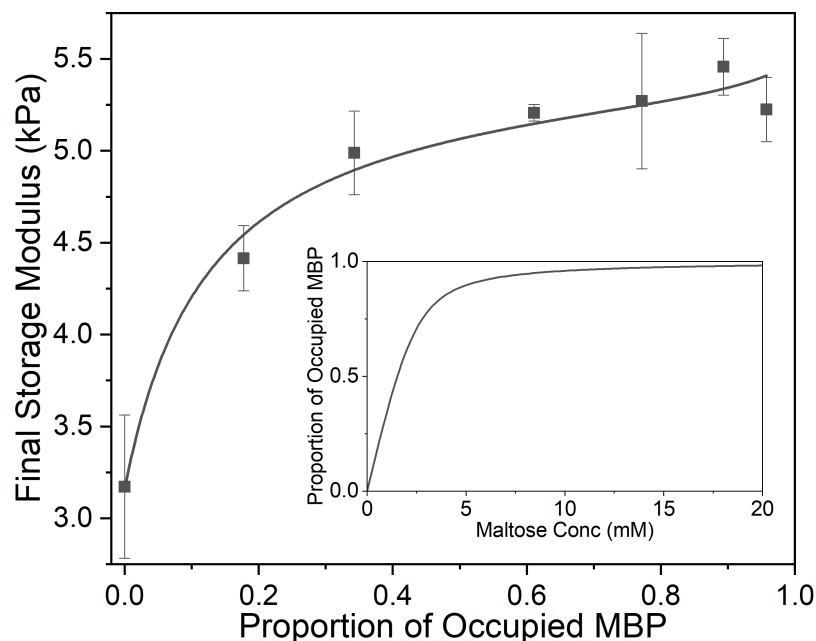


Figure 3.2.4.1: Final storage modulus as a function of proportion of ligand occupied MBP. Fitted using equation 3.2.4.1 and 3.2.4.2. Where the concentration of MBP, $\Delta G'$ and G_0' are taken to be 2.4mM, 2.25kPa and 3.16kPa respectively. (inset) The proportion of occupied MBP as a function of maltose concentration as modelled by equation 3.2.4.2 using the values 2.4mM and $800\mu\text{M}$ for MBP concentration and apparent MBP: maltose dissociation constant (as extracted from DSC data in figure 3.2.3.1), respectively.

From figure 3.2.4.1 it is clear that the trend of storage modulus with the proportion of more stable ‘occupied MBP’ is not linear (as would be expected from a simple springs in parallel model), increasing rapidly at low proportion and slower at higher proportions (>0.2). This result demonstrates that the translation of stability across length scales in hierarchically structure network is highly non-trivial. Since the storage modulus increases as the proportion of ‘occupied’ MBP increases, we are able to fit figure 3.2.4.1 with a modified form of the Langmuir binding equation (Eqn. 3.2.4.1) and extract the apparent K_d value.

$$G'_{[maltose]} = \frac{\Delta G' \cdot [maltose]}{K_d + [maltose]} + G'_0 \quad (3.2.4.1)$$

where

$$[maltose] = \frac{K_d \cdot P_{occ}}{(1 - P_{occ})} + P_{occ}[MBP] \quad (3.2.4.2)$$

The K_d value extracted from the rheology data (3.2.4.1) was found to be $(300 \pm 100) \mu\text{M}$, compared to $(290 \pm 90) \mu\text{M}$ (in pre-gel solution) and $(800 \pm 200) \mu\text{M}$ (*in situ* in the gel) extracted from the DSC data (Fig. 3.2.3.1). A similar value for apparent K_d of $(400 \pm 200) \mu\text{M}$ was extracted from the rheology data in Fig 3.2.1.1b. While these value do not match exactly with those found in the DSC experiments it is of the correct order of magnitude and is still over two-orders of magnitude larger than that previously determined in low concentration MBP solutions.

In figure 3.2.1.1 it was noted that above a critical concentration of 2 mM maltose the storage modulus was insensitive to maltose content, suggesting a saturation of the MBP binding sites. However, figure 3.2.4.1(inset) shows that the proportion of occupied MBP is only 0.6 at 2 mM maltose concentration, implying the critical concentration is not a saturation point of available protein–ligand binding sites. Instead, it suggests that the network mechanics plateaus when a 0.6 proportion of MBP is occupied, implying a 0.4 proportion of MBP makes little contribution to the mechanical properties of the network. We examine this further in figure 3.2.4.1 which shows the steepest rate of increase in final storage modulus between 0 and 0.2 occupation, implying the mechanics of the protein network can be dominated by relatively few (1 in 5) protein building blocks. So we have shown that by controlling the proportion of mechanically robust ‘occupied’ MBP we are able to tune the storage modulus of hydrogels constructed from MBP. In addition our results imply that only a small proportion of the protein building blocks contribute to the mechanical stability of the network and approximately 40% effectively may not contribute at all.

3.3 Modulation of Hydrogel Structure

We have shown that the mechanical strength of a protein network is determined by the stability of the protein building block. This increase in the shear modulus of the network could, however, also arise due to an alteration of the mesoscopic structure. In order to investigate this possibility small angle neutron (SANS) and x-ray (SAXS) scattering measurements were employed, (Fig. 3.3.0.1).

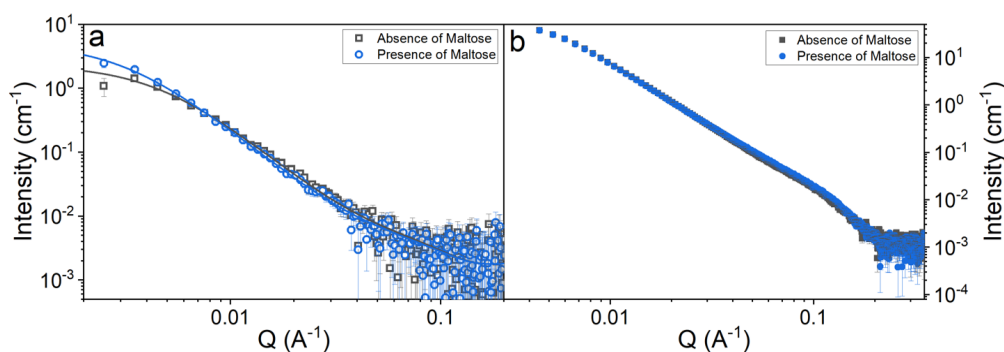


Figure 3.3.0.1: SANS curves (a) and SAXS curves (b) of folded MBP hydrogels, (final concentrations: MBP 100 mg/ml, NaPS 30mM, Ru 100 μ m) in the absence (grey) and presence (blue) of 10mM Maltose. Solid lines show fits to equation 3.3.0.1.

Figure 3.3.0.1a, b show the scattering curves of MBP hydrogels, in the absence and presence of maltose (illuminated by neutron and x-ray beams respectively). In both graphs very little difference can be seen between samples, suggesting that the differences in the mechanical properties of the gel are not due to a mesoscopic structural change. However, it is important to note that there is a difference in the gels at lower Q values of the SANS measurements, representing differences between the gels at larger length scales, highlighting the need for lower Q value measurements in order to structurally characterise protein-based hydrogels. To facilitate fitting of the data, SANS and SAXS measurements were also performed on 5-10mg/ml MBP in solution (Fig. C.2.0.1) to determine the form factor of the MBP building block. Analysis of these data sets show that there is negligible change in the form between samples in the presence and absence of maltose. Fitting the data in figure 3.3.0.1 using equations 3.3.0.1 and 3.3.0.2, allows us to extract quantitative information about the structure of folded protein-based hydrogels (Table 3.3.0.2).

$$I(q) = \phi V_{block} \Delta\rho^2 P(q) \cdot [(1 - p_c) + p_c S(q)] \quad (3.3.0.1)$$

Where ϕ is the volume fraction of protein, V_{block} is the volume of the protein building block, $\Delta\rho$ is the contrast difference between the building block and the solvent and p_c is the proportion of protein in fractal-like clusters within the gel network. $P(q)$ is the form factor of the MBP protein monomer, which from both crystallography structures and low concentration SAS measurements (Fig. C.2.0.1) is determined to effectively modelled by a ellipsoid form factor with a radius of gyration of $(24\pm 1)\text{\AA}$ and $(23\pm 1)\text{\AA}$ in the absence and presence of maltose. And $S(q)$;

$$S(q) = \frac{D_f \Gamma(D_f - 1)}{\left[1 + \frac{1}{(q\xi)^2}\right]^{\frac{D_f - 1}{2}}} \cdot \frac{\sin [(D_f - 1)\tan^{-1}(q\xi)]}{(qR_0)^{D_f}} \quad (3.3.0.2)$$

is the fractal structure factor [185, 186] (see derivation B.3) to model the geometry of the clustering of objects of the form $F(q)$. D_f , ξ and R_0 are defined as the mass fractal dimension, correlation length and minimum cut-off length scale defined by the ellipsoid form factor. Previous structural characterisation of folded protein based hydrogel, (using a two-lorentzian function) suggested the presence of clusters of cross-linked folded protein with fractal-like nature in the gel [134]. Based on these findings a fractal structure factor is used to model the scattering in this work (Eqn. 3.3.0.2). Three key parameters can be extracted from the data. The first two are; the correlation length representing the size of the clusters of cross-linked proteins and the fractal dimension of these clusters. D_f can be defined as the space-filling capacity of a fractal object which can (and often does) differ from the dimension of the topological space in which the object is embedded. D_f can also be interpreted as measure of how the structural detail in an object changes with the scale at which the object is measured [187]. Sometimes called the mass fractal dimension, it gives a measure of how the ‘mass’ (an intrinsic property) of an object scales with its size (and extrinsic property). For example, if size of the object increased by a factor of 2, then the ‘mass’ of the object would increase by a factor 2^{D_f} . For our system D_f can be thought of intuitively as related to the density of the clusters of cross-linked

folded protein. ξ , then, is an imposed parameter representing the upper limit length-scale over which D_f is a valid measure of hierarchical structure. We interpret this as indicative of the size of the fractal clusters within the network, with the associated lower limit of fractal behaviour being the size of an individual protein building block.

Matlose Conc. (mM)	Correlation length (\AA)	Fractal dimension	'Kiessig' length (\AA)
SANS (Fig. 3.3.0.1a)			
0	250 ± 30	2.41 ± 0.05	1000 ± 300
10mM	340 ± 40	2.33 ± 0.04	1000 ± 300
SAXS (Fig. 3.3.0.1b)			
0	230 ± 1	2.60 ± 0.03	N/A
10mM	250 ± 2	2.58 ± 0.03	N/A

Table 3.3.0.2: The results of the two fitted parameters, correlation length and fractal dimension extracted using equation 3.3.0.1, and the 'Kiessig' length extracted by performing peak to peak analysis of the Kiessig fringes.

The correlation length is over 10x larger than the radius of gyration of the MBP subunit unit ($\approx 23\text{\AA}$), this decade of separation between relevant length scales gives confidence in the validity of the fractal fit used. The third parameter here termed 'Kiessig' length is one that is only present in our SANS data and is extracted through peak to peak analysis of the Kiessig fringes (Fig. C.2.0.2). Kiessig fringes are the result of an interference effect due to the scattering from two separated interfaces (where the separation is much larger than the incident wavelength) such that the Bragg condition is satisfied [188, 189]. So the emergence of such fringes implies the existence of a repeating length scale of approximately 1000\AA in the system. The lack of definition in these fringes is what leads to the large error in these values but also is indicative that the length scale is not well defined in the system i.e has a large standard deviation. The only parameter that genuinely varies between samples is the correlation length of the clusters, which increases in the presence of maltose, however this increase in length is not very significant (two MBP diameters). The invariance of the fractal dimension and the

small change in the cluster size implies that the structure of the hydrogel is reasonably the same in the absence and presence of maltose. The consistency of the gel network's structural motifs (in the presence and absence of 10mM maltose) demonstrates that the increase in shear modulus of the network is due to the increase in stability of the protein building block, not a change in the mesoscopic structure caused by this increased stability. Together, the parameters extracted from the scattering data shows that folded MBP hydrogels contain fractal-like clusters ($D_f \approx 2.4$ for SANS, and ≈ 2.6 for SAXS) that vary in size from 250\AA to 340\AA with an additional preserved length scale of 1000\AA , and that this structure is unchanged by the addition of maltose.

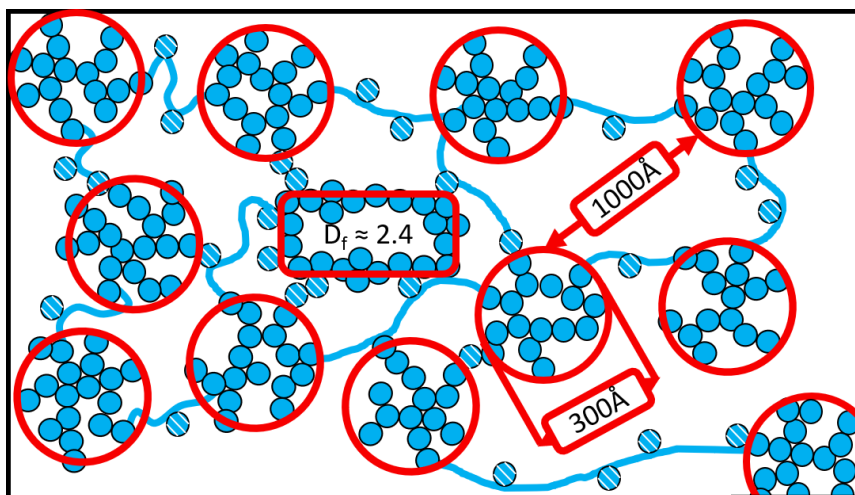


Figure 3.3.0.2: Schematic representation of the predicted structure MBP hydrogels. Where fractal-like clusters (highlighted by red rings) of folded protein (solid blue circles) are connected by unfolded protein (blue lines). Stripped blue circles represent folded protein not contained within clusters.

Combining the results of the scattering measurements with CD spectroscopy experiments, which demonstrate that there is a population of unfolded protein present in the gels, we propose a structural model of our hydrogels (Fig. 3.3.0.2). Our proposed structure consists of fractal-like clusters of cross-linked folded MBP proteins linked together by an inter-cluster region of predominantly unfolded protein giving rise to an inter-cluster distance of 1000\AA . It is worth noting at this point that the Kiessig fringes we see in our data are not well defined and since these fringes arise due to Bragg interference this suggests that the length scale, we extract is also not well defined i.e. has a large distri-

bution of sizes. We speculate that this structure is critically regulated by the rupture force of the protein building block, instead of other mechanisms such as diffusion limited cluster aggregation (DLCA). In DLCA the size of a cluster formed is only dependant on the diffusion rate and volume fraction of the monomer units[190, 191], and since these are equivalent between samples in the absence and presence of maltose it would be expected that the size of clusters formed would be the same. However, observed cluster sizes are larger in hydrogels construct from the more stable bound-MBP, leading us to suggest that force and force-induced unfolding plays a crucial role in the formation of the hydrogel architecture.

3.4 Modulation of Hydrogel Dynamics

Stabilisation of the protein building block through ligand binding leads to an enhancement in the storage modulus of the gels, however analysis of the kinetics of gel formation performed by rheology concurrently during light induced gel formation reveals other effects of ligand binding.

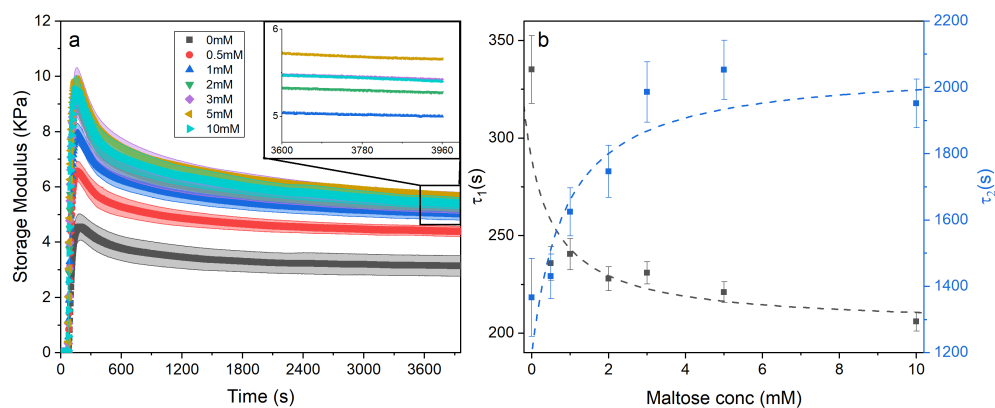


Figure 3.4.0.1: (a) Gelation curves (showing storage modulus vs. time) of chemical crosslinked MBP hydrogels (final concentrations: 100 mg/ml MBP, 30mM NaPS, 100 μ M Ru(II)bpy₃²⁺) as a function of maltose concentration. Illuminated at $t = 60$ s till $t = 360$ s. (inset) Magnification of the boxed section in figure 3.4.0.1a, with the error bar ribbon removed for clarity. (b) Relaxation time constant of the first and second relaxation mode, τ_1 (black) and τ_2 (blue) as a function of maltose concentration.

The gelation curves in figure 3.4.0.1a, show the evolution of the storage modulus with time as a function of maltose concentration. The gelation curves all have the same general shape i.e during illumination they increase to a maximum value before relaxing to a final value (G'_∞), which increases as a function of maltose concentration in agreement with end point rheology data (Fig. 3.2.1.1b and 3.2.2.1b). While the presence of maltose increases the storage modulus of the gel, the gelation time remains the same in the presence and absence of maltose (Fig. C.1.0.8). In previously literature[192] it has been noted that such overshoot behaviour during gelation can be due to deswelling of the gel causing slipping between the sample and the rheometer plate. To investigate this possibility we consider the measured force normal to the plane of shear during gelation (Fig. C.1.0.9) and calculate a maximum negative (downwards) stress of -1kPa, several times small than previously reported (-3.2kPa) [193]. Here, a possible explanation for the gelation behaviour is speculated on. In order to analyse these relatively complex kinetic profiles in more detail we fitted an empirical function to these data sets (Eqn. 3.4.0.1, Example of fit shown in Fig. C.1.0.10)

$$G'_t = \frac{1}{(1 + e^{-C(t-t_0)})} \cdot \left(G'_\infty + B_1 e^{-\frac{t-t_0}{\tau_1}} + B_2 e^{-\frac{t-t_0}{\tau_2}} \right) + G'_0 \quad (3.4.0.1)$$

Equation 3.4.0.1 shows the functional form of the gelation curves and contains two key components. The first is the sigmoidal component, which models the initial increase in the storage modulus up to the final value G'_∞ , where C is the rate of increase and t_0 the midpoint position of the increase to the maximum in the storage modulus. The second are the two exponential terms that model the relaxation (with coefficients B_1 and B_2 and time constants of τ_1 and τ_2 , respectively) of the gels from the maximum value to the final value G'_∞ . Two exponential terms are required to adequately fit the gelation curves, implying that there are two distinct relaxation modes for the hydrogels during formation, one modelled by the time constant τ_1 and the other by τ_2 . The two time constants differ by approximately a factor of 10 from each other and figure 3.4.0.1b shows how these time constants vary as a function of maltose concentration. The two time constants show inverse relationships to one another. Two possible mechanisms that

could be attributed to these relaxation modes are the relaxation of the newly percolated cross-linked network into a lower energy state, and the unfolding of the MBP domains.

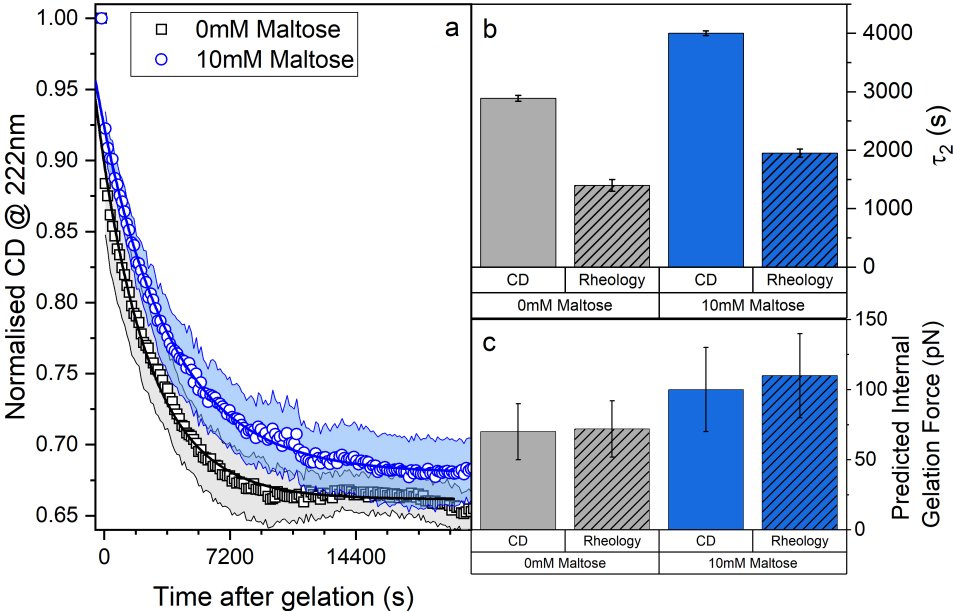


Figure 3.4.0.2: (a) Proportion of folded protein in the gel as a function of time post illumination, in the absence (black) and presence (blue) of maltose. (b) Second relaxation mode and (c) predicted internal gelation forces in the absence (grey) and presence (blue) and the measurement method (empty columns for CD and shaded for rheology).

We employed CD to measure the evolution of the secondary structure of MBP solutions and hydrogels over the course of 10 hours, shown in figure 3.4.0.2a. (Note that these curves were corrected for dehydration in the samples over the long course of the measurements, see section 2.4.1). The normalised CD curves show a decaying relationship that plateaus to the same value of approximately 67% folded protein, taking a different amount of time to reach this plateau. The time constants of this decay (Fig. 3.4.0.2b) are approximately (2900 ± 50) s and (4000 ± 50) s in the absence and presence of 10mM maltose, respectively. These values are almost exactly a factor of two larger than those determined from rheology, implying that the longer τ_2 relaxation is due to the unfolding of the MBP building block. The factor of two difference may be due to the application of external strain on the system during gelation on the rheometer that is not present in the CD measurements. Interestingly we can use these time constants to

predict the forces present in the gel during gelation, [194] shown in figure 3.4.0.2c. The applied force during gelation lowers the energy barrier of unfolding in a linear manner. The energy being defined as $F \cdot x_u$ at force, F , where x_u is the measure of the distance to the unfolded state in the energy landscape, previously determine by Rief et al. [81, 82]. The expression for the rate constant of unfolding at force, F , $k_{u,F}$ is defined as:

$$k_{u,F} = k_{u,0} e^{-\frac{F \cdot x_u}{k_b T}} \quad (3.4.0.2)$$

rearranging this equation gives the expression,

$$F = \ln \left(\frac{k_{u,F}}{k_{u,0}} \right) \cdot \frac{k_b T}{x_u} \quad (3.4.0.3)$$

where $k_{u,0}$ is the unfolding rate constant in the absence of an applied force, and has been previously measured in literature [195], and other symbols have their usual meanings. Equation 3.4.0.3 allows for the prediction of the internal forces present in the gel in the post-gelation relaxation process. The results in figure 3.4.0.2b show good correlation between rheology and CD as both time constant and predicted force increase in the presence of the ligand. The predicted gelation forces (Fig. 3.4.0.2c) are higher in samples measured by rheology, as expected due to the additional external strain on the system. There is also an increase in the predicted gelation force in samples containing maltose, possibly suggesting that the final structure by the gels is reasonably invariant and as a result of this invariance there is a high gelation force due to the increased stability of bound MBP.

3.5 Discussion

We have demonstrated that increasing the stability of MBP through ligand binding results in enhanced mechanical characteristics of the hydrogels. Using both SANS and SAXS we have shown that the addition of maltose does not affect the mesoscale structure

of our hydrogel adding further evidence that the enhancement in protein stability at the molecular level scales directly to the macroscale. We propose an occupation model of this modulation, due to increased probability of more robust ligand bound MBP with increasing maltose concentration. A wealth of literature on the reinforcement of gels using so-called ‘fillers’ exists, in which large particles are added to fill space in the gel matrix leading to reinforcement of the gel and an increase mechanical strength [100, 101, 105, 106, 196]. Other methods, discussed in section 1.3.1, which have been used to reinforce hydrogel networks: include the interweaving of a secondary network to act as a scaffold to the first [110, 111]; and strengthening the self-assembly cross-linking interaction [114, 115, 117]. All of these methods rely in principle on altering the cross-linking network. By contrast in this study, rather than filling the space within gel network pores or altering the cross-linking network, we modify the molecular building block stability, namely MBP, and demonstrate the translation of increased stability to the mechanical stability of the gel network. Interestingly, our data suggests that by stabilising only 20% of the folded protein blocks the mechanical properties of the protein network can be significantly increased. While the underlying mechanism is not known it is likely heavily related to the hierarchical structure of the network and warrants future in-depth investigation. Furthermore, this study demonstrates that in order to construct a complete theory linking the building block and network mechanical properties, the stability of the building block must be considered.

We use our scattering data and combine it with the results of CD to postulate a structure of folded protein-based hydrogels, where there are fractal-like clusters of cross-linked folded MBP proteins linked together by strands of unfolded proteins, due to the stresses of gelation. With this structural model in place we speculate that the architecture of networks formed by mechanically labile folded proteins is critically limited and regulated by the rupture force of the protein building block. We also investigated the effect of maltose stabilisation on the kinetics of hydrogel formation. During gel formation, post the initial cross-linking reaction there is a relaxation to a final plateau shear modulus, by fitting these gelation curves with a bespoke empirical function we find that there is an increase in the time constant of this relaxation. Using CD, we are

able to demonstrate that this increase in relaxation time is also due to the stabilising effect of maltose on the MBP domain. These results are interesting and warrant further investigation, in particular into the presence of contraction of the gel during gelation and its effect on the measured gelation behaviour. Other further work would include the modulation of the relaxation behaviour under permanent strain, which would be important and relevant for biomedical and bio-mechanical applications.

By controlling the proportion of building block subunits with enhanced stability it is possible to tune the mechanical and dynamical behaviour of a network of such subunits. Furthermore, this tuning of the mechanical and dynamical properties of the hydrogel network does not come at the expense of altering the mesoscopic structure. This is an important step in understanding and, in future, exploiting the translation of building block stability on network behaviour and opening the door to environmentally responsive hydrogels with many broad applications.

Chapter 4

Unravelling Nature's Networks: *In situ* protein unfolding defines network architecture and mechanics of protein hydrogels

In chapter 3 a structural model for the architecture of folded globular protein hydrogels was proposed (Fig. 3.3.0.2). This proposed structural model consisted of fractal-like clusters of cross-linked folded protein connected by an inter-cluster region populated by predominately unfolded protein. The observed dimensionality of the clusters in MBP hydrogels was unaffected by an increase in the thermodynamic and mechanical stability of the MBP building block upon the binding of maltose. Interestingly, while the internal structure of the clusters was unaffected by an increase in the building block stability, an increase was observed in the cluster size. This result led to the speculation that the hydrogel structure is crucially regulated by force and force-induced unfolding of the protein building block. This speculation inspired the question that this chapter will address; what is the functional role of *in situ* protein building block unfolding in defining the structural and mechanical properties of a protein network?

Recent studies [197–199] have attempted to address the role of protein unfolding *in vivo* including studies on the giant muscle protein titin [198, 200] and bacterial adhesion proteins [201]. These studies demonstrate that protein unfolding plays an important role in regulating bio-polymer properties for specific *in vivo* biological functions. For example, unfolding of the Ig-domains in titin allows for the fine tuning of the energy storage and dissipation behaviour allowing the protein to tailor itself (and by extension the tissue) to the current situation e.g. running, lifting, writing a thesis etc. In 2002 Li et al. [198] presented a study which related the single molecule mechanical properties of the I band region¹ of N2B titin² to the physiological properties of muscle tissue. Using SMFS techniques the authors showed that over a physiological range the majority of titin elasticity is described by an entropic model due to extension of the PEVK region³. However at higher extensions the behaviour of titin deviates significantly from an entropic model, with only small changes in applied force observed for large increases in protein extension. This departure from the entropic model is attributed to the unfolding of several of the Immunoglobulin (Ig) domains in titin. These results suggest that unfolding of protein domains acts as a buffer to protect muscle fiber from becoming damage when exposed to very high strain. This study demonstrates the *in vivo* mechanical role of protein unfolding in human muscles and that unfolding is a crucial method to regulate the mechanics of a hierarchical protein network (in this case muscle tissue). However these studies do not directly measure how the transition of a protein from the rigid folded state to the flexible unfolded state defines the architecture of a hierarchical protein network and how the alteration of network structure translates to the mechanical behaviour. The study presented in this chapter aims to address this gap in understanding by controlling the ability of a protein building block to undergo force-induced unfolding, via intramolecular covalent stapling, and investigating the subsequent effects on the structural and mechanical properties of a protein hydrogel network.

This chapter starts by discussing the selection of bovine serum albumin (BSA) as a model protein, before presenting results confirming the rationale of the selection. Next

¹The region of titin that has been identified to be functionally elastic

²The shortest isoform of titin found in cardiac muscle tissue

³Large unstructured region in titin, rich in proline(P), glutamate(E), valine(V) and lysine(K)

the alteration of the hydrogel architecture due to modulation of the protein building block's force liability is explored using a newly developed analysis to extract additional structural information, in particular regarding the inter-cluster region. In addition to the structural characterisation, the effects of protein unfolding on the linear and non-linear mechanics of the hydrogels are presented and discussed before finally summarising the defining role of *in situ* protein unfolding on hierarchical network architecture and mechanics.

4.1 Selection of model protein and design of model system to investigate the role of *in situ* protein unfolding in network architecture and mechanics

The desired properties of a model protein hydrogel building block needed to study the higher order effects of *in situ* protein unfolding on a hierarchical protein network will be outlined in this section, before discussing why BSA was selected as an ideal model protein.

4.1.1 Selection of BSA as a model protein

Similar to the study presented in chapter 3 (see section 3.1.1) a model protein hydrogel building block requires at least 4 surface exposed tyrosine residues (to allow for network formation through photo-chemical cross-linking) and must be easily obtainable in large quantities (to allow for the samples sizes necessary for complete characterisation). In addition to these two criteria, which are generic to any of the hydrogels used in this work, there is a third criteria of the model protein specific to this study i.e. there is an external method to toggle the force liability of the model protein building block. This requirement is essential to restrict or permit the *in situ* unfolding of the protein building block and hence, allowing for the direct investigation of protein unfolding on the architecture and mechanics of protein hydrogel networks.

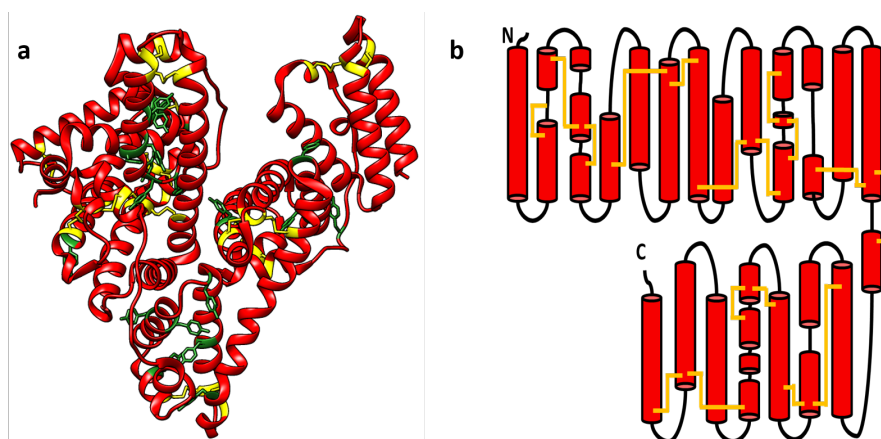


Figure 4.1.1.1: a) Crystal structures (PDB code: 3v03) and b) 2D topograph of BSA, where disulphide bonded cysteine residues and tyrosine (only show in 3D structure) residues are coloured yellow and green respectively.

BSA was selected as a model protein to investigate effects of unfolding of the protein building block *in situ* on the properties of a cross-linked hydrogel network. BSA is the bovine variant of serum albumin, a family of all α -helical (Fig. 4.1.1.1) blood proteins which one of the most abundant in the blood of humans (3.5 g/dl to 5 g/dl) and other animals, and functions predominately as a carrier protein of steroids, fatty acids and thyroid hormones [202]. In 1946 Edwin J. Cohn developed the Cohn process to fractionate blood serum and extract serum albumin using organic solvents [203], modern versions of this process instead use heat-shock to allow the safe and cheap extraction of reasonably pure serum albumins (>98%). Heat-shock fractionation means that BSA is readily purchasable in large quantities (>10g). BSA is an ideal model globular protein as it contains over 4 solvent exposed tyrosine cross-linking residues (18 residues with accessibility of greater than 1\AA^2 determined from the PDB structure in USCF Chimera 1.14). In addition previous work in literature [128, 134, 136] has demonstrated that BSA is an effective hydrogel building block, forming robust gels via the same photo-chemical cross-linking process used in this work (section 2.3.3). However, most importantly for this study BSA contains 17 structural disulphide bonds (Fig. 4.1.1.1a and b). Disulphide bonds are prevalent in many protein families that function in an extracellular environment including serum albumins, defensins and insulins and have been shown through SMFS studies to be essentially mechanically resistant[204] withstanding forces significantly higher than

20-100pN [135, 205](Fig. 3.4.0.2), forces thought to be generated during photo-chemical gelation. This robustness means that the 17 structural disulphide bonds in BSA effectively ‘staple’ the folded structure together, however despite the relative mechanical robustness of disulphide bonds they can be rapidly removed by reducing agents such as dithiothreitol (DTT) used in this study.

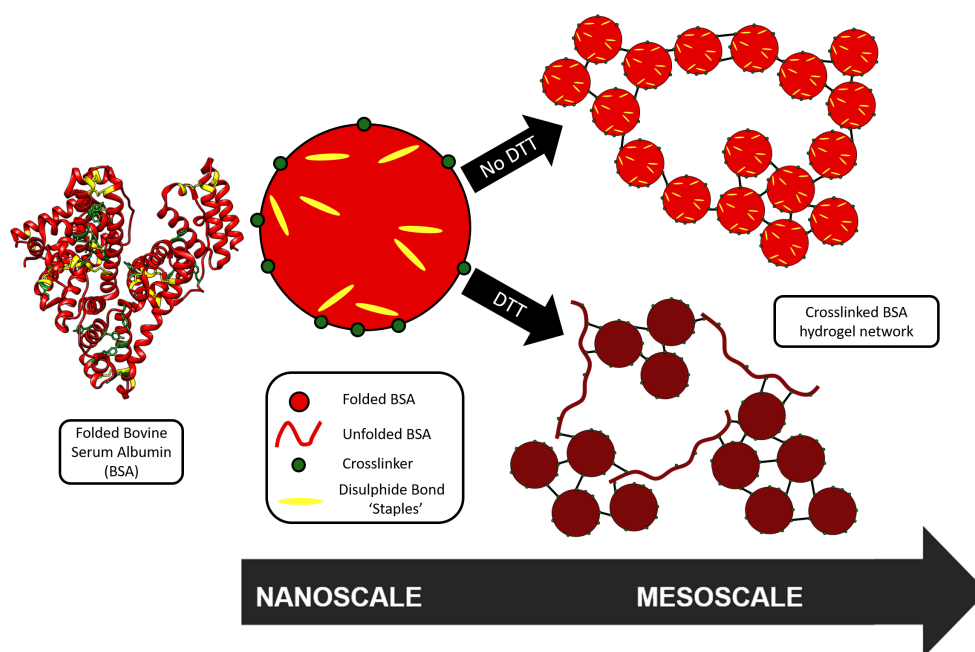


Figure 4.1.1.2: Schematic representation of the BSA (light red), BSA:DTT (dark red) model hydrogel, where the presence and absence of disulphide bonds (yellow) controlled by the addition of DTT, is expected to restrict or allow the unfolding of the BSA building block, respectively.

Figure 4.1.1.2 shows a schematic of the BSA hydrogel system used in this study, and illustrates what is believed to be the effect of the disulfide staples and their removal upon photo-chemical gelation. The schematic shows, in principle, that the intra-molecular disulphide staples prevent the protein from undergoing force-induced unfolding due to gelation, however with the addition of DTT the staples can be removed and allow the protein to unfold. This toggling of the protein force lability by the addition of reducing agent makes BSA-based hydrogel an ideal model system to study the importance of *in situ* protein unfolding on network architecture and mechanics.

4.2 Modulation of structure on the molecular scale

In order to confirm the rationale of the selection of BSA as a model protein (section 4.1.1), circular dichroism (CD) spectroscopy was employed to investigate the structure of the BSA protein in the presence and absence of disulphide bonds (i.e. absence and presence of DTT, respectively) both in solution and *in situ* in the hydrogel.

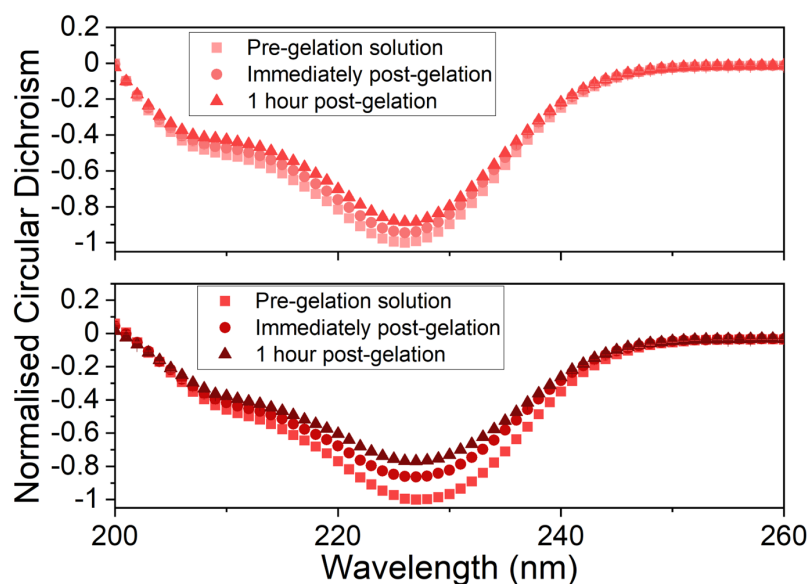


Figure 4.2.0.1: Normalised circular dichroism spectra of BSA hydrogels (final concentrations: 100mg/ml BSA, 50mM NaPS, $100\mu\text{MRu(II)bpy}_3^{2+}$) in the absence (top) and presence (bottom) of 3mM DTT, before gelation, immediately post gelation and one-hour post gelation.

Figures 4.2.0.1a and b show the spectra of BSA hydrogels in the absence and presence of DTT respectively in the pre-gelation solution, in the hydrogel immediately after gelation and one hour after gelation. The spectra in all cases show a negative peak at ≈ 209 nm and ≈ 222 nm, indicative of α -helices and what would be expected for an all α -helical protein [206] such as BSA. It should be noted that the comparative intensities between the peaks (i.e. the peak at 209 nm less intense than the peak at 222 nm) does not agree with previous CD measurements of BSA in literature [207] (where the peak at 209 nm is more intense than the peak at 222 nm), this discrepancy is attributed to the very high protein concentration used here leading to a reduction in the signal

to noise ratio at lower wavelengths as indicated by the high tension of the CD spectrometer (Fig. D.0.0.1). The spectra show a reduction in the protein's CD signal at 222 nm between the pre- to post-gelation measurements, which can be interpreted as a reduction in the amount of folded protein in the hydrogel network (α -helix secondary structure in this case). In the absence of DTT (i.e. the intra-protein disulphide bonds are present) this reduction is observed to be much smaller than in the presence of DTT (i.e. the intra-protein disulphide bonds are broken), suggesting that there is a lower degree of unfolding present in hydrogel constructed from BSA in the absence of DTT compared to those in the presence. This indicates that the rationale discussed in section 4.1.1 is correct i.e. that the intra-protein disulphide staples restricts the ability of the BSA to unfold and that reduction of the disulphide bonds with DTT makes the BSA building block force-labile. To further investigate the effects of the disulphide staples on the molecular level structure of BSA a quantitative measure of the proportion of folded protein was extracted from the spectra in figure 4.2.0.1.

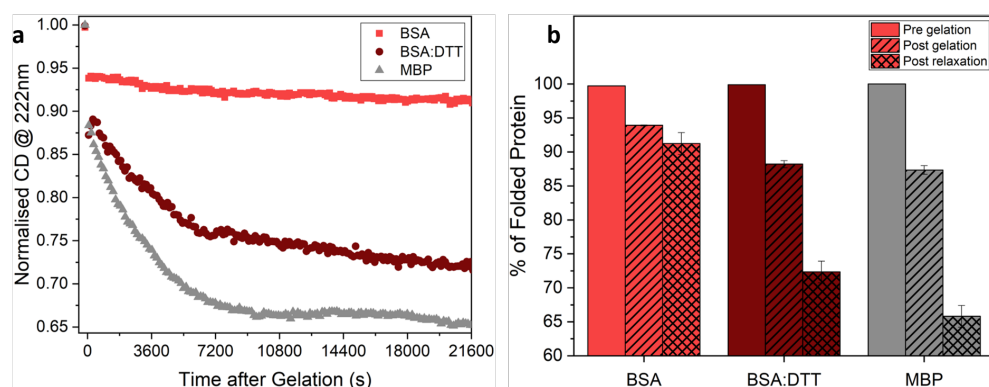


Figure 4.2.0.2: a) Normalised CD signal at 222nm of BSA (light red) and BSA:DTT (dark red) hydrogels, which can be interpreted as the proportion of folded protein *in situ* in the hydrogel, as a function of time post gelation, with data on an apo-MBP hydrogel (grey) taken from figure 3.4.0.2 and added for reference. b) Percentage of folded protein remaining in each hydrogel system, pre-gelation (open), post-gelation (striped), and post-relaxation (cross-hatched). Y-Axis begins at 60% for clarity of the difference between BSA, BSA:DTT and MBP systems.

A time-course of CD signal at 222 nm, which is a measure of the proportion of folded protein remaining in the system, recorded *in situ* for hydrogel maturation over 6 hours (Fig. 4.2.0.2a) shows that the proportion of folded protein in each hydrogel decays over time, approaching end point values after 6 hours. For BSA, there is a striking difference

between the proportion of folded protein in the absence and presence of DTT. While in both chemical conditions there is a reduction in the amount of folded protein after gelation, the extent and rate of reduction is far greater in the presence of DTT (exponential fits to the curves in figure 4.2.0.2a extract end point values of 9% and 28% signal reduction in the absence and presence of DTT respectively). These results imply that removal of these structural staples increases the extent of the gelation-induced unfolding, consistent with the spectra in figure 4.2.0.1 and the view that structural disulphide bonds provide molecular reinforcement in the BSA folded structure and prevent unfolding of the building block protein. In accordance with this hypothesis, another folded globular protein tested in this work which lacks any disulphide bonds [163] and so is also labile to force (MBP [81, 82]) showed behaviour similar to disulphide-reduced, unreinforced BSA (Fig. 4.2.0.2a,b). These results show that the intra-molecular disulphide bonds act as molecular staples, reinforcing the BSA building block against force induced unfolding due to gelation, which leads to the low degree of unfolding observed *in situ*. In contrast, the unstapled BSA in the presence of DTT show higher degree of unfolding *in situ* due to their force labile structures. To eliminate the possibility that the difference in proportion of folded protein is not caused simply by the addition of DTT in solution, the CD solution spectra (Fig. D.1.0.1a) and solution SAXS profile of BSA in the absence and presence of DTT are compared and no significant difference is observed. The comparison of the solution CD and SAXS data and of the three protein systems (i.e. BSA, BSA:DTT and MBP) demonstrates that force induced unfolding occurs as a consequence of gelation. It has been demonstrated in this section that *in situ* protein unfolding occurs in folded protein based hydrogels and that restricting or allowing the building block to unfold changes the molecular level structure of the hydrogel network.

4.3 Modulation of structure on the network scale

4.3.1 Characterisation of BSA hydrogel network architecture via small-angle scattering

To investigate and understand whether the *in situ* gelation-induced unfolding observed by CD (Fig. 4.2.0.1 and 4.2.0.2) affected the structure of the cross-linked BSA network, we used SANS and SAXS.

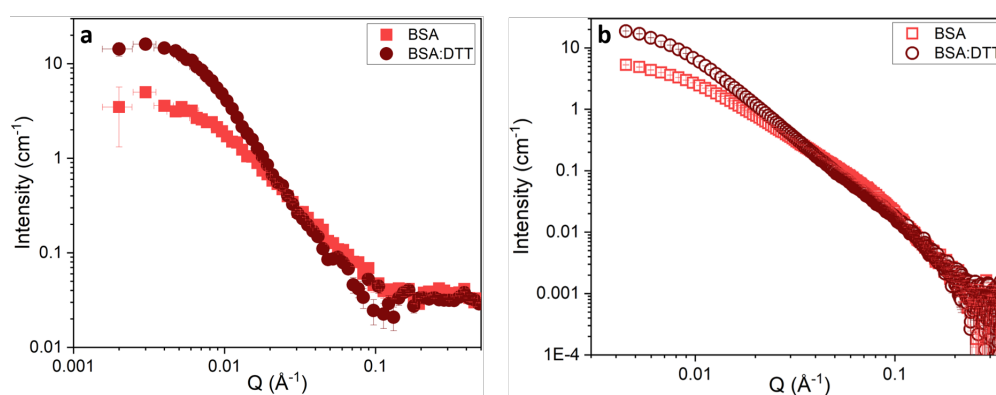


Figure 4.3.1.1: a) SANS curves and b) SAXS curves of folded BSA hydrogels (final concentrations: 100mg/ml BSA, 50mM NaPS, $100\mu\text{MRu(II)bpy}_3^{2+}$) in the absence (light red) and presence (dark red) of DTT.

The SANS and SAXS curves of the BSA hydrogels in the absence and presence of DTT are shown in figures 4.3.1.1 a and b, respectively. A qualitative assessment of the scattering curves suggests there are significant structural differences between BSA hydrogels in the absence and presence of DTT, as shown by the reduced intensity at low q values, and the shallower slope in the mid q range in the absence of DTT. Interestingly, the BSA hydrogels with DTT show markedly similar profiles to MBP hydrogels (Fig. 3.3.0.1 and D.1.0.2), which one might reasonably expect considering the CD results showing that both protein systems are force labile. Previous SAS characterisation of folded globular protein hydrogels constructed from MBP (Fig. 3.3.0.1) has shown the presence of discrete fractal-like clusters of cross-linked folded protein in the network structure (Fig. 3.3.0.2).[135]

With this model in mind, the same fitting (Eqn. 3.3.0.1) is used to extract similar quantitative structural information from the SAS curves of BSA hydrogels in figures 4.3.1.1a and b:

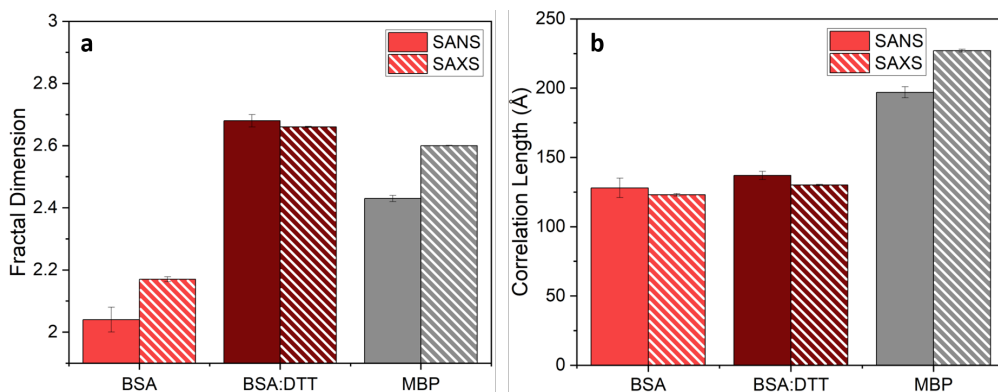


Figure 4.3.1.2: The a) fractal dimension and d) correlation length of cross-linked clusters of folded protein present in BSA hydrogels, extracted from the SANS (solid) and SAXS (striped) curves using equation 3.3.0.1 in the absence (light red) and presence (dark red) of DTT. The results of similar structural analysis on an apo-MBP hydrogel (grey) are included for reference (taken from 3.3.0.2).

Similar to the structural analysis in chapter 3 (section 3.3) two key parameters of interest are extracted from the SAS data, namely the fractal dimension of the fractal-like cluster of cross-linked folded protein, D_f , and the correlation of these clusters, ξ . The results in figure 4.3.1.2a show that the measured fractal dimension of a cross-linked cluster is significantly larger in BSA hydrogels formed in the presence of DTT, ($D_f = 2.66 \pm 0.01$ and 2.17 ± 0.01 in the presence and absence of DTT, respectively), while the correlation length increases in the presence of DTT ($\xi = 130 \pm 1 \text{ \AA}$ and $123 \pm 1 \text{ \AA}$ in the presence and absence of DTT, respectively) it is not a large increase (Fig. 4.3.1.2b). This suggests that hydrogels made from force-labile reduced BSA form ‘denser’ fractal-like clusters of a slightly larger size compared to the relatively ‘sparser’ clusters present in hydrogels in the absence of DTT. These results suggest that while the cluster size is unchanged with and without molecular reinforcement, the dimensionality or ‘density’ of the clusters is increased in BSA hydrogels in the presence of DTT. Previously characterised MBP (which has no disulphide bonds) is shown for reference (Fig. 3.3.0.2), and is again similar to the BSA hydrogels in the presence of DTT, exhibiting clusters of protein with similar dimensionality ($D_f = 2.60 \pm 0.01$) and the same order of size.

To gain more insight into hydrogel cluster size and morphology we consider the radial distribution function, $g(r)$, determined by Teixeira[185, 186] to derive the fractal structure factor (Eqn. 3.3.0.2, see derivation B.3):

$$g(r) = \frac{\rho_k D_f}{4\pi\phi r_0^{D_f}} r^{D_f-3} e^{-\frac{r}{\xi}}, \quad (4.3.1.1)$$

where ρ_k is the maximum packing density of the system i.e. for randomly assembled spheres 0.637, and r_0 is the minimum cut-off distance of the fractal cluster i.e. the effective radius of the building block, which for BSA is 33Å (as determined from the crystal structure in figure 4.1.1.1 and previous SAXS characterisation of the form factor [136]). The exponential term is introduced with the parameter ξ to act as a cut-off distance[185], imposing a maximum size on the fractal cluster (as discussed in derivation B.3). Multiplying the radial distribution function by the volume fraction of the system and integrating over r , gives an expression for the number of individual building blocks in a sphere of radius, R , from the centre of the cluster (Eqn. 4.3.1.2, for full derivation see section B.4):

$$N(r) = \rho_k D_f \left(\frac{\xi}{r_0}\right)^{D_f} \gamma\left(D_f, \frac{R}{\xi}\right) \quad (4.3.1.2)$$

where $\gamma(D_f, R/\xi)$ is the lower incomplete gamma function. Figure 4.3.1.3a shows how the number of protein building blocks varies as a function of distance from the centre of a fractal-like cluster in units of the building block radius.

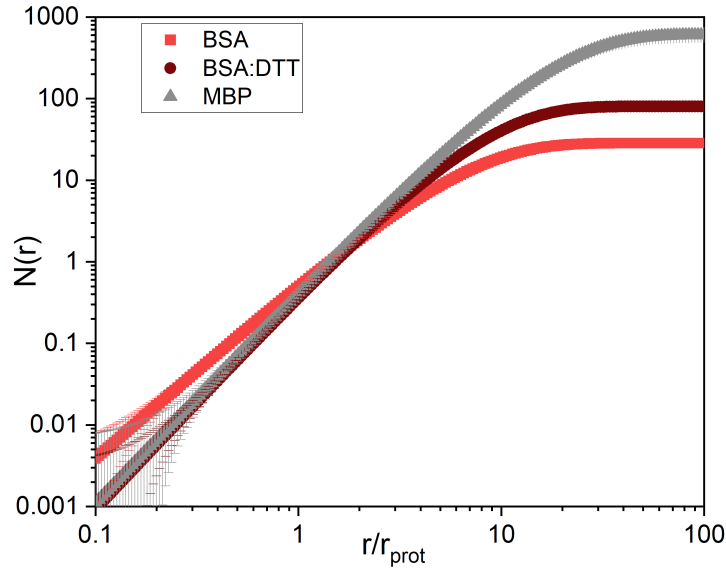


Figure 4.3.1.3: The number of protein monomers in a cluster for BSA hydrogels in the absence (light red) and presence (dark red) of 3mM DTT as a function of distance from the centre of the cluster, as predicted by equation 4.3.1.2 using the extracted values in figure 4.3.1.2.

In all cases the curves increase at a rate related to the fractal dimension of the cluster and plateau at large distances from the cluster centre. This is expected given the exponential term in equation 4.3.1.1, giving a measure of the maximum number (plateau value of the curve) and radius (point of turnover to plateau) of building blocks in a cluster. We find that BSA hydrogels have approximately 7 times more protein in each cluster in the presence of DTT, suggesting an extremely important role of protein unfolding in determining the cross-linked cluster density. There is also an increase in the cluster size in the presence of DTT, consistent with the same increase observed in the correlation length, which is to be expected as the distance at which $N(r)$ plateaus (Fig. 4.3.1.3) is completely dependent upon the correlation length. From the calculated curves in figure 4.3.1.3 we can extract an estimate of number of protein monomers in a fractal-like cluster as well as the radius of said clusters (Fig. D.1.0.3). Using estimates of the cluster size and proportion of protein in the fractal-like clusters, we can calculate the volume fraction of a fractal-like cluster in isolation (ϕ_c), using equation 4.3.1.3, and

the associated inter-cluster space (ϕ_{ic}) using equation 4.3.1.4 (Fig. 4.3.1.4).

$$\phi_c = N_{tot}^c \left(\frac{R_{MBP}}{R_{cluster}} \right)^3 \quad (4.3.1.3)$$

$$\phi_{ic} = \frac{\phi_{system} - p_{Vol}^c}{1 - p_{Vol}^c} \quad (4.3.1.4)$$

where N_{tot}^c is the total number of protein monomers in a cluster, ϕ_{system} is the overall volume fraction of protein in the whole system and p_{Vol}^c is the proportion of the total volume of the system that is occupied by clusters, defined as,

$$p_{Vol}^c = \frac{4}{3} \pi R_{cluster}^3 \cdot \frac{p_c \cdot n_d^{system}}{N_{tot}^c} \quad (4.3.1.5)$$

with n_d^{system} being the over number density of protein in the system.

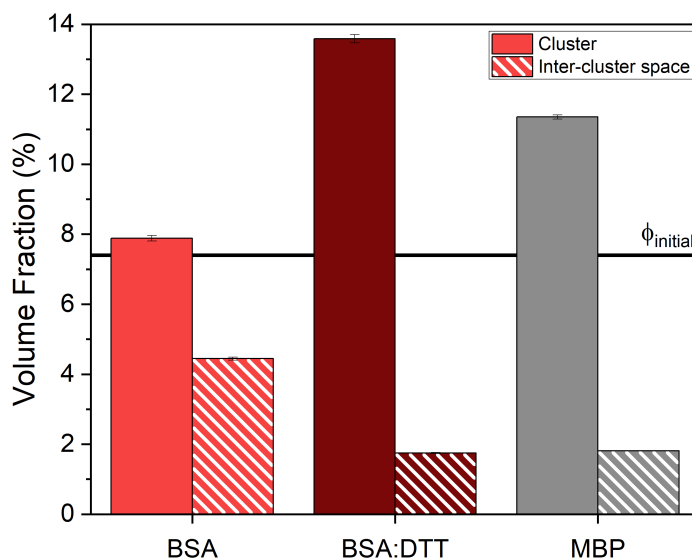


Figure 4.3.1.4: Volume fraction of a cluster (solid colour) and the inter-cluster space (red and white striped) for each hydrogel system (BSA in light red, BSA:DTT in dark red and apo-MBP added for reference and comparison in grey) determined using equations 4.3.1.3 and 4.3.1.4. Line added at 7.4% to denote the initial volume fraction of the system pre-gelation, $\phi_{initial}$.

In both the absence and presence of DTT, ϕ_c is larger than ϕ_{ic} , suggesting a heterogeneous hydrogel network dominated by clusters of proteins. The volume fractions of clusters and inter-cluster regions change upon addition of DTT, with denser clusters and a sparser inter-cluster space, suggesting a more heterogeneous network. Interestingly, for BSA the clusters formed in the absence of DTT have a volume fraction remarkably close to the initial volume fraction pre-gel solution ($7.89 \pm 0.08\%$ versus 7.4%). This result is consistent with what is expected from diffusion limited cluster aggregation theory [208, 209], in which individual particles undergoing Brownian motion aggregate together to form clusters of such particles. A consequence of this theory is that clusters will continue to grow in size, until their volume fraction is equal to the initial volume fraction of the solution. This result implies that the predominate mechanism in the formation of BSA hydrogels in the absence of DTT is diffusion limited cluster aggregation, as opposed to reaction limited aggregation [210, 211]. In the presence of DTT however,

the volume fraction of BSA clusters ($13.6\pm 0.1\%$) differs significantly from the initial pre-gel volume fraction, suggesting an additional mechanism involved in the formation of these hydrogels. For reference, this new method of analysis to extract the volume fractions of an individual cluster and the inter-cluster space was performed on the previously obtained SAS data on apo-MBP hydrogels (Fig. 3.3.0.1). The results of this new analysis on apo-MBP hydrogels has been included in figures 4.3.1.2 and 4.3.1.4, and show similarly large levels of heterogeneity in the network comparable to that of BSA hydrogels in the presence of DTT. All the data therefore suggests that both BSA in the presence of DTT and native MBP will yield and unfold to applied force, whereas native stapled BSA does not yield to applied force. Combining the force liability of the protein building block, CD and SAS structural analysis, we propose a model of the network structure of folded globular protein hydrogels, shown in figure 4.3.1.5. Folded proteins with covalent intra-molecular disulphide bonds are unyielding to force and form hydrogel networks with fractal-like clusters made up of proteins connected by inter-molecular di-tyrosine cross-links, with clusters linked together by multiple folded proteins (Fig. 4.3.1.5a). Breakage of the intra-molecular disulphide bonds, yields a force labile protein and denser fractal-like clusters are formed, with clusters connected by unfolded protein (Fig. 4.3.1.5b). The force liability of the protein is crucial in modulating the structure of the hydrogel networks. This section demonstrates the power of SAS techniques and the wealth of structural information that can be obtain about the end point structures of these hydrogel systems, however the SAS measurements in this work are unable to give information about the formation of these structures.

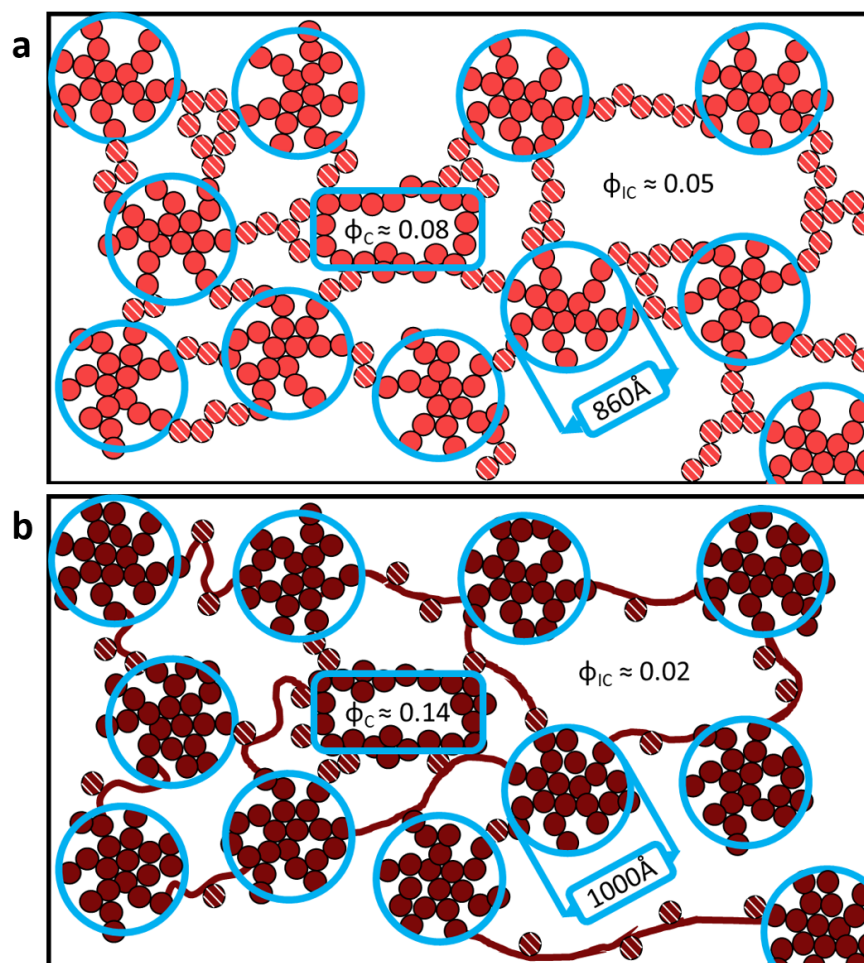


Figure 4.3.1.5: Schematic representation of the predicted structures of the BSA hydrogel networks in the a) absence (light red) and b) presence (dark red) of 3mM DTT. Networks consist of cross-linked fractal-like clusters with a cluster volume fraction of ϕ_c (represented by solid circles and highlighted by light blue rings) connected by an inter-cluster region of protein with a cluster volume fraction of ϕ_{ic} (represented by white striped circles). Solid dark red lines represent unfolded BSA protein strands in the inter-cluster region in the presence of DTT.

4.3.2 Computational modelling of BSA hydrogel network formation

In order to gain insight into the evolution of the structure from mono-dispersed solution to a self-supported network, we employ a previously used dynamic computational model; BioNet [212, 213]. BioNet can model individual folded protein monomers by representing them as freely diffusing and rotating, pseudo-deformable (soft-core potential) spheres with explicit cross-linking sites defined at the sphere surface. When within 3 Å of one another, a rigid bond will form between these sites to represent the cross-linking mechanism. To approximately model the BSA subunit, each sphere was given a radius of 33 Å with 14 evenly spaced cross-linking sites defined (representing the tyrosine residues in BSA), and another 4 randomly placed in the remaining space. These spheres then undergo a Brownian dynamics protocol with a local drag on each sphere. We are also able to model unfolded BSA as a chain of interacting binding sites connected by Hookean springs. These Hookean springs represent the end-to-end fluctuations expected of the worm-like chain polymer model, specifically where the length of the overall polymer is significantly greater than its persistence length as is the case for fully unfolded protein. To ensure the relative diffusion timescales of the unfolded protein components were appropriate, we assigned a local drag to each point-like binding site to approximately match the drag on each segment of amino-acid chain between binding sites. We consider two key cases; one where the simulation is initialised with 91% of the monomers in a “folded” state and one initialised where 72% of the monomers are in the “folded” state. These were chosen as close approximations of BSA hydrogel in the absence and presence of DTT respectively (Fig. 4.2.0.2b). The simulations were robustly initialised with periodic boundary conditions applied and continued until the networks were sufficiently percolated. We emphasise that in these simulations, the explicit unfolding of protein monomers during the “gelation” process is not modelled as protein unfolding is highly non-trivial due to the complexity of the pulling direction [76], and also crowding [214]. Once the simulations are complete, a box counting method was employed to extract an explicit value for the fractal dimension from each of the simulated cross-linked clusters (Fig. D.1.0.4).

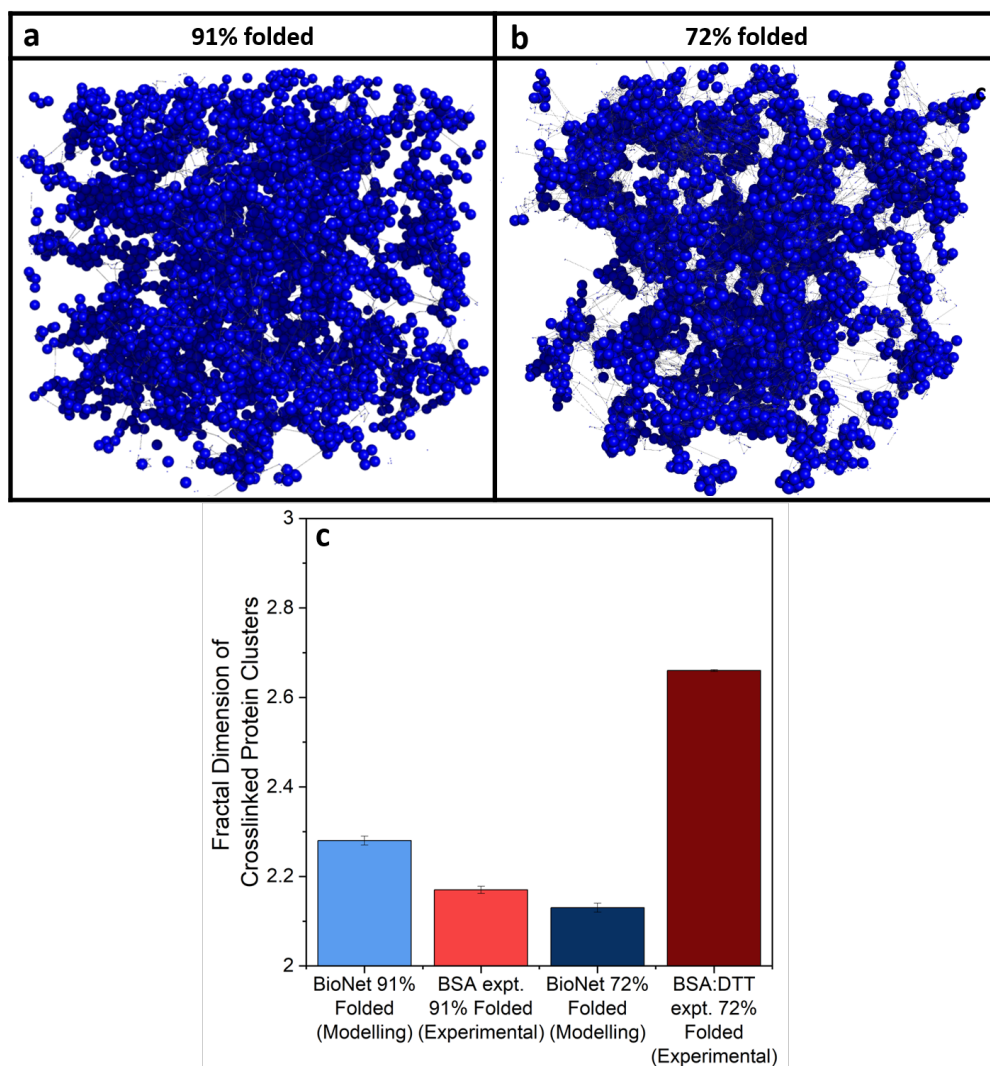


Figure 4.3.2.1: a,b) Schematics representing the explicit structures calculated using BioNet simulations[212, 213], where the blue spheres represent folded protein and the lines represent connections made by unfolded protein. c) Fractal dimensions of cross-linked clusters extracted from both BioNet simulations of a “single cluster” (calculated using a box counting method) and experimental SAS data (Fig. 4.3.1.2). The proportion of unfolded protein for the experimental results are the post-relaxation end point values taken from figure 4.2.0.2. In contrast for the simulations the proportions of folded protein represents the fixed amount of unfolded present in the simulation box over the course of the simulation. Simulations and analysis of the computational modelling was performed by Dr Benjamin Hanson and graciously provided for use in this work.

The fractal dimensions extracted from both the simulations and experimental data are shown in figure 4.3.2.1. The fractal dimension extracted from the simulation with 91% folded monomers (2.28 ± 0.01) is in good agreement with experimentally measured

BSA hydrogels in the absence of DTT (2.16 ± 0.01). However, the fractal dimension extracted from simulations containing only 72% folded monomers (2.13 ± 0.01), is significantly different to the comparable experimental results of BSA hydrogel in the presence of DTT (2.66 ± 0.01). Hence, comparison of the simulation and experimental results (Fig. 4.3.2.1) indicates that a general, homogenous presence of unfolded protein throughout the system during gelation is not sufficient to cause the large structural changes in the hydrogel architecture observed in our experimental SAS data (Fig. 4.3.1.1, 4.3.1.2 and 4.3.1.4). The combination of these computational results with the experimental results in section 4.3.1 therefore suggests that it is the act of unfolding of specific force labile protein building blocks during gelation itself that is crucial in defining the hydrogel architecture. To confirm this hypothesis, further investigation beyond the scope of this work would be required, including rapid frame acquisition SAXS and computational modelling that accurately models dynamic unfolding during gelation.

4.4 Modulation of Mechanics on the Bulk Scale

The results above show that removal of disulphide cross-links within BSA monomers affects the resulting hydrogel structure at the molecular and network level, due to the force-induced unfolding of the BSA building block that occurs in the absence of disulphide “staples”.

4.4.1 Effects of *in situ* unfolding on the linear mechanical response of BSA hydrogels

To investigate the effects of these observed structural changes on the macroscopic mechanics, rheology experiments were performed on BSA hydrogels in the absence and presence of DTT.

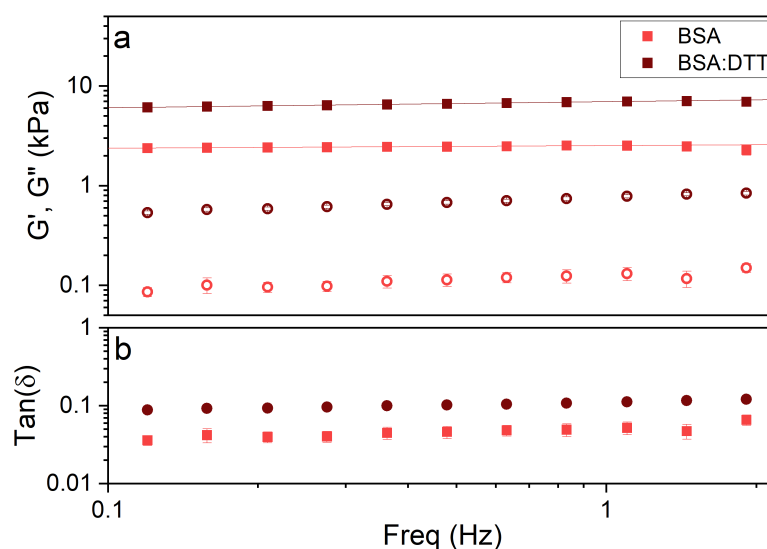


Figure 4.4.1.1: a) Frequency sweeps showing the (filled) storage, G' , and (open) loss moduli, G'' , of chemically cross-linked BSA hydrogels (final concentrations: 100mg/ml BSA, 50mM NaPS, $100\mu\text{MRu(II)bpy}_3^{2+}$) in the absence and presence of 3mM DTT. An oscillatory strain of 0.5% was applied to each sample. b) Loss ratio, $\tan(\delta)$, of BSA hydrogels as a function of applied frequency in the absence and presence of DTT. An oscillatory strain of 0.5% was applied to each sample.

Figure 4.4.1.1a and b show how G' and G'' (storage and loss moduli respectively), and the loss ratio, $\tan(\delta)$, of BSA hydrogels vary with applied oscillatory frequency in the absence and presence of DTT. The storage modulus, which is a measure of the hydrogel elasticity, is approximately 3-fold higher in the presence of DTT, while the loss modulus, which is a measure of the hydrogel viscosity, is approximately 5-fold larger. Fitting a linear function to the storage modulus allows for the extraction of the power law exponent giving an insight into the dynamics of the system. The extracted exponents are 0.027 ± 0.002 and 0.061 ± 0.001 in the absence and presence of DTT respectively. The increase in exponent in the presence of DTT suggests that these hydrogels have a greater increase in their solid-like behaviour as the time-scale of measurement is shortened compared to hydrogels in the absence of DTT. This trend in the exponent is likely due to the increased proportion of unfolded protein present in the hydrogel (Fig. 4.2.0.2), leading to more 'collisions' between unfolded protein strands that cannot be resolved within the time scale of the measurement. This is also consistent with the results in figure 4.4.1.1b in which $\tan(\delta)$ is higher in the presence of DTT, showing a higher level of viscosity in BSA hydrogels in the presence of DTT. In addition to the enhancement of the storage modulus in the presence of DTT there is also an increase in the viscous behaviour of the hydrogel as denoted by an increase in the loss ratio, which is consistent with the increased amount of unfolded protein in system in the presence of DTT as confirmed by CD (Fig. 4.2.0.2). This increase in the storage modulus of BSA hydrogels gelled in the presence of DTT may be due to additional cross-links in the inter-cluster region, either physical or chemical, between the force unfolded protein chains. To explore this further, a BSA hydrogel formed in the absence of DTT (i.e. the building block is restricted from unfolding) was soaked *in situ* on the rheometer in a 3mM DTT solution post-gelation (Fig. 4.4.1.2a), which resulted in a decrease in the storage modulus (Fig. 4.4.1.2b).

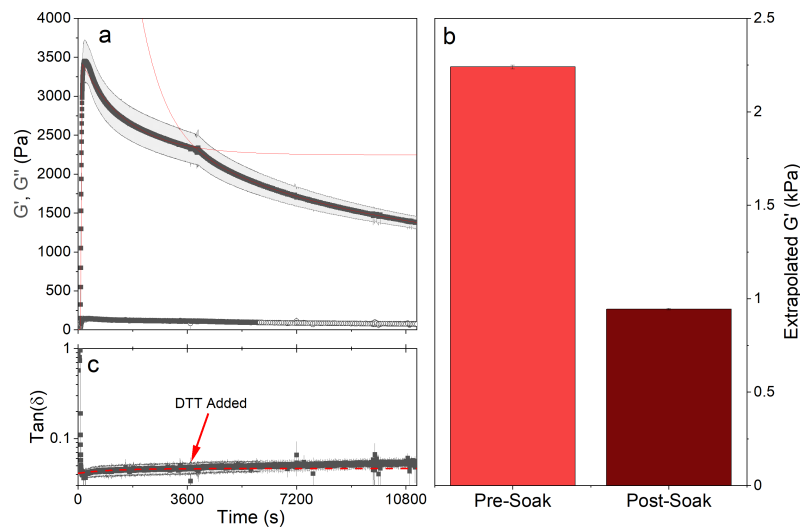


Figure 4.4.1.2: (a) Gelation curve of BSA hydrogel in the absence of DTT, showing storage (closed symbols) and loss moduli (open symbols) vs time of a BSA hydrogel, where a DTT soak is added at $t= 3960$ s. Red lines denote fits to extrapolate and extract the storage modulus and the relaxation timescales of the gel. (b) Extrapolated G' values with and without the DTT soak extract from the fits in (a). (c) Loss ratio of a BSA hydrogel as a function of time, where DTT soak is added at $t=3960$ s, denoted by the red arrow.

This decrease in storage modulus can be attributed to the force induced unfolding of load bearing BSA building blocks as the DTT diffuses into the gel. Upon soaking of the BSA hydrogel in DTT an increase in the loss ratio (Fig. 4.4.1.2c) is noted, demonstrating an increase in the viscous behaviour, which is consistent with an increase in the amount of unfolded protein in the gel. This decrease in the storage modulus (and simultaneous increase in the viscous behaviour) upon soaking suggests that no additional physical cross-links are being formed between the unfolded protein chains, as we would expect this to increase the value of G' . The enhancement to the storage modulus of BSA hydrogels in the presence of DTT (Fig. 4.4.1.1a) is therefore a result of additional chemical cross-links formed by the force unfolded protein chains during the photo-chemical gelation process.

To further investigate the molecular reinforcement of the protein and its impact on hydrogel formation, we analysed the changes in storage (G') and loss (G'') moduli of

BSA hydrogels in the absence and presence of DTT during gelation, as a function of time, again using rheology (Fig. 4.4.1.3).

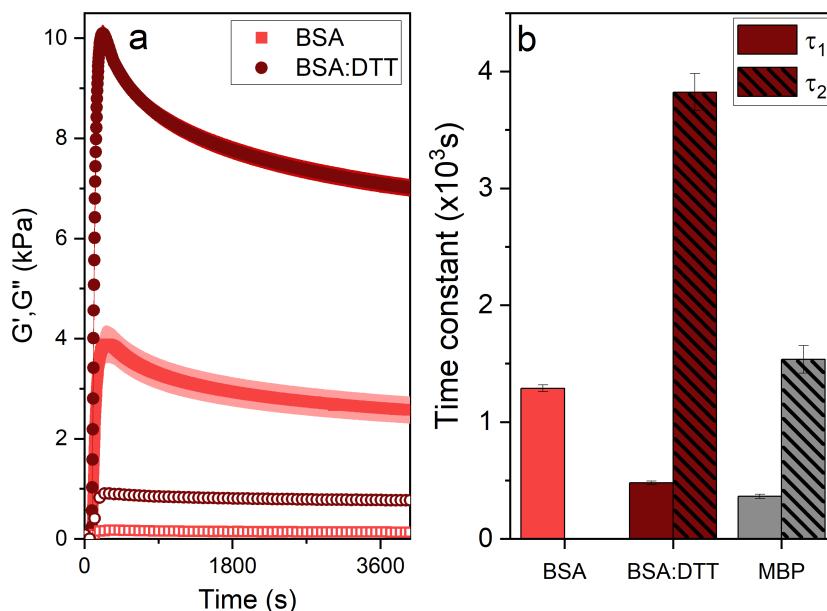


Figure 4.4.1.3: a) Gelation curves, showing storage (closed symbols) and loss moduli (open symbols) vs time of chemically cross-linked BSA hydrogels (final concentrations: 100mg/ml BSA, 50mM NaPS, 100 μ MRu(II)bpy₃²⁺) in the absence (light red) and presence (dark red) of DTT. Illuminated with blue light of wavelength $\lambda \approx 452$ nm (see section 2.3.3 at $t=60$ s till $t=360$ s. d) Timescales of the relaxation modes in BSA hydrogels, extracted by fitting equation 3.4.0.1 to the gelation curves. Time constants for the relaxation of an apo-MBP hydrogel (grey) added for reference and comparison (Values taken from figure 3.4.0.1)

Both cases exhibit the previously observed gelation profile for photo-chemically cross-linked [134–136] (Fig. 3.4.0.1) namely; the curves initially show a dramatic increase in G' during the photochemical cross-linking process, which is then followed by a large relaxation to a final value of G' . The gelation curves show that the value of G' in the presence of DTT is ≈ 3 -fold larger than gels in the absence of DTT, similarly a larger G'' is also observed in the presence of DTT, these observations are consistent with the results of the frequency sweep experiments (Fig. 4.4.1.1a). Additionally, it could be qualitatively argued that there is a slight difference in the relaxation behaviour in the absence and presence of DTT. In order to determine if there is indeed a difference in the relaxaton

behaviour of the two different systems these curves were fitted with a previously used empirical function (Eqn. 3.4.0.1) allowing for the extraction of quantitative information on the relaxation behaviour of the system. Figure 4.4.1.3b shows the extracted time constants of relaxation of the system, τ_1 and τ_2 . The difference between the relaxation behaviour of BSA hydrogels in the absence and presence of DTT is striking, with the former having one mode of relaxation ($\tau_1 = 1290 \pm 30$ s) while the later has two distinct relaxation modes ($\tau_1^{DTT} = 480 \pm 10$ s, $\tau_2^{DTT} = 3800 \pm 200$ s). The study of MBP hydrogels in varying concentrations of maltose in the previous chapter, also measured two modes of relaxation post-photo-chemical cross-linking. A fast relaxation was attributed to the formation of a percolated hydrogel network, and a second, slower relaxation was attributed to the unfolding of the protein building block. Interestingly, BSA in the absence of DTT displays one relaxation mode, while in the presence of DTT we see two (exemplar fits shown in Fig. D.2.0.2). The τ_2^{DTT} values extracted from the gelation curves in the presence of DTT are similar to the timescale of unfolding observed in CD and in our previous work [135]. In combination with CD data (Fig. 4.2.0.2a) this suggests that the emergence of two-relaxation modes is inherently linked to force lability of the protein during gelation. Note, this same behaviour is observed for hydrogels formed from stapled BSA which are then soaked in DTT solution (Fig. D.2.0.1). Therefore, it has been demonstrated that the relaxation behaviour of folded protein-based hydrogels is intimately linked to the force lability of the protein building block. Furthermore *in situ* unfolding of the protein building block results in significant changes to linear mechanical response of the network, however for a more complete understanding of the cross-length effects on hydrogel mechanics the load and non-linear behaviour of the gels needs to be explored.

4.4.2 Effects of *in situ* unfolding on the behaviour of BSA hydrogels under load

To provide a great insight into the effects of *in situ* unfolding on the load-unload behaviour of folded protein hydrogels, stress-strain measurements were performed on BSA hydrogels in the absence and presence of DTT.

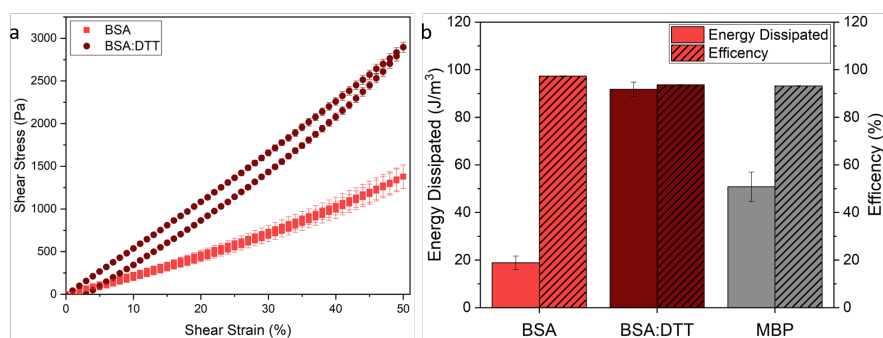


Figure 4.4.2.1: a) Stress-Strain curves of chemically cross-linked BSA hydrogels (final concentrations: 100mg/ml BSA, 50mM NaPS, 100 μ MRu(II)bpy₃²⁺) in the absence and presence of 3mM DTT. Samples were strained to 50% at a rate of 1%/s and then unloaded down to 0% at the same rate. b) Energy dissipation (open) and efficiency (striped) during load-unload cycle of BSA hydrogels in the absence (light red) and presence (dark red) of DTT. Data on an apo-MBP hydrogels (grey) added for comparison and reference.

Figure 4.4.2.1a shows shear stress-strain loading curves of BSA hydrogels from applied rotational rheology in the absence and presence of DTT. In either condition, the stress-strain curves show linear elasticity at shear strains of less than 25%. Fitting this linear region yields storage moduli (G') of 2.6 ± 0.3 kPa and 6.3 ± 0.2 kPa (in the absence and presence of DTT, respectively) in good agreement with the values obtained from the frequency sweeps (Fig. 4.4.1.1). Similar to the MBP hydrogels measured in chapter 3.2.2.1, the stress-strain curves of BSA hydrogels also display hysteresis behaviour upon unloading of the sample and is particularly prominent in BSA hydrogels in the presence of DTT. As stated in the previous chapter the hysteresis area enclosed by the stress-strain curves is a quantitative measure of the energy dissipated to the internal energy of the system. Integrating the stress-strain curves allows for the extraction and calculation of the energy dissipated and efficiency (Eqn. 3.2.2.1) of the hydrogels (shown in Fig. 4.4.2.1b). In the presence of DTT there is an over 4-fold increase in the energy dissipated, while there is only a 3% reduction in the efficiency of the gels from 97% in the absence and 94% in the presence of DTT. This increase in energy dissipation is likely due to larger amounts of unfolded protein in samples in the presence of DTT which is consistent with the CD results (Fig. 4.2.0.2) and our structural model (Fig. 4.3.1.5).

4.4.3 Effects of *in situ* unfolding on the non-linear behaviour of BSA hydrogels

Finally, the non-linear mechanical behaviour of the BSA hydrogels was investigated, the shear moduli and loss ratio of the hydrogels under increasing strain are shown in figure 4.4.3.1 respectively.

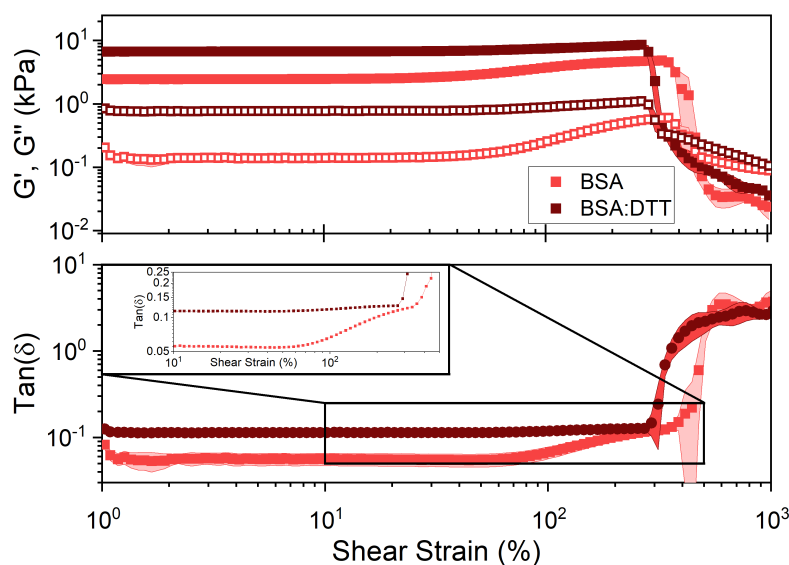


Figure 4.4.3.1: The a) storage, G' , and loss, G'' , moduli and b) the loss ratio, $\tan(\delta)$, of BSA hydrogels (final concentrations: 100mg/ml BSA, 50mM NaPS, $100\mu\text{MRu(II)bpy}_3^{2+}$) in the absence (light red) and presence (dark red) of 3mM DTT as a function of applied oscillation strain at a frequency of 1 Hz. (insert) Enlargement of the strain-stiffening regime, plotted without error bar ribbon for clarity.

The graphs show a linear trend up to strains of approximately 40%, after which there is a stiffening region until rupture at strains of approximately 300%. Interestingly a far larger degree of strain stiffening is noted in the reinforced BSA hydrogels than in hydrogels in the presence of DTT. This difference is likely due to the difference in structures (Fig. 4.3.1.5), in which the native BSA gels has many folded domains that will act as load bearing molecules as the strain is increased, whereas gels in the presence of DTT have a large proportion of unfolded proteins which uncoil towards their full contour length under strain meaning very little change would be seen in the shear moduli.

4.5 Discussion

We have demonstrated that control of protein force lability has an important role in defining the architecture and mechanics of cross-linked protein hydrogels. We show that a network made from an internally stapled protein building block retains 91% of its protein in the folded state compared to 72% folded protein in a network made from unreinforced protein (Fig. 4.2.0.2). This result implies protein reinforcement reduces the probability of force induced protein unfolding during gelation. The network structure formed from a disulphide-protected folded protein, that is unyielding to force, consists of fractal-like clusters made up of cross-linked protein, with the linking inter-cluster region populated by folded proteins (Fig. 4.3.1.5a). Without molecular reinforcement, the protein building block is force labile and denser fractal-like clusters are formed, with the connecting inter-cluster region populated by unfolded protein (Fig. 4.3.1.5b). By complementing our experimental work with computational modelling (Fig. 4.3.2.1), we deduce that it is the act of unfolding of specific force labile protein building blocks during gelation, rather than the presence of unfolded protein, that is crucial in defining the hydrogel architecture. To confirm this hypothesis, further investigation beyond the scope of this work would be needed including rapid frame acquisition SAXS and computational modelling that accurately models unfolding during gelation. Controlling the force lability of the protein building block also has a significant impact on the mechanics as well as the architecture of the protein hydrogel network. Networks formed from force labile protein exhibit a higher elasticity (storage modulus approximately 3-fold higher), enhanced viscous behaviour and energy dissipation, relative to the networks formed from internally stapled protein. We suggest that this increase in viscous behaviour is due to a higher prevalence of unfolded protein in the inter-cluster region of the hydrogel network constructed from the force labile protein building block. The increase in the elasticity of the network is attributed to additional chemical cross-links in the inter-cluster region of the network, formed between the strands of force-induced unfolded protein in the inter-cluster region of the network. These results suggest that controlling the building block unfolding and cross-link density in the inter-cluster region is key in regulating and defining the mechanics of the network. Interestingly, the dominance of the inter-cluster

region on the mechanical response of a network has been observed by other groups in colloidal systems. Del Gado et al. and Frust et al. have found that the connections between clusters in the inter-cluster region, termed the ‘rigidity percolation network’, are key in regulating the mechanics of colloidal networks both theoretically [215, 216] and experimentally [217]. These studies similarly found that heterogeneity in the network structure was crucial in governing the mechanical response of the network. Conversely, studies on peptide-based hydrogels have shown that as the network becomes more homogeneous [115, 116] the mechanical strength is enhanced. We speculate that this difference is due to the contrasting structures between the two systems, with inter-connected clusters and web-like fibrous structures exhibited by folded protein and peptide gels, respectively. Restriction of unfolding of the protein building block also has a significant impact on the relaxation behaviour of the hydrogels. While a single mode of relaxation describes the networks formed from reinforced protein, a dual relaxation mode is necessary for networks formed from the unreinforced protein. We propose the additional mode of relaxation in unreinforced protein network corresponds to unfolding of the force labile protein. Additionally, the relaxation mode corresponding to unfolding is observed in hydrogels constructed from reinforced protein soaked in DTT post-gelation accompanied by an approximate factor of 2 reduction in the storage modulus, consistent with previously published literature [131] comparing rigid and flexible building blocks. The modulation the force lability of the building block plays a fundamental role in defining the network architecture and mechanics. The transition of building block from a rigid folded state to a flexible unfolded state emerges as a powerful method for controlling the inter-cluster region of the network structure and the subsequent mechanical response. This study has demonstrated the necessity of combined structural and mechanical characterisation to understand the translation of complex molecular properties across length scales. By understanding the crucial role of building block unfolding on hierarchical networks, we demonstrate the importance of *in situ* unfolding in defining the structural and mechanical behaviour of the network and reveal building block unfolding as a method for the design of novel biomimetic and bioinspired materials.

Chapter 5

A Tale of Two Stabilities: Deconvoluting the Roles of Protein Thermodynamic and Mechanical Stability in Hierarchical Networks

5.1 Introduction

Previous work [135] shown in chapter 3 demonstrated that a simultaneous increase in both the thermodynamic and mechanical stability of the protein building block, via ligand mediated stabilisation, translates across length-scales to the mechanical strength of the protein network. However, this study was unable to determine the contributing role of each type of stability in the increase in network strength. As discussed in chapter 1 the thermodynamic and mechanical stability of a protein fold are not equivalent [218]. The thermodynamic stability of a protein originating from the enthalpic contributions of a number of different non-covalent interactions, and the entropic contributions due

to the hydrophobic interactions [50, 59, 64]. In contrast the mechanical stability of a protein is due to the hydrogen bonding network between secondary structure elements and in particular the orientation of the applied force to this network [76, 92, 219]. So, it is possible for two proteins to have similar thermodynamic stabilities but strikingly different mechanical characteristics. This chapter seeks to address the shortcoming of our previous study [135] (chapter 3) by determining how protein building block stability governs the structural and mechanical properties of the network. More broadly, we investigate the relative importance of local molecular stability compared to global molecular stability, and how this relates to the structural and mechanical properties of multi-molecular hierarchical networks. To achieve these aims, MBP-based hydrogels are utilised as a model system. To independently control and vary stability, measurements are completed on MBP hydrogels in the absence and presence of maltose, with the addition of varying concentrations of the denaturant urea.

Initially in this chapter, the rationale behind the selection of MBP as the model hydrogel building block for this study will be discussed. The design of the model system of MBP hydrogels in the absence and presence of urea will also be outlined to show that urea is the ideal protein denaturant to use in this study. The chapter will go on to discuss the molecular level characterisation of the MBP building block's thermodynamic stability, before going into detail on the effects of the thermodynamic and mechanical stability of the building block on the structural properties of the hydrogel network, investigated via SAXS. The core of this chapter will cover the results of bulk mechanical characterisation of MBP hydrogels and the effects of each type of molecular level stability on the bulk mechanical behaviour of the network. Finally, the chapter will end by summarising the roles of the thermodynamic and mechanical stability of the building block in governing the properties of a hierarchical network, and will suggest a possible underlying mechanism for these distinct roles.

5.2 Selection of model protein building block and design of model system

In order to investigate the differential effects of building block thermodynamic and mechanical stability on the structure, we require a model protein building block with similar properties as discussed in chapter 3 (section 3.1.1). MBP stands out as an ideal protein building block to determine the distinct roles of thermodynamic and mechanical stabilities in protein hierarchical networks, for two key reasons: firstly, MBP has been previously characterised [135] in chapter 3 as an effective hydrogel building block; secondly, upon the binding of maltose to MBP there is an increase in both the thermodynamic [133] and mechanical [81, 82] stability of the protein. In order to be able to deconvolute the effects of these two types of stability on the overall network properties, they need to be controlled and varied independently of one another. This can be achieved for the thermodynamic stability of the MBP building block via the addition of small amounts of the denaturant urea to the system, in the presence and absence of maltose.

5.2.1 Effects of urea on folded proteins

Urea is an uncharged organic compound, with two amide groups (-NH₂) connected by a carbonyl (C=O) functional group, that is highly soluble in water and is neither acidic or basic. Importantly, urea acts as a strong denaturant of folded globular proteins [220]. Figure 5.2.1.1b shows the energy landscape of a simple two-state unfolding transition from the folded state (F) to the unfolded state (U) through a transition state (TS). A similar figure shown in chapter 1 (section 1.2.2.1), defines the free energy difference between the folded and unfolded states, ΔG_{un} , as the thermodynamic stability of the protein fold; likewise the free energy difference between the folded and transition state, ΔG_{TS} , is defined as the energy barrier to unfolding [221]. The schematic in figure 5.2.1.1 depicts the transition in the absence and presence of urea.

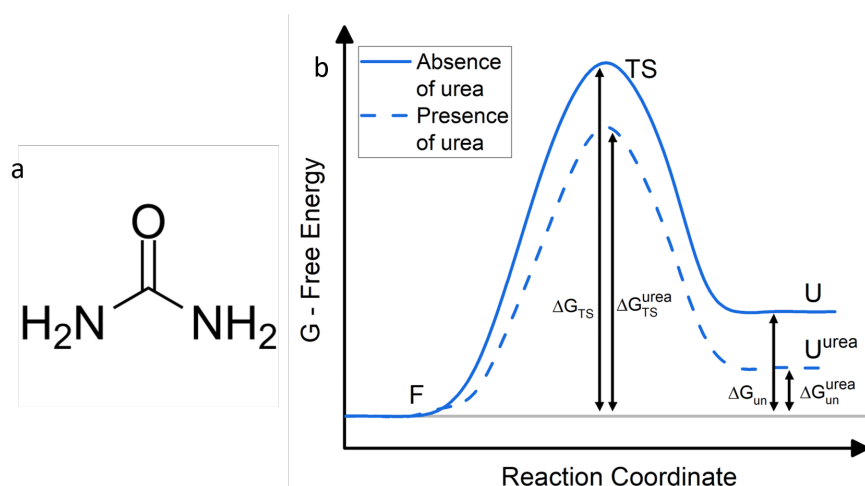


Figure 5.2.1.1: a) Skeletal formula showing the molecular structure of the denaturant urea. b) Schematic of a two-state unfolding process from the folded state (F) to the unfolded state (U) through the transition state (TS) in the absence (solid line) and presence of urea (dashed line). Where ΔG_{un} and ΔG_{un}^{urea} are the difference in free energy between the folded and the unfolded state in the absence and presence of maltose, respectively. Similarly ΔG_{TS} and ΔG_{TS}^{urea} are the difference in free energy between the folded and the transition state in the presence and absence of urea, respectively.

The addition of urea to a protein results in a reduction in both the thermodynamic stability of the protein, ΔG_{un} , and the energy barrier to unfolding, ΔG_{TS} , meaning protein will more readily unfold in the presence of urea as would be expected from a denaturant. The underlying mechanism of this alteration to the energy landscape in the presence of urea stems from the preferential interaction of urea with the protein peptide backbone [220, 222–224]. In water the intra-protein-protein interaction is more stable than the protein-water interaction, however this condition is inverted when considering urea, i.e. the intra-protein-protein interaction is less stable compared to the protein-urea interaction [225]. The comparative increased stability of the protein-urea interaction is what leads to the decrease in ΔG_{un} in the presence of urea. The relationship between thermodynamic stability and the concentration of urea is known [226].

$$\Delta G_{un}^{[urea]} = \Delta G_{un} - m \cdot [urea] \quad (5.2.1.1)$$

Where m is the protein dependant strength of urea destabilisation, which is related

to the solvent accessible surface area of the protein [226]. Therefore, in high enough concentrations of urea the thermodynamic stability is lowered such that $\Delta G_{un} < 0$, the protein readily unfolds to maximise the urea exposure of the peptide backbone. This means the urea promotes and stabilises the unfolded state rather than directly weakening the bonds of the folded state. The mechanism of urea-mediated protein destabilisation shows why urea is an ideal denaturant for the study of the effect of changing the thermodynamic stability of the building block on the overall network properties. In principle small concentrations of urea ($[\text{urea}] \ll \frac{\Delta G_{un}}{m}$) are able to alter the thermodynamic stability of the protein building block without significantly affecting the native state of the protein e.g. by breaking bonds in the folded protein structure. Importantly, unlike other popular protein denaturants e.g. guanidinium chloride, urea is not charged and when dissolved in water it is neither acidic nor basic, so will not affect the ionic strength or pH of the system.

5.3 Characterisation of building block stability

Initially DSC was employed to determine the melting point and enthalpy change associated with the ‘melting’ of MBP in the absence (apo state) and presence (bound state) of maltose at relevant concentrations (100mg/ml) in varying concentrations of urea. From these results it was possible to calculate the change in the Gibbs free energy due to unfolding (ΔG_{un}) as a function of urea concentration (Fig. 5.3.0.1), and hence determine the change of thermodynamic stability of both apo and bound MBP.

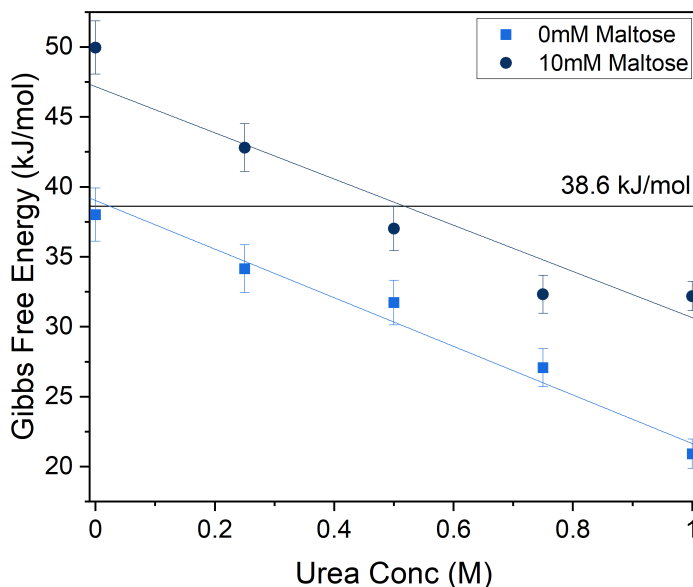


Figure 5.3.0.1: Gibbs free energy of unfolding of MBP in the absence (light blue) and presence (dark blue) of maltose as determined by DSC, at varying concentrations of urea. Solid lines represent linear fits consistent with established linear relationship between ΔG_{un} and urea concentration. Black horizontal line represents the fitted value of thermodynamic stability of MBP in the apo state.

Figure 5.3.0.1 shows the decrease in ΔG_{un} of MBP as the concentration of the denaturant urea is increased, both in the presence and absence of the stabilising ligand. As expected, in the absence of denaturants, MBP has a higher thermodynamic stability (characterised by an increased ΔG_{un}) when the ligand maltose is bound (48 ± 2 kJ/mol) compared to the apo (39 ± 1 kJ/mol), this corroborates the stabilising effect of the ligand maltose on MBP. The destabilising effect of urea is observed to be linear with concentration, with a destabilising coefficient of 16 ± 2 kJ \cdot mol $^{-1}$ M $^{-1}$ and 18 ± 3 kJ \cdot mol $^{-1}$ M $^{-1}$ in the absence and presence of maltose, respectively. The destabilisation coefficient is understood to be related to the solvent-accessible surface area of the globular protein, and so these DSC results imply that there is a slight increase in the solvent accessible surface area upon the binding of maltose, despite small-angle x-ray scattering (SAXS) data showing no significant differences in form between the apo and bound state (Fig. E.0.0.1). However, the values for the destabilising coefficient are within error of each

other so this difference could be simply due to experimental error. It is important to note that at an approximate concentration of 0.5M urea and 10mM maltose the thermodynamic stability of MBP is equivalent to its apo state in the absence of urea. This is a crucial comparison as while the thermodynamic stability is equivalent, there is a difference in the mechanical stability due to the bound maltose molecule.

So, by controlling the concentration of urea and presence of maltose in the system, it is possible to tune the thermodynamic stability of the network building block, while simultaneously modulating its mechanical stability. This molecular level characterisation is both crucial in understanding resultant higher order changes in the network and demonstrates that MBP is a model system to investigate the distinct roles played by building block thermodynamic and mechanical stability in hierarchical networks.

5.4 Effect of thermodynamic and mechanical stability on hydrogel network architecture

To study and determine the differential effects of the global thermodynamic and the local mechanical stability of the hydrogel building block on the network architecture, we perform SAXS measurements on MBP hydrogels with varying concentrations of urea in the absence and presence of maltose (Fig. 5.4.0.1).

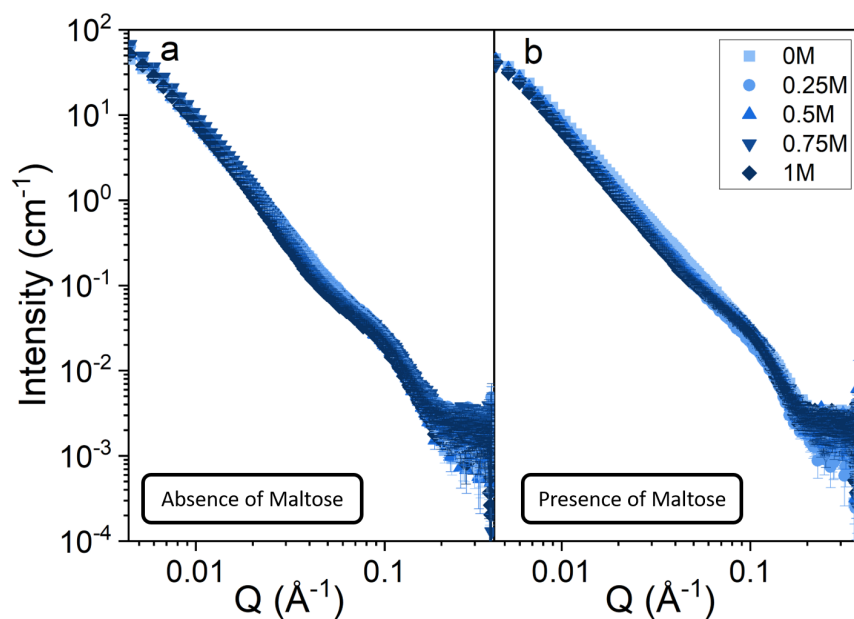


Figure 5.4.0.1: SAXS curves of chemically crosslinked folded MBP hydrogels (final concentrations: 100mg/ml MBP, 30mM NaPS, 100mM Ru(II)bpy₃²⁺) as a function of urea concentration in the a) absence and b) presence of maltose.

Figure 5.4.0.1a and b show the scattering curves of MBP hydrogel in varying concentrations of urea (illuminated by an X-ray beam) in the absence and presence of maltose respectively. In both the apo and bound MBP hydrogels very little change is observed in the curves as the concentration of urea is increased. Broadly speaking this suggests that the general architecture of the gels remains similar in all samples. Some subtle differences are noted in the curves: i) the turnover to plateau at low Q (Guinier region) is shifted to higher Q values as urea concentration is increased, and ii) in the absence of maltose the gradient of the mid- Q region steepens with increasing urea concentration. The former of these changes suggests that the size of the largest scattering object decreases with increasing urea concentration, while the latter observation suggests some change in the geometry of this large scattering object occurs with increasing urea concentration but only in the absence of maltose. Previous structural characterisation of MBP (section 3.3) and other folded protein hydrogels [134, 136] has shown the presence of fractal-like clusters of cross-linked fold protein linked together by an inter-cluster region populated by unfolded protein. By applying the same model used in our previous studies, and fitting the curves in figure 5.4.0.1 with equation 3.3.0.1 we can extract key parameters

of the system in a similar fashion to SAS curves in chapters 3 and 4. Fitting the SAXS curves in figure 5.4.0.1 allows for the extraction of the fractal dimension, D_f , and the correlation length/characteristic length-scale, ξ , of the fractal-like cross-linked clusters (Fig. 5.4.0.2).

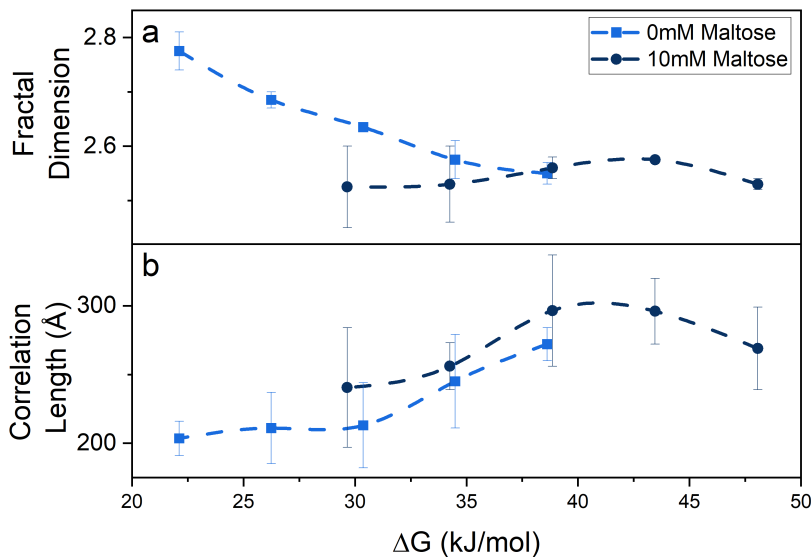


Figure 5.4.0.2: a) fractal dimension and b) correlation length values extracted from fitting equation 3.3.0.1 to the SAXS curves in figure 5.4.0.1 as a function of the thermodynamic stability (determined by DSC (Fig. 5.3.0.1)) in the absence and presence of 10mM maltose. The error bars here show the standard error for measurements taken in duplicate. Dashed lines are added as a guide to the eye.

As previously described (see section 3.3) D_f in our system can be thought of intuitively as related to the density of the cluster of cross-linked folded protein, while ξ is an imposed parameter representing the upper-limit of fractal behaviour and can be interpreted as related to the size of the fractal clusters. By combining these extracted parameters with the results of our DSC building block stability results (Fig. 5.3.0.1) we obtain figure 5.4.0.2a and b, which shows how D_f and ξ vary as a function of ΔG_{un} in both the absence and presence of maltose, respectively. There is a striking difference in the ΔG_{un} dependency of the fractal dimension in the presence and absence of maltose (Fig. 5.4.0.2a). In the presence of maltose, D_f of the clusters remains fairly constant over all values of ΔG_{un} , however in the absence of maltose there is an approximately

linear increase in D_f with decreasing ΔG_{un} . This difference in trend suggests that the density of the fractal-like clusters increases as the thermodynamic stability of MBP decreases, unless the protein building block has increased local mechanical stability (in the presence of its ligand maltose), in which case the cluster density is unaffected by a change in the thermodynamic stability of the MBP building block. ξ also varies as a function of ΔG_{un} , exhibiting a decrease in cluster size as the thermodynamic stability is decreased, however the trend is consistent in both apo- and bound-MBP hydrogels. The consistency of the ΔG_{un} dependency of ξ in the presence and absence of maltose suggests that the size of the fractal-like clusters of folded protein is governed by the global thermodynamic stability of the protein rather than any enhanced local mechanical stability. It can be seen from these results that there are distinct roles played by both the thermodynamic and mechanical stabilities of the building block in governing the structural properties of the network. In particular the global thermodynamic stability of MBP governs the geometry and size of the fractal-like clusters of cross-linked folded protein, while the local mechanical stability plays a more conservative role in preserving the morphology of the cross-linked fractal-like cluster.

We can extract additional information about the structure of the hydrogel network, including information about the connecting inter-cluster region, by performing the analysis [136] previously detailed in chapter 4 (section 4.3.1). This analysis makes use of these extracted parameters (D_f and ξ) to determine the number of protein monomers in a cluster as a function of distance from the centre of the cluster. From this the cluster size and the total number of monomers can be determined and used to calculate volume fractions of both the clusters and the inter-cluster space.

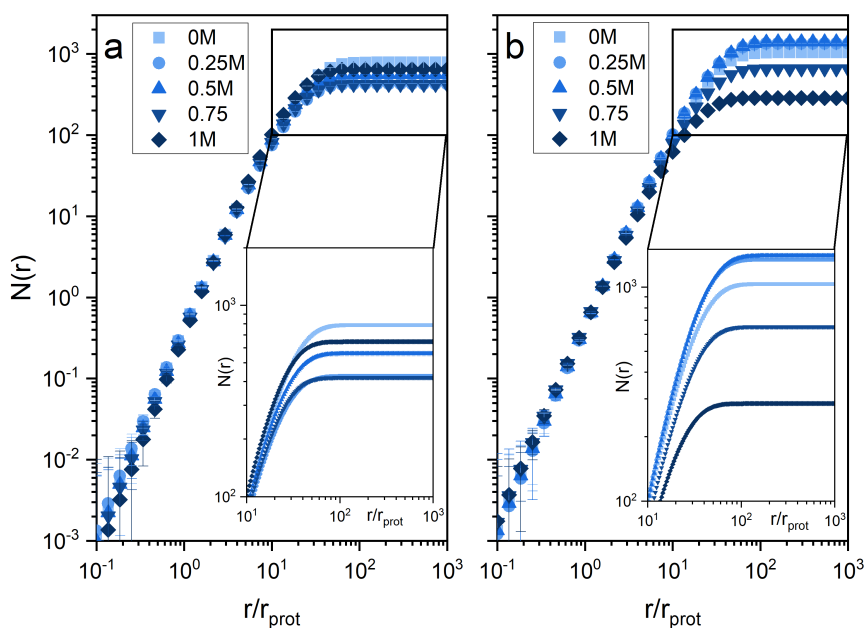


Figure 5.4.0.3: Number of protein monomers in a cluster as a function of distance from the centre of a cluster in the a) absence and b) presence of maltose. Every tenth point is shown for clarity. (insets) Magnification of the boxed section in figures 5.4.0.3a and b, for clarity.

The curves in figure 5.4.0.3 show how the number of the proteins in a cluster vary with the normalised distance from the centre of the fractal-like cluster (normalised by the radius of the MBP). Similar to the $N(r)$ curves in chapter 4 (Fig. 4.3.1.3) these curves in figure 5.4.0.3 initially increase at a rate that is related to the fractal dimension of the system before plateauing at some value N for large r . As expected, the gradient of the linear section in the absence of maltose increases with increasing urea concentration (decreasing ΔG_{un}) while in bound-MBP hydrogels it remains unchanged with urea concentration, mirroring the trends observed in the fractal dimension. In the absence of maltose the curves show no strong trend of the plateau value with urea concentration. Conversely in the presence of maltose a weak negative correlation of decreasing plateau value with increasing urea concentration (decreasing ΔG_{un}) is observed, meaning that the number of protein monomers in a cluster is only dependant on the thermodynamic stability of the building block with the addition of enhanced mechanical stability. There is also a subtle trend in the position of the turnover to plateau (i.e. the turnover occurs

at lower r in the presence of urea) indicating smaller clusters in the presence of urea in both the absence and presence of maltose. This is consistent with the trend observed from the correlation length (Fig. 5.4.0.2b). We would expect this to be the case as the exponential term containing ξ in the radial distribution function governs the size of the cluster predicted by the model. A larger variance for the plateau values are observed in samples that contain maltose compared to hydrogel samples contracted from the apo protein. This larger range of values for the number of monomers in a cluster could be a consequence of the invariance of the fractal dimension with ΔG_{un} and the shrinking cluster size with increasing urea concentration in the presence of maltose, leading to less protein in each cluster in order to preserve the cluster morphology.

In order to gain more insight into the effects of building block thermodynamic and mechanical stabilities we calculate the volume fractions of the fractal-like clusters, ϕ_c , and the inter-cluster region, ϕ_{ic} . This calculation is achieved by first extracting the total number of protein monomers in a cluster (by fitting the plateau value of the curves) and the average cluster size (exemplar graph shown in Fig. D.1.0.3) from the curves in figure 5.4.0.3 and then applying equations 4.3.1.3 and 4.3.1.4 (as detailed in section 4.3.1).

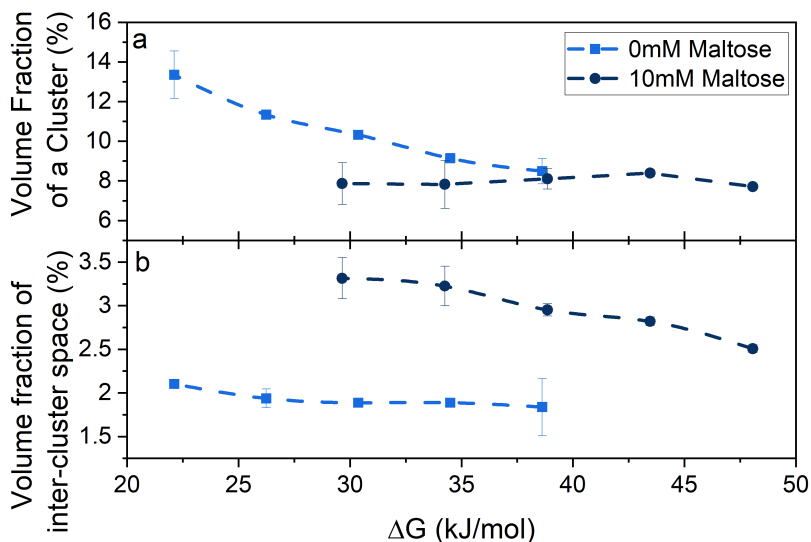


Figure 5.4.0.4: Average volume fraction of folded protein a) in a single fractal-like cross-linked cluster and b) in the connecting inter-cluster space in MBP-based hydrogels as a function of thermodynamic stability the MBP building block, in the absence and presence of maltose. Error bars are standard error from samples measured in duplicate. Dashed lines are added as guide to the eye.

Combining our DSC stability results (Fig. 5.3.0.1) with our scattering results and analysis the volume fractions of folded protein in fractal-like clusters and inter-cluster region can be shown as a function of the ΔG_{un} in the presence and absence of maltose (Fig. 5.4.0.4). Immediately a striking difference in the volume fraction of single clusters can be seen, where in the absence of maltose an increase in volume fraction of a cluster is observed with decreasing ΔG_{un} , in contrast to samples in the presence of maltose which exhibit no significant change in the cluster volume fraction as the ΔG_{un} is changed. These trends mirror those observed in the fractal dimension i.e. an increase in cluster density with decreasing global thermodynamic stability, except in the presence of enhanced local mechanical stability. This supports our suggestion that the global thermodynamic stability plays a key role in governing the architecture of the fractal-like clusters of chemically cross-linked folded protein. In juxtaposition to this the local mechanical stability of the building block plays a more conservative role, preserving the morphology of the fractal-like clusters.

These distinct roles of each stability are clear to see from figure 5.4.0.4a, especially if we consider the points at $\Delta G_{un} \approx 38$ kJ/mol, 35 kJ/mol and 30 kJ/mol. At 38 kJ/mol the cluster volume fractions are approximately equal in the absence and presence of maltose, however as ΔG_{un} is lowered they begin to diverge: at 35 kJ/mol the volume fraction of the clusters in both cases remain within error of each other; once ΔG_{un} drops to 30 kJ/mol the volume fraction of clusters in the absence and presence of maltose completely diverge from one another, with clusters becoming denser in the absence of maltose and remaining the same density in the presence of maltose. These results demonstrate the preservation effect that local mechanical stability has on the architecture of the fractal-like clusters of cross-linked folded protein against the morphology changes caused by the building block thermodynamic stability.

Interestingly, the preservation effect of enhanced mechanical stability is not observed in the architecture of the connecting inter-cluster region. Figure 5.4.0.4b shows how the volume fraction of folded protein in the inter-cluster region varies as a function of ΔG_{un} in the presence and absence of maltose. As the thermodynamic stability of the building block is reduced the volume fraction of the inter-cluster region increases, however a larger increase is observed in the presence (increase of 0.8% from 2.5% at $\Delta G_{un} \approx 48$ kJ/mol to 3.3% at $\Delta G_{un} \approx 30$ kJ/mol) than in the absence (increase of 0.3% from 1.8% at $\Delta G_{un} \approx 38$ kJ/mol to 2.1% at $\Delta G_{un} \approx 22$ kJ/mol) of maltose, meaning that the conservative effect of enhanced mechanical stability on preserving the cluster architecture is not also exhibited in architecture of the inter-cluster region. These results also show that samples in the presence of maltose have a more dense inter-cluster region compared with equivalent samples in the absence of maltose (e.g. at $\Delta G_{un} \approx 38$ kJ/mol $\phi_{ic} = 2.95 \pm 0.07\%$ in presence and $\phi_{ic} = 1.8 \pm 0.3\%$ in the absence of maltose), which is likely due to the enhanced mechanical stability of MBP in the presence of maltose allowing the protein in the inter-cluster region to resist the internal gelation force originating from swelling of the system. This result is consistent with the results of the structural study in chapter 4, which found that hydrogels formed from the natively mechanically reinforced BSA had denser inter-cluster regions compared

with hydrogels constructed from the unreinforced BSA. The increase in the density of the inter-cluster region with decreasing ΔG_{un} could be driven by the morphology, density and size of the fractal-like cluster i.e. as the cluster size shrinks more protein is required to cross the inter-cluster region and link the clusters together, leading to an increase in the volume fraction of the inter cluster region. If this explanation is the case then the invariance of the cluster density in the presence of maltose, along with the shrinking cluster size with decreasing ΔG_{un} , could explain why gels in the presence of maltose exhibit a larger increase in ϕ_{ic} with decreasing ΔG_{un} . As the cluster size is reduced, more protein must be excluded from clusters in order to preserve the cluster density, hence leaving more protein in the inter-cluster space compared to hydrogels in the absence of maltose in which the cluster density increases with decreasing ΔG_{un} leading to comparatively less protein in the inter-cluster space. The results of this analysis are consistent with the suggestion that ΔG_{un} governs the morphology and size of the fractal-like clusters while the enhanced mechanical stability helps to preserve the morphology of the clusters in the protein network. Furthermore, this volume fraction analysis show that this control on the fractal-like cluster's morphology and properties has knock-on effect and leads to changes in the architecture of the connecting inter-cluster region. By combining our structural analysis in this study with previous observations [135, 136] (Fig. 3.3.0.2 and 4.3.1.5) we are able to construct a model for how the structural properties of folded protein hydrogel networks are affected by both building block thermodynamic and mechanical stabilities.

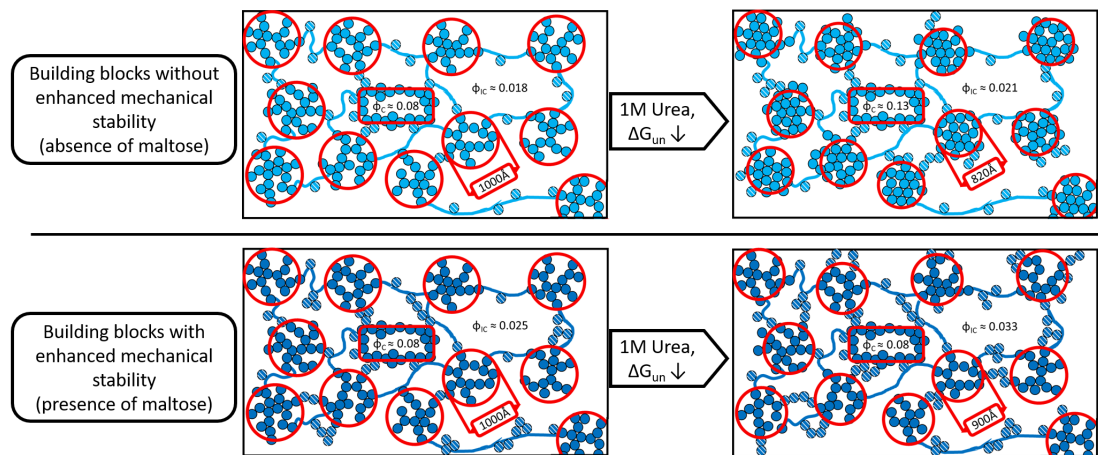


Figure 5.4.0.5: Schematics showing the predicted structural model of MBP hydrogels in the absence (light blue) and presence of maltose (dark blue) and the structural changes that occur as the thermodynamic and mechanical stabilities of the MBP building block are altered. Where solid circles represent folded protein in fractal-like clusters (highlighted by red rings) of volume fraction, ϕ_c , and striped circles represent folded protein in the connecting inter-cluster region of volume fraction, ϕ_{ic} . Blue lines represent unfolded protein in the system as a result of force-induced unfolding during gelation.

Previously we have proposed a structure for folded protein hydrogels constructed from MBP and other force labile proteins (Fig. 3.3.0.2) which consists of fractal-like clusters of chemically cross-linked folded protein connected by an inter-cluster region populated by folded and unfolded protein. By considering this previously determined model as a base, it is possible to construct a new model which accounts for the individual roles and importance of the different building block stabilities which have been demonstrated in this study (Fig. 5.4.0.5).

In this section the global thermodynamic and local mechanical stability of the building block have both been shown to play key but distinct roles in governing the structural properties of protein networks. The thermodynamic stability of the network building block has a more dominant role in governing the architecture, density and size of the fractal-like clusters of folded protein, where decreases in the thermodynamic stability lead to smaller, denser clusters. In contrast, the local mechanical stability of the building block does not change the architecture of the clusters but rather preserves the architecture against alterations due to changes in the thermodynamic stability of the building

block i.e. clusters constructed from mechanically enhanced building blocks do not increase in density upon the lowering of the building block' thermodynamic stability, but still reduce in size. The inter-cluster region architecture is defined as a knock-on effect of the alteration/preservation of the cluster architecture. Although lowering the thermodynamic stability of the building block results in increased density of the inter-cluster region within the hydrogel network, the largest increase in the density of the inter-cluster region is observed in samples with increased building block mechanical stability. This is concurrent with our previous finds in BSA hydrogels (see section 4.3.1.5). Thus, both the thermodynamic and mechanical stability of the network building block play crucial but distinct roles in defining the network architecture from the morphology and size of the clusters of building blocks to the architecture of the inter-cluster region.

5.5 Differential effects of building block thermodynamic and mechanical stability on network bulk mechanics

5.5.1 Effects on linear mechanical behaviour

To investigate the differential effects of protein building block thermodynamic and mechanical stability on the bulk mechanical properties of a cross-linked networks of protein, we employed shear rheology. Pseudo-strain controlled rheology experiments were performed on photo-chemically cross-linked MBP at various concentrations of urea in the presence and absence of maltose.

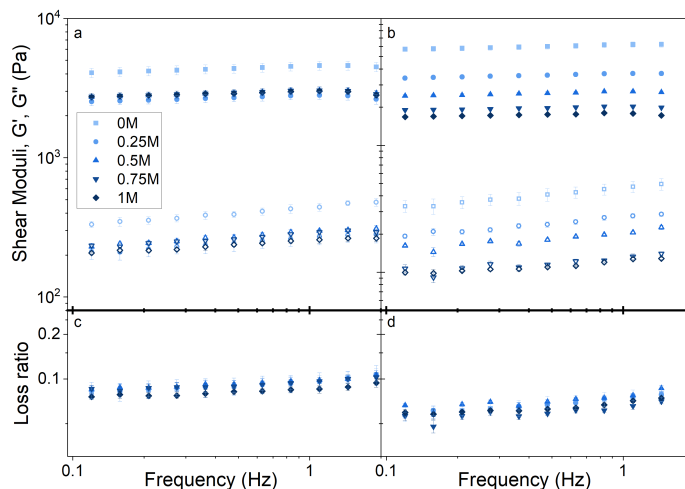


Figure 5.5.1.1: Frequency sweeps showing the (filled) storage, G' , and (open) loss moduli, G'' of chemically cross-linked MBP hydrogels (final concentrations: 100 mg/ml^{-1} MBP, 30 mM NaPS, $100 \mu\text{M}$ Ru(II)bpy_3^{2+}) in the a) absence (left) and b) presence of maltose, as a function of urea concentration. Bottom panels show the loss ratio of MBP hydrogels in the c) absence and d) presence of maltose

Figure 5.5.1.1a,b shows the variation with frequency of the storage, G' , and loss, G'' , modulus, which are the real and imaginary components of the complex shear modulus and describe elasticity and inelasticity of MBP hydrogels, respectively. Both moduli decrease linearly below 1Hz in all samples as the measurement frequency is decreased. The loss ratio for all samples is below 0.1 at all measured frequencies and decreases as frequency approaches zero, demonstrating that the elastic behaviour of the MBP hydrogels is dominant over the viscous behaviour at all relevant time scales. The loss ratio is slightly lower in the presence of maltose indicating an increase in the dominance of elastic behaviour. This is similar to results obtained from BSA hydrogels, where this behaviour was attributed to an increase in the amount of folded protein in the system (see section 4.4.1). Fitting the linear section of the frequency sweeps in figures 5.5.1.1 allows for the extraction of the storage modulus at a frequency of 1Hz. By combining the results of the frequency sweep data with our DSC results (Fig. 5.3.0.1) figure 5.5.1.2 is obtained, showing how G' at 1 Hz varies with the thermodynamic stability of the MBP building block, ΔG_{un} , in the absence and presence of maltose.

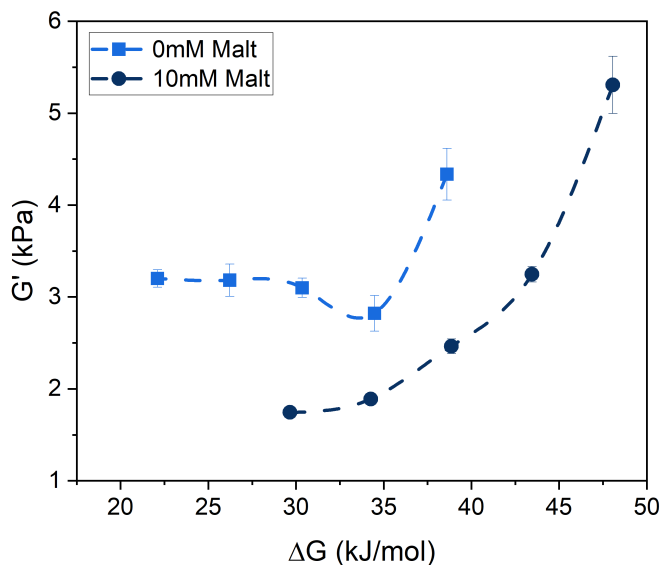


Figure 5.5.1.2: Shear moduli of cross-linked MBP hydrogels extracted from the frequency sweep data in figure 5.5.1.1 at frequency of 1Hz as a function of MBP thermodynamic stability in the absence and presence of 10mM maltose. Dashed lines shown as a guide for the eye.

The curves in figure 5.5.1.2 show that in general, as the thermodynamic stability of the building block is reduced there is a reduction in the storage moduli of MBP hydrogel, in both the absence and presence of maltose, however there is a difference in the trends. In the presence of maltose the G' values decrease continuously with decreasing ΔG_{un} , seemingly down to a plateau (not in the measured range); conversely in the absence of maltose G' does not continue to decrease with ΔG_{un} , but instead inflects (at $\Delta G_{un} \approx 35$ kJ/mol) and increases to a plateau value at $G' \approx 3$ kPa. Furthermore, in the presence of maltose, lower G' values are observed when compared to hydrogels constructed from building blocks of comparable thermodynamic stability (e.g. at $\Delta G_{un} \approx 38$ kJ/mol $G' = 4.3 \pm 0.3$ kPa and 2.46 ± 0.08 kPa in the absence and presence of maltose, respectively). The reduction in G' with decreasing ΔG_{un} suggests that the thermodynamic stability of the building block governs the overall strength of the network, i.e. as the thermodynamic stability of the building block is reduced so is the storage modulus of the hydrogel network. In contrast, the reduction in G' in the presence of maltose suggests that increased mechanical stability of the building block results in a mechanically weaker

network overall. This interpretation initially appears counter-intuitive, as previous work has suggested that increasing the stability of the building block results in a more rigid network (chapter 3). However this behaviour is similar to that observed in BSA hydrogels in the absence and presence of DTT (Fig. 4.4.1.1) in which hydrogels constructed from the natively mechanically reinforced BSA exhibited lower storage moduli when compared to hydrogels constructed from unreinforced BSA. This result was attributed to a decrease in the amount of unfolded protein in the inter-cluster region of the network and by extension a reduction in the number of cross-links formed between unfolded protein strands. The CD data confirms that there is a 3% increase in the amount of folded MBP in hydrogels containing 10 mM maltose (Fig. 3.2.2.3) implying that the reduction in G' as a result of increased building block mechanical stability is likely due to a similar mechanism as observed in BSA hydrogels. So the results in figure 5.5.1.2 suggest that the thermodynamic stability plays a direct role in governing the mechanical strength of the overall network, while the mechanical stability plays a more conservative role in preserving the integrity of the folded protein building block thereby indirectly affecting the mechanical properties of the network e.g. by altering the unfolding of protein in the network. This role of building block mechanical stability was similarly observed in the structural data presented in this study. The difference in trends of G' with building block thermodynamic stability in the absence and presence of maltose can be explained by considering these distinct roles of each type of stability. In the absence of maltose the structural integrity of the folded protein building block is not as strongly preserved due to the lack of enhanced mechanical stability. In turn, this could lead to more rapid unfolding of the building block during the early stages of gelation, as ΔG_{un} is decreased and less energy is needed to unfold the building block. This more rapid unfolding of the building block protein during the early stages of gelation, could result in protein unfolding occurring in unfavourable positions early in the network formation thus resulting in an increase in entanglement of unfolded protein strands and by extension an increase in the storage moduli. To investigate the possibility that more rapid unfolding of the building block occurs in the absence of maltose occurs and causes excessive entanglement in the system, the gelation curves of MBP hydrogels are analysed at varying urea concentrations in the absence and presence of maltose.

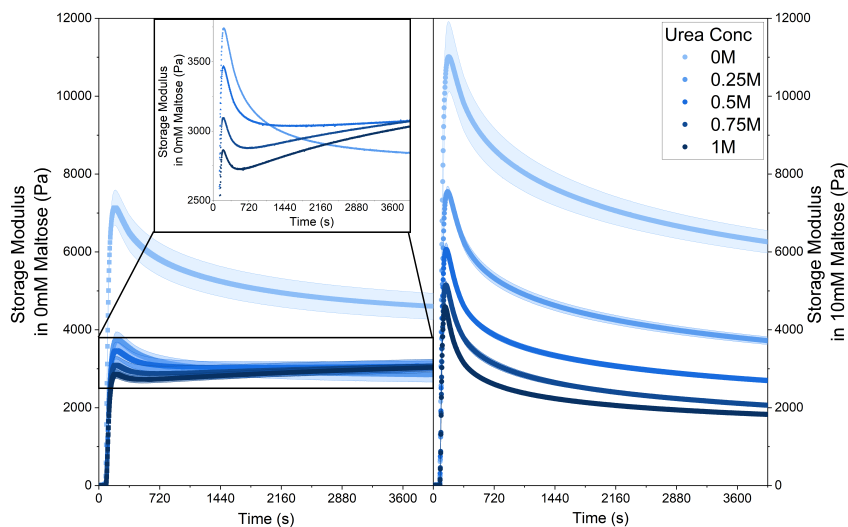


Figure 5.5.1.3: Gelation curves of MBP hydrogels (100mg/ml MBP, 30mM NaPS and $100\mu\text{M Ru(II)bpy}_3^{2+}$), depicting the evolution of G' as a function of time in the absence (left) and presence (right) of maltose at various urea concentrations. (insert) Magnification of the boxed section, with the error bar ribbon removed for clarity. G' values were recorded every 3s at 0.5% strain and a frequency of 1Hz.

The gelation curves (Fig. 5.5.1.3) show the evolution of the shear modulus (G') during the formation of MBP hydrogels at various urea concentrations in the absence and presence of maltose. Without the addition of urea, the gelation curves show the expected profile of initial sharp increase in G' followed by slow relaxation down to a plateau value, with great values of G' observed in the presence of maltose, in agreement with our previous work on MBP hydrogels [135]. The end point G' values observed from the gelation curves are consistent with those observed from frequency sweep measurements (Fig. 5.5.1.2). Interestingly, in the absence of maltose the gelation profile deviates from the standard profile (i.e. initial sharp increase followed by slow relaxation) to a more complex profile, as the concentration of urea is increased. This deviation in the gelation profile in the absence of maltose is greatest at 1M urea and can be described as a sharp increase followed by a more rapid relaxation and ending with slow exponential increase up to the final plateau value of G' . In contrast, though a decrease in G' values is observed with increasing urea concentration, the gelation of MBP in the presence of maltose shows

no significant alteration of the gelation curve profile regardless of urea concentration. The change in the relaxation behaviour with increasing urea concentration in the absence of maltose, from reducing G' with time to increasing G' with time, is indicative of additional cross-links forming over time. This change in gelation profile is what would be expected if the relaxation mechanism shifted to being dominated by entanglement of unfolded protein, with additional physical cross-links forming overtime. In order to analyse these complex kinetic profiles in more detail we fitted a previously used empirical equation to these data sets (Eqn 3.4.0.1).

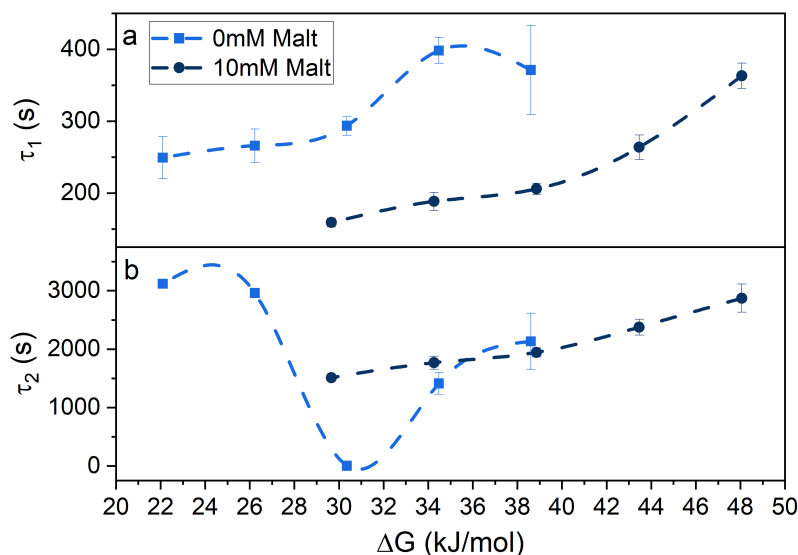


Figure 5.5.1.4: Relaxation time constants of the first and second relaxation mode, τ_1 (top) and τ_2 (bottom) extracted from the gelation curves in figure 5.5.1.3 as a function of MBP thermodynamic stability, in the absence (light blue) and presence (dark blue) of maltose. Dashed lines shown as a guide for the eye.

Fitting the gelation curves with this function allows the extraction of several key parameters related to the relaxation behaviour including the time constants of the relaxation modes, τ_1 and τ_2 and the relaxation coefficients of these modes, B_1 and B_2 . In previous work [135] we have attributed the shorter, first relaxation mode to the rearrangement of the network immediately post-photo-chemical cross-linking and demonstrated that the longer second relaxation mode is due to the unfolding of the protein building block. Figure 5.5.1.4 shows how these time constants vary with ΔG_{un} : in both the

absence and presence of maltose a reduction in τ_1 is observed with decreasing thermodynamic stability. This reduction suggests faster network rearrangement, possibly due to a softer overall network as a result of the less thermodynamic stable building block, allowing for easier relaxation of the network. This interpretation is consistent with the shear moduli values observed in figure 5.5.1.2 i.e. weaker hydrogels exhibit faster network rearrangement timescales.

Similar to τ_1 a reduction in τ_2 is observed for decreasing ΔG_{un} suggesting an increased rate of protein building block unfolding, but importantly only for hydrogels in the presence of maltose (i.e. enhanced building block mechanical stability). Samples in the absence of maltose exhibit a more complex ΔG_{un} dependency for τ_2 , where initially a reduction in τ_2 with decreasing ΔG_{un} is observed, with τ_2 values in good agreement with those observed in the presence of maltose (i.e. at $\Delta G_{un} \approx 38$ kJ/mol $\tau_2 = 2100 \pm 500$ s (absence) and 1900 ± 100 s (presence) and at $\Delta G_{un} \approx 34$ kJ/mol $\tau_2 = 1400 \pm 200$ s (absence) and 1700 ± 100 s (presence)). This indicates that it is the thermodynamic stability that governs the unfolding rate of the protein building block. However, this consistency of τ_2 in the absence and presence of maltose is broken: as ΔG_{un} continues to decrease a large drop down to $\tau_2 \approx 5$ s at $\Delta G_{un} = 30.4$ kJ/mol is observed in the absence of maltose; followed by a sharp increase up to ≈ 3000 s as ΔG_{un} is further reduced. This inflection in the ΔG_{un} dependency of τ_2 in hydrogels constructed from MBP with lower mechanical stability (i.e. in the absence of maltose) is suggestive of two regime behaviour: one regime where the post-cross-linking behaviour is dominated by unfolding of the building block and the other where it is dominated by the entanglement of unfolded protein. These results suggest that the thermodynamic stability of the building block governs the unfolding time-scale of the protein building, while the preservation effects of the building block mechanical stability on the protein fold integrity controls the relaxation regime of the system i.e. unfolding dominated or entanglement dominated. If there were such two regime behaviour we would expect to see an inversion of the parity of the coefficient of the second relaxation at low ΔG_{un}^{MBP} .

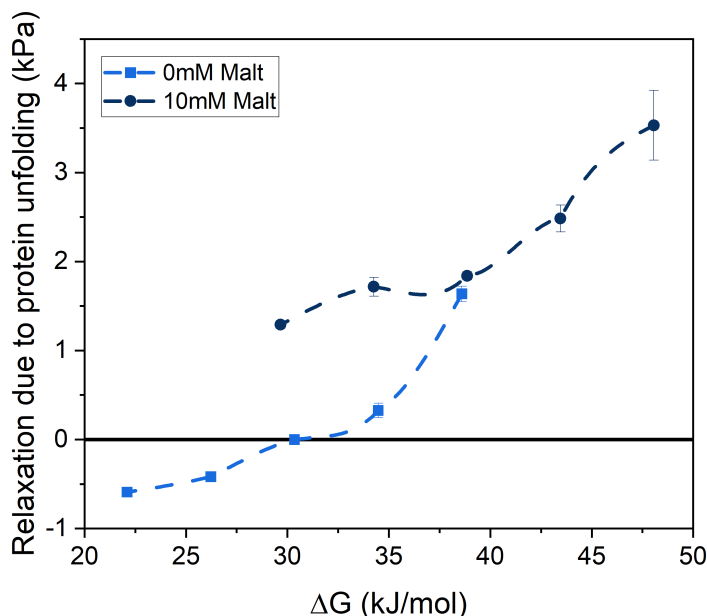


Figure 5.5.1.5: MBP thermodynamic stability dependency of the relaxation coefficient of the second relaxation mode, B_2 , from Eqn. 3.4.0.1, which characterises the reduction in storage modulus as the MBP building block unfolds post-photo-chemical gelation. Dashed lines shown as a guide for the eye.

Figure 5.5.1.5 shows the value for the coefficient of the second relaxation mode, B_2 , which characterises the loss in the storage modulus due to folding of the protein building block post-photo-chemical cross-linking. A reduction in B_2 can be interpreted as a reduction in the amount of protein unfolding that occurs after photo-chemical cross-linking is complete and a simultaneous increase in the amount of protein that unfolds during photo-chemical cross-linking. Initially, it can be seen in both the presence and absence of maltose that B_2 decreases with decreasing ΔG_{un} . This suggests that the loss in G' post-gelation is reduced as the thermodynamic stability of the building block is reduced. Importantly, in the absence of maltose the value of B_2 dips below zero at low ΔG_{un} i.e. the value changes parity. This is what we would expect if the post-gelation relaxation behaviour were to change from being dominated by the unfolding of the MBP building block to be dominated by entanglement of unfolded protein, as suggested by the profile of the gelation curves (Fig. 5.5.1.3) and the analysis of τ_2 (Fig. 5.5.1.4). These results support the interpretation that there is a regime change in the post-

photo-chemical cross-linking reaction from an unfolding dominated to an entanglement dominated regime. Furthermore these results demonstrate that the regime change is driven in part by the thermodynamic stability of the building block but is ultimately controlled by the mechanical stability of the building block. However, this interpretation relies on the assumption that the level of unfolded protein remains constant in the hydrogels as the thermodynamic stability of the protein building block is varied. Our rheology results imply that this assumption holds true, namely the invariance of the loss ratio determined from frequency sweep experiment (Fig. 5.5.1.1c and d) with urea concentration, suggesting no significant change in the unfolded population between samples. In order to support this interpretation further and eliminate the possibility of a reduction in the amount of unfolded protein in the system, load-unload measurements on the MBP hydrogel samples were performed and the efficiency of them analysed.

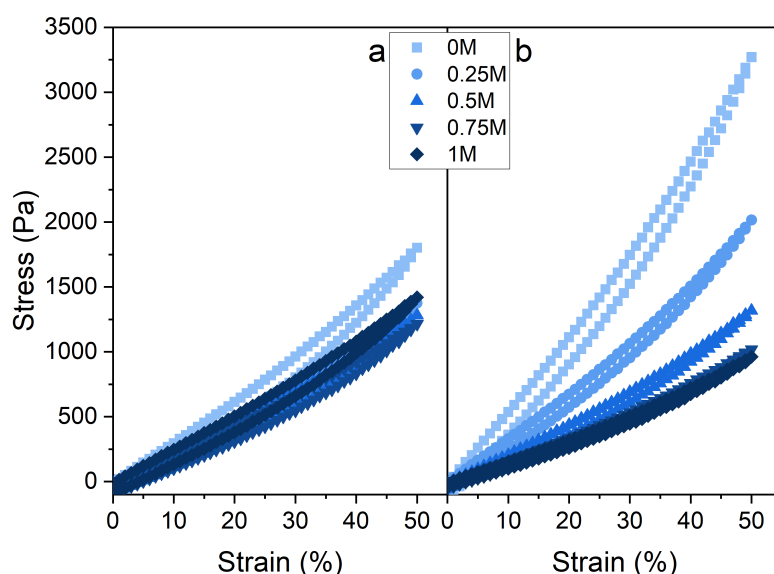


Figure 5.5.1.6: Stress-strain curves of chemically cross-linked MBP hydrogels (final concentrations: 100mg/ml^{-1} MBP, 30mM NaPS, $100\mu\text{M}$ Ru(II)bpy_3^{2+}) in the a) absence and b) presence of maltose as a function of urea concentration. Samples were strained to 50% at a rate of $1\%/s$ and then unloaded down to 0% at the same rate.

All MBP hydrogels exposed to loading up to 50% exhibit linear behaviour up to $\approx 30\%$ followed by slight shear stiffening up to 50% strain regardless of urea concentration or

the presence of maltose. Fitting this linear region and extracting the gradient allows for determination of the storage moduli of the hydrogel samples. The storage moduli extracted via this method are in good agreement with the shear moduli determined by frequency sweep measurements (Fig. 5.5.1.1 and 5.5.1.2) showing similar values and trends with respect to ΔG_{un} in the presence and absence of maltose. Upon unloading back to 0% strain, all samples display prominent hysteresis behaviour, the area of which is indicative of the energy dissipated to the internal energy of the system. Figure 5.5.1.6 shows that the hysteresis decreases with increasing urea concentration regardless of the presence of maltose, This suggests a reduction in the energy dissipated in all hydrogels in the presence of increasing urea. The area enclosed by the hysteresis can be extracted and gives quantitative measure of the energy dissipated by the hydrogel system in the load-unload cycle (Fig. 5.5.1.7a).

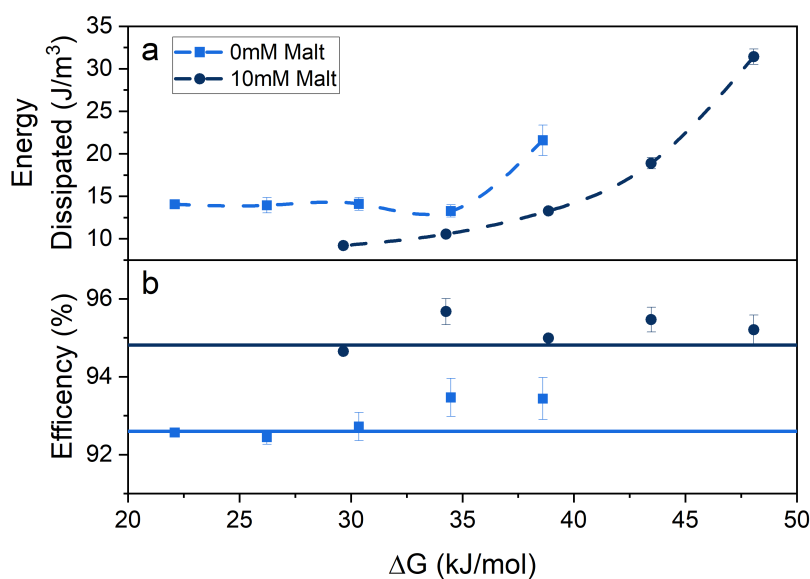


Figure 5.5.1.7: a) Energy dissipation and b) efficiency during load–unload cycle of MBP hydrogels in the absence (light blue) and presence (dark blue) of maltose as a function of MBP thermodynamic stability. Solid lines represent average fits to the efficiency data in the absence and presence of maltose. Dashed lines shown as a guide for the eye.

Once again by combining the rheology and DSC results (Fig. 5.3.0.1) we obtain the extracted values for the energy dissipation of MBP hydrogels, as a function of the

thermodynamic stability in the absence and presence of maltose (Fig. 5.5.1.7). In the absence of maltose a decrease in the energy dissipated down to a plateau value of approximately 14 J/m^3 is observed with decreasing thermodynamic stability. Similarly in the presence of maltose there is a decrease in the energy dissipated as ΔG_{un} is reduced, except that a plateau value is not observed in the measured range. As stated previously, in folded protein hydrogels the main source of energy dissipation is thought to be force-induced unfolding of the protein building block [120, 129], where less energy is required to unfold the less thermodynamically stable MBP building block. In chapter 4 another source of energy dissipation in folded protein hydrogels was identified, namely the level of unfolded protein present in the hydrogel network. It is important to consider each of these sources of energy dissipation as both are relevant in explaining the changes in the energy dissipation behaviour observed in MBP hydrogels when the thermodynamic and mechanical stability of the building block are altered. The energy dissipated by MBP hydrogels in both the absence and presence of maltose is reduced as the thermodynamic stability of the MBP building block is reduced (Fig. 5.5.1.7a) likely due to a decrease in the energy necessary to unfold individual protein building blocks. In the presence of maltose lower energy dissipation is observed, this is likely due to a lower level of unfolded protein present in the network when the mechanical stability of the building block is enhanced (consistent with observations of BSA hydrogels made in chapter 4 of this work). A plateau is observed in the absence of maltose (Fig. 5.5.1.7a), possibly be due to the shift of the post-gelation relaxation behaviour from the unfolding-dominated region to the entanglement-dominated regime, leading to larger losses of internal energy to the unfolded protein strands due to the additional physical cross-links from entanglements. In general, decreasing the thermodynamic stability of the building block results in protein networks with reduced energy dissipation due to a lower amount of energy required to unfold the protein building block. Similarly enhancing the mechanical stability results in lower energy dissipation due to a reduction in the level of unfolded protein present in the network.

As well as giving information on the energy dissipation, the hysteresis area, combined with the max stress values of the stress-strain curves (Fig. 5.5.1.6), can be used to

determine the efficiency of the MBP hydrogels using equation 3.2.2.1, shown as a function of ΔG_{un} in the presence and absence of maltose in figure 5.5.1.7b. As previously stated, the efficiency is a measure of the ability of the folded protein based hydrogel to return the energy input in straining it and is inhibited by two main mechanisms: i) the number of force-induced unfolding events of the protein building block taking place to accommodate the strain and ii) the level of unfolded protein in the system. The efficiency of MBP hydrogels in the absence and presence of maltose are fairly consistent across all ΔG_{un} values. It should be noted that hydrogels in the presence of maltose exhibit a higher level of efficiency than those in the absence, suggesting a higher level of folded protein, which is consistent with previous CD measurements on MBP hydrogels (Fig. 3.2.2.3) showing that there is approximately 3% more folded protein in the presence of 10 mM maltose. The invariance of the efficiency within each subset (i.e. in the absence and presence of maltose) suggests that the number of protein unfolding events that are occurring to accommodate strain and the level of unfolded protein are both not changing with respect to the ΔG_{un} . This result suggests that the level of unfolded protein remains constant as ΔG_{un} is changed. This supports the interpretation that the observed reduction in the level of post-photo-chemical cross-linking relaxation is not due to a lower the amount of unfolded protein in the system. Instead rapid unfolding of the protein building block during the photo-chemical cross-linking process, which in turn leads to increased entanglement of the unfolded protein strands and a regime change in the post-cross-linking relaxation behaviour.

Characterisation of the linear mechanics of MBP hydrogels in varying concentrations of urea and in the absence and presence of maltose, has given insight into the roles of the building block thermodynamic and mechanical stabilities. Both the thermodynamic and mechanical stabilities play key but distinct roles in governing the strength, energy storage and relaxation behaviours of folded protein hydrogels. The global thermodynamic stability of the building block plays a direct role in governing the rigidity and energy dissipation behaviour of the hydrogel network, i.e. lower building block thermodynamic stability results in hydrogels with lower storage moduli and decreased energy dissipation.

Furthermore, the thermodynamic stability of the building block governs the post-photochemical cross-linking rate of relaxation due to the unfolding of the protein building block and drives the regime change in the relaxation from an unfolding-dominated regime to an entanglement-dominated regime.

In contrast, the local mechanical stability of the building block protein plays a more indirect role in defining the network's mechanical properties. This indirect role is a consequence of the local mechanical stability preserving the integrity of the folded protein building block during gelation. Hydrogels, constructed from building blocks with enhanced mechanical stability, exhibit lower mechanical rigidity and energy dissipation behaviour compared to hydrogels constructed from building blocks that lack enhanced mechanical stability but equivalent thermodynamic stability. This counter-intuitive result is attributed to a reduction in the amount of folded protein in the system and by extension a reduction in the number of cross-links between unfolded protein strands in the inter-cluster region of the network, similar to what is observed in BSA hydrogels in the presence and absence of DTT (chapter 4). Interestingly, while the mechanical stability of the building block does not alter the rate of relaxation due to unfolding, it is the limiting factor in the relaxation regime switching from being dominated by protein unfolding to being dominated by the entanglement of unfolded protein strands.

5.5.2 Effects on non-linear mechanical behaviour

Finally, as biological hierarchical networks are well-documented to exhibit interesting non-linear mechanical characteristics, we also investigate the effects of global thermodynamic and local mechanical stability on the non-linear behaviour of photo-chemically cross-linked MBP hydrogels at varying urea concentrations in the absence and presence of maltose.

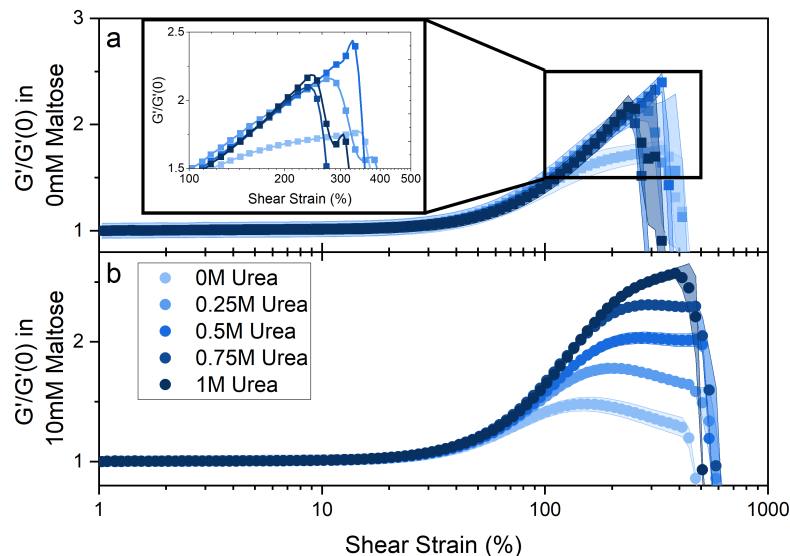


Figure 5.5.2.1: Strain amplitude ramps showing the normalised storage moduli of MBP hydrogel in the a) absence and b) presence of maltose as a function of urea concentration. The measurement frequency was set to 1 Hz. Values are normalised to the G' values extracted from the frequency sweep data (Fig. 5.5.1.2). (inset) Magnification of the boxed region with the error ribbon removed for clarity, solid lines added as guide to the eye.

Figure 5.5.2.1 shows strain amplitude ramps of MBP hydrogels as a function of urea concentration in the absence and presence of maltose. The curves show that these gels exhibit linear mechanical behaviour up to $\approx 30\%$ strain, before beginning to strain stiffen, in good agreement with the results of the stress-strain measurements (Fig. 5.5.1.6). At strains in excess of 50% interesting, non-linear mechanical behaviour is exhibited by MBP hydrogels in the both the absence and presence of maltose. The curves also show that all hydrogels exhibit rupture at high strain values, with hydrogels in the presence of maltose exhibiting higher rupture strain values ($\approx 600\%$), compared to those in the absence ($\approx 350\%$). Hydrogels in the absence of maltose show a maximum strain stiffening in the range of $\approx 1.5x$ to $2x$ $G'(0)$ as the concentration of urea is varied; with a similar range of maximum strain stiffening observed in the presence of maltose ($1.5x$ to $2.5x$ $G'(0)$). Furthermore, the profiles of shear stiffening are reasonably similar without the addition of urea, exhibiting strain stiffening up to $\approx 1.5x$ before breakage. Notably, while samples in the absence of maltose and urea shear stiffen continuously

until rupture, the addition of maltose causes the hydrogels to instead undergo shear softening before rupture. This is an interesting difference between apo- and bound-MBP hydrogels which was overlooked in our initial study using MBP hydrogels (chapter 3). This strain-weakening at high strains is possibly due to the unbinding of maltose from MBP. Under high strain the additional hydrogen bonds across the ‘mouth’ of MBP (Fig. 3.1.2.1 and 3.1.2.2) could break, leading to the unbind of maltose. Once the maltose unbinds the mechanical and thermodynamic stability of MBP is reduced back to its apo-state, which results in a decrease in the rigidity of the work and the apparent shear weakening behaviour in MBP hydrogels in the presence of maltose at high strains. Another possible mechanism for the shear softening before rupture stems from structural differences in the inter-cluster region between MBP hydrogels in the absence and presence of maltose i.e. MBP hydrogels exhibit denser inter-cluster regions in the presence of maltose compared to those in the absence. This increased population of folded protein in the inter-cluster region of MBP hydrogels will likely unfold in order to accommodate the high strain placed on the system. As the protein in the connecting inter-cluster region unfolds, it reduces the number of rigid building blocks connecting the clusters which will eventually result in a weakening of the hydrogel. While this is also likely to happen in hydrogels in the absence of maltose, the reduced density of folded protein in the inter-cluster region of these gels and increase level of unfolded protein in the system means less protein will undergo unfolding to accommodate the strain and so its effects are less likely to be measurable before rupture. Experimentally it is difficult to determine between these two possible mechanism. It would be possible to investigate these mechanisms using combined rheology SAXS (rheo-SAXS) experiments and cross length-scale computational modelling that accurately captured binding kinetics and the unfolding of protein domains.

Upon addition of urea to these systems the similarities seen between the strain profiles is removed. Figure 5.5.2.1a shows the difference in strain profiles of MBP in the absence of maltose when urea is added to the system. The addition of urea to apo-MBP hydrogels (in the absence of maltose) results in a almost binary switch from the strain profile described above to a profile more similar to a power law increase in G' until

rupture. This profile is exhibited by all apo-MBP hydrogels that contain urea, with no discernible trend in gradient or rupture strain. This change in the strain profiles suggests some threshold thermodynamic stability below which there is a regime change. This regime change could be similar to the regime change observed in the linear mechanical characterisation (see section 5.5.1), where the relaxation behaviour switches from being dominated by unfolding of the protein building block to dominated by the entanglement of the unfolded protein strands. If this is the case then, similar to the linear mechanical measurements, we would expect very different non-linear behaviour exhibited from MBP hydrogels as the urea concentration is increased in the presence of maltose compared to those in the absence. Indeed, strikingly different non-linear behaviour is observed as the urea concentration is increased. In the presence of maltose the general shape of the strain profile of the hydrogel is preserved, however there is still an increase in the level of shear stiffening of the network as the urea concentration is increased. The increase in the level of shear stiffening suggests that the thermodynamic stability of the building block plays a rather counter-intuitive role in governing the shear stiffening behaviour, i.e. as the thermodynamic stability is decreased the level of shear stiffening is increased. However, a more likely explanation is obtained by considering the volume fraction of folded protein in the inter-cluster region. Figure 5.4.0.4b shows that as the thermodynamic stability of MBP decreases in the presence of maltose, the density of the inter-cluster region increases, meaning there is more folded protein linking the clusters together. This can be interpreted as more ‘springs’ in the system that are pulled on as the slack in the system is removed under strain, resulting in higher levels of strain stiffening. So, lower thermodynamic stability of the protein building block results in hydrogels with increased levels of shear stiffening. On the other hand, enhanced building block mechanical stability leads to hydrogels with interesting non-linear strain profiles, with gels exhibiting both strain stiffening, then strain weakening before rupture. These results show that folded protein-based hydrogels exhibit interesting non-linear mechanical behaviour and demonstrate that by controlling the thermodynamic and mechanical stability of the building block it is possible to tune the non-linear mechanical properties of the hydrogel network. We have suggested mechanisms to explain the dependencies of the non-linear properties of the hydrogel on the thermodynamic and mechanical stabilities

of the building block (Fig. 5.5.2.1). However, further experimentation beyond the scope of this work is required, in particular Rheo-SAXS and cross-length scale computational modelling to understand how the structure is altered at high strains.

5.6 Conclusion

Utilising MBP-based hydrogels, this chapter has demonstrated that both the thermodynamic and mechanical stability of the network building block have key but distinct roles in governing the structural and mechanical properties of the network. The study in this chapter shows that the global thermodynamic stability of the building block translates more directly to the mechanical and structural properties of the network; while the local mechanical stability of the building block preserves the integrity of the folded protein building block which causes knock-on effects that indirectly lead to changes in the structural and mechanical properties of the network.

The thermodynamic stability of the building block directly governs the overall strength of the hydrogel network and the energy dissipation behaviour, i.e. reduced thermodynamic stability of the building block results in a network with reduced mechanical strength (lower storage moduli) and lower energy dissipation. This dependency is attributed to a lower amount of energy needed to strain or unfold the protein block, which would result in a softer network and less energy dissipated due to unfolding. Furthermore, the thermodynamic stability governs the relaxation behaviour due to protein unfolding, with hydrogels constructed from thermodynamically less stable protein exhibiting faster relaxation behaviour. This faster relaxation is due to unfolding becoming more likely because less energy is required to unfold the protein building block. Interestingly, the thermodynamic stability of the building block drives the post-gelation regime change from an unfolding dominated regime to an entanglement dominated one. This regime change is likely due to large amounts of protein unfolding occurring during the photo-chemical cross-linking process, leading to large amount of unfolded protein distributed more randomly throughout the network resulting in entanglements forming during the relaxation of the network. Though this interpretation relies on the assumption

that the level of unfolded protein in hydrogels in the absence and presence of maltose does not vary as a function of thermodynamic stability. While no direct evidence of the level of unfolded protein in hydrogels has been taken, there is plenty of suggestive evidence (i.e. the invariance of the loss ratio and efficiency of the hydrogels as the thermodynamic stability of the building block is altered) that supports the assumption that the level of unfolded protein in the apo- and bound- MBP gels is constant as the thermodynamic stability is lowered. In order to eliminate the possibility of a larger amount of unfolded protein in the hydrogels as the thermodynamic stability is lowered, CD measurements should be performed on the apo- and bound-MBP hydrogels.

The mechanical stability of the building block plays a more indirect role in governing the mechanical properties of the hydrogel network, often producing counter-intuitive results. These effects seem to stem from the apparent conservation effect of enhanced mechanical stability on preserving the integrity of the folded protein building block. For example, hydrogels constructed from protein with increased local mechanical stability exhibit lower storage moduli than those constructed from protein lacking mechanical enhancement. This result is similar to what has been observed in BSA hydrogels in the absence and presence of DTT. In fact, many of the results of hydrogels constructed from MBP with enhanced mechanical stability (i.e. in the presence of maltose) are similar to the results of BSA hydrogels (chapter 4). The similarity between these two systems suggests that the root cause of the behaviour is the same in both cases. In chapter 4 the difference in behaviour is attributed to a lower level of unfolded protein, forming cross-links in the inter-cluster region. CD results in chapter 3 (Fig. 3.2.2.3) show that there is a 3% decrease in the level of unfolded protein in MBP hydrogels in the presence of maltose, suggesting that this is the right interpretation of the data presented here. So it can be seen that the change in hydrogel properties was not a direct result of the increased mechanical stability of the building block but rather a downstream consequence of such an enhancement of the building block i.e. a change in the level of unfolded protein and cross-linking in the inter-cluster region. Another example of this mechanism is the relaxation behaviour of MBP hydrogels. While it is the thermodynamic stability that drives the regime change in the relaxation behaviour

it is ultimately limited by the local mechanical stability. Building blocks with enhanced mechanical stabilities (in the presence of maltose) do not exhibit this two-regime behaviour, due to the conservative effects of enhanced mechanical stability has on preserving the integrity of the protein folded structure.

The structural results in this chapter concur with previous structural characterisation of MBP hydrogels, suggesting that MBP hydrogels are constructed from fractal-like clusters of cross-linked folded protein which are linked together by a connecting inter-cluster region populated by folded and unfolded protein. The thermodynamic and mechanical stabilities of the building block have crucial roles in altering and defining the structure of folded protein hydrogels. The thermodynamic stability of the network building block affects the morphology, density and size of the fractal-like cluster, with lower thermodynamically stable building blocks leading to smaller denser clusters. This could be due to the fact that protein on the edges of the clusters more readily unfold, shrinking the cluster radius and leaving the denser core of the fractal-like cluster. Conversely the mechanical stability plays a role in preserving the morphology of the fractal-like clusters i.e. the density and morphology of clusters constructed from building blocks with enhanced mechanical stability is invariant with respect to thermodynamic stability. Although the cluster size still decreases with decreasing thermodynamic stability. Interestingly, bound-MBP hydrogels exhibited increase density of the inter-cluster region as the thermodynamic stability of the building block is reduced. Previously published work by Del Gado et al. [215, 216] and Furst et al. [217], demonstrated theoretically and experimentally, that the arrangement and linking between clusters in colloidal glass systems, is the dominant factor in defining the mechanics of the network. The work of Del Gado et al. and Furst et al. suggests that hydrogels with higher density of protein in the inter-cluster region should exhibit a higher storage moduli, however the opposite is observed. Bound-MBP hydrogels show decreasing G' values with decreasing thermodynamic stability, despite an increase in the density of folded protein in the inter-cluster region of the network. The results of this chapter suggests that the view that only the architecture of the inter-cluster region governs the mechanical behaviour of the network

may be too simplistic to describe networks constructed from complex building blocks with intrinsic properties and stabilities, such as folded protein networks.

In order to understand how the thermodynamic and mechanical stabilities of the building block lead to alterations in the hydrogel network structures observed in this chapter, the formation process of folded protein hydrogels must be understood. To gain insight into the hydrogel network formation, multiple additional experiments would be required including: rapid frame acquisition SAXS and computational modelling of hydrogel formation that accurately captures the unfolding process *in situ*. Such additional measurements would also help to elucidate the regime change in the relaxation behaviour from unfolding dominated to entanglement observed in apo-MBP hydrogels with reduced thermodynamic stability.

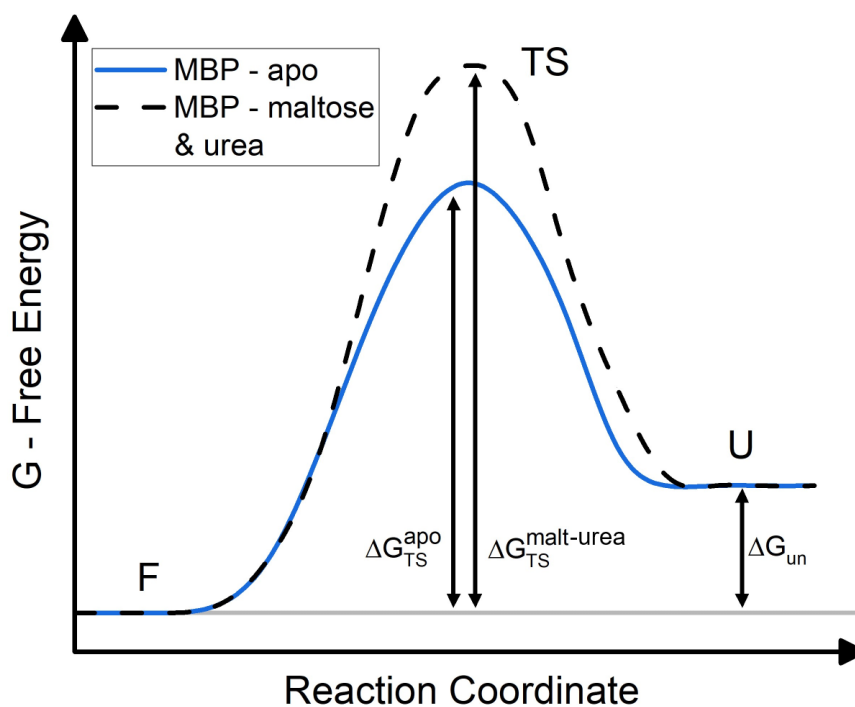


Figure 5.6.0.1: Schematics of an energy landscape of a two-state unfolding pathway of MBP (in both its apo-state (solid light blue) and in its bound-state in the presence of urea (dashed dark blue)) from the folded state (F) to the unfolded state (U) through a transition state (TS). Where ΔG_{un} is the difference in free energy between the folded and the unfolded state. Similarly ΔG_{TS}^{apo} and $\Delta G_{TS}^{malt-urea}$ are the difference in free energy between the folded and the transition state in the absence of maltose and urea and the other in the presence of both.

Finally, based on the results and analysis of our combined structure and mechanical characterisation approach, we propose a model for the underlying mechanism by which the thermodynamic and mechanical stabilities of the network building block exhibit such distant defining roles on network properties. Figure 5.6.0.1 shows a schematic of a free energy landscape, of a simple two-state unfolding transition from the folded state (F) and to the unfolded state (U), of apo-MBP and bound-MBP in the presence of urea. For the purposes of simplicity it is being assumed that MBP undergoes two-state unfolding. From the schematic it can be seen that bound-MBP in the presence of urea has the same thermodynamic stability, ΔG_{un} , (the urea concentration necessary to achieve this effect is $\approx 0.5\text{M}$ (Fig. 5.3.0.1) implying that the same amount of energy is required to unfold either protein, so it would be expected that networks constructed from MBP in both these chemical environments would exhibit the same properties. However, this is not what is observed experimentally when apo- and bound-MBP hydrogels have the same ΔG_{un} value, which could be because while ΔG_{un} values are equal, the values for ΔG_{TS} is higher in the presence of maltose. This would suggest a higher energy barrier to overcome in order to unfold, which would slow the rate at which bound-MBP would deform and unfold even compared to apo-MBP of the same thermodynamic stability. This is the proposed origin of the differential effects of the protein building block's thermodynamic and mechanical stability on the properties of the overall network i.e. it is likely that the direct translation of thermodynamic stability to the mechanical properties of the network would be better described as the energy required to deform and/or unfolded the folded protein building block. Likewise, the preservation effects caused by enhanced local mechanical stability, would be more accurately described as an increase in the energy barrier to unfolding. For example, if a single location in the building block is made more stable such that it affects the transition of the building block from a folded to an unfolded state then this would result in an increase in the energy barrier to unfolding rather than a change in the Gibbs free energy of the transition. Na et al. [195] showed that bound-MBP in 0.5M urea had a lower unfolding rate than in the apo state in the absence of urea ($k_{un} = (2.2 \pm 0.8) \times 10^{-8} \text{ s}^{-1}$ in the bound state in 0.5M urea compared to $k_{un} = (6.0 \pm 1.6) \times 10^{-7} \text{ s}^{-1}$ in the apo state in 0M urea). This suggests that despite the equivalent thermodynamic stability there is a higher energy barrier in the bound MBP

than the apo mbp, supporting our proposed model. However in spite of this supportive literature this model remains speculative and further measurements beyond the scope of this work would be necessary to prove it. To confirm this model more work beyond single molecule force spectroscopy of MBP in the presence of both urea and maltose would be required. Additionally experiments performed in this chapter should also be completed with engineered mutant variants of MBP with disulphide staples to provide enhanced local mechanical stability in different areas of the building block and thereby effect the transition pathway in different ways.

Chapter 6

Discussion and Future Work

The results of this thesis, as presented in chapters 3 - 5, have demonstrated that the properties of an individual building block not only effect the collective properties of a network but crucially, define them. In particular this body of work has demonstrated, through a combined structural and mechanical approach, that the intrinsic properties of the building block have significant effects on the architecture and mechanics of hierarchical networks. Furthermore our results suggest that the simplistic view that the properties of a network emerge entirely as result of the density and geometry of cross-linking [215–217, 227–230] is not sufficient to describe the complete behaviour of hierarchical networks in both living systems and novel bio-materials [123, 128, 129, 198, 200]. All of the studies in this thesis have relied upon a combined structural and mechanical characterisation approach and have demonstrated that in order to draw meaningful conclusions about the underlying design principles these techniques must probe multiple length-scales from the nano to the macro. Finally the results of this thesis serve as the basis for powerful design principles to design and construct novel bio-mimetic and bio-inspired materials.

This final chapter summarises the main conclusions and the impact of these results on the understanding of biological hierarchical networks and the development of novel bio-mimetic/bio-inspired materials. The results demonstrating the translation of molecular-level stability to the macro-level mechanics of multi-molecular network are discussed

in section 6.1. The section also highlights the distinct roles of thermodynamic and mechanical stability of the building block on the structural and mechanical properties of the network (section 6.1.1). Section 6.2 details the results that demonstrate the importance of *in situ* unfolding of the protein building block on defining the overall architecture and mechanics of protein hierarchical network. Finally section 6.3 outlines the possible future directions that could be taken in order to expand and extend upon the work presented in this thesis.

6.1 The translation of intrinsic stability of the network building block to the structural and mechanical properties of the network

In chapter 3 the stabilising effect of ligand binding was exploited in MBP-based hydrogels to explore the translation of molecular level stability to the bulk mechanics of a network. Upon the binding of maltose, MBP increases in both thermodynamic and mechanical stability, rheological characterisation of MBP-based hydrogels showed increased storage moduli and energy dissipation with increasing maltose concentration up to a plateau. This result demonstrated that an increase in the molecular-level stability of the building block translates across length scales to the bulk mechanical properties of a hydrogel network. Structural analysis of MBP hydrogels using SAXS and SANS showed that the structure of MBP hydrogels consists of fractal-like clusters connected by an inter-cluster region populated by unfolded protein observed via CD spectroscopy. The measured structure and level of unfolded protein is not observed to change in the presence and absence of maltose providing further evidence that the enhancement of protein stability at the molecular level scales directly to the macroscale.

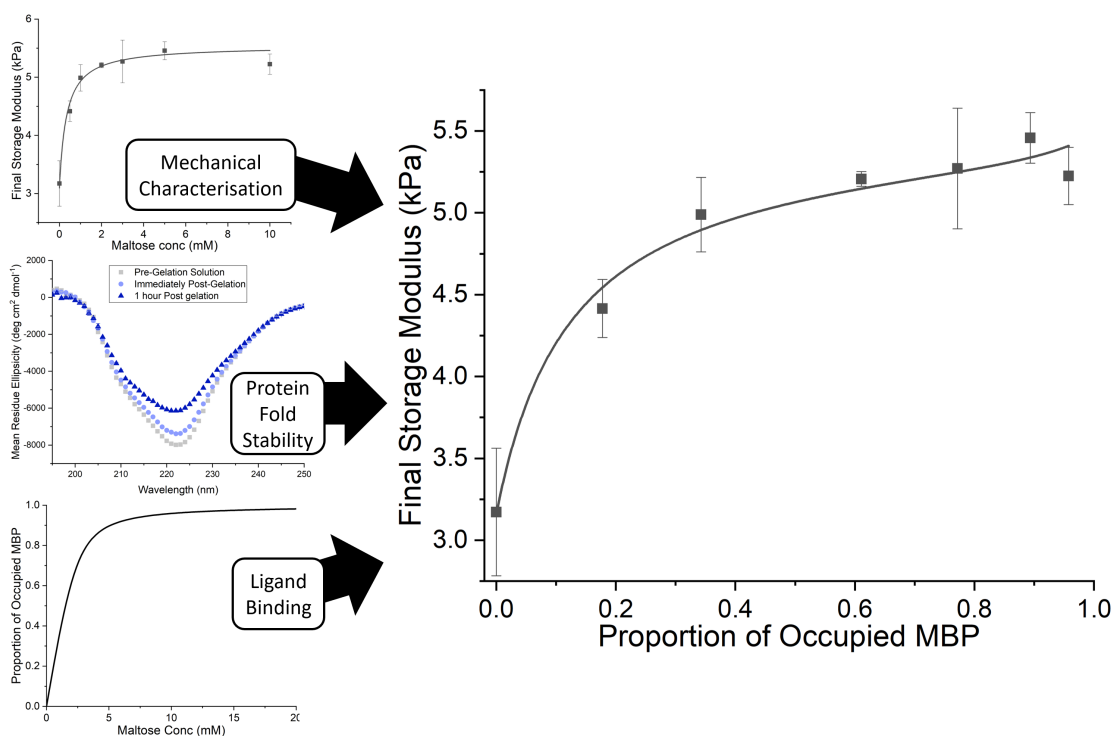


Figure 6.1.0.1: Summary figure of the main results of chapter 3. (left) Combination of mechanical characterisation of MBP-based hydrogels in varying concentrations of maltose (Fig. 3.2.1.1b), protein fold stability measurements (Fig. 3.2.2.3) and ligand binding assays (Fig. 3.2.3.1 and 3.2.4.1(inset)) of MBP *in situ* in varying concentrations of maltose to determine (right) the change in storage moduli of MBP-based hydrogels as a function of proportion of stable and robust maltose ‘occupied’ MBP (Fig. 3.2.4.1).

Combining the rheological mechanical characterisation, structural measurements and DSC ligand binding assays we proposed an occupation model to describe the modulation of the mechanical strength (storage modulus) of the hydrogel network (Fig. 6.1.0.1). In this model the increased concentration of maltose promotes an increase in the proportion of more robust ligand bound MBP which directly correlates to an increase in the storage modulus and energy dissipation of the hydrogel network. Interestingly this modulation of the storage modulus is highly non-trivial, and shows that stabilising only one fifth of the total number of building blocks leads to most significant enhancement in mechanical properties of the network. This result suggests that only a small fraction of the monomers are involved in governing the mechanical properties of the network, the underlying mechanism for this is likely heavily tied into the hierarchical structure of the network. In work by Del Gado et al. [215, 216], on colloidal gels, the mechanics of a

network was demonstrated to emerge as a consequence of connections in the inter-cluster region. Since the structures (and by extension the connections in the inter-cluster) do not change in the presence and absence of maltose, this implies that simply considering the connections in the inter-cluster region is not sufficient to completely describe the emergence of mechanics in a hierarchical network. Furthermore this offers a potential explanation of the non-trivial relationship of the storage modulus with the proportion of ‘occupied’ MBP, namely that the more mechanical robust ‘occupied’ MBP monomers are more likely to be located in the inter-cluster region which results in the significant enhancement of bulk mechanical behaviour are low proportions of occupation (<20%). The process during network formation which promotes more robust ligand MBP to be in the inter-cluster space is as yet unknown and requires investigation, involving both rapid frame acquisition SAXS and computational modelling, to determine and confirm this speculation.

In addition the effects of ligand-mediated molecular-level stabilisation on the kinetic behaviour of hydrogels during formation was investigated. The gelation curves of MBP hydrogels in varying concentrations of maltose showed that there was a post-photo-chemical cross-linking relaxation of the storage modulus. Analysis of these curves with a bespoke empirical equation showed that the relaxation of the hydrogel network consists of two relaxation modes, with one taking approximately 10x longer than the other. Comparing the time constants extracted from rheology to those observed via CD spectroscopy of MBP *in situ* we attributed the faster relaxation mode ($\tau \sim 100\text{s}$) to network rearrangement, and the longer relaxation mode ($\tau \sim 1000\text{s}$) to the unfolding of the protein building block due to the stresses of gelation. As the concentration of maltose is increased i.e. the proportion of more robust ligand-bound MBP is increased, the time constant related to relaxation due to unfolding is also increased, once again demonstrating the translation of molecular-level stability of the building block to the bulk properties of the overall network. It would not be possible to draw these conclusions about the translation of molecular level stability to the bulk mechanical properties without the intense CD characterisation presented in this study. Such characterisation of the folded state of the protein *in situ* is not commonly performed on folded protein

hydrogels reported in the literature, apart from some exceptions[123, 134].

The results presented in chapter 3 show that a simultaneous increase in the thermodynamic and mechanical stability of the protein hydrogel building block results in an enhancement of the mechanical behaviour of the protein network, and reveal that controlling the molecular-level stability of the building block as novel method to tuning the rigidity of a hydrogel network. In contrast, previous methods to modulate the behaviour of hydrogels discussed in section 1.3.1, including using filler particles [100, 101, 105, 106, 196], interweaving a secondary scaffold network [110, 111], etc, all in principle rely on altering the cross-link network within the hydrogel (e.g. altering the density, geometry or strength of cross-links). In classical network theory the shear modulus of a network is proportional to the cross-link density, μ , and thermal energy, k_bT , such that: [231]

$$G = C_0\mu k_bT \quad (6.1.0.1)$$

Where C_0 is a prefactor that depends on the network structure (i.e. dangling ends, trapped entanglements, etc.) which in Flory's affine network model is equal to 1 [227, 228], and equal to $\frac{1}{2}$ in James and Guth's phantom network model [230]. Importantly in these models the mechanical strength of the network is completely dependant on the upon the number of cross-links and their structure. These models imply that any change in the stability of the building block that does not alter the cross-linking network should not result in a change in the mechanical strength of the network. However in this study it has been shown that the shear modulus can be modulated without any alteration to the cross-linking and network structure. Similarly work by Kim et al.[131] demonstrated larger discrepancies between theoretical models and experimental result with hydrogels constructed from rigid building blocks compared to those constructed from flexible building blocks. These results suggest that in order to construct a complete theory linking the building block and network mechanical properties, the stability of the building block must be considered. This is an important step in understanding and, in future, exploiting the translation of building block stability on network behaviour and

opening the door to environmentally responsive hydrogels with many broad applications.

6.1.1 Deconvolution of the distinct roles of building block thermodynamic and mechanical stability in hierarchical protein networks

Despite the important step in understanding presented in chapter 3, the study was unable to determine whether the change in thermodynamic stability or a change mechanical stability of the building block was responsible for the changes observed in the bulk mechanical properties of the network. To address the convolution of the effects of the thermodynamic and mechanical stability of the building block on hierarchical network properties the study presented in chapter 5 characterised the structural and mechanical properties of both apo- and bound-MBP hydrogels in varying concentrations of the denaturant urea. The rationale was that the thermodynamic stability of the building block could be varied by urea concentration, while the mechanical stability was independently toggled by the addition of maltose.

Hydrogels constructed from thermodynamically less stable building blocks exhibit lower storage moduli (Fig. 6.1.1.1) and energy dissipation, as shown by rheology. The modulation of the storage modulus and energy dissipated is attributed to a direct decrease in the amount of energy needed to deform or unfold the protein building block. In addition to the change in network rigidity altering the thermodynamic stability of the building block, it also changes the post-photo-chemical relaxation behaviour of the network, with networks constructed from less thermodynamic stable building blocks exhibiting more rapid relaxation due to unfolding. Similar to the change in network rigidity and energy dissipation, the reduction in the relaxation time constant due to unfolding, is attributed to a reduction in the amount of energy needed to unfold, promoting more rapid unfolding of the protein building block. Interestingly, in the absence of enhanced mechanical stability the change in thermodynamic stability drives a regime change in the relaxation behaviour from unfolding-dominated to entanglement-dominated i.e. hydrogels constructed from thermodynamically less stable building blocks do not exhibit a reduction in rigidity at long times but instead exhibit an increase to a plateau due

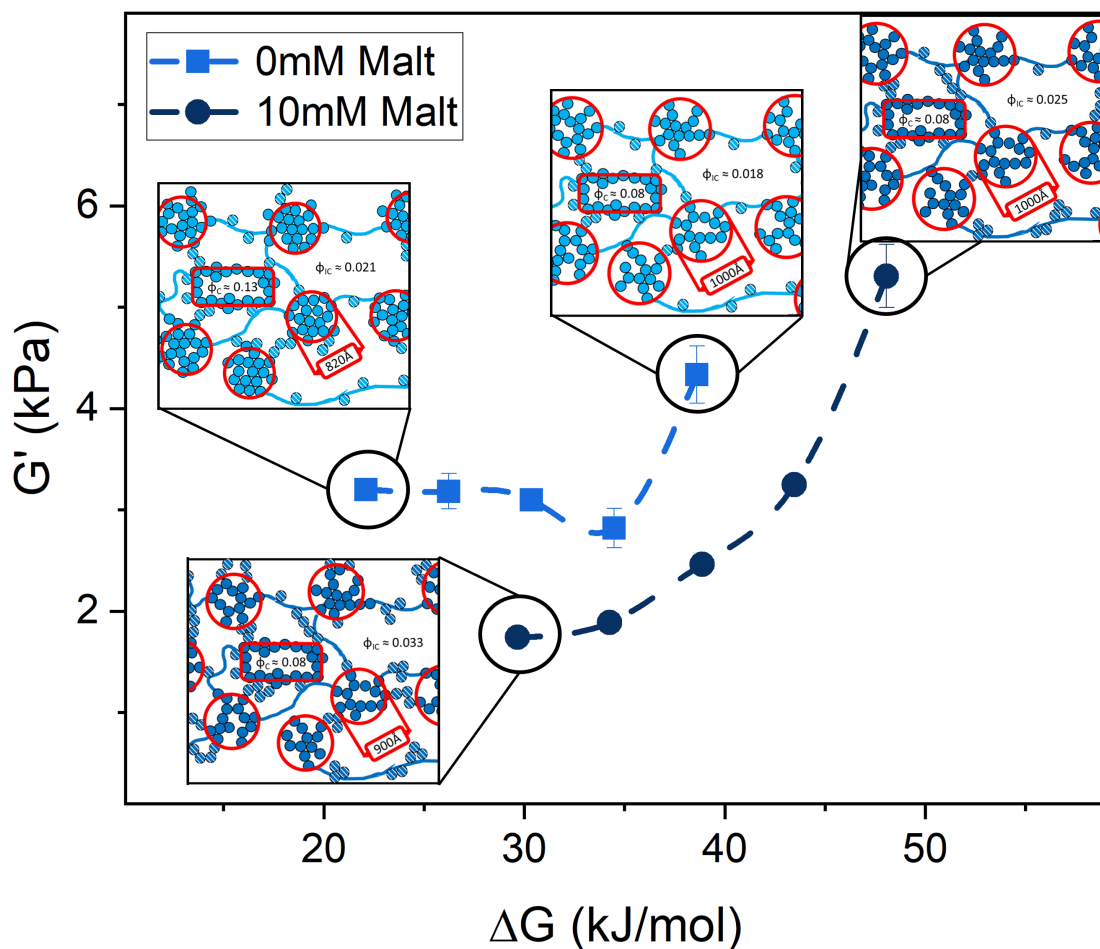


Figure 6.1.1.1: Summary figure of the main results of chapter 5. Storage modulus of MBP hydrogels as a function of thermodynamic stability of the MBP building block in the absence and presence of maltose (Fig. 5.5.1.2). (Insets) The predicted hydrogel architectures (Fig. 5.4.0.5) of the associated circled data points.

to entanglement of the unfolded protein. However the same regime change is not observed in hydrogels constructed from building block with enhanced mechanical stability, indicating the preserving effect of mechanical stability on the integrity of the protein fold. This is an example of the more indirect role of mechanical stability in defining the structural and mechanical properties of a hierarchical protein network. Another example of this indirect role is the reduced strength (storage modulus) of hydrogels constructed from more mechanically stable building blocks, compared to those constructed from buildings block of comparable thermodynamic stability but without mechanically enhancement. This reduction is attributed to the slight increase in the proportions of

folded protein, which has the knock-on effect of reducing the level of physical cross-links due to entanglement, hence reducing the rigidity of the network. So, rather than directly altering the mechanics of the network the mechanical stability of the building block alters the state and properties of the building block on the molecule-level (e.g. changing the proportion of folded protein *in situ*) which indirectly effects the bulk mechanics of the network. These observations suggest that the translation of building block stability to the macro-level mechanics observed in chapter 3 is due to an increase in the thermodynamic stability of MBP, rather than an increase in the mechanical stability. Indeed many of the results of the initial study on MBP hydrogels (chapter 3) agree with the interpretation that increased thermodynamic stability more directly governs hydrogel mechanical properties, including increased storage moduli and energy dissipation when the ensemble thermodynamic stability is increased (i.e. the proportion of bound- or ‘occupied’ MBP is increased).

Similar roles of building block thermodynamic and mechanical stability are observed in the determination of the hydrogels network architecture, where the thermodynamic stability governs the structure of protein networks. Hydrogels constructed from less thermodynamically stable building blocks exhibited significantly denser, smaller, fractal-like clusters of chemically cross-linked folded protein connected by inter-cluster regions populated with folded and unfolded protein. The change in the density and structure of the fractal-like clusters is likely driven by the more rapid unfolding of the protein observed by rheological measurements of the gelation. However, these structural changes are ultimately limited by the mechanical stability of the protein building block, as the network structure is largely unaffected by a change in the building block thermodynamic stability in hydrogels constructed from mechanically enhanced protein monomers. Once again demonstrating the preserving role of the mechanical stability of the building block. To confirm the underlying processes that lead to the change/preservation of the hydrogel structure, the formation of the protein hydrogels should be probed using both rapid acquisition SAXS to capture to the transition from a mono-dispersed solution of monomers to a fully formed network.

Many works [127, 134, 205, 232] in the folded protein hydrogel field select proteins

based on the mechanical stability of the folded protein, determined from SMFS studies [194, 233, 234]. However, we have demonstrated here that the building block mechanical stability is only a single piece of the puzzle for the translation of single molecule properties to the bulk mechanical properties of the network. In fact our results demonstrate that the thermodynamic stability of the protein building block plays a more direct role in the defining the mechanical properties of the network, compared to the mechanical stability. To explain the origin of the differential and distinct roles of building block thermodynamic and mechanical stability, we proposed an energy landscape model. In this model the direct effects on the structure and mechanics of the network due to thermodynamic stability (e.g. change in the cluster density or modulation of the network storage) are described by a change in the difference in free energy between the folded and unfolded state. Whereas the indirect effects of mechanical stabilisation (e.g. limiting the regime change in the relaxation behaviour) originate from a change in the transition state of the protein's unfolding pathway i.e. resulting in a higher energy barrier to unfolding. While this model is able to explain the observed effects of manipulating the two stabilises of MBP on the subsequent hydrogel network, further work beyond the scope of this thesis is necessary to confirm the legitimacy of this model including SMFS studies on MBP and mutant MBP with specifically located disulphide bonds.

The crucial and distinct roles of building block thermodynamic and mechanical stability on the properties of hierarchical protein networks have been demonstrated in this work and a model to explain the route of these differential effects has been proposed (beyond the scope of this project is necessary to confirm this proposed model). This chapter also demonstrates the importance of intensive characterisation and selectivity of the network building block to produce a network with precisely tailored mechanical properties for applications, whether these applications are naturally derived [24, 27, 28, 42, 43, 179], e.g. the actin cytoskeleton or for *in vitro* use [95, 235, 236] e.g. hydrogel wound dressings. Understanding and tuning the thermodynamic and mechanical stabilities of the build block emerges as a novel way to tune not just the mechanical strength of a network but a whole host of properties including the relaxation behaviour, energy dissipation and structural properties of the network.

6.2 The defining role of *in situ* unfolding on hierarchical network architecture and subsequent mechanics

The structural characterisation of MBP-based hydrogels presented in chapter 3 speculated that the proposed structure of folded protein hydrogels was critically limited by the unfolding of the protein building. By toggling the force liability of the naively disulphide stapled protein BSA via the addition of DTT and effectively restricting or permitting unfolding, the defining role of *in situ* unfolding on the network's structure and mechanical properties was demonstrated.

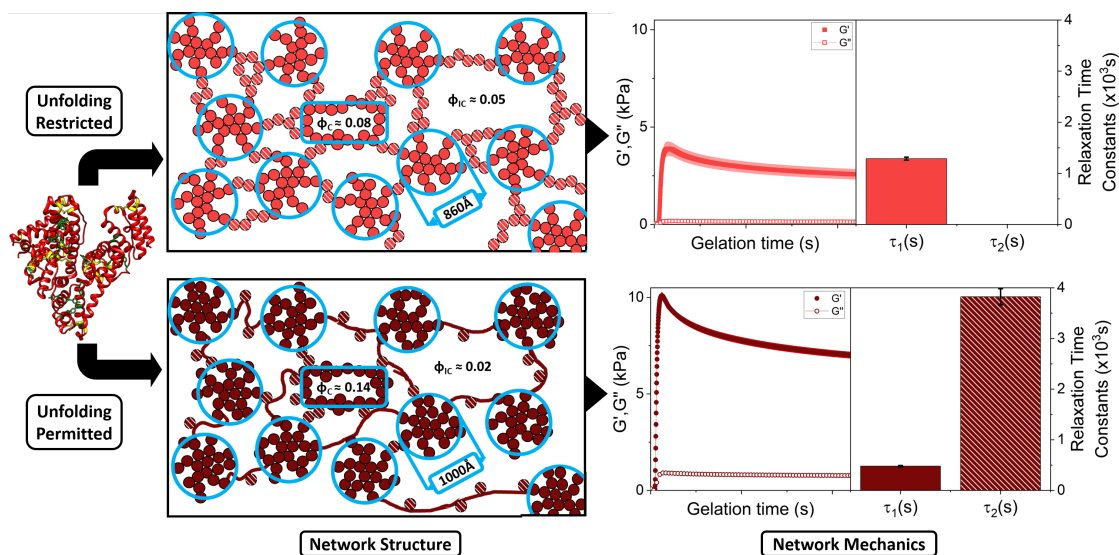


Figure 6.2.0.1: Summary figure of the main results of chapter 4. (left) Predicted network architectures of BSA hydrogels in the (top) absence and (bottom) presence of DTT. (right) Gelation curves showing storage and loss moduli as a function of gelation time and the extracted time constants of post-photo-chemical cross-linking relaxation (where τ_1 and τ_2 are attributed to the relaxation due to network rearrangement and unfolding of the hydrogel building block respectively) of BSA hydrogels in the (top) absence and (bottom) presence of DTT.

Measurement of BSA hydrogels in the absence and presence of DTT using SAXS and SANS that there is a significant difference in the architecture of the BSA hydrogels when the disulphide staples, restricting the unfolding of BSA, are removed. Analysis of the curves with a fractal structure model suggested the presence of fractal-like clusters of cross-linked folded protein connected by an inter-cluster region populated by either folded

or unfolded protein (in the absence and presence of DTT, respectively), in agreement with the previously determined structure in MBP hydrogels. Using a new analysis the density of folded protein in a fractal-like cluster and the connecting inter-cluster region can be determined. This analysis showed that allowing the protein building block to unfold, leads to a more heterogeneous network with dense fractal-like clusters connected by an inter-cluster region populated by unfolded protein and sparsely by folded BSA. While restricting unfolding leads to the formation of more heterogeneous networks with comparatively sparser fractal joined by a connecting inter-cluster more densely populated by folded protein. The significant alteration in network architecture demonstrates that *in situ* unfolding is crucial in defining the structure of protein network. To complimented this structural analysis with computational modelling (courtesy of Dr Benjamin Hanson) to investigate hydrogel network formation, which showed that a homogeneous presence of unfolded protein during gelation was not sufficient to cause the significant change in the fractal dimension of the cross-linked cluster that is observed in our experimental. From this we deduce that it is the act of unfolding of specific force labile protein building blocks during gelation, rather than the presence of unfolded protein, that is crucial in defining the hydrogel architecture. To confirm this hypothesis, further investigation beyond the scope of this work would be needed including rapid frame acquisition SAXS and computational modelling that accurately models unfolding during gelation.

The unfolding of proteins has been utilised in folded protein hydrogels to imbue them with interesting properties such as shape memory [129] and stimuli-responsive mechanical behaviour [123], demonstrating the interesting applications that *in situ* unfolding can give rise to. However, these studies do not perform structural analysis on the hydrogel network architecture, nor the effects building block unfolding has on it. This study has performed the most in-depth analysis and characterisation folded protein hydrogel architectures to-date, to the best of our knowledge. And has shown that in order to gain complete understanding of the role of protein unfolding in hierarchical networks, intense structural characterisation is required.

The architecture changes that arise from the regulation the ability of the protein building block to unfold has significant effects on the bulk mechanics of the network.

Networks formed from force labile protein exhibit storage moduli that are 3-fold higher than those formed from disulphide reinforced protein, as well as enhanced viscous and energy dissipation behaviour. The increased viscous behaviour was attributed to the higher prevalence of unfolded protein in the connecting inter-cluster region of hydrogels constructed from the force labile building block. The increase in the elasticity of the network was attributed to additional chemical cross-links formed between the force-induced unfolded protein strand in the inter-cluster region, suggesting that building block unfolding and cross-link density in the inter-cluster region is key in modulating the mechanics of the network. Indeed the governing role of connections in the inter-cluster region has been observed in other soft matter systems such as colloidal gels. Del Gado et al. [215, 216] and Frust et al. [217] observed that the so called ‘rigidity percolation network’ was key in regulating the mechanical properties of the network and similarly found that heterogeneity in the network structure crucial in governing the mechanical response of the network. We have shown similar behaviour in hydrogels of significantly lower volume fraction ($\approx 7\%$) than the previously published colloidal gels ($\approx 40\text{-}50\%$), suggesting that the dependency of the mechanics on the inter-cluster region is independent of the volume fraction of the system.

The difference in relaxation behaviour of BSA hydrogels constructed from disulphide reinforced and force labile protein is striking. To describe the post-photo-chemical cross-linking relaxation of networks formed from reinforced protein a single relaxation mode is required. In contrast networks formed from force labile protein required two relaxation modes in order to adequately describe the relaxation behaviour. By utilising CD spectroscopy and recording the change in the proportion of folded protein in the gel over time post-photo-chemical gelation, this additional relaxation mode is proposed to be due to the unfolding of the force labile building block protein post-photo-chemical cross-linking. Demonstrating the direct translation of a change in the structure at the molecular-level to an alteration of the mechanics at the macro-level. Additionally, BSA hydrogels soaked in DTT post-formation exhibit the additional relaxation mode as well as a factor of 2 reduce in the storage modulus. The reduction in storage modulus upon soaking of the network is consistent with previous measurements of protein based hydrogels by Kim et

al., who demonstrated that by replacing a rigid connecting building block with similarly sized flexible one results in a 2-fold decrease in network rigidity [131].

In situ unfolding of the protein network plays a fundamental role in defining the network architecture and mechanics of the network. While all studies demonstrate the necessity for combined structural and mechanical characterisation at multiple length scales, it is most effectively shown in this study where conclusions could only be effectively drawn by understanding what was happening at each level of hierarchy within the system. Toggling the transition of the protein building block from a rigid folded state to a flexible unfolded state emerges as a powerful method for controlling the inter-cluster region of the network structure and the subsequent mechanical response, and is significantly important in the development of novel bio-mimetic and bio-inspired materials.

6.3 Future Work

The work detailed in this thesis has attempted to address the difficulty of predicting the translation of the properties of an individual building block to the collective properties of a network of such individuals. Although significant progress was made, particularly in understanding the cross-length scale translation of building block stability, many questions still remain. Some examples generated as a direct result of this work are:

- i) What is the underlying mechanism behind the non-trivial dependency of storage modulus vs proportion of more mechanically robust ligand? And why only 20% of the building block needs to be made more robust to lead to the most significant increase in network mechanic?
- ii) During the gelation process which proteins undergo unfolding? And what is the underlying mechanism? When during the gelation process does unfolding occur and how are protein building blocks ‘selected’?
- iii) The work in this thesis focuses on networks constructed from globular folded proteins, while many naturally derived protein networks are constructed from fibrous

proteins. So, how will the results presented in this work map to fibrous protein networks?

6.3.1 Determination of the formation process of photo-chemically cross-linked protein networks

The majority of work in this thesis focus on the end point mechanics and structure of folded protein hydrogels, however to allow greater understanding of the translation of molecular stability and the formation process of folded protein based hydrogels need to be investigated in detail. In order to do this two key techniques are required: rapid frame acquisition SAXS and computational modelling that is able to accurately capture the unfolding kinetics of proteins *in situ*.

Rapid acquisition SAXS measurements would allow for the tracking and structural characterisation at each stage as the system transitions from a mono-dispersed solution of monomers to a fully formed cross-linked network. These scattering measurements would also serve as benchmarks for simulations able to simultaneously model the photo-chemical cross-linking process and the complex kinetics of *in situ* protein unfolding. The combination of both these techniques would aid understanding of how more robust building block affect the formation process (i.e. are they preferentially found in specific areas of the structure such as the inter-cluster region) and which proteins are most likely to unfold and lead to the interesting structural changes we have observed in folded protein hydrogels.

6.3.2 Crossover from globular to fibrous protein networks

While the results of this project focus on protein network constructed folded globular protein, many hierarchical protein networks found in nature are fibrous in nature including α -lamins [43], the actin cytoskelton [7] and collagen [42]. It is unclear how the relationships and dependencies observed and determined from folded globular protein networks map on to networks constructed from more fibrous proteins. One of the major

difference between these systems is one of geometry i.e. in fibrous hydrogels the building block monomer is many times longer than it is wide, whereas globular proteins have comparatively similar lengths and widths. This difference in aspect ratio could be the source of any discrepancies between globular and fibrous protein networks.

To investigate this and determine the crossover from globular to fibrous protein networks, engineered polyprotein constructs of varying lengths should be used to construct protein hydrogels. Using the methods and analyses in this project, the structural and mechanical properties of protein networks could be determined as a function of building block aspect ratio. Furthermore if the correct protein is selected to include in the polyprotein construct, for example MBP, the effects of changing building block stability as function of aspect ratio could also be determined. This would allow for the mapping of the results measured on globular protein networks to fibrous protein networks and vice versa, which would be extremely useful in the development of novel bio-inspired materials.

Appendix A

List of chemicals and experimental apparatus

This section gives a list of the apparatus, kits and manufacturers used in this project.

AKTAprime plus	GE Healthcare, UK
Avanti J-26 XP Centrifuge	Beckman Coulter, USA
Autoclave	Prestige Medical, UK
BUCHI Vac V-500 vacuum pump	Sigma Aldrich, USA
Cell disruptor	Constant Cell Disruption Systems, UK
Chirascan CD Spectrometer	Applied photophysics, UK
GenFuge 24D Centrifuge	Progen Scientific, UK
HANNA pH 20 pH Meter	HANNA Instruments Ltd, UK
HisTrap HP 5 ml column	GE Healthcare, UK
Modular Compact Rheometer 302	Anton Parr Ltd, Austria
Nano-inXider SAXS/WAXS instrument	Xenocs, France
Snakeskin Pleated Dialysis Tubing, 3'500	Thermo Scientific, UK
MWCO	
UltraSpec 2100 Pro UV/Visible Spectropho- tometer	GE Healthcare, UK

A.1 List of Chemicals

This section lists the chemical used in this project and the corresponding suppliers. The buffers and media in this project were all made with Purite 18M Ω distilled (Milli-Q) water.

Chemical name	Company
A	
Agar	Melford Laboratories, UK
B	
Benzamidine	Sigma Aldrich, USA
BSA heat shock fraction, protease free, essentially globulin free, pH 7, >98%	Sigma Aldrich, USA
C	
Carbenicillin disodium salt	Formedium, UK
Deoxyribonuclease, DNAase	Sigma Aldrich, UK
1,2-Dithiothretol, DTT	Formedium, UK
E	
Ethanol	Fisher scientific, UK
G	
Glycerol	Fischer scientific, UK
H	
Hydrochloric acid/HCl	Fischer scientific, UK
I	
Imidazole	Sigma Aldrich, UK
L	
Luria-Bertani Broth, LB broth (ready mixed)	Melford Laboratories, UK
M	
Magnesium sulphate/MgSO ₄	Sigma Aldrich, USA
D-(+)-Maltose monohydrate/C ₁₂ H ₂₂ O ₁₁ ·H ₂ O	Sigma Aldrich, USA
P	

Phenylmethanesulphonyl fluoride, PMSF	Sigma Aldrich, USA
S	
Sodium chloride/NaCl	Fischer scientific, UK
Sodium hydroxide/NaOH	Fisher scientific, UK
Sodium Persulfate/Na ₂ S ₂ O ₈	Sigma Aldrich, USA
Sodium phosphate dibasic/Na ₂ HPO ₄	Sigma Aldrich, USA
Sodium phosphate monobasic/NaH ₂ PO ₄	Sigma Aldrich, USA
T	
Tris(2,2'-bipyridyl)ruthenium(II) dichloride hexahydrate/ C ₃₀ H ₂₄ Cl ₂ N ₆ Ru·6H ₂ O	Sigma Aldrich, USA
Tris-(hydroxymethyl)-aminomethane, Tris	Fisher scientific, UK
Triton-X	VWR (USA)
U	
Urea/CO(NH ₂) ₂	Sigma Life Science, USA

Appendix B

Additional Formulae and Derivations

B.1 Derivation of the proportion of bound-MBP

By considering the definition of the dissociation constant, K_d of the apo-, bound-MBP equilibrium reaction

$$K_d = \frac{[MBP_{apo}] \cdot [maltose_{unbound}]}{[MBP_{bound}]} \quad (\text{B.1.0.1})$$

Substituting

$$[MBP_{apo}] = [MBP] - [MBP_{bound}] \quad (\text{B.1.0.2})$$

$$[maltose_{unbound}] = [maltose] - [maltose_{bound}] \quad (\text{B.1.0.3})$$

$$[MBP_{bound}] = P_{occ}[MBP] \quad (\text{B.1.0.4})$$

into equation B.1.0.1 and rearranging for P_{occ} gives

$$P_{occ} = \frac{([MBP] + [maltose] + K_d) - \sqrt{([MBP] + [maltose] + K_d)^2 - 4[MBP][maltose]}}{2[MBP]} \quad (\text{B.1.0.5})$$

B.2 Langmuir-type equation

$$X_{[maltose]} = \frac{\Delta X [maltose]}{K_d + [maltose]} + X_0 \quad (\text{B.2.0.1})$$

Where X study is substituted for either melting temperature, shear moduli or energy dissipated.

B.3 Derivation of fractal structure factor

Start by considering the N of monomers of size, r_0 , in a fractal of radius, r,

$$N(r) = \rho_k \left(\frac{r}{r_0} \right)^{D_f} \quad (\text{B.3.0.1})$$

where ρ_k is the packing fraction (which for randomly packed spheres is ≈ 0.639). Equation B.3.0.1 can be used to determine the radial number density of a fractal,

$$\rho(r) = \frac{dN(r)}{dV} = \frac{\rho_k \cdot D_f}{4\pi r_0^{D_f}} \cdot r^{D_f-3} \quad (\text{B.3.0.2})$$

The radial number density, $\rho(r)$, can be written in radial distribution function, $g(r)$,

$$\rho(r) = \phi_0 g(r) \quad (\text{B.3.0.3})$$

where ϕ is the mean volume fraction of the monomers over the whole system. Rearranging equation B.3.0.3 and substituting in equation B.3.0.2 gives

$$g(r) = \frac{\rho_k \cdot D_f}{4\pi\phi r_0^{D_f}} \cdot r^{D_f-3} \quad (\text{B.3.0.4})$$

Fractal systems in reality are not ideal mathematical fractals and as such do not continue *ad infinitum*, so in order to model the finite size of real-world fractal aggregates an exponential term, $e^{-\frac{r}{\xi}}$, is introduced into $g(r)$ where ξ is the cut-off length of fractal behaviour (i.e. the mass of the system scales with respect to the fractal dimension)

$$g(r) = \frac{\rho_k \cdot D_f}{4\pi\phi r_0^{D_f}} \cdot r^{D_f-3} e^{-\frac{r}{\xi}} \quad (\text{B.3.0.5})$$

The structure factor is defined as the Fourier transformation of $g(r)$

$$S(q) = \int_0^\infty g(r) \cdot e^{-i\hat{q}\hat{r}} d^3r \quad (\text{B.3.0.6})$$

Assuming that the fractal object is radial symmetric $S(q)$ becomes

$$S(q) = \int_0^\infty g(r) \cdot 4\pi r^2 \cdot \frac{\sin(qr)}{qr} dr \quad (\text{B.3.0.7})$$

Subbing equation B.3.0.5, cancelling out and rearranging gives

$$S(q) = \frac{\rho_k \cdot D_f}{q\phi r_0^{D_f}} \int_0^\infty r^{D_f-2} e^{-\frac{r}{\xi}} \cdot \sin(qr) dr \quad (\text{B.3.0.8})$$

Completing the integral and rearranging gives the functional of the fractal structure factor used in this work.

$$S(q) = \frac{D_f \Gamma(D_f - 1)}{\left[1 + \frac{1}{(q\xi)^2}\right]^{\frac{D_f-1}{2}}} \cdot \frac{\sin \left[(D_f - 1) \tan^{-1}(q\xi) \right]}{(qR_0)^{D_f}} \quad (\text{B.3.0.9})$$

B.4 Derivation of the number of monomers in a finite-sized fractal

Considering the formula which describes $g(r)$ given in previous derivation (section B.3)

$$\rho(r) = \phi_0 g(r) \quad (\text{B.3.0.3})$$

rearranging, substituting $\rho(r) = \frac{dN(r)}{dV}$ and assuming radial symmetry of the system (i.e. $dV = 4\pi r^2 dr$) gives

$$dN(r) = \phi_0 g(r) 4\pi r^2 dr \quad (\text{B.4.0.1})$$

Substituting in $g(r)$ for finite-sized fractal aggregates of monomers (Eqn B.3.0.5) and cancelling down results in

$$dN(r) = \frac{\rho_k \cdot D_f}{r_0^{D_f}} \cdot r^{D_f-1} dr \quad (\text{B.4.0.2})$$

By integrating with substitution (where $u = r/\xi$) equation B.4.0.2 with respect to r from 0 to a radius, R , from the centre of the fractal aggregate

$$dN(r) = \int_0^R \frac{\rho_k \cdot D_f}{r_0^{D_f}} \cdot r^{D_f-1} dr \quad (\text{B.4.0.3})$$

gives an expression for the total number of monomers in a sphere of radius, R , from the centre of the fractal cluster

$$N(r) = \rho_k \cdot D_f \cdot \left(\frac{\xi}{r_0}\right)^{D_f} \gamma\left(D_f, \frac{R}{\xi}\right) \quad (\text{B.4.0.4})$$

where $\gamma\left(\frac{R}{\xi}\right)$ is the lower incomplete gamma function, which is defined as

$$\gamma\left(D_f, \frac{R}{\xi}\right) = \int_0^{\frac{R}{\xi}} x^{D_f-1} e^{-x} dx \quad (\text{B.4.0.5})$$

Appendix C

Supplementary info for chapter 3

C.1 Additional rheological measurements of MBP hydrogels

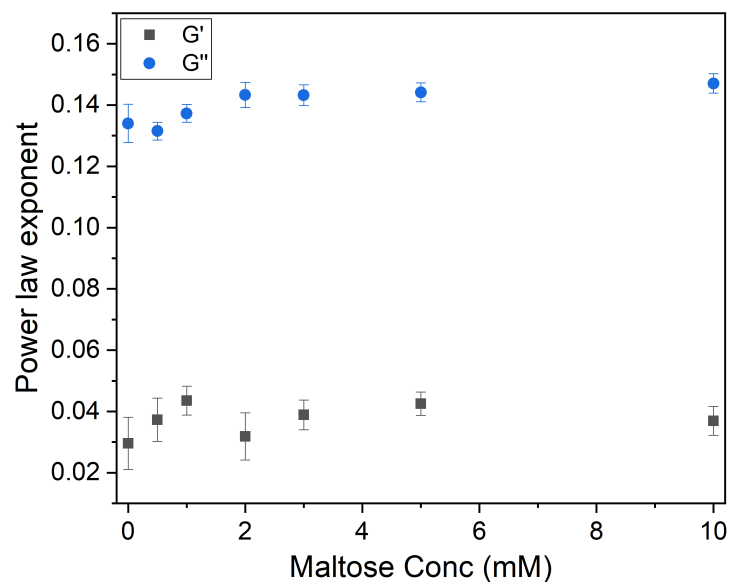


Figure C.1.0.1: The value of the power law exponent, extracted from the frequency dependence of the storage and loss moduli in Fig. 3.2.1.1, as a function of maltose concentration.

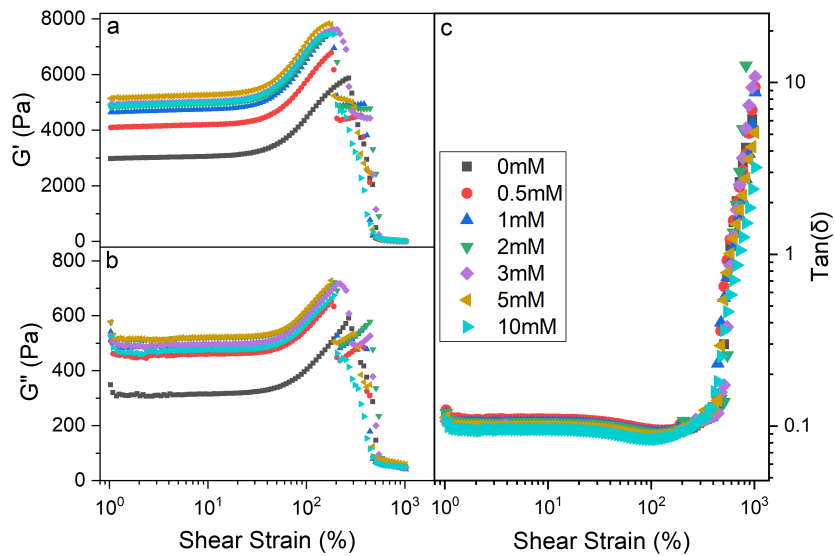


Figure C.1.0.2: Strain amplitude ramps showing the (a) storage and (b) loss moduli of chemically cross-linked MBP hydrogels as a function of the maltose concentration. The large drop occurring at approx. $300 \pm 60\%$ in both moduli is attributed to rupture of the gel and shows no statistically significant trend with maltose concentration. (c) Ratio of loss to storage modulus as a function of strain and maltose concentration, an upturn is noted at strains of approx. 300% after which $\tan(\delta)$ becomes larger than one, meaning the viscous forces now dominate the system, demonstrating rupture of the gel network.

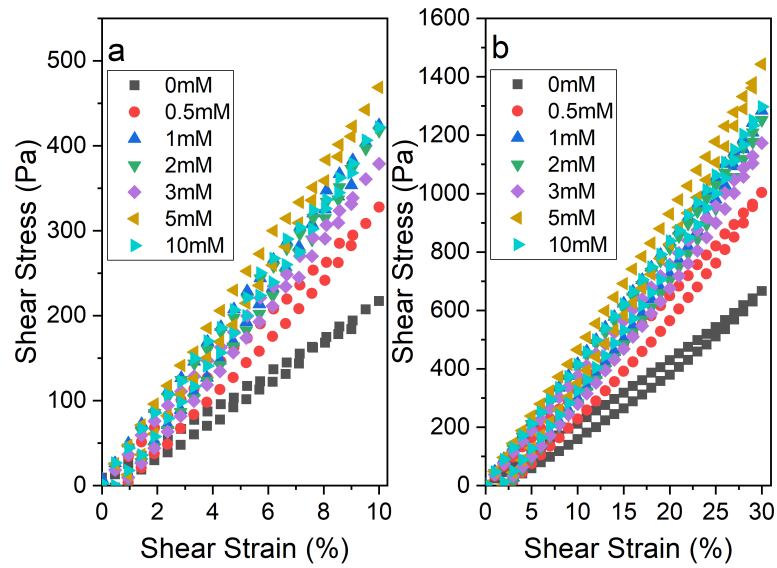


Figure C.1.0.3: Stress-Strain curves of chemically cross-linked MBP hydrogels as a function of maltose concentration. Samples were strained to (a) 10% and (b) 30% at a rate of 1%/s and then unloaded down to 0% at the same rate. Similar trends are seen in these curves as shown in the main text (Fig. 3.2.2.1).

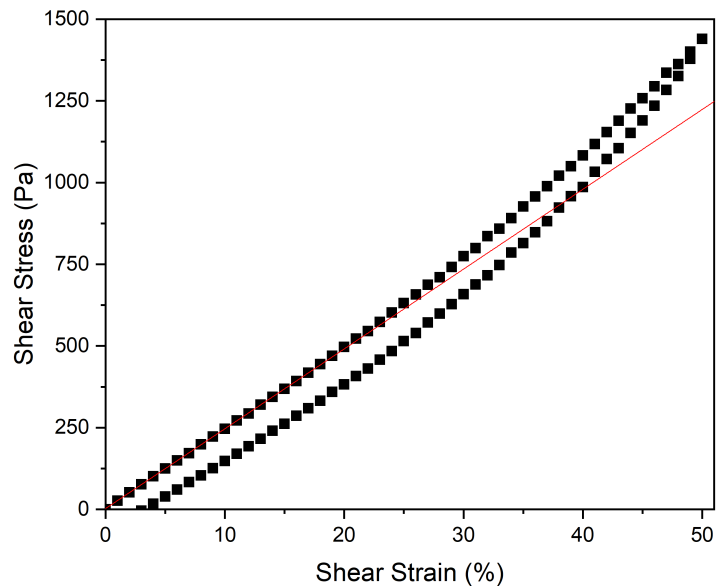


Figure C.1.0.4: Exemplar stress-strain curves of chemically cross-linked MBP hydrogels. Red lines show linear fit below 15% strain, the gradient of which is interpreted as the storage modulus of the hydrogel in the linear regime.

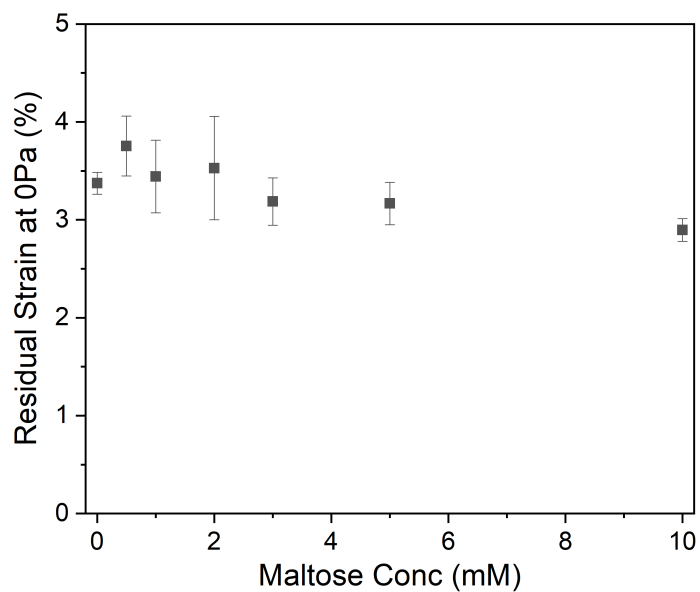


Figure C.1.0.5: Residual strain at 0 Pa extracted from the strain-strain curves in figure 3.2.2.1 upon unloading of MBP hydrogels strained to 50% as a function of maltose concentration in the hydrogel.

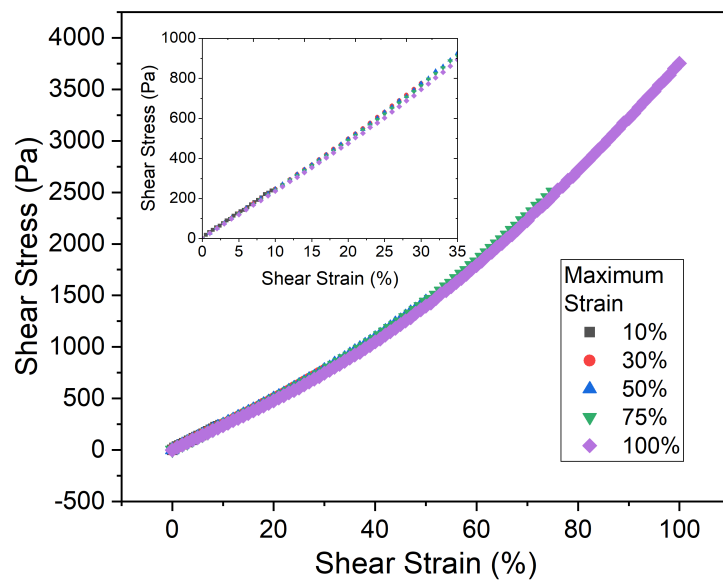


Figure C.1.0.6: Exemplar stress-strain load curves of MBP based hydrogels as a function of maximum strain. All strain loading was performed at a rate of 1%/s up to the maximum strain before unloading and restraining. Note that all curves overlay i.e. follow the same strain path, demonstrating that at strains up to 75% the gel is not damaged or permanently deformed.

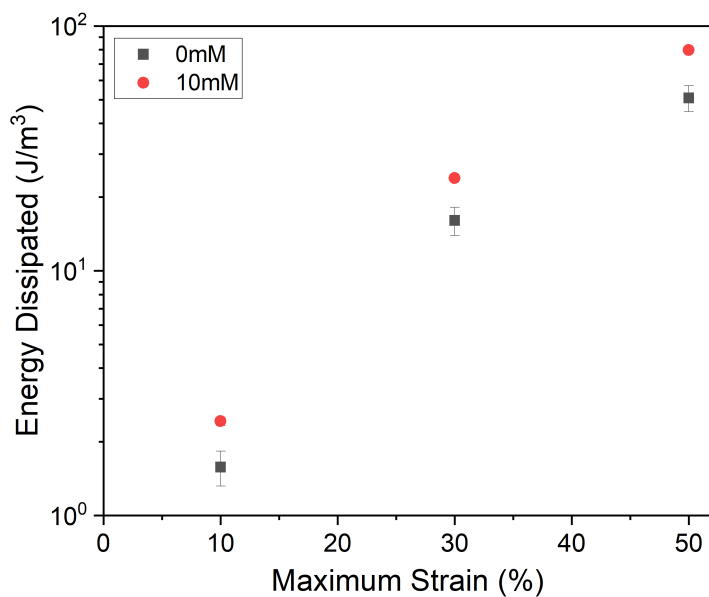


Figure C.1.0.7: Energy dissipated of MBP hydrogels extracted from stress-strain curves as a function of maximum applied strain in the presence and absence of 10mM maltose.

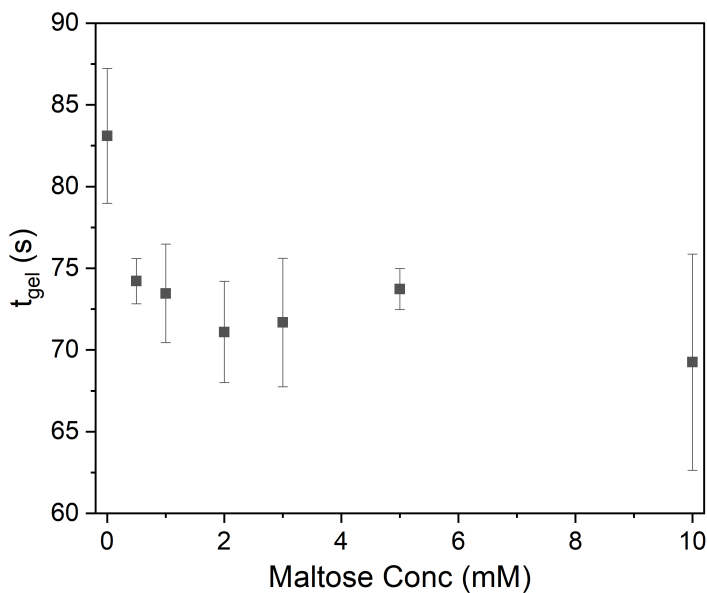


Figure C.1.0.8: Gelation time, t_{gel} , of photo-chemically crosslinked MBP hydrogels (final concentrations: 100mg/ml MBP, 30mM NaPS, 100 μ M Ru(II)bpy₃²⁺), illuminated at t=60s till t=360s, as a function of maltose concentration. (insert) Exemplar gelation curve demonstrating the definition of t_{gel} used in this work.

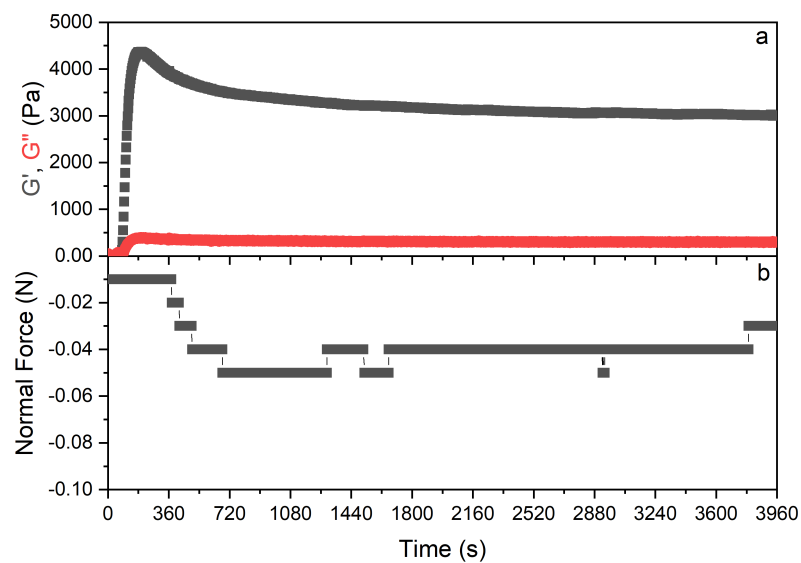


Figure C.1.0.9: (a) Exemplar gelation curve (showing storage and loss moduli vs time) of photo-chemical cross-linked MBP hydrogels (final concentrations: 100mg/ml MBP, 30mM NaPS, $100\mu\text{M Ru(II)bpy}_3^{2+}$). Illuminated at $t=60\text{s}$ till $t=360\text{s}$. (b) Measured force normal to the plane of shear (The positive direction is defined as upwards) during gelation of a MBP-based hydrogel.

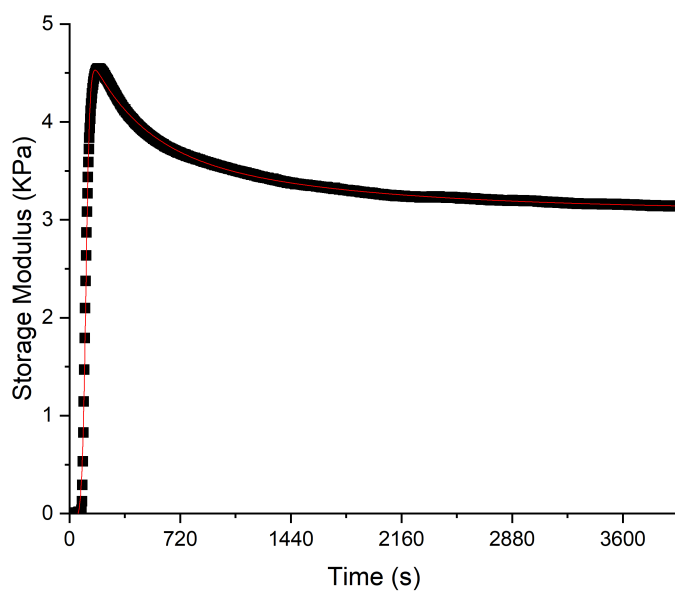


Figure C.1.0.10: Exemplar gelation curve (showing storage modulus vs time) of chemical cross-linked MBP hydrogels (final concentrations: 100mg/ml MBP, 30mM NaPS, 100 μ M Ru(II)bpy₃²⁺). Red line shows fit of empirical fitting function (eqn 3.4.0.1) to the gelation curve data.

C.2 SAS form factor measurements of MBP and exemplar SAS fitting

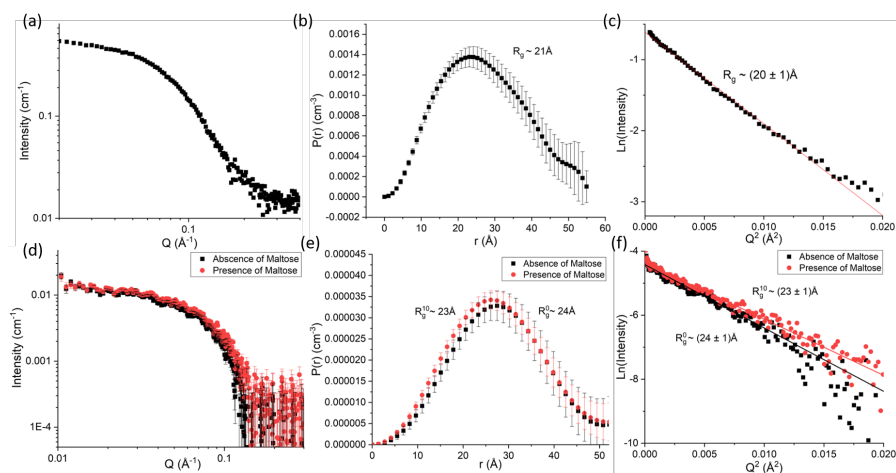


Figure C.2.0.1: (a) SANS scattering curve of MBP in 25mM sodium phosphate buffer pH 7.4, at a concentration of 10mg/ml. (b) $P(r)$ inversion analysis of the data in figure C.2.0.1a, extracting an R_g value of $\approx 21\text{\AA}$. (c) Guinier plot of the data in figure C.2.0.1a, fitting this curve with a linear fit extracts a value for R_g of $(20 \pm 1)\text{\AA}$. (d) SAXS scattering curves of MBP in 25mM sodium phosphate buffer pH 7.4, at a concentration of 10mg/ml. Experiments performed in the presence and absence of 10mM maltose. (e) $P(r)$ inversion analysis of the data in figure C.2.0.1d, extracting a R_g value of $\approx 24\text{\AA}$ (absence of maltose) and $\approx 23\text{\AA}$ (presence of maltose). (f) Guinier plot of the data in figure C.2.0.1d, fitting this curve with a linear fit extracts a value for R_g of $(24 \pm 1)\text{\AA}$ in the absence and $(23 \pm 1)\text{\AA}$ in the presence of maltose.

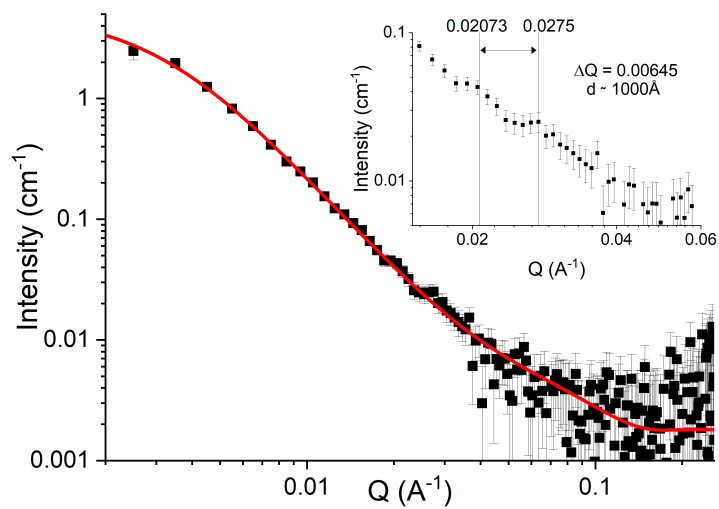


Figure C.2.0.2: SANS curve of MBP hydrogel in the presence of 10mM maltose, taken on the time-of-flight diffractometer instruments ZOOM the ISIS Spallation Source (Didcot, UK). The red line showing the fit from equation 3.3.0.1. Insert: Magnification of the scattering curve to clearly show the presence of Kiessig fringes and the peak to peak analysis

Appendix D

Supplementary info for chapter 4

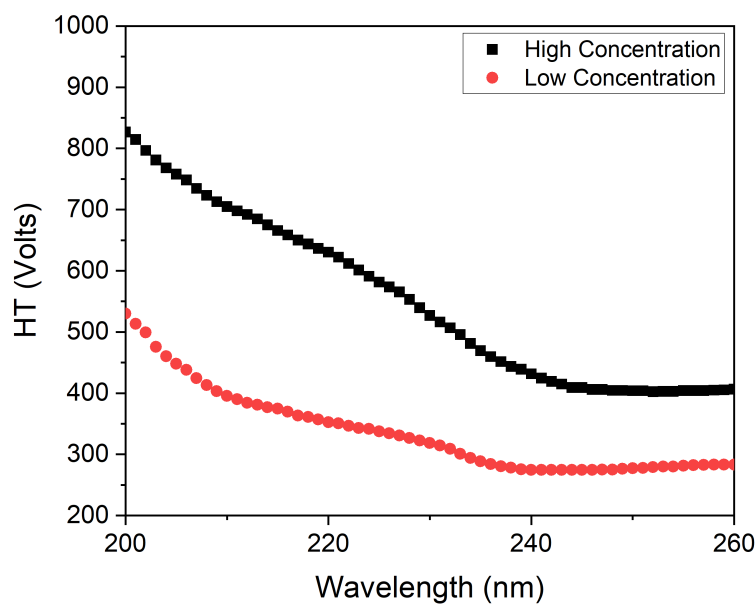


Figure D.0.0.1: High tension (HT) of the CD spectrometer as a function of wavelength when measuring BSA at high (100mg/ml) and low (~ 0.2 mg/ml) concentrations. As the signal from the sample is reduced the detector must increase its sensitivity, so a high HT signal indicates a low signal-to-noise ratio of the signal form the sample. At 1000V the sensitivity of the detector is saturated.

D.1 Additional structural information for the modulation of architecture due to *in situ* protein unfolding

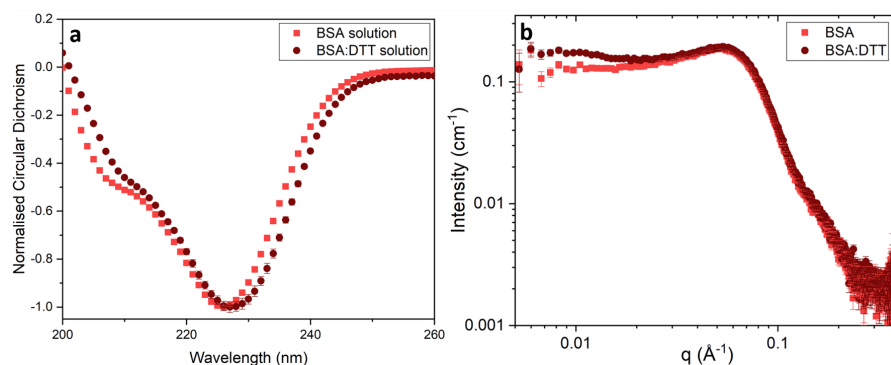


Figure D.1.0.1: (a) Normalised circular dichroism spectra of BSA in solution (100mg/ml) in the absence (light red) and presence (dark red) of 3mM DTT. (b) SAXS curves of 100mg/ml BSA solutions in the absence (light red) and presence (dark red) of 3mM DTT.

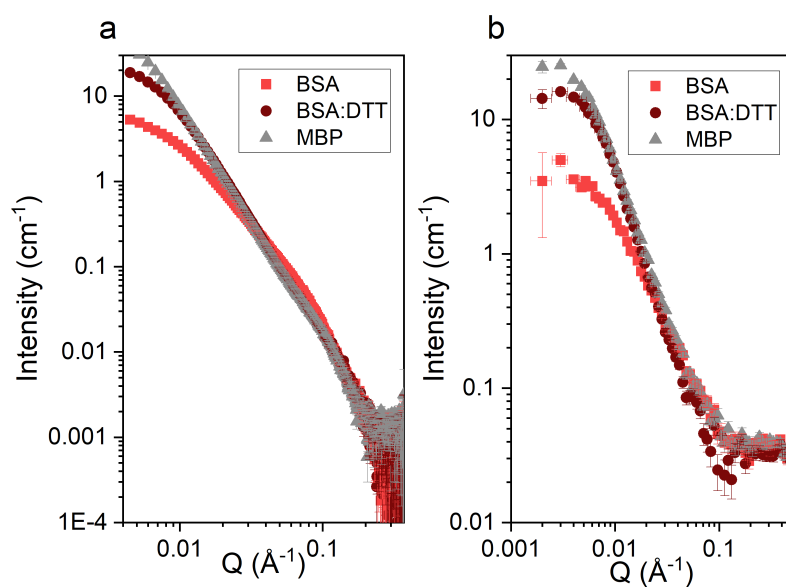


Figure D.1.0.2: a) SAXS curves and b) SANS curves of folded BSA hydrogels (final concentrations: 100mg/ml BSA, 50mM NaPS, 100µMRu(II)bpy₃²⁺) in the absence (light red) and presence (dark red) of DTT. Where SAS data from an apo-MBP is included in grey (Taken from figure 3.3.0.1).

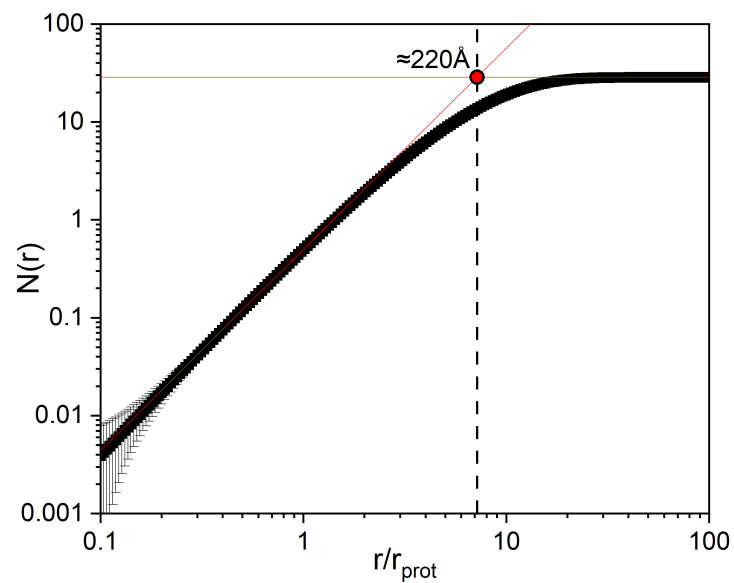


Figure D.1.0.3: Exemplar plot of the number of protein monomers in a cluster as a function of distance from the centre of the cluster, determined by equation 4.3.1.2 and the extracted scattering parameters in figure 4.3.1.2. Intersection of the red fitted lines (red dot) used to extract the number of proteins per cluster and estimate the cluster radius (dashed line).

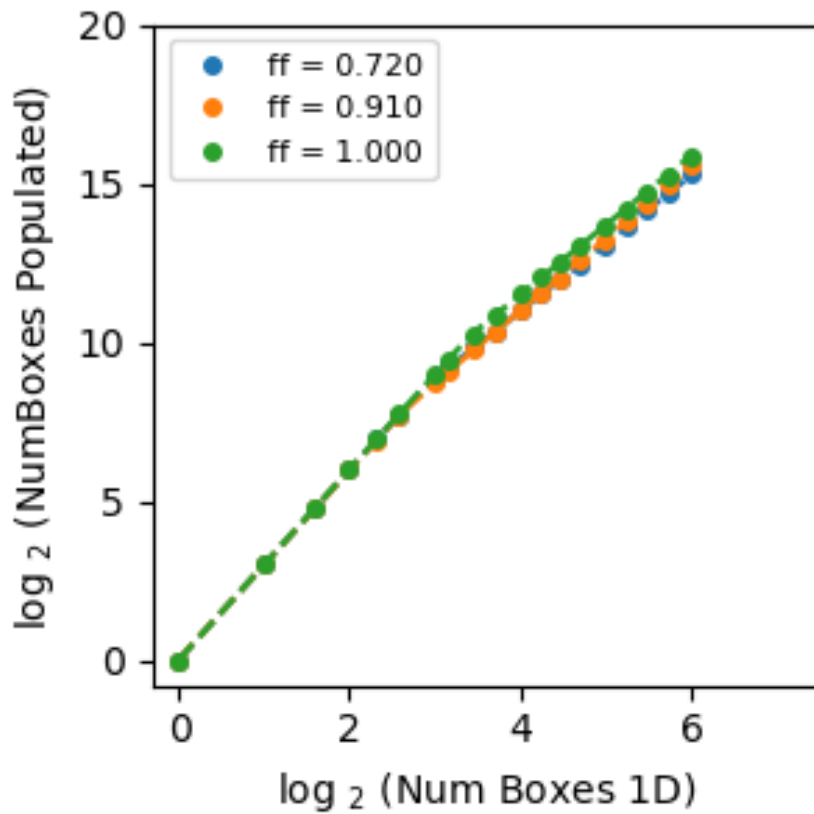


Figure D.1.0.4: Number of boxes ‘filled’ as a function of total number of boxes, in the BioNet simulations with periodic boundary conditions. Using a two-segment piecewise fit, the first has gradient of three, the fractal dimension of cross-linked clusters in BioNet is given by the second gradient. “ff” is the folded-fraction. This analysis was performed by Dr Benjamin Hanson and gratuitously given to be used in this work.

D.2 Additional information regarding the mechanical characterisation of BSA hydrogels

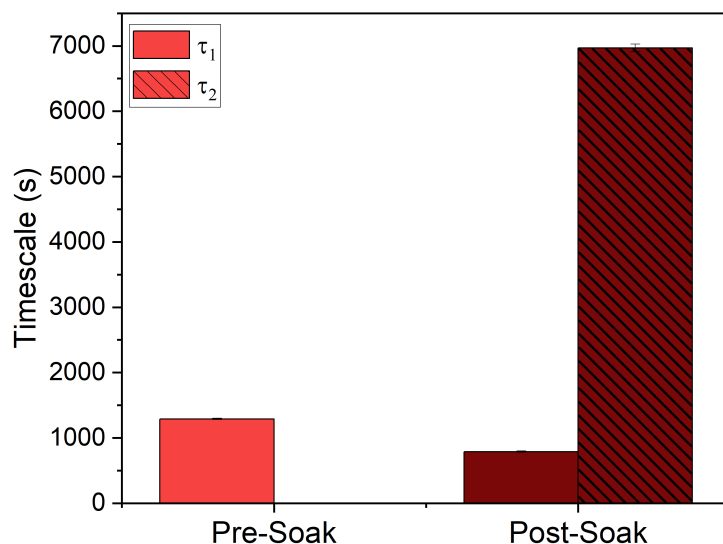


Figure D.2.0.1: Timescales of relaxation extracted from the fits in figure 4.4.1.2, where the filled column is the time constant of the network relaxation and the striped column is the time constant of the protein unfolding relaxation mode.

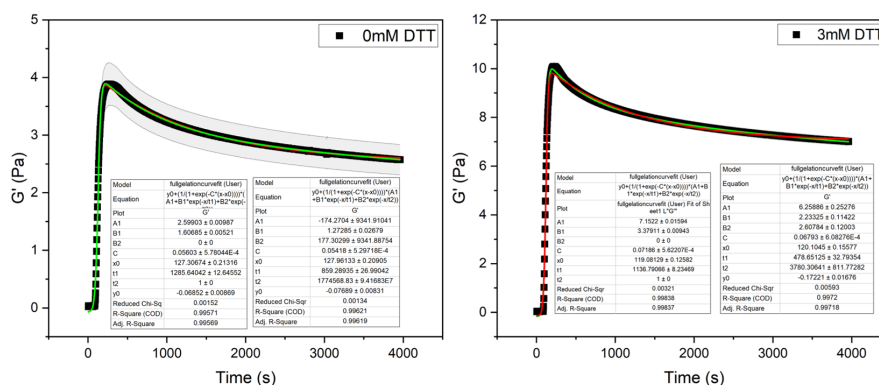


Figure D.2.0.2: Gelation curves, showing storage (closed symbols) vs time of a BSA hydrogel in the absence (left) and presence (right) of DTT. The red lines shows fits where only one relaxation mode is included in the model (i.e. B_2 in equation 3.4.0.1 is set to zero), and the green lines show the fit when two relaxation modes are included in the model. Tables of fit values are included to demonstrate non-sensical values when fitting BSA in the absence of DTT with two relaxation mode model.

Appendix E

Supplementary info for chapter 5

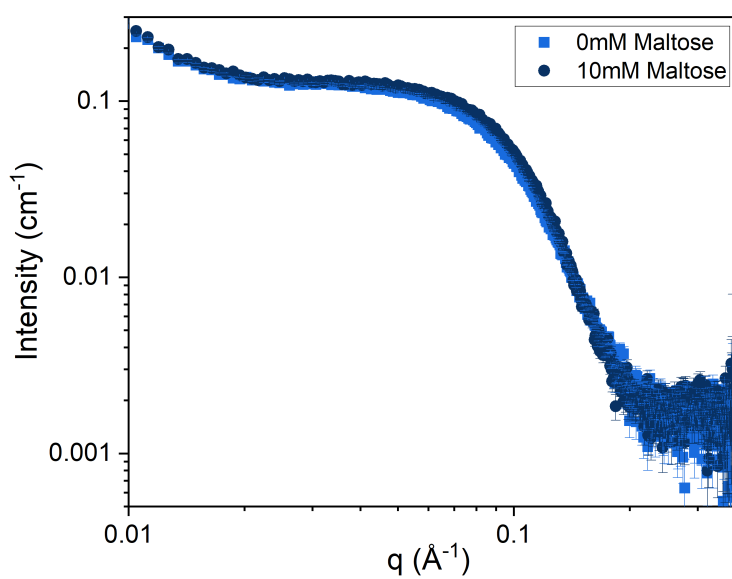


Figure E.0.0.1: SAXS curves of 100mg/ml BSA solutions in the absence (light blue) and presence (dark blue) of 10mM maltose.

Bibliography

- [1] Roderic Lakes. Materials with structural hierarchy. *Nature*, 361(6412):511–515, feb 1993.
- [2] Bone Biology and Mechanics Lab at IUPUI. General Introduction to Bone: Collagen and Mineral, 2021.
- [3] John Illingworth. Molecular Cell Biology. *Biochemical Education*, 15(2):101, 1987.
- [4] M. (Masao) Doi and S. F. (Sam F) Edwards. *The theory of polymer dynamics*. Clarendon Press, 1986.
- [5] Daniel A. Fletcher and R. Dyche Mullins. Cell mechanics and the cytoskeleton, 2010.
- [6] Federica Burla, Yuval Mulla, Bart E. Vos, Anders Aufderhorst-Roberts, and Gijse H. Koenderink. Biopolymers: life’s mechanical scaffolds. *Nature Reviews Physics*, 1(4):249–263, dec 2018.
- [7] Ekta Seth Chhabra and Henry N. Higgs. The many faces of actin: matching assembly factors with cellular structures. *Nature Cell Biology*, 9(10):1110–1121, oct 2007.
- [8] Kerry Hosmer Caffall and Debra Mohnen. The structure, function, and biosynthesis of plant cell wall pectic polysaccharides. *Carbohydrate Research*, 344(14):1879–1900, sep 2009.
- [9] Ovijit Chaudhuri, Sapun H. Parekh, and Daniel A. Fletcher. Reversible stress softening of actin networks. *Nature*, 445:295–298, 2007.
- [10] Cornelis Storm, Jennifer J. Pastore, F. C. MacKintosh, T. C. Lubensky, and Paul A. Janmey. Nonlinear elasticity in biological gels. *Nature*, 435:191–194, 2005.
- [11] Paul A. Janmey, Margaret E. McCormick, Sebastian Rammensee, Jennifer L. Leight, Penelope C. Georges, and Fred C. MacKintosh. Negative normal stress in semiflexible biopolymer gels. *Nature Materials*, 6:48–51, 2007.
- [12] Julia Liu, Debashish Das, Fan Yang, Andrea G. Schwartz, Guy M. Genin, Stavros Thomopoulos, and Ioannis Chasiotis. Energy dissipation in mammalian collagen fibrils: Cyclic strain-induced damping, toughening, and strengthening. *Acta Biomaterialia*, 80:217–227, 2018.
- [13] R. E. Burge, A. G. Fowler, and D. A. Reaveley. Structure of the peptidoglycan of bacterial cell walls. I. *Journal of Molecular Biology*, 117(4):927–953, 1977.

- [14] R. E. Burge, R. Adams, H. H.M. Balyuzi, and D. A. Reaveley. Structure of the peptidoglycan of bacterial cell walls. II. *Journal of Molecular Biology*, 117(4):955–974, 1977.
- [15] Anetta Undas and Robert A.S. Ariëns. Fibrin Clot Structure and Function. *Arteriosclerosis, Thrombosis, and Vascular Biology*, 31(12), dec 2011.
- [16] Peter Fratzl and Richard Weinkamer. Nature’s hierarchical materials. *Progress in Materials Science*, 52(8):1263–1334, nov 2007.
- [17] Naoki Sasaki and Shingo Odajima. Elongation mechanism of collagen fibrils and force-strain relations of tendon at each level of structural hierarchy. *Journal of Biomechanics*, 29(9):1131–1136, sep 1996.
- [18] J. P. R. O. Orgel, Thomas C. Irving, Andrew Miller, and Tim J. Wess. Microfibrillar structure of type I collagen in situ. *Proceedings of the National Academy of Sciences*, 103(24):9001–9005, jun 2006.
- [19] S. Weiner and H. D. Wagner. THE MATERIAL BONE: Structure-Mechanical Function Relations. *Annual Review of Materials Science*, 28(1):271–298, aug 1998.
- [20] Markus J. Buehler and Sophie Y. Wong. Entropic Elasticity Controls Nanomechanics of Single Tropocollagen Molecules. *Biophysical Journal*, 93(1):37–43, jul 2007.
- [21] G. N. RAMACHANDRAN and GOPINATH KARTHA. Structure of Collagen. *Nature*, 176(4482):593–595, sep 1955.
- [22] Markus J. Buehler and Yu Ching Yung. Deformation and failure of protein materials in physiologically extreme conditions and disease. *Nature Materials*, 8(3):175–188, mar 2009.
- [23] Markus J. Buehler. Nature designs tough collagen: Explaining the nanostructure of collagen fibrils. *Proceedings of the National Academy of Sciences*, 103(33):12285–12290, aug 2006.
- [24] Himadri S. Gupta, Jong Seto, Wolfgang Wagermaier, Paul Zaslansky, Peter Boesecke, and Peter Fratzl. Cooperative deformation of mineral and collagen in bone at the nanoscale. *Proceedings of the National Academy of Sciences of the United States of America*, 2006.
- [25] R. Puxkandl, I. Zizak, O. Paris, J. Keckes, W. Tesch, S. Bernstorff, P. Purslow, and P. Fratzl. Viscoelastic properties of collagen: synchrotron radiation investigations and structural model. *Philosophical Transactions of the Royal Society of London. Series B: Biological Sciences*, 357(1418):191–197, feb 2002.
- [26] Huajian Gao, Baohua Ji, I. L. Jager, Eduard Arzt, and Peter Fratzl. Materials become insensitive to flaws at nanoscale: Lessons from nature. *Proceedings of the National Academy of Sciences*, 100(10):5597–5600, may 2003.
- [27] John W. Weisel and Rustem I. Litvinov. *Fibrin Formation, Structure and Properties*. Springer, Cham, 2017.
- [28] A. E. X. Brown, Rustem I. Litvinov, Dennis E. Discher, Prashant K. Purohit, and John W. Weisel. Multiscale Mechanics of Fibrin Polymer: Gel Stretching with Protein Unfolding and Loss of Water. *Science*, 325(5941):741–744, aug 2009.

- [29] John W. Weisel. The mechanical properties of fibrin for basic scientists and clinicians. *Biophysical Chemistry*, 112(2-3):267–276, dec 2004.
- [30] Robley C. Williams. Morphology of bovine fibrinogen monomers and fibrin oligomers. *Journal of Molecular Biology*, 150(3):399–408, aug 1981.
- [31] Cecil E. Hall and Henry S. Slayter. The Fibrinogen Molecule: Its Size, Shape, and Mode of Polymerization. *The Journal of Biophysical and Biochemical Cytology*, 5(1):11–27, jan 1959.
- [32] Harold P. Erickson and Walter E. Fowler. ELECTRON MICROSCOPY OF FIBRINOGEN, ITS PLASMIC FRAGMENTS AND SMALL POLYMERS. *Annals of the New York Academy of Sciences*, 408(1 Molecular Bio):146–163, jun 1983.
- [33] Irina N. Chernysh, Chandrasekaran Nagaswami, and John W. Weisel. Visualization and identification of the structures formed during early stages of fibrin polymerization. *Blood*, 117(17):4609–4614, apr 2011.
- [34] MW Mosesson, JP DiOrio, KR Siebenlist, JS Wall, and JF Hainfeld. Evidence for a second type of fibril branch point in fibrin polymer networks, the trimolecular junction. *Blood*, 82(5):1517–1521, sep 1993.
- [35] Fred J. Roska and John D. Ferry. Studies of fibrin film. I. Stress relaxation and birefringence. *Biopolymers*, 21(9):1811–1832, sep 1982.
- [36] Izabela K. Piechocka, Rommel G. Bacabac, Max Potters, Fred C. MacKintosh, and Gijsje H. Koenderink. Structural Hierarchy Governs Fibrin Gel Mechanics. *Biophysical Journal*, 98(10):2281–2289, may 2010.
- [37] Oleg V. Kim, Rustem I. Litvinov, John W. Weisel, and Mark S. Alber. Structural basis for the nonlinear mechanics of fibrin networks under compression. *Biomaterials*, 35(25):6739–6749, aug 2014.
- [38] Yuval Mulla, F. C. Mackintosh, and Gijsje H. Koenderink. Origin of Slow Stress Relaxation in the Cytoskeleton. *Physical Review Letters*, 122:218102, 2019.
- [39] Oliver Lieleg, Mireille M.A.E. Claessens, and Andreas R. Bausch. Structure and dynamics of cross-linked actin networks. *Soft Matter*, 6:218–225, 2010.
- [40] Paula de Almeida, Maarten Jaspers, Sarah Vaessen, Oya Tagit, Giuseppe Portale, Alan E. Rowan, and Paul H.J. Kowar. Cytoskeletal stiffening in synthetic hydrogels. *Nature Communications*, 10(-):609, 2019.
- [41] Maria Simonet Roda, Erika Griesshaber, Andreas Ziegler, Ulrich Rupp, Xiaofei Yin, Daniela Henkel, Vreni Häussermann, Jürgen Laudien, Uwe Brand, Anton Eisenhauer, Antonio G. Checa, and Wolfgang W. Schmahl. Calcite fibre formation in modern brachiopod shells. *Scientific Reports*, 9(-):598, 2019.
- [42] Karin A. Jansen, Albert J. Licup, Abhinav Sharma, Robbie Rens, Fred C. MacKintosh, and Gijsje H. Koenderink. The Role of Network Architecture in Collagen Mechanics. *Biophysical Journal*, 114(11):2665–2678, 2018.
- [43] Joe Swift, Irena L. Ivanovska, Amnon Buxboim, Takamasa Harada, P. C. Dave P. D. P. Dingal, Joel Pinter, J. David Pajerowski, Kyle R. Spinler, J.-W. Jae Won Shin, Manorama Tewari, Florian Rehfeldt, David W. Speicher, and Dennis E. Discher. Nuclear lamin-A scales with tissue stiffness and enhances matrix-directed differentiation. *Science*, 341(6149):1240104–1240104, aug 2013.

- [44] C. P. Broedersz and F. C. Mackintosh. Modeling semiflexible polymer networks. *Reviews of Modern Physics*, 86(3):995–1036, jul 2014.
- [45] Marcos Fernandez-Castano Romera, René P.M. Lafleur, Clément Guibert, Ilja K. Voets, Cornelis Storm, and Rint P. Sijbesma. Strain Stiffening Hydrogels through Self-Assembly and Covalent Fixation of Semi-Flexible Fibers. *Angewandte Chemie - International Edition*, 56(30):8771–8775, 2017.
- [46] Diederik W.R. Balkenende, Sally M. Winkler, and Phillip B. Messersmith. Marine-inspired polymers in medical adhesion. *European Polymer Journal*, 116:134–143, 2019.
- [47] Hailong Fan and Jian Ping Gong. Fabrication of Bioinspired Hydrogels: Challenges and Opportunities. *Macromolecules*, 53(8):2769–2782, 2020.
- [48] Ying Li, Bin Xue, and Yi Cao. 100th Anniversary of Macromolecular Science Viewpoint: Synthetic Protein Hydrogels. *ACS Macro Letters*, 9(4):512–524, apr 2020.
- [49] Alain J Cozzzone. Proteins: Fundamental Chemical Properties. In *Encyclopedia of Life Sciences*. John Wiley & Sons, Ltd, Chichester, feb 2002.
- [50] Alexei Finkelstein. *Protein Physics*. Academic Press, 2002.
- [51] J Berg, J Tymoczko, and L Stryer. *Biochemistry, 5th edition*. W H Freeman, New York, 2002.
- [52] Thomas M Devlin. *Textbook of biochemistry : with clinical correlations / edited by Thomas M. Devlin*. Wiley-Liss New York, 2011.
- [53] M. Lieberman, A.D. Marks, C.M. Smith, and D.B. Marks. *Marks' Basic Medical Biochemistry*. Lippincott Williams and Wilkins, Philadelphia 2007, 2007.
- [54] Senadhi Vijay-kumar, Charles E. Bugg, and William J. Cook. Structure of ubiquitin refined at 1.8 Å resolution. *Journal of Molecular Biology*, 194(3):531–544, apr 1987.
- [55] Massimo Paoli, Robert Liddington, Jeremy Tame, Anthony Wilkinson, and Guy Dodson. Crystal Structure of T State Haemoglobin with Oxygen Bound At All Four Haems. *Journal of Molecular Biology*, 256(4):775–792, mar 1996.
- [56] Jacob Israelachvili. *Intermolecular and Surface Forces*. Academic Press London, 2011.
- [57] S.K. Burley and G.A. Petsko. Weakly Polar Interactions In Proteins. In *Advances in Protein Chemistry*, pages 125–189. Elsevier, 1988.
- [58] Kim A. Sharp and S.Walter Englander. How much is a stabilizing bond worth? *Trends in Biochemical Sciences*, 19(12):526–529, dec 1994.
- [59] C.Nick Pace. Conformational stability of globular proteins. *Trends in Biochemical Sciences*, 15(1):14–17, jan 1990.
- [60] José Nelson Onuchic, Zaida Luthey-Schulten, and Peter G. Wolynes. THEORY OF PROTEIN FOLDING: The Energy Landscape Perspective. *Annual Review of Physical Chemistry*, 48(1):545–600, oct 1997.

- [61] Michael Schlierf and Matthias Rief. Single-Molecule Unfolding Force Distributions Reveal a Funnel-Shaped Energy Landscape. *Biophysical Journal*, 90(4):L33–L35, feb 2006.
- [62] Song-Ho Chong and Sihyun Ham. Folding Free Energy Landscape of Ordered and Intrinsically Disordered Proteins. *Scientific Reports*, 9(1):14927, dec 2019.
- [63] C Nick Pace, Gerald R Grimsley, J Martin Scholtz, and Kevin L Shaw. Protein Stability. In *eLS*. John Wiley & Sons, Ltd, Chichester, UK, feb 2014.
- [64] C. Nick Pace, Bret A. Shirley, Marsha McNutt, and Ketan Gajiwala. Forces contributing to the conformational stability of proteins. *The FASEB Journal*, 10(1):75–83, jan 1996.
- [65] Brian K. Shoichet, Walter A. Baase, Ryota Kuroki, and Brian W. Matthews. A relationship between protein stability and protein function. *Proceedings of the National Academy of Sciences*, 92(2):452–456, jan 1995.
- [66] Joyeeta Mukherjee and Munishwar Nath Gupta. Increasing importance of protein flexibility in designing biocatalytic processes. *Biotechnology Reports*, 6:119–123, jun 2015.
- [67] Toni Hoffmann and Lorna Dougan. Single molecule force spectroscopy using polyproteins. *Chemical Society Reviews*, 41(14):4781, 2012.
- [68] David J. Brockwell. Force Denaturation of Proteins - an Unfolding Story. *Current Nanoscience*, 3(1):3–15, feb 2007.
- [69] David J Brockwell and Sheena E Radford. Intermediates: ubiquitous species on folding energy landscapes? *Current Opinion in Structural Biology*, 17(1):30–37, feb 2007.
- [70] David J. Brockwell, Godfrey S. Beddard, Emanuele Paci, Dan K. West, Peter D. Olmsted, D. Alastair Smith, and Sheena E. Radford. Mechanically Unfolding the Small, Topologically Simple Protein L. *Biophysical Journal*, 89(1):506–519, jul 2005.
- [71] Hui Lu and Klaus Schulten. Steered molecular dynamics simulation of conformational changes of immunoglobulin domain I27 interpret atomic force microscopy observations. *Chemical Physics*, 247(1):141–153, aug 1999.
- [72] Toni Hoffmann, Katarzyna M. Tych, David J. Brockwell, and Lorna Dougan. Single-molecule force spectroscopy identifies a small cold shock protein as being mechanically robust. *Journal of Physical Chemistry B*, 117(6):1819–1826, 2013.
- [73] M. Carrion-Vazquez, A. F. Oberhauser, S. B. Fowler, P. E. Marszalek, S. E. Broedel, J. Clarke, and J. M. Fernandez. Mechanical and chemical unfolding of a single protein: A comparison. *Proceedings of the National Academy of Sciences*, 96(7):3694–3699, mar 1999.
- [74] Mariano Carrion-Vazquez, Andres F Oberhauser, Thomas E Fisher, Piotr E Marszalek, Hongbin Li, and Julio M Fernandez. Mechanical design of proteins studied by single-molecule force spectroscopy and protein engineering. *Progress in Biophysics and Molecular Biology*, 74(1-2):63–91, jul 2000.

- [75] M. Carrion-Vazquez, Teri Yoo, and Hongbin Li. Mechanical and chemical unfolding of a single protein: A comparison. *PNAS*, 96(7):3694–3699, aug 2008.
- [76] David J. Brockwell, Emanuele Paci, Rebecca C. Zinober, Godfrey S. Beddard, Peter D. Olmsted, D. Alastair Smith, Richard N. Perham, and Sheena E. Radford. Pulling geometry defines the mechanical resistance of a β -sheet protein. *Nature Structural & Molecular Biology*, 10(9):731–737, sep 2003.
- [77] Hendrik Dietz and Matthias Rief. Elastic Bond Network Model for Protein Unfolding Mechanics. *Physical Review Letters*, 100(9):098101, mar 2008.
- [78] Elizabeth A. Shank, Ciro Cecconi, Jesse W. Dill, Susan Marqusee, and Carlos Bustamante. The folding cooperativity of a protein is controlled by its chain topology. *Nature*, 465(7298):637–640, jun 2010.
- [79] B. Jagannathan, P. J. Elms, C. Bustamante, and S. Marqusee. Direct observation of a force-induced switch in the anisotropic mechanical unfolding pathway of a protein. *Proceedings of the National Academy of Sciences*, 109(44):17820–17825, oct 2012.
- [80] Morten Bertz, Andrea Kunfermann, and Matthias Rief. Navigating the Folding Energy Landscape of Green Fluorescent Protein. *Angewandte Chemie International Edition*, 47(43):8192–8195, oct 2008.
- [81] Morten Bertz and Matthias Rief. Mechanical Unfoldons as Building Blocks of Maltose-binding Protein. *Journal of Molecular Biology*, 378(2):447–458, 2008.
- [82] Morten Bertz and Matthias Rief. Ligand Binding Mechanics of Maltose Binding Protein. *Journal of Molecular Biology*, 393(5):1097–1105, 2009.
- [83] H. Dietz, F. Berkemeier, M. Bertz, and M. Rief. Anisotropic deformation response of single protein molecules. *Proceedings of the National Academy of Sciences*, 103(34):12724–12728, aug 2006.
- [84] H. Dietz and M. Rief. Protein structure by mechanical triangulation. *Proceedings of the National Academy of Sciences*, 103(5):1244–1247, jan 2006.
- [85] Pai-Chi Li and Dmitrii E. Makarov. Simulation of the mechanical unfolding of ubiquitin: Probing different unfolding reaction coordinates by changing the pulling geometry. *The Journal of Chemical Physics*, 121(10):4826–4832, sep 2004.
- [86] Yongnan Devin Li, Guillaume Lamour, Jörg Gsponer, Peng Zheng, and Hongbin Li. The Molecular Mechanism Underlying Mechanical Anisotropy of the Protein GB1. *Biophysical Journal*, 103(11):2361–2368, dec 2012.
- [87] Gaël Radou, Marta Enciso, Sergei Krivov, and Emanuele Paci. Modulation of a Protein Free-Energy Landscape by Circular Permutation. *The Journal of Physical Chemistry B*, 117(44):13743–13747, nov 2013.
- [88] Zhuoyun Zhuang, Andrew I Jewett, Patricia Soto, and Joan-Emma Shea. The effect of surface tethering on the folding of the src-SH3 protein domain. *Physical Biology*, 6(1):015004, feb 2009.
- [89] Mateusz Sikora, Joanna I. Sulikowska, and Marek Cieplak. Mechanical strength of 17 134 model proteins and cysteine slipknots. *PLoS Computational Biology*, 5(10):e1000547, oct 2009.

- [90] Mateusz Sikora, M. Ciepack, and J. I. Sulkowska. Bio-molecule stretching database, 2010.
- [91] M. Sikora, J. I. Sulkowska, B. S. Witkowski, and M. Cieplak. BSDB: the biomolecule stretching database. *Nucleic Acids Research*, 39(Database):D443–D450, jan 2011.
- [92] Toni Hoffmann, Katarzyna M. Tych, Megan L. Hughes, David J. Brockwell, and Lorna Dougan. Towards design principles for determining the mechanical stability of proteins. *Physical Chemistry Chemical Physics*, 15(38):15767, 2013.
- [93] J. V. Alemán, A. V. Chadwick, J. He, M. Hess, K. Horie, R. G. Jones, P. Kratochvíl, I. Meisel, I. Mita, G. Moad, S. Penczek, and R. F. T. Stepto. Definitions of terms relating to the structure and processing of sols, gels, networks, and inorganic-organic hybrid materials (IUPAC Recommendations 2007). *Pure and Applied Chemistry*, 79(10):1801–1829, jan 2007.
- [94] O. WICHTERLE and D. LÍM. Hydrophilic Gels for Biological Use. *Nature*, 185(4706):117–118, jan 1960.
- [95] Elbadawy A. Kamoun, El Refaie S. Kenawy, and Xin Chen. A review on polymeric hydrogel membranes for wound dressing applications: PVA-based hydrogel dressings. *Journal of Advanced Research*, 8(-):217–233, 2017.
- [96] Allan S. Hoffman. Hydrogels for biomedical applications. *Advanced Drug Delivery Reviews*, 64:18–23, dec 2012.
- [97] Azadeh Peivandi, Lei Tian, Randi Mahabir, and Zeinab Hosseinidoust. Hierarchically Structured, Self-Healing, Fluorescent, Bioactive Hydrogels with Self-Organizing Bundles of Phage Nanofilaments. *Chemistry of Materials*, 31(15):5442–5449, aug 2019.
- [98] Amber M. Hilderbrand, Eden M. Ford, Chen Guo, Jennifer D. Sloppy, and April M. Kloxin. Hierarchically structured hydrogels utilizing multifunctional assembling peptides for 3D cell culture. *Biomaterials Science*, 8(5):1256–1269, 2020.
- [99] Yusen Zhao, Bozhen Zhang, Bowen Yao, Yu Qiu, Zihang Peng, Yucheng Zhang, Yousif Alsaid, Imri Frenkel, Kareem Youssef, Qibing Pei, and Ximin He. Hierarchically Structured Stretchable Conductive Hydrogels for High-Performance Wearable Strain Sensors and Supercapacitors. *Matter*, 3(4):1196–1210, oct 2020.
- [100] Diego B. Genovese. Shear rheology of hard-sphere, dispersed, and aggregated suspensions, and filler-matrix composites. *Advances in Colloid and Interface Science*, 171-172:1–16, 2012.
- [101] T. van Vliet. Rheological properties of filled gels. Influence of filler matrix interaction. *Colloid and Polymer Science*, 266(6):518–524, jun 1988.
- [102] Rajinder Pal. Complex Shear Modulus of Concentrated Suspensions of Solid Spherical Particles. *Journal of Colloid and Interface Science*, 245(1):171–177, jan 2002.
- [103] Stefanie Utech and Aldo R. Boccaccini. A review of hydrogel-based composites for biomedical applications: enhancement of hydrogel properties by addition of rigid inorganic fillers. *Journal of Materials Science*, 51(1):271–310, jan 2016.

- [104] M.A. Rao and G.V. Barbosa-Cánovas. *Rheology of fluid and semisolid foods*. Springer, 2007.
- [105] Jun Yang, Chun Rui Han, Feng Xu, and Run Cang Sun. Simple approach to reinforce hydrogels with cellulose nanocrystals. *Nanoscale*, 6:5934–5943, 2014.
- [106] Akihide Sugawara, Taka Aki Asoh, Yoshinori Takashima, Akira Harada, and Hiroshi Uyama. Composite hydrogels reinforced by cellulose-based supramolecular filler. *Polymer Degradation and Stability*, 177, 2020.
- [107] Animesh Agrawal, Nima Rahbar, and Paul D. Calvert. Strong fiber-reinforced hydrogel. *Acta Biomaterialia*, 9(2):5313–5318, 2013.
- [108] Matthew J. Glassman and Bradley D. Olsen. Structure and mechanical response of protein hydrogels reinforced by block copolymer self-assembly. *Soft Matter*, 9(29):6814–6823, 2013.
- [109] J.P. Gong, Yoshinori Katsuyama, Takayuki Kurokawa, and Yoshihito Osada. Double-Network Hydrogels with Extremely High Mechanical Strength. *Advanced Materials*, 15(14):1155–1158, jul 2003.
- [110] Qiang Chen, Hong Chen, Lin Zhu, and Jie Zheng. Fundamentals of double network hydrogels. *Journal of Materials Chemistry B*, 3(18):3654–3676, 2015.
- [111] Jeong Yun Sun, Xuanhe Zhao, Widusha R.K. Illeperuma, Ovijit Chaudhuri, Kyu Hwan Oh, David J. Mooney, Joost J. Vlassak, and Zhigang Suo. Highly stretchable and tough hydrogels. *Nature*, 489(7414):133–136, 2012.
- [112] Ziqing Tang, Qiang Chen, Feng Chen, Lin Zhu, Shaoping Lu, Baiping Ren, Yanxian Zhang, Jia Yang, and Jie Zheng. General Principle for Fabricating Natural Globular Protein-Based Double-Network Hydrogels with Integrated Highly Mechanical Properties and Surface Adhesion on Solid Surfaces. *Chemistry of Materials*, 31(1):179–189, 2019.
- [113] Jun Cui, Melissa A. Lackey, Ahmad E. Madkour, Erika M. Saffer, David M. Griffin, Surita R. Bhatia, Alfred J. Crosby, and Gregory N. Tew. Synthetically simple, highly resilient hydrogels. *Biomacromolecules*, 13(3):584–588, 2012.
- [114] Jacek K. Wychowaniec, Maria Iliut, Mi Zhou, Jonathan Moffat, Mohamed A. Elsayy, Wagner A. Pinheiro, Judith A. Hoyland, Aline F. Miller, Aravind Vijayaraghavan, and Alberto Saiani. Designing Peptide/Graphene Hybrid Hydrogels through Fine-Tuning of Molecular Interactions. *Biomacromolecules*, 19:2731–2741, 2018.
- [115] Jie Gao, Claire Tang, Mohamed A. Elsayy, Andrew M. Smith, Aline F. Miller, and Alberto Saiani. Controlling Self-Assembling Peptide Hydrogel Properties through Network Topology. *Biomacromolecules*, 18:826–834, 2017.
- [116] Jacek K. Wychowaniec, Andrew M. Smith, Cosimo Ligorio, Oleksandr O. Mykhaylyk, Aline F. Miller, and Alberto Saiani. Role of Sheet-Edge Interactions in β -sheet Self-Assembling Peptide Hydrogels. *Biomacromolecules*, 21(6):2285–2297, 2020.
- [117] Eleanor F. Banwell, Edgardo S. Abelardo, Dave J. Adams, Martin A. Birchall, Adam Corrigan, Athene M. Donald, Mark Kirkland, Louise C. Serpell, Michael F. Butler, and Derek N. Woolfson. Rational design and application of responsive α -helical peptide hydrogels. *Nature Materials*, 8:596–600, 2009.

- [118] Thomas E. Fisher, Andres F. Oberhauser, Mariano Carrion-Vazquez, Piotr E. Marszalek, and Julio M. Fernandez. The study of protein mechanics with the atomic force microscope. *Trends in Biochemical Sciences*, 24(10):379–384, 1999.
- [119] Elias M. Puchner and Hermann E. Gaub. Force and function: probing proteins with AFM-based force spectroscopy. *Current Opinion in Structural Biology*, 19(5):605–614, 2009.
- [120] Shanshan Lv, Daniel M. Dudek, Yi Cao, M. M. Balamurali, John Gosline, and Hongbin Li. Designed biomaterials to mimic the mechanical properties of muscles. *Nature*, 465(7294):69–73, 2010.
- [121] Hongbin Li, Na Kong, Bryce Laver, and Junqiu Liu. Hydrogels Constructed from Engineered Proteins. *Small*, 12(8):973–987, feb 2016.
- [122] Kongchang Wei, Berna Senturk, Martin T. Matter, Xi Wu, Inge K. Herrmann, Markus Rottmar, and Claudio Toncelli. Mussel-Inspired Injectable Hydrogel Adhesive Formed under Mild Conditions Features Near-Native Tissue Properties. *ACS Applied Materials and Interfaces*, 11(51):47707–47719, 2019.
- [123] Na Kong, Linglan Fu, Qing Peng, and Hongbin Li. Metal Chelation Dynamically Regulates the Mechanical Properties of Engineered Protein Hydrogels. *ACS Biomaterials Science and Engineering*, 3(5):742–749, 2017.
- [124] Ming Liang Zhou, Zhi Gang Qian, Liang Chen, David L. Kaplan, and Xiao Xia Xia. Rationally Designed Redox-Sensitive Protein Hydrogels with Tunable Mechanical Properties. *Biomacromolecules*, 17(11):3508–3515, 2016.
- [125] Tianyu Duan and Hongbin Li. In Situ Phase Transition of Elastin-Like Polypeptide Chains Regulates Thermoresponsive Properties of Elastomeric Protein-Based Hydrogels. *Biomacromolecules*, 2020.
- [126] Linglan Fu, Amanda Haage, Na Kong, Guy Tanentzapf, and Hongbin Li. Dynamic protein hydrogels with reversibly tunable stiffness regulate human lung fibroblast spreading reversibly. *Chemical Communications*, 55(36):5235–5238, 2019.
- [127] Na Kong, Qing Peng, and Hongbin Li. Rationally designed dynamic protein hydrogels with reversibly tunable mechanical properties. *Advanced Functional Materials*, 24(46):7310–7317, 2014.
- [128] Luai R. Khoury, Marina Slawinski, Daniel R. Collison, and Ionel Popa. Cation-induced shape programming and morphing in protein-based hydrogels. *Science Advances*, 6(18):6112, 2020.
- [129] Luai R. Khoury and Ionel Popa. Chemical unfolding of protein domains induces shape change in programmed protein hydrogels. *Nature Communications*, 10:5439, 2019.
- [130] Junhua Wu, Pengfei Li, Chenling Dong, Heting Jiang, Bin Xue, Xiang Gao, Meng Qin, Wei Wang, Bin Chen, and Yi Cao. Rationally designed synthetic protein hydrogels with predictable mechanical properties. *Nature Communications*, 9(620):–, 2018.
- [131] David S. Knoff, Haley Szczublewski, Dallas Altamirano, Kareen A. Fajardo Cortes, and Minkyu Kim. Cytoskeleton-Inspired Artificial Protein Design to Enhance Polymer Network Elasticity. *Macromolecules*, 53(9):3463–3471, 2020.

- [132] Emily R. Draper, Bart Dietrich, Kate McAulay, Christopher Brasnett, Haleh Abdizadeh, Ilias Patmanidis, Siewert J. Marrink, Hao Su, Honggang Cui, Ralf Schweins, Annela Seddon, and Dave J. Adams. Using Small-Angle Scattering and Contrast Matching to Understand Molecular Packing in Low Molecular Weight Gels. *Matter*, 2(3):764–778, mar 2020.
- [133] Valery Novokhatny and Kenneth Ingham. Thermodynamics of maltose binding protein unfolding. *Protein Science*, 6(1):141–146, 1997.
- [134] Marcelo a. Da Silva, Samuel Lenton, Matthew Hughes, David J. Brockwell, and Lorna Dougan. Assessing the Potential of Folded Globular Polyproteins As Hydrogel Building Blocks. *Biomacromolecules*, 18(2):636–646, 2017.
- [135] Matt D. G. Hughes, Sophie Cussons, Najet Mahmoudi, David J. Brockwell, and Lorna Dougan. Single molecule protein stabilisation translates to macromolecular mechanics of a protein network. *Soft Matter*, 16(27):6389–6399, 2020.
- [136] Anders Aufderhorst-Roberts, Matt D. G. Hughes, Andrew Hare, David A. Head, Nikil Kapur, David J. Brockwell, and Lorna Dougan. Reaction Rate Governs the Viscoelasticity and Nanostructure of Folded Protein Hydrogels. *Biomacromolecules*, 21(10):4253–4260, oct 2020.
- [137] Claude V. Maina, Paul D. Riggs, Andres G. Grandea, Barton E. Slatko, Laurie S. Moran, John A. Tagliamonte, Larry A. McReynolds, and di Guan Chu. An Escherichia coli vector to express and purify foreign proteins by fusion to and separation from maltose-binding protein. *Gene*, 74(2):365–373, dec 1988.
- [138] Paul Riggs. Expression and Purification of Maltose-Binding Protein Fusions. *Current Protocols in Molecular Biology*, 28(1), oct 1994.
- [139] A. Kalnins, K. Otto, U. Rütther, and B. Müller-Hill. Sequence of the lacZ gene of Escherichia coli. *The EMBO Journal*, 2(4):593–597, apr 1983.
- [140] F. William Studier. Protein production by auto-induction in high density shaking cultures. *Protein expression and purification*, 41(1):207–234, may 2005.
- [141] Paul Cutler. Affinity Chromatography. In *Protein Purification Protocols*, pages 157–168. Humana Press, New Jersey, 1996.
- [142] Joshua A. Bornhorst and Joseph J. Falke. [16] Purification of proteins using poly-histidine affinity tags. In *Methods in Enzymology*, pages 245–254. Elsevier, 2000.
- [143] R.P. Wayne, C.E. Wayne. *Photochemistry*. Oxford University Press, 1996.
- [144] David a. Fancy and Thomas Kodadek. Chemistry for the analysis of protein-protein interactions: Rapid and efficient cross-linking triggered by long wavelength light. *Proceedings of the National Academy of Sciences of the United States of America*, 96(11):6020–6024, 1999.
- [145] David A. Fancy, Carilee Denison, Kyonghee Kim, Yueqing Xie, Terra Holdeman, Frank Amini, and Thomas Kodadek. Scope, limitations and mechanistic aspects of the photo-induced cross-linking of proteins by water-soluble metal complexes. *Chemistry & Biology*, 7(9):697–708, sep 2000.

- [146] Sharon M. Kelly, Thomas J. Jess, and Nicholas C. Price. How to study proteins by circular dichroism. *Biochimica et Biophysica Acta (BBA) - Proteins and Proteomics*, 1751(2):119–139, aug 2005.
- [147] Dave3457. No Title, 2021.
- [148] Norma J. Greenfield and Gerald D. Fasman. Computed circular dichroism spectra for the evaluation of protein conformation. *Biochemistry*, 8(10):4108–4116, oct 1969.
- [149] Norma J. Greenfield. Using circular dichroism spectra to estimate protein secondary structure. *Nature Protocols*, 1(6):2876–2890, dec 2006.
- [150] Giuseppe Zaccai. How Soft Is a Protein? A Protein Dynamics Force Constant Measured by Neutron Scattering. *Science*, 288(5471), 2000.
- [151] Wolfgang F. HÖHNE, Günther; Hemminger. *Differential scanning calorimetry*. Springer-Verlag Berlin Heidelberg, 2013.
- [152] J. M. Sanchez-Ruiz. *Differential scanning calorimetry of proteins.*, 1995.
- [153] Christopher Hammond. *The Basics of Crystallography and Diffraction*. Oxford University Press, may 2015.
- [154] B. T. M. Willis and C.J. Carlile. *Experimental Neutron Scattering*. Oxford University Press Inc. New York, NY, 2009.
- [155] D.S. Sivia. *Elementary Scattering Theory*. Oxford University Press, jan 2011.
- [156] W.H. Bragg and W.L. Bragg. The reflection of X-rays by crystals. *Proceedings of the Royal Society of London. Series A, Containing Papers of a Mathematical and Physical Character*, 88(605):428–438, jul 1913.
- [157] Ron Bracewell. *The Fourier Transform and Its Applications (2nd Ed.)*. McGraw-Hill, 1986.
- [158] R. K. Heenan, J. Penfold, and S. M. King. SANS at Pulsed Neutron Sources: Present and Future Prospects. *Journal of Applied Crystallography*, 30(6):1140–1147, dec 1997.
- [159] John D. Ferry. *Viscoelastic properties of polymers*. John Wiley & Sons, Inc., 1980.
- [160] Leyou Zhang and Xiaoming Mao. Fracturing of topological Maxwell lattices. *New Journal of Physics*, 20(6):063034, jun 2018.
- [161] P. Duplay, H. Bedouelle, A. Fowler, I. Zabin, W. Saurin, and M. Hofnung. Sequences of the malE gene and of its product, the maltose-binding protein of *Escherichia coli* K12. *Journal of Biological Chemistry*, 259(16):10606–10613, aug 1984.
- [162] Sherry L. LaPorte, Charles M. Forsyth, Brian C. Cunningham, Larry J. Miercke, David Akhavan, and Robert M. Stroud. De novo design of an IL-4 antagonist and its structure at 1.9 Å. *Proceedings of the National Academy of Sciences*, 102(6):1889–1894, 2005.

- [163] Xiaoqun Duan and Florante A. Quioco. Structural evidence for a dominant role of nonpolar interactions in the binding of a transport/chemosensory receptor to its highly polar ligands. *Biochemistry*, 41(3):706–712, 2002.
- [164] Chris Green. Pac-Man, 2002.
- [165] Jeffrey D. Fox and David S. Waugh. Maltose-Binding Protein as a Solubility Enhancer. In *E. coli Gene Expression Protocols*, pages 99–118. Humana Press, New Jersey, 2003.
- [166] Jan Philipp Junker, Fabian Ziegler, and Matthias Rief. Ligand-dependent equilibrium fluctuations of single calmodulin molecules. *Science*, 323(5914):633–637, 2009.
- [167] Sri Rama Koti Ainavarapu, Lewyn Li, Carmen L. Badilla, and Julio M. Fernandez. Ligand binding modulates the mechanical stability of dihydrofolate reductase. *Biophysical Journal*, 89(5):3337–3344, nov 2005.
- [168] Yi Cao, Teri Yoo, Shulin Zhuang, and Hongbin Li. Protein-Protein Interaction Regulates Proteins’ Mechanical Stability. *Journal of Molecular Biology*, 378:1132–1141, 2008.
- [169] Yi Cao, M. M. Balamurali, Deepak Sharma, and Hongbin Li. A functional single-molecule binding assay via force spectroscopy. *Proceedings of the National Academy of Sciences of the United States of America*, 104:15677–15681, 2007.
- [170] Michael Zocher, Cheng Zhang, Søren G.F. Rasmussen, Brian K. Kobilka, and Daniel J. Müller. Cholesterol increases kinetic, energetic, and mechanical stability of the human β 2-adrenergic receptor. *Proceedings of the National Academy of Sciences of the United States of America*, 109:E3463–E3472, 2012.
- [171] Chien Chung Wang, Tian Yow Tsong, Yau Heiu Hsu, and Piotr E. Marszalek. Inhibitor binding increases the mechanical stability of staphylococcal nuclease. *Biophysical Journal*, 100:1094–1099, 2011.
- [172] J. C. Spurlino, G. Y. Lu, and F. A. Quioco. The 2.3-Å resolution structure of the maltose- or maltodextrin-binding protein, a primary receptor of bacterial active transport and chemotaxis. *Journal of Biological Chemistry*, 266(8):5202–5219, 1991.
- [173] C. Nick Pace, J. Martin Scholtz, and Gerald R. Grimsley. Forces stabilizing proteins, 2014.
- [174] Michael Schlierf and Matthias Rief. Temperature softening of a protein in single-molecule experiments. *Journal of Molecular Biology*, 354(2):497–503, 2005.
- [175] Hans Bisswanger. *Enzyme Kinetics*. ILEY-VCH Verlag GmbH & Co. KGaA, Weinheim, Germany, mar 2008.
- [176] Patrick G Telmer and Brian H Shilton. Insights into the Conformational Equilibria of Maltose-binding Protein by Analysis of High Affinity Mutants. *Journal of Biological Chemistry*, 278(36):34555–34567, sep 2003.
- [177] Iris H. Walker, Pei-chung Hsieh, and Paul D. Riggs. Mutations in maltose-binding protein that alter affinity and solubility properties. *Applied Microbiology and Biotechnology*, 88(1):187–197, sep 2010.

- [178] Matthieu Pouzot, Taco Nicolai, Lazhar Benyahia, and Dominique Durand. Strain hardening and fracture of heat-set fractal globular protein gels. *Journal of Colloid and Interface Science*, 293(2):376–383, 2006.
- [179] Jan Michael Y. Carrillo, Fred C. MacKintosh, and Andrey V. Dobrynin. Nonlinear elasticity: From single chain to networks and gels. *Macromolecules*, 46(9):3679–3692, 2013.
- [180] Bavand Keshavarz, Thibaut Divoux, Sébastien Manneville, and Gareth H. McKinley. Nonlinear Viscoelasticity and Generalized Failure Criterion for Polymer Gels. *ACS Macro Letters*, 6(7):633–667, 2017.
- [181] T. Baumberger and O. Ronsin. From thermally activated to viscosity controlled fracture of biopolymer hydrogels. *Journal of Chemical Physics*, 130(6):–, 2009.
- [182] Daniel Bonn, Hamid Kellay, Michaël Prochnow, Karim Ben-Djemaa, and Jacques Meunier. Delayed fracture of an inhomogeneous soft solid. *Science*, 280(5361):265–267, 1998.
- [183] Mathieu Leocmach, Christophe Perge, Thibaut Divoux, and Sébastien Manneville. Creep and fracture of a protein gel under stress. *Physical Review Letters*, 133(3):038303, 2014.
- [184] Irving Langmuir. THE ADSORPTION OF GASES ON PLANE SURFACES OF GLASS, MICA AND PLATINUM. *Journal of the American Chemical Society*, 40(9):1361–1403, sep 1918.
- [185] J. Teixeira. Small-angle scattering by fractal systems. *Journal of Applied Crystallography*, 21(6):781–785, dec 1988.
- [186] Sow-Hsin Chen and José Teixeira. Structure and Fractal Dimension of Protein-Detergent Complexes. *Physical Review Letters*, 57(20):2583–2586, nov 1986.
- [187] Jens Feder. *Fractals*. Springer US, 1988.
- [188] Heinz Kiessig. Untersuchungen zur Totalreflexion von Röntgenstrahlen. *Annalen der Physik*, 402(6):–, 1931.
- [189] Christopher Hammond. *The Basics of Crystallography and Diffraction (2nd edn)*. OUP Oxford, 2002.
- [190] T. A. Witten and L. M. Sander. Diffusion-Limited Aggregation, a Kinetic Critical Phenomenon. *Physical Review Letters*, 47(19):1400–1403, nov 1981.
- [191] T. A. Witten and L. M. Sander. Diffusion-limited aggregation. *Physical Review B*, 27(9):5686–5697, may 1983.
- [192] H. Zhang, M. Yoshimura, K. Nishinari, M. A.K. Williams, T. J. Foster, and I. T. Norton. Gelation behaviour of konjac glucomannan with different molecular weights. *Biopolymers*, 59(38), 2001.
- [193] Bosi Mao, Thibaut Divoux, and Patrick Snabre. Normal force controlled rheology applied to agar gelation. *Journal of Rheology*, 60(3):473–489, 2016.

- [194] David J. Brockwell, Godfrey S. Beddard, Emanuele Paci, Dan K. West, Peter D. Olmsted, D. Alastair Smith, and Sheena E. Radford. Mechanically Unfolding the Small, Topologically Simple Protein L. *Biophysical Journal*, 89(1):506–519, jul 2005.
- [195] Yu Ran Na and Chiwook Park. Investigating protein unfolding kinetics by pulse proteolysis. *Protein Science*, 18(2):268–276, 2009.
- [196] Lucie Ducloué, Olivier Pitois, Julie Goyon, Xavier Chateau, and Guillaume Ovarlez. Coupling of elasticity to capillarity in soft aerated materials. *Soft Matter*, 10(28):5093–5098, 2014.
- [197] Sabita Sharma, Smrithika Subramani, and Ionel Popa. Does protein unfolding play a functional role in vivo ? *The FEBS Journal*, page febs.15508, sep 2020.
- [198] Hongbin Li, Wolfgang A. Linke, Andres F. Oberhauser, Mariano Carrion-Vazquez, Jason G. Kerkvliet, Hui Lu, Piotr E. Marszalek, and Julio M. Fernandez. Reverse engineering of the giant muscle protein titin. *Nature*, 418(6901):998–1002, aug 2002.
- [199] Sumit Prakash and Andreas Matouschek. Protein unfolding in the cell. *Trends in Biochemical Sciences*, 29(11):593–600, nov 2004.
- [200] Wolfgang A. Linke and Nazha Hamdani. Gigantic Business. *Circulation Research*, 114(6):1052–1068, mar 2014.
- [201] Lukas F. Milles, Klaus Schulten, Hermann E. Gaub, and Rafael C. Bernardi. Molecular mechanism of extreme mechanostability in a pathogen adhesin. *Science*, 359(6383):1527–1533, mar 2018.
- [202] Rajat N. Moman and Matthew Varacallo. *Physiology, Albumin*. StatPearls Publishing, 2019.
- [203] E. J. Cohn, L. E. Strong, W. L. Hughes, D. J. Mulford, J. N. Ashworth, M. Melin, and H. L. Taylor. Preparation and Properties of Serum and Plasma Proteins. IV. A System for the Separation into Fractions of the Protein and Lipoprotein Components of Biological Tissues and Fluids. *Journal of the American Chemical Society*, 1946.
- [204] Arun P. Wiita, Sri Rama Koti Ainavarapu, Hector H. Huang, and Julio M. Fernandez. Force-dependent chemical kinetics of disulfide bond reduction observed with single-molecule techniques. *Proceedings of the National Academy of Sciences*, 103(19):7222–7227, may 2006.
- [205] Jie Fang, Alexander Mehlich, Nobuyasu Koga, Jiqing Huang, Rie Koga, Xiaoye Gao, Chunguang Hu, Chi Jin, Matthias Rief, Juergen Kast, David Baker, and Hongbin Li. Forced protein unfolding leads to highly elastic and tough protein hydrogels. *Nature Communications*, 4(1):2974, dec 2013.
- [206] Igor N. Serdyuk, Nathan R. Zaccai, and Joseph Zaccai. *Methods in Molecular Biophysics*. Cambridge University Press, Cambridge, 2007.
- [207] Sandip Paul, Nasim Sepay, Shrabana Sarkar, Pritam Roy, Swagata Dasgupta, Pinki Saha Sardar, and Anjoy Majhi. Interaction of serum albumins with fluorescent ligand 4-azido coumarin: spectroscopic analysis and molecular docking studies. *New Journal of Chemistry*, 41(24):15392–15404, 2017.

- [208] J. Bibette, T. G. Mason, Hu Gang, and D. A. Weitz. Kinetically induced ordering in gelation of emulsions. *Physical Review Letters*, 69(6):–, 1992.
- [209] Marina Carpineti and Marzio Giglio. Spinodal-type dynamics in fractal aggregation of colloidal clusters. *Physical Review Letters*, 1(1):–, 1992.
- [210] M. Y. Lin, H. M. Lindsay, D. A. Weitz, R. C. Ball, R. Klein, and P. Meakin. Universality in colloid aggregation. *Nature*, 339(6223):360–362, jun 1989.
- [211] Svetlana Jungblut, Jan-Ole Joswig, and Alexander Eychmüller. Diffusion- and reaction-limited cluster aggregation revisited. *Physical Chemistry Chemical Physics*, 21(10):5723–5729, mar 2019.
- [212] Benjamin S. Hanson, David Head, and Lorna Dougan. The hierarchical emergence of worm-like chain behaviour from globular domain polymer chains. *Soft Matter*, 15(43):8778–8789, 2019.
- [213] Benjamin S. Hanson and Lorna Dougan. Network Growth and Structural Characteristics of Globular Protein Hydrogels. *Macromolecules*, 53(17):7335–7345, sep 2020.
- [214] Olga V. Stepanenko, Olga I. Povarova, Anna I. Sulatskaya, Luisa A. Ferreira, Boris Y. Zaslavsky, Irina M. Kuznetsova, Konstantin K. Turoverov, and Vladimir N. Uversky. Protein unfolding in crowded milieu: what crowding can do to a protein undergoing unfolding? *Journal of Biomolecular Structure and Dynamics*, 34(10):2155–2170, oct 2016.
- [215] Shang Zhang, Leyou Zhang, Mehdi Bouzid, D. Zeb Rocklin, Emanuela Del Gado, and Xiaoming Mao. Correlated Rigidity Percolation and Colloidal Gels. *Physical Review Letters*, 123(5):058001, jul 2019.
- [216] Alessio Zaccone, Hua Wu, and Emanuela Del Gado. Elasticity of Arrested Short-Ranged Attractive Colloids: Homogeneous and Heterogeneous Glasses. *Physical Review Letters*, 103(20):208301, nov 2009.
- [217] Kathryn A. Whitaker, Zsigmond Varga, Lilian C. Hsiao, Michael J. Solomon, James W. Swan, and Eric M. Furst. Colloidal gel elasticity arises from the packing of locally glassy clusters. *Nature Communications*, 10(1):2237, dec 2019.
- [218] Jonathan J. Booth and Dmitrii V. Shalashilin. Fully Atomistic Simulations of Protein Unfolding in Low Speed Atomic Force Microscope and Force Clamp Experiments with the Help of Boxed Molecular Dynamics. *The Journal of Physical Chemistry B*, 120(4):700–708, feb 2016.
- [219] Toni Hoffmann and Lorna Dougan. Single molecule force spectroscopy using polyproteins. *Chemical Society Reviews*, 41(14):4781, 2012.
- [220] Peter J. Rossky. Protein denaturation by urea: Slash and bond. *Proceedings of the National Academy of Sciences*, 105(44):16825–16826, nov 2008.
- [221] A.V. Finkelstein and O.V. Galzitskaya. Physics of protein folding. *Physics of Life Reviews*, 1(1):23–56, apr 2004.
- [222] Matthew Auton, Luis Marcelo F. Holthauzen, and D. Wayne Bolen. Anatomy of energetic changes accompanying urea-induced protein denaturation. *Proceedings of the National Academy of Sciences*, 104(39):15317–15322, sep 2007.

- [223] Lan Hua, Ruhong Zhou, D. Thirumalai, and B. J. Berne. Urea denaturation by stronger dispersion interactions with proteins than water implies a 2-stage unfolding. *Proceedings of the National Academy of Sciences*, 105(44):16928–16933, nov 2008.
- [224] Deepak R. Canchi and Angel E. García. Backbone and Side-Chain Contributions in Protein Denaturation by Urea. *Biophysical Journal*, 100(6):1526–1533, mar 2011.
- [225] Atanu Das and Chaitali Mukhopadhyay. Urea-Mediated Protein Denaturation: A Consensus View. *The Journal of Physical Chemistry B*, 113(38):12816–12824, sep 2009.
- [226] Jeffrey K. Myers, C. Nick Pace, and J. Martin Scholtz. Denaturant m values and heat capacity changes: Relation to changes in accessible surface areas of protein unfolding. *Protein Science*, 4(10):2138–2148, oct 1995.
- [227] Paul J. Flory and John Rehner. Statistical Mechanics of Cross-Linked Polymer Networks II. Swelling. *The Journal of Chemical Physics*, 11(11):521–526, nov 1943.
- [228] Paul J. Flory and John Rehner. Statistical Mechanics of Cross-Linked Polymer Networks II. Swelling. *The Journal of Chemical Physics*, 11(11):521–526, nov 1943.
- [229] Werner Kuhn. Über die Gestalt fadenförmiger Moleküle in Lösungen. *Kolloid-Zeitschrift*, 68(1):2–15, feb 1934.
- [230] Hubert M. James and Eugene Guth. Theory of the Elastic Properties of Rubber. *The Journal of Chemical Physics*, 11(10):455–481, oct 1943.
- [231] Michael Rubinstein and Ralph H. Colby. *Polymer Physics*. Oxford University Press, 2003.
- [232] Hongbin Li and Yi Cao. Protein mechanics: From single molecules to functional biomaterials. *Accounts of Chemical Research*, 43(10):1331–1341, oct 2010.
- [233] Yi Cao and Hongbin Li. Polyprotein of GB1 is an ideal artificial elastomeric protein. *Nature Materials*, 6:109–114, 2007.
- [234] Katarzyna M. Tych, Megan L. Hughes, James Bourke, Yukinori Taniguchi, Masaru Kawakami, David J. Brockwell, and Lorna Dougan. Optimizing the calculation of energy landscape parameters from single-molecule protein unfolding experiments. *Physical Review E - Statistical, Nonlinear, and Soft Matter Physics*, 91(1):1–9, 2015.
- [235] Congqi Yan and Darrin J Pochan. Rheological properties of peptide-based hydrogels for biomedical and other applications. *Chemical Society Reviews*, 39(9):3528–3540, 2010.
- [236] Enas M Ahmed. Hydrogel: Preparation, characterization, and applications: A review, 2015.